UNDERSTANDING THE ORIGINS OF YELLOWSTONE HOT SPOT MAGMAS THROUGH ISOTOPE GEOCHEMISTRY, HIGH-PRECISION GEOCHRONOLOGY, AND MAGMATIC-THERMOMECHANICAL COMPUTER MODELING

by

DYLAN PATRICK COLÓN

A DISSERTATION

Presented to the Department of Earth Sciences
and the Graduate School of the University of Oregon
in partial fulfillment of the requirements
for the degree of
Doctor of Philosophy

June 2018

DISSERTATION APPROVAL PAGE

Student: Dylan Patrick Colón

Title: Understanding the Origins of Yellowstone Hot Spot Magmas Through Isotope Geochemistry, High-Precision Geochronology, and Magmatic-Thermomechanical Computer Modeling

This dissertation has been accepted and approved in partial fulfillment of the requirements for the Doctor of Philosophy degree in the Department of Earth Sciences by:

Ilya Bindeman	Chairperson
Eugene Humphreys	Core Member
Paul Wallace	Core Member
Catherine Page	Institutional Representative

and

Sara D. Hodges	Interim Vice Provost and Dean of the Graduate School

Original approval signatures are on file with the University of Oregon Graduate School.

Degree awarded June 2018.

DISSERTATION ABSTRACT

Dylan Patrick Colón

Doctor of Philosophy

Department of Earth Sciences

June 2018

Title: Understanding the Origins of Yellowstone Hot Spot Magmas Through Isotope Geochemistry, High-Precision Geochronology, and Magmatic-Thermomechanical Computer Modeling

The last several years have seen renewed interest in the origin of silicic magmas thanks to the developments of new microanalytical techniques allowing the measurement of the isotopic and trace element compositions of erupted magmas on sub-crystal length scales. Concurrently, there has been rapid improvement in the sophistication of computer modeling of igneous systems. This dissertation is an interdisciplinary study of the rhyolites of the Yellowstone hotspot track using both techniques.

Chapters II-IV, which have all been published in existing journals, are a detailed study of the O and Hf isotopic compositions of zircon phenocrysts from large rhyolitic eruptions in the central Snake River Plain, and from rhyolites which erupted in Oregon, Idaho, and Nevada coeval with the Columbia River flood basalts. They show that rhyolites are derived from combinations of fractionates of mantle-derived basalts and of different crustal end-members which are identifiable by their distinct isotopic end-member compositions. In the Snake River Plain and Yellowstone, they recognize a common trend where early erupted rhyolites have a strong signature of melting of ancient Precambrian crust, whereas later erupted rhyolites more closely resemble the mantle in their radiogenic isotopes and are more likely to be depleted in oxygen isotopes. Diversity

in zircon grain compositions also documents a batch mixing process in which multiple compositionally distinct magma bodies are assembled into a larger common magma body prior to eruption.

In Chapters V and VI, the former of which has been published with the latter in preparation, a new series of magmatic-thermomechanical models is presented which assume that melts rising through the crust are arrested by strong rheological contrasts. The strongest such contrast occurs at the brittle-ductile transition at 5-10 km depth, leading to the formation of a 10-15 km thick mafic mid-crustal sill, which separates upper and lower-crustal zones of partial melt, corroborating previous geophysical imaging studies. In Chapter VI, the above isotopic trends are replicated in the modeling scheme, which shows that the source depth of crustal melts tends to shallow with time through a combination of crustal heating and repeated caldera collapses.

This dissertation includes both previously published co-authored material.

CURRICULUM VITAE

NAME OF AUTHOR: Dylan Patrick Colón

GRADUATE AND UNDERGRADUATE SCHOOLS ATTENDED:

University of Oregon, Eugene
University of Wisconsin-Madison

DEGREES AWARDED:

Doctor of Philosophy, 2018, Earth Sciences, University of Oregon
Bachelor of Science, 2011, Geology and Physics, University of Wisconsin Madison

AREAS OF SPECIAL INTEREST:

Isotope geochemistry
Igneous petrology
Volcanology
Magmatic-thermomechanical modeling

PROFESSIONAL EXPERIENCE:

Graduate employee, Department of Earth Sciences, University of Oregon, Fall 2012-Spring 2018

Student Researcher, Rare Gas Geochronology Laboratory, Department of Geology, University of Wisconsin, Summer 2009-Summer 2011

GRANTS, AWARDS, AND HONORS:

University of Oregon Research Recognition Award, 2018.

University of Oregon Staples Scholarship, 2015, 2016.

Geological Society of America Graduate Student Research Grant, "Understanding the origins of extension-related rhyolites in large igneous provinces: a case study from the Columbia River Large Igneous Province," 2016.

Goldschmidt Student Assistance Grant, 2015.

University of Oregon Outstanding Graduate Teaching Fellow Award, 2015.

University of Oregon McMurray Award, 2014.

University of Oregon Johnston Fellowship, 2012.

University of Wisconsin-Madison Bernhard-Knapp Scholarship, 2007-2011.

University of Wisconsin-Madison Chancellor's Scholarship, 2007-2011.

Shell Undergraduate Research Grant, 2011.

PUBLICATIONS:

Colón, D. P., Bindeman, I. N., & Gerya, T. V. (2018). Thermomechanical modeling of the formation of a multilevel, crustal-scale magmatic system by the Yellowstone plume. *Geophysical Research Letters*, *45*(9), 3873–3879. https://doi.org/10.1029/2018GL077090

Colón, D. P., Bindeman, I. N., Wotzlaw, J.-F., Christiansen, E. H., & Stern, R. A. (2018). Origins and evolution of rhyolitic magmas in the central Snake River Plain: insights from coupled high-precision geochronology, oxygen isotope, and hafnium isotope analyses of zircon. *Contributions to Mineralogy and Petrology*, *173*(2), 11. https://doi.org/10.1007/s00410-017-1437-y

Lhuillier, F., Gilder, S. A., Wack, M., He, K., Petersen, N., Singer, B. S., … **Colon, D.** (2016). More stable yet bimodal geodynamo during the Cretaceous superchron? *Geophysical Research Letters*, *43*(12), 6170–6177. https://doi.org/10.1002/2016GL069303

Colón, D. P., Bindeman, I. N., Stern, R. A., & Fisher, C. M. (2015). Isotopically diverse rhyolites coeval with the Columbia River Flood Basalts: Evidence for mantle plume interaction with the continental crust. *Terra Nova*, *27*(4), 270–276. https://doi.org/10.1111/ter.12156

Colón, D. P., Bindeman, I. N., Ellis, B. S., Schmitt, A. K., & Fisher, C. M. (2015). Hydrothermal alteration and melting of the crust during the Columbia River Basalt-Snake River Plain transition and the origin of low-$\delta^{18}O$ rhyolites of the central Snake River Plain. *Lithos*, *224–225*, 310–323. https://doi.org/10.1016/j.lithos.2015.02.022

ACKNOWLEDGMENTS

A Ph.D. is both a personal journey and a deeply collaborative process. As such, it is hard to overstate the degree to which I owe my success in this dissertation to a supporting community of scholars and friends at the University of Oregon over these past six years. I'd like to first thank Ilya Bindeman for performing the pivotal role in guiding me towards being a fully-fledged scientist, through both the good and rough times.

I would also like to thank the denizens of the stable isotope lab at the University of Oregon, including Jim Palandri, without whom I never would have analyzed anything, and the advice and support of Dana Drew, Angie Seligman, David Zakharov, Matt Loewen, Mike Hudak, and Rachel Hampton, who have been great peers in the lab, the office, and the bars over the years.

My sincere gratitude also goes towards my other committee members, Gene Humphreys and Paul Wallace, who have given me years' worth of valuable feedback and encouragement concerning my constantly changing research directions, as well as the rest of the faculty in the Department of Earth Sciences, who have made the academic environment a positive and encouraging one. I also thank the Department for the travel and research funding which has made much of my research and learning possible.

I'd like to thank my coauthors for their invaluable contributions to this project, which is really the result of a lot of great collaboration as much as it is my achievement, so thanks to Ilya Bindeman (obviously and again), Ben Ellis, Axel Schmitt, Chris Fisher, Richard Stern, Jörn Wotzlaw, Eric Christiansen, were all great to work with. Special thanks goes to Taras Gerya for teaching me his thermomechanical modeling code and for giving me the chance to enter a whole new field of research.

Thanks to my other collaborators who contributed to this research, including Mark Ferns, Chris Henry, Martin Streck, Matt Loewen, Bin Fu, Andrew Kylander-Clark, Scott Boroughs, Jade Star Lackey, and Catherine Annen. All played vital roles at some point for each of the chapters below. I also would like to thank those who provided peer review for the published material below.

This work was supported by NSF grant EAR/CAREER0844772, by NSF grant EAR/1447337, the University of Oregon Earth Sciences Department Staples Fellowship, the ETH Zürich postdoctoral program, the US Department of Energy and the International Continental Drilling Program, and the ion microprobe facility at UCLA utilized during this study is partly supported by grant 1029193 from the Instrumentation and Facilities Program, Division of Earth Sciences, National Science Foundation.

For my parents, who encouraged my love of volcanoes from the very beginning.

TABLE OF CONTENTS

Chapter Page

I. INTRODUCTION 1

II. HYDROTHERMAL ALTERATION AND MELTING OF THE CRUST DURING THE COLUMBIA RIVER BASALT-SNAKE RIVER PLAIN TRANSITION AND THE ORIGIN OF LOW-δ18O RHYOLITES OF THE CENTRAL SNAKE RIVER PLAIN 7

2.1. Introduction 7

2.2. J-P Desert Stratigraphy and Sampling 10

2.3. Analytical Methods 11

2.4. Results 14

2.4.1. U-Pb Geochronology 14

2.4.2. Major Phenocryst O Isotopes and Whole Rock Hf and Nd Isotopes 15

2.4.3. Zircon Isotopic and Trace Element Compositions 17

2.5. Discussion 23

2.5.1. Linking J-P Desert and Bruneau-Jarbidge/Twin Falls Volcanism 23

2.5.2. Linking J-P Desert and Jarbidge Mountains Volcanism 24

2.5.3. Origin of Extremely Unradiogenic Nd and Hf Isotope Ratios in J-P Desert and Jarbidge Magmas 25

2.5.4. Significance of Low-$\delta^{18}O$ Magmas 27

2.5.5. The Origins of Low-$\delta^{18}O$ Volcanism at the J-P Desert and Bruneau-Jarbidge/Twin Falls 29

2.5.6. Constraining Crustal Melting End-Members and Magmatic Evolution Using Trace Elements and Isotopes in Zircons 34

2.5.7. Total Basaltic Input into the Crust 40

2.6. Conclusion 42

Chapter Page

2.7. Bridge 43

III. ISOTOPICALLY DIVERSE RHYOLITES COEVAL WITH THE COLUMBIA RIVER FLOOD BASALTS: EVIDENCE FOR MANTLE PLUME INTERACTION WITH THE CONTINENTAL CRUST 45

3.1. Introduction 45

3.2 Samples and Analytical Methods 46

3.3 Results 48

3.4 Discussion 51

3.4.1 High and Low-$\delta^{18}O$ Rhyolites: Evidence for Large-Scale Plume-Driven Crustal Remelting 51

3.4.2. Plume-Driven Crustal Hydrothermal Alteration 54

3.4. Bridge 57

IV. ORIGINS AND EVOLUTION OF RHYOLITIC MAGMAS IN THE CENTRAL SNAKE RIVER PLAIN: INSIGHTS FROM COUPLED HIGH-PRECISION GEOCHRONOLOGY, OXYGEN ISOTOPE, AND HAFNIUM ISOTOPE ANALYSES OF ZIRCON 59

4.1. Introduction 59

4.2. Geologic Setting 61

4.3. Sampling of Bruneau-Jarbidge and Twin Falls Rhyolites 64

4.4. Sample Preparation and Methods 66

4.4.1. Measurement of Major Phenocryst $\delta^{18}O$ Values via Laser Fluorination 66

4.4.2. Ion Microprobe Measurement of Zircon $\delta^{18}O$ Values 67

4.4.3. Laser Ablation U-Pb Dating and Hf Isotope Analysis of Zircon 69

4.4.4. Thermal Ionization Mass Spectrometry Measurements of Zircon 71

Chapter Page

4.5. Results 73

4.5.1. Zircon Ages 74

4.5.2. Oxygen and Hafnium Isotopes 76

4.5.3 Xenocrystic Zircon 79

4.6. Discussion 80

4.6.1. Recycling and Inheritance of Zircon Grains 80

4.6.2. Isotopic Heterogeneity in Zircon and Batch Assembly of Pre-Eruptive Magma Chambers 85

4.6.3. Crustal Sources of Rhyolitic Magmas 87

4.6.4. Time Dependence of Crustal Reservoir Contributions to Erupted Magmas 91

4.7. Conclusions 96

4.8 Bridge 98

V. THERMOMECHANICAL MODELING OF THE FORMATION OF A MULTILEVEL, CRUSTAL-SCALE MAGMATIC SYSTEM BY THE YELLOWSTONE PLUME 99

5.1. Introduction 99

5.2. Model Setup 101

5.3. Melt Emplacement Method 103

5.4. Emplacement of the Two-Level Magmatic System 104

5.5. Influence of Model Parameters 107

5.5.1. Constraining Crustal Structure 107

5.5.2. Constraining Plume Parameters 109

5.6. Conclusion 111

Chapter Page

5.7. Bridge 112

VI. MAGMATIC, CHEMICAL, AND ISOTOPIC EVOLUTION OF YELLOWSTONE HOT SPOT SILICIC MAGMATISM BY MAGMATIC THERMOMECHANICAL MODELING 113

6.1. Introduction 113

6.1.1. Motivation 113

6.1.2. Numerical Modeling Insight into Magma Petrogenesis 114

6.2. Geologic Background: Geochemical Trends in Yellowstone Hot Spot Silicic Calderas 117

6.2.1 Chemical and Thermal Evolution of Erupted Rhyolites 118

6.2.2. Radiogenic Isotopes 119

6.2.3. O Isotopes 122

6.3. Methods 124

6.3.1 I2VIS Magmatic-Thermomechanical Models 124

6.3.2. Melt Transport in the I2VIS Model 125

6.3.3. Isotopic Modeling 128

6.3.4. Heat2D Modeling 130

6.4. Goals of the Present Study and Model Setup 130

6.5. Results 133

6.5.1. Development of the Mid-Crustal Sill Complex 133

6.5.2. Evolution of the Geothermal Gradient 135

6.5.3. Production of Rhyolitic Liquids 137

6.5.4. Rhyolite Production vs. Eruption Rate as a Function of Frequency of Eruption 139

Chapter Page

6.5.5. Width of the Zone of Intrusion 142

6.5.6. Isotopic Trends in Erupted Rhyolites 145

6.5.7. Chemical and Eruptive Temperature Trends in Erupted Rhyolites 149

6.6. Discussion 150

6.6.1. Eruption Rate Control on Erupted Volume 150

6.6.2. The Origin of Isotopically Ancient Rhyolites 152

6.6.3. Caldera Collapse-Driven Crustal Melting and the Production of Low-$\delta^{18}O$ Magmas 153

6.6.4. Origin of Low-$\delta^{18}O$ Magmas by Sill-Induced Splitting and Burial 157

6.6.5. Combining Hf and O Isotopic Trends 158

6.7. Conclusions 160

VII. SUMMARY 162

APPENDICES

A. MATERIAL FOR CHAPTER II 164

A.1. Supplementary Figures and Tables 165

B. MATERIAL FOR CHAPTER III 190

B.1. Detailed Methods 190

B.1.1. Phenocryst Extraction Methods 190

B.1.2 Laser Fluorination Methods 190

B.1.3. Ion-Microprobe Methods 191

B.1.4. Laser Ablation ICP-MS Methods 193

B.2. Sources of Data for Fig. 3.1 193

Chapter Page

B.3. Sources of Data for Figs. 3.2 and 3.3 and Table B.2 194

B.4 Sample Descriptions 196

B.5. Supplementary Figures and Tables 204

C. MATERIAL FOR CHAPTER IV 227

C.1. Supplementary Figures and Tables 227

D. MATERIAL FOR CHAPTER V 244

D.1. Introduction 244

D.2. Detailed Methods 244

D.2.1 Model Setup 245

D.2.2 Governing Equations 247

D.2.3 Rheology of Rocks and Melts 248

D.2.4 Melting of Mantle and Crust 249

D.2.5 Melting Equations 251

D.2.6. Melt Extraction, Transport and Emplacement 252

D.2.7 Recombination of Lagrangian Markers 259

D.2.8 Topography and Erosion 260

D.3. Supplementary Models 261

D.3.1 Fraction of Melt that Cools in Dikes 261

D.3.2 Parameters Governing Melt Distribution Between Sills 262

D.4. Supplementary Figures and Tables 264

E. MATERIAL FOR CHAPTER VI 281

E.1. Melt Transport Detailed Methods 281

Chapter Page

E.2. Modeling Melt Propagation Through Melt Bodies 284

E.3. Compositional Changes in Markers During Melt Extraction..... 286

E.4. Marker Recombination..... 291

E.5. Detailed Heat2D Methods 291

REFERENCES CITED..... 295

LIST OF FIGURES

Figure		Page
2.1.	Regional and local maps of the study area	8
2.2.	$^{238}U/^{206}Pb$ ages of J–P Desert rhyolites and the Jarbidge Rhyolite	15
2.3.	Whole-rock Hf and Nd isotope values for the Jarbidge Rhyolite and J-P Desert Rhyolites and of other rocks in the region	16
2.4.	Plot of $\delta^{18}O$ (‰ SMOW) values for units from this study and evolution of melt with time	17
2.5.	Hf (ε_{Hf}) and O (‰ SMOW) isotopes in individual zircons relative to isotopic end-members	19
2.6.	Trace element compositions of zircons vs. Hf isotopes	22
2.7.	Schematic sketch illustrating the model for production of low-$\delta^{18}O$ and low-ε_{Hf} rhyolites in an area of extension and plume-driven intrusion of basalt	32
2.8.	Block diagram showing the requirements of meteoric water and intruding basalt to hydrothermally alter 15,000 km^3 of shallow crust	42
3.1	Map of the volcanism that occurred over the Yellowstone plume head from 17 to 14 Ma	46
3.2.	Isotopic and chemical trends in syn□CRB rhyolites	49
3.3.	Plume influence on the continental crust through tectonism and melt production at the suture between the thick craton and thin, young accreted terranes	51
4.1.	Map of the Yellowstone hotspot track, showing the major volcanic centers that formed after the onset of the eruption of the Columbia River Flood Basalts	60
4.2.	Stratigraphy of the Kimberly Borehole	66
4.3.	Cathodoluminescence image of a complexly zoned zircon grain	70
4.4.	Diversity in both hafnium and oxygen isotopes in zircon from all studied rhyolites	71

Figure Page

4.5. Collection of all age data from this study 73

4.6. Probability density curves for the zircon LA-MC-ICP-MS ages..... 76

4.7. Comparison of the two methods of dating zircon 77

4.8. Plot of all CA-ID-TIMS dates against the corresponding oxygen isotope measurements of the same zircon 78

4.9. Oxygen and hafnium isotopes in zircon from rhyolites throughout the Snake River Plain..... 88

4.10. Hafnium isotopes vs. time c oxygen isotopic compositions of zircon vs. time..... 93

4.11. Conceptual model of Snake River Plain caldera volcanism to explain the isotopic evolution 95

5.1. Map showing Yellowstone and the youngest part of the Snake River Plain 100

5.2. Evolution of our reference model. 102

5.3. View of the modeled Yellowstone system after 7 Myr of runtime..... 106

5.4. Views of models with differing crustal composition and plume power from the reference model 108

5.5. Effect of varying lithospheric thickness and mantle plume temperature..... 110

6.1. Map of the Yellowstone hot spot track in continental North America 117

6.2. Development of the Yellowstone magmatic system in the I2VIS model..... 134

6.3. Evolution of the geothermal gradient in the growing magmatic system 135

6.4. Evolution of the melt bodies in the model..... 137

6.5. Production rates of rhyolitic liquids from lower crustal melting, upper crustal melting, and fractionation of intruding basalts. 139

Figure Page

6.6. Comparison of cumulative erupted volumes over time for four different models using different average eruption repose times 140

6.7. Melt production in Heat2D assuming an initial geotherm of 20°C/km, a sill accumulation rate of 7.5 km/Myr for 50 km diameter circular intrusions..... 142

6.8. Comparison of different intrusion widths. 144

6.9. Comparison of eruptive rates for the different intrusion width scenarios 145

6.10. Isotopic values of melts forming in the crust as the system matures..... 147

6.11. Intracaldera isotopic stratigraphy from the I2VIS model 148

6.12. Temperature and SiO_2 content of erupted magmas over time 149

6.13. Evolution of a Heat2D model where 15 km of basalt intrudes at a depth of 7 km over a duration of 2.0 Myr. 154

6.14. Map of oxygen isotopes in the upper and mid crust in our standard model 158

6.15. Plot of bulk eruption $\delta^{18}O$ and ε_{Hf} values. 159

A.1. Miocene volcanic stratigraphy of the J-P Desert 165

A.2. A view of Sheep Creek Canyon with exposures of the Rough Mountain Rhyolite..... 166

A.3. Detail of columnar jointing in the Rough Mountain Rhyolite..... 166

A.4. Map of the J-P Desert field area. 167

A.5. Rare earth element compositions of the Johnstons Camp Rhyolite..... 167

A.6. Rare earth element compositions the Lapilli Tuff of Sheep Creek..... 168

A.7. Rare earth element compositions the Rough Mountain Rhyolite 168

A.8. Rare earth element compositions the Jarbidge Rhyolite..... 169

B.1. Collection of all $\delta^{18}O$ data obtained by laser fluorination for this study 204

Figure Page

B.2. Plot calculating the crustal contribution for Silver City rhyolites 205

B.3. Syn-CRB rhyolites from this study plotted on the discrimination diagrams of Pearce (1984) 206

B.4. Comparison of the trace-element composition of the syn-CRB rhyolites with the range of compositions observed in the Central Snake River Plain 207

B.5. Dinner Creek eruptive center trace element compositions (and nearby units). 208

B.6. McDermitt eruptive center trace element compositions 208

B.7. Dooley Mountain eruptive center trace element compositions..... 209

B.8. Malheur Gorge eruptive center trace element compositions. 209

B.9. Lake Owyhee eruptive center trace element compositions..... 210

B.10. Eastern centers and the Northern Nevada Rift trace element compositions. 210

C.1. Oxygen and hafnium isotopes for zircons from this study 227

C.2. Laser ablation MC-ICP-MS ages vs SIMS spot analyses for $\delta^{18}O$ from this study 228

C.3. Laser ablation MC-ICP-MS ages vs LA-MC-ICP-MS spot analyses for ε_{Hf} from this study 229

C.4. CA-ID-TIMS ages vs LA-MC-ICP-MS spot analyses for ε_{Hf} from this study 230

D.1. Depth vs. melt fraction curves for mantle plumes of different temperatures and melting curves for materials in the crust. 264

D.2. Melt transport and accumulation protocol. 265

D.3. In the model with marker interpolation and recombination, we see that the overall structure is preserved 266

D.4. Demonstration of the effect of changing the fraction of intruding melt distributed along dike paths 267

Figure Page

D.5. Effect of varying n in equation 5.2 268

D.6. Effect of varying L on rates of volcanic eruption 269

D.7. Further illustration of the effect of varying the value of L 270

D.8. Plume temperature and lithospheric thickness effects on the tectonomagmatic evolution of Yellowstone system 271

D.9. Illustration of the effect of changing the lithospheric thickness and the temperature of the mantle plume 272

D.10. Comparison of different crustal compositions on the intrusion geometry produced..... 273

D.11. Additional experiments testing the robustness of our model against variations in crustal composition..... 274

LIST OF TABLES

Table		Page
2.1.	Whole rock and major phenocryst isotope data	20
2.2.	Zircon $\delta^{18}O$, $^{206}Pb/^{238}U$, and ε_{Hf} of J–P Desert and Jarbidge Rhyolite zircons.	21
A.1.	Zircon and Standard Trace Element Compositions	170
A.2.	Whole Rock Trace Element Compositions (XRF)	183
A.3.	Whole Rock Trace Element Compositions (ICP-MS)	186
A.4.	Whole rock Hf and Nd isotope compositions	187
A.5.	Lu-Hf isotope compositions of zircon	188
B.1.	Sample Locations	212
B.2.	Summary of all major phenocryst $\delta^{18}O$ measurements	213
B.3.	XRF data for a subset of samples	216
B.4.	ICP-MS trace element analyses of selected units	223
B.5.	Zircon Lu-Hf isotope analyses	224
B.6.	Zircon oxygen isotope analyses	225
C.1.	Sample locations for Bruneau-Jarbidge units	230
C.2.	Zircon laser ablation and ion microprobe data	231
C.3.	CA-ID-TIMS data part 1	241
C.4.	CA-ID-TIMS data part 2	242
D.1.	Rheological parameters of rock types	276
D.2.	Summary of selected representative models	277

Table Page

E.1. Summary of melting-related variables used to determine the distribution of extracted melts 283

E.2. Summary of melting-related variables attached to individual Lagrangian markers..... 288

CHAPTER I

INTRODUCTION

In the last 17 million years, the Yellowstone mantle plume has produced Earth's youngest and best-preserved example of a continental flood basalt province, the Columbia River basalts, and one of the largest concentrations of anorogenic, "A-type," rhyolites in the world, culminating in the recent activity at the Yellowstone plateau itself (Camp & Ross, 2004; Christiansen, 2001; Pierce & Morgan, 2009; Reidel et al., 2013). This, along with the relative accessibility of the deposits compared to similar features around the world, represents a unique opportunity to study the genesis of silicic magmas in intracontinental settings. Understanding the evolution and structure of these systems also provides valuable constraints on the behavior of so-called "supereruptions," among the rarest but also most dramatic of all geologic hazards.

In Chapters II-IV of this dissertation, I employ zircon and whole rock/major phenocryst isotope geochemistry to constrain the origins, timescales of formation, and storage conditions of the rhyolitic magmas which have erupted over the last 17 million years at coeval with the Columbia River basalts and along the Yellowstone hot spot track. The Snake River Plain and Yellowstone is host to the largest identified concentration of low-$\delta^{18}O$ magmas (Bindeman & Simakin, 2014; Bonnichsen et al., 2011; Boroughs et al., 2012; Hildreth & Christiansen, 1984), which itself puts strong constraints on their origin, as the low-$\delta^{18}O$ signature can only be derived from the melting of hydrothermally altered rocks. A key goal of this dissertation is to further characterize the origin of this isotopic anomaly, and to understand the mechanisms by which low-$\delta^{18}O$ crust can be melted and incorporated into eruptible rhyolites. As oxygen isotopes alone provide an incomplete

picture of the crustal sources of melting, I also measured Nd and Hf isotope compositions to gauge the degree to which melting of old Precambrian contributes to the production of rhyolites in the Snake River Plain. Combining multiple isotopic systems in this way allows for much more detailed characterization of the sources of erupted magmas. The key to these studies is the mineral zircon, which can be easily dated and once formed is relatively resistant to remelting and alteration (Bindeman & Melnik, 2016), allowing the analysis of not only the erupted bulk composition of eruptions but also the composition and ages of the different magma batches which were parental to the pre-eruptive magma body. Chapters II-IV of this dissertation consist of three published papers using combinations of whole rock and major phenocryst isotope geochemistry and the detailed O isotope, Hf isotope, and age populations of zircon to develop models of the origins of silicic magamas in the 15-6 Ma central Snake River Plain rhyolites and in the 16-14 Ma rhyolites which erupted coeval with the Columbia River Basalts in eastern Oregon, western Idaho, and northern Nevada.

In Chapter II of this dissertation, which was published in *Lithos* and coauthored with Ilya Bindeman (University of Oregon), Ben Ellis (ETH Zürich), Axel Schmitt (University of California-Los Angeles), and Christopher Fisher (Washington State University), I investigate the Hf isotope, O isotope, and trace element compositions of zircon from rhyolites from the poorly-studied J-P Desert locality which predates the main phase of volcanism at the Bruneau-Jarbidge volcanic center, which is perhaps the most voluminous part of the entire post-Columbia River Basalt part of the hot spot track (Bonnichsen et al., 2008). These are compared to a sample of the coeval off-axis Jarbidge rhyolite, notable for its highly Precambrian crust-like radiogenic isotope composition. I

found extreme diversity in both O and Hf isotopes in the J-P desert units, suggesting that the magma genesis is best explained in terms of three end-member compositions: ancient Precambrian basement rocks, shallow low-$\delta^{18}O$ material, and differentiates of mantle derived basalts. We further suggest that because these rhyolites represent the earliest Yellowstone-related eruptions in the area, the low-$\delta^{18}O$ signature of the rocks is likely derived from hydrothermal alteration along fault lines which were active coeval with crustal deformation associated with the arrival of the mantle plume.

These ideas were further developed in Chapter III, coauthored with Ilya Bindeman, Richard Stern (University of Alberta), and Christopher Fisher, and published in *Terra Nova*. This paper is a broad regional study of rhyolites which erupted during and in the immediate aftermath of the main phase of Columbia River Basalt eruptions, again combining analyses of major phenocryst $\delta^{18}O$ values with detailed microanalysis of O and Hf isotopes in zircons from representative units from a subset of the broad sample set. I found a broad range of O isotope compositions, but the low-$\delta^{18}O$ rhyolites were found to specifically be distributed on or near a band of east-west extending syn-volcanic grabens which roughly parallel the boundary of the old continent with younger accreted terranes. As at the J-P Desert, I suggest that the main driver of the low-$\delta^{18}O$ signal is hydrothermal alteration along fault lines associated with the grabens. I further propose that these formed in direct response to the differential uplift driven by the mantle plume in the accreted terranes relative to the thicker continental lithosphere. Further underlining this relationship between low-$\delta^{18}O$ rhyolites and the transition between types of lithosphere, this paper notes that the low-$\delta^{18}O$ rocks have slightly more old crust-like Hf

isotopes in their zircons than the normal- $\delta^{18}O$ magmas which erupted farther to the west, away from the lithospheric transition zone and the associate faulting.

In Chapter IV of this dissertation, published in *Contributions to Mineralogy and Petrology*, and coauthored with Ilya Bindeman, Jörn Wotzlaw (ETH Zürich), Eric Christiansen (Brigham Young University), and Richard Stern, these methods are employed in their greatest detail yet to a selection of rhyolites from the Bruneau-Jarbidge and Twin Falls centers of the Snake River Plain. This study combined several hundred spot analyses of Hf isotopes, O isotopes, and U-Pb ages in zircon crystals with high-precision TIMS dating of the same zircon crystals. Unlike the previous two chapters, this study also involved many core-rim pair analyses of both isotopes and ages from single zircon crystals. Several of the studied units were found to have significantly less diverse rims than cores with respect to both isotopic systems, providing clear evidence for assembly of zircon phenocrysts from separate magma chambers into a single homogenized magma chamber prior to eruption. High-precision dating of zircon grains also demonstrates that this batch-assembly process occurs within timescales of several thousand years or less, but also that many of the zircon cores can be as much as 3 million years older than the eruption itself, suggesting a complex magmatic history with multiple phases of melt production, eruption, and remelting of earlier intrusions. Compiling zircon isotopic analyses from these and several other studies, this paper shows a clear transition from magmas with very ancient crust-like compositions to magmas with more mantle-like radiogenic isotopes and depleted (low-$\delta^{18}O$) oxygen isotopes. Understanding the origins of these trends is a central goal of the work in Chapters V-VI of this dissertation.

In Chapters V-VI of this dissertation both coauthored with Ilya Bindeman and Taras Gerya (ETH Zürich), I employ a series of magmatic thermomechanical models modified from the I2VIS code of Gerya & Yuen (2003). These are regional-scale finite difference models with a 2×2 km grid size with Lagrangian markers used to advect material and separate melts from their source rocks. In Chapter V, which has been published in *Geophysical Research Letters*, I introduce a scheme for determining where melts rising from the mantle or the lower crust stop and accumulate which assumes that the reason that dikes rising through the crust are stopped and captured as sills is when they hit large discontinuities in the effective viscosity of the host rocks and/or partial melts. The two most significant such discontinuities are at the Moho and at the brittle-ductile transition which occurs at depths of 5-10 km once the lower crust has been heated by the early stages of magmatism. The tendency of basalts to accumulate at that depth leads to the formation of a 10-15 km thick mid-crustal gabbroic sill complex, matching the observations of previous seismic imaging studies of the eastern Snake River Plain (Peng & Humphreys, 1998). This sill complex is the engine that fuels rhyolite production, both through the production of fractionated melts and through the heating and melting of the surrounding crust. The cooling of this sill and its depletion of fractionated melts allows it to solidify and form a barrier between upper and lower melt zones, providing an explanation for the two-tiered structure first observed via seismic tomography by Huang et al. (2015). Finally, constraining eruption rates by varying the temperature and depth of mantle melting allows the modern Yellowstone plume to be constrained to be approximately 175°C hotter than the surrounding mantle, and the thickness of the overlying North American lithosphere to be approximately 80 km thick.

In Chapter VI of this dissertation, I attempt to link the thermomechanical modeling scheme developed for Chapter V with the geochemical trends in continental crust-hosted caldera complexes observed and described in Chapters II and IV. Attaching simple isotopic and chemical composition trackers to the Lagrangian markers in the model, this study successfully replicates the isotopic trends seen in Chapter IV, particularly the propensity for the early part of each eruptive cycle to host low-ε_{Hf} (ancient crust-like) rhyolites. This is explained by there being rare ancient but fertile ancient rocks at the upper-mid crust boundary, which are quickly consumed in the early part of the magmatic cycle, before giving way to melting of shallower upper crustal rocks, which are frequently low-$\delta^{18}O$. This study also demonstrates a new potential method of producing low-$\delta^{18}O$ magmas: warm but still solid upper crustal rocks are hydrothermally altered and then overplated by intrusions of basalt. Over hundreds of thousands of years, these rocks are overplated by yet more basalt until they are advected to depths where they are heated and melt, giving rise to similarly low-$\delta^{18}O$ rhyolites. Finally, this study documents an interesting positive correlation between eruption rates and total eruptive volumes, suggesting that they most thermodynamically efficient way to generate and erupt melts is to quickly advect them to the surface after they form, allowing intruding basalts to quickly begin melting additional solid crust.

CHAPTER II

HYDROTHERMAL ALTERATION AND MELTING OF THE CRUST DURING THE COLUMBIA RIVER BASALT-SNAKE RIVER PLAIN TRANSITION AND THE ORIGIN OF LOW-$\delta^{18}O$ RHYOLITES OF THE CENTRAL SNAKE RIVER PLAIN

This chapter is taken from a paper published in *Lithos* in 2015, of which I was the lead author. Ilya Bindeman (University of Oregon) was the main advisor on the project, provided the Jarbidge Rhyolite sample, and aided in revisions of this manuscript. Ben Ellis (ETH Zürich) provided the J-P Desert samples, and performed the trace element analyses in zircon. Axel Schmitt (University of California, Los Angeles) performed the oxygen isotope in situ analyses in zircon, and assisted with the U-Pb dating. Christopher Fisher (Washington State University) performed the Hf and Nd isotope measurements. Schmitt and Ellis also assisted in writing the methods section of this paper. My role as lead author included sample preparation, collecting isotopic data, and making interpretations and writing of the manuscript. The published manuscript is available at doi:10.1016/j.lithos.2015.02.022.

2.1. Introduction

The time transgressive series of eruptive centers along the Yellowstone hotspot track connects the modern eruptive center at the Yellowstone Plateau with the ~ 16 Ma Columbia River flood basalts (CRBs) (e.g., Pierce & Morgan, 1992). The flood basalts and their associated silicic magmatism, together with the younger hotspot track, are most commonly interpreted as the expression of a deep-sourced mantle plume (Camp & Ross, 2004; Schmandt et al., 2012), though other interpretations are also discussed (Carlson,

1984; Christiansen et al., 2002; Liu & Stegman, 2012). Unlike the focused silicic centers that characterize past and present activity along the hotspot track of the Snake River Plain(SRP) and Yellowstone, the syn-CRB silicic volcanism occurred nearly simultaneously over a roughly circular region at least 400 km across which is presumed to have been underlain by the head of the Yellowstone plume (Fig. 2.1) (Camp & Ross, 2004; Coble & Mahood, 2012; Ferns & McClaughry, 2013).

In this study we investigate a group of rhyolites in the J-P Desert of Idaho, which is defined as the area between Sheep Creek and the Bruneau River in Owyhee County, southwest Idaho, and compare them to one sample of the Jarbidge Rhyolite 45 km southwest of the J-P Desert locality in northern Nevada (Fig. 2.1b). This places them on the geographic boundary between the broad unfocused silicic volcanism that accompanied the CRBs and the more focused silicic volcanism that characterizes the volcanic centers of the SRP. Additionally, these units are overlain by ashflow tuffs

---

Fig. 2.1 (next page). Regional and local maps of the study area. (a) Extent of volcanism due to the Yellowstone Plume at 14.5–17 Ma. Red areas show the region covered by the CRBs (including the Northern Nevada Rift), which erupted from 17 to 15.5 Ma (Camp & Ross, 2004; Reidel et al., 2013; Wolff et al., 2008). Dike swarms that fed the flood basalt eruptions are shown in dark red (Camp & Ross, 2004). Syn-CRB rhyolites of age 14.5 Ma and older are shown in pink (Coats, 1987; Coble & Mahood, 2012; Ferns & McClaughry, 2013; Steiner & Streck, 2013; Streck et al., 2011). Mapped centers of rhyolitic volcanism are not exhaustive, but show all centers estimated as having at least 20 km^3 of rhyolite by Coble & Mahood (2012, appendix). Large inferred or observed volcanic centers that occurred along the Yellowstone hotspot track from 14.5 Ma to the present are indicated by dotted lines. These include the Owyhee–Humboldt–Juniper Mountain (OH), Bruneau–Jarbidge (BJ), Twin Falls (TF), Picabo (PB), Heise (HS), and Yellowstone (YS) centers (Bonnichsen et al., 2008; Drew et al., 2013). All of these large post-14.5 Ma caldera centers have been host to low-$\delta^{18}O$ volcanism. Additional mapped features include the Archean crustal blocks of Foster et al. (gray) (2006), locations of Eocene volcanism of the Challis and Absaroka volcanics (yellow) (Norman & Mertzman, 1991), Cretaceous and Eocene intrusives of the Idaho batholith, Challis intrusives, and adjacent areas (Boroughs et al., 2012; Coats, 1987; Gaschnig et al., 2011).

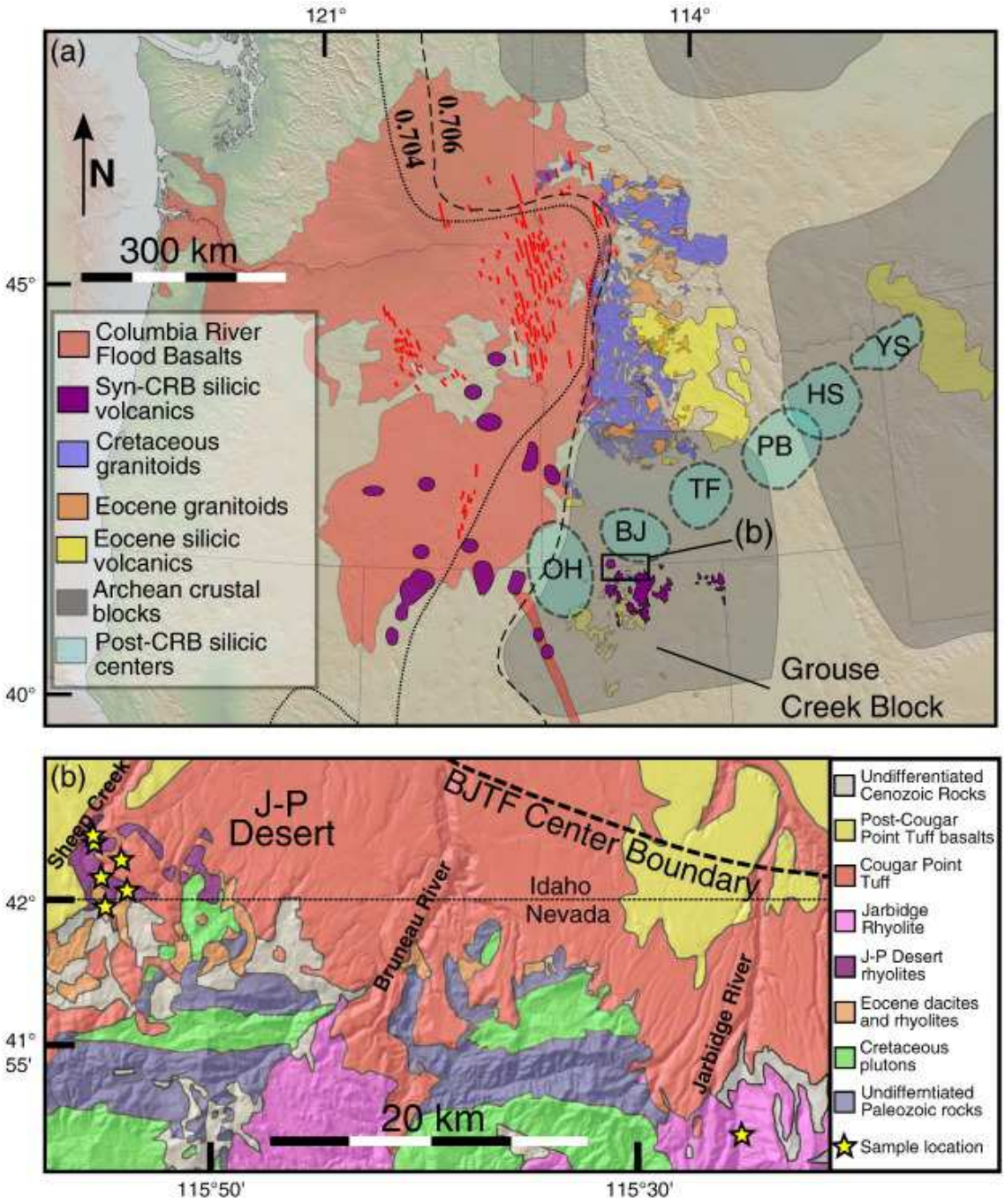

identified as belonging to the Bruneau–Jarbidge volcanic center, the oldest of the major eruptive centers of the Snake River Plain (Bernt & Bonnichsen, 1982; Bonnichsen et al., 2008), making them also temporally intermediate between the majority of the SRP rhyolites and the older CRB related rhyolites. This allows us to group the J-P Desert rhyolites with both the Columbia River Basalt-age rhyolites and the Snake River Plain

hotspot track rhyolites, and identify them as transitional between the two. Investigating the timing and origins of the J-P Desert volcanism is therefore crucial to reconstructing the conditions governing the transition between these two mantle plume-driven volcanic regimes. In this study we combine U–Pb geochronology and analyses of Hf, Nd, and O isotopes and trace elements in whole rocks and mineral separates to determine ages and to distinguish sources of the J-P Desert and Jarbidge rhyolite magmas to better constrain the magma-tectonic interactions that produced them.

2.2. J-P Desert stratigraphy and sampling

The Miocene silicic tuffs and lavas of the southern J-P Desert in southwest Idaho outcrop on top of older ~ 50 Ma Eocene calc-alkaline andesites and dacites of the Bieroth volcanics, which were named and mapped by Bernt and Bonnichsen (1982) (Fig. 2.1b). The welded ignimbrite called the Rough Mountain Rhyolite is the oldest Miocene unit of the J-P Desert suite, outcropping directly above Eocene Bieroth volcanics (see appendix for photographs). It is more than 170 m thick in places, and has been interpreted as a caldera infill deposit on the basis of its thickness (Bernt & Bonnichsen, 1982), although we note that distinguishing between strongly welded ignimbrites and rhyolitic lavas in the SRP remains difficult (e.g., Branney et al., 2008). The overlying Lapilli Tuff of Sheep Creek is up to 40 m thick, well-bedded, and unwelded. It was interpreted as a near-vent fallout deposit (Bernt & Bonnichsen, 1982). The Johnstons Camp Rhyolite comprises a series of flows over 60 m thick that also lies above the Rough Mountain Rhyolite, but these lava flows are of uncertain stratigraphic relationship with the Lapilli Tuff of Sheep Creek (Bernt & Bonnichsen, 1982). Other

younger Miocene units in the area include the Whiskey Draw Rhyolite, the Tuff of Browns Basin, and the Rattlesnake Draw Tuff (Fig. 2.1b). Most if not all of these rocks have experienced substantial post-emplacement hydrothermal alteration, evident from silicification and the growth of secondary minerals. Lying on top of these ~ 15 Ma units is the ~ 13–10 Ma Cougar Point Tuff succession originating from the Bruneau–Jarbidge volcanic center of the central SRP just to the north, which we suggest is a continuation of the J-P Desert volcanism. Volcanism at Bruneau–Jarbidge was followed by activity Twin Falls complex (Fig. 2.1a), with no significant pause in volcanism during the 13–8 Ma duration of both centers (Bonnichsen et al., 2008). From this, and their similar isotopic character (discussed below), we group them together for the remainder of this paper as a single volcanic field (BJTF). The volcanic relicts which are preserved in the J-P Desert were also coeval with eruptions of the ~ 16.1–15.0 Ma Jarbidge Rhyolite 50 km to the southeast in northern Nevada, which consists of several voluminous lavas totaling up to 500 km^3 that erupted over a ~ 60 km × 30 km area (Fig. 2.1a) (Brueseke et al., 2014). We analyzed in detail one sample of the main body of the Jarbidge Rhyolite collected just south of the town of Jarbidge, Nevada.

2.3. Analytical methods

Zircon crystals were extracted from four units (Table 2.2, Fig. 2.1) via bulk dissolution of ~ 100 g of each sample in cold 48% hydrofluoric acid for two to three days following the extraction protocol in Bindeman (2003, appendix), which is the preferred method for crystal-poor altered volcanic rocks. Because zircon is not readily soluble in cold HF, it is then easy to extract from the resulting residue via either direct picking or

density separation. The use of separate containers during digestion minimizes the potential for cross-sample zircon contamination. Hand-picked zircons were mounted in epoxy, sectioned by grinding with abrasives (SiC and diamond), and cleaned and coated with a conductive Au layer for isotope analysis.

Zircon $\delta^{18}O$ and U–Pb analyses were conducted using the CAMECA IMS1270 at the University of California-Los Angeles. Instrumental bias was corrected by interspersed analyses of AS3 standard zircon (1099.1 Ma; Paces & Miller, 1993; $\delta^{18}O$ = 5.3‰ SMOW; Trail et al., 2007) mounted in close physical proximity to the unknowns. External reproducibility of the AS3 standards was 1.6% (n = 14) for $^{206}Pb/^{238}U$ and 0.20‰ (1 s.d.) for $\delta^{18}O$; accuracy was tested by standard intercalibration using zircon 91500 (Wiedenbeck et al., 2004), which was found to be within the stated analytical uncertainties for $^{206}Pb/^{238}U$ and $\delta^{18}O$. The $\delta^{18}O$ ($^{133}Cs^+$ beam) and U–Pb age (^{16}O beam) analyses were performed in sequential analytical session overlapping ~ 30 μm spots (the second directly on top of a pre-existing pit), which were then confirmed to be in zircon cores by cathodoluminescence images obtained at the University of Oregon.

Zircons were then repolished and laser ablation analysis spots ~ 30 μm in diameter for ε_{Hf} were placed in close to locations for $\delta^{18}O$ and U–Pb analyses. Zircon ε_{Hf} analyses were performed with a ThermoFinnigan Neptune multi-collector inductively-coupled plasma mass-spectrometer (LA-MC-ICPMS) at Washington State University, following the method of Fisher et al. (2014) using Plešovice zircon standard with a $^{176}Hf/^{177}Hf$ ratio of 0.282482 (Sláma et al., 2008) (measured at 0.282439 and corrected accordingly). It should be noted that LA-ICP-MS spots, while of approximately the same diameter as ion microprobe spots, sample a much larger volume of zircon.

Whole rock powders from the same samples were used to determine the bulk Hf and Nd isotopic compositions using the Neptune MC-ICPMS at WSU, following the methods of Gaschnig et al. (2011) and using standards of JMC 475 ($^{176}Hf/^{177}Hf = 0.282160$) with a reproducibility of ± 0.000005 (2 s.d.) and LaJolla ($^{143}Nd/^{144}Nd = 0.511858$) with a reproducibility of 0.000011 (2 s.d.). Whole rock samples of the J-P Desert units were carefully crushed and powdered using standard techniques at the GeoAnalytical Laboratory in Washington State University. Low-dilution, doubly fused glass beads were then made for analysis of major and trace elements with a ThermoARL Advant XP for major and trace elements via X-ray fluorescence and an Agilent 7700 ICP-MS for traces and rare earth elements. The Jarbidge Rhyolite was analyzed for major and trace elements via X-ray fluorescence at Pomona College. Additional spot analyses of zircon for Ti and other trace elements were performed at the Eidgenössische Technische Hochschule (ETH) Zürich using a 193 nm Resonetics ArF excimer laser coupled to a Thermo Element XR ICPMS within the Institute of Geochemistry and Petrology. Spot sizes were 30 μm and the output energy of the laser beam was typically 3.5 J/cm^2. NIST 612 was used as the primary standard and two secondary standards, the GSD-1G glass and GJ-1 zircon, were used to monitor data quality. All trace elemental data from zircons were reduced using the ETH-developed SILLS program (Guillong et al., 2008). Trace elemental abundances are considered to have a precision of < 5%.

Phenocrysts of quartz and feldspar for oxygen isotope measurements were obtained after careful petrographic examination of crystals under a binocular microscope. As all collected units were weathered and secondarily silicified, particular care was

devoted to identifying primary magmatic phenocrysts, which are typically equant, as opposed to secondary minerals, which are often singly terminated or irregular in appearance. The presence of (volumetrically insignificant) inclusions was used as an additional guiding principle in selecting magmatic crystals. Crystals also had residual glass cleaned off of them via a wash in cold HF for 1–2 h. Oxygen isotopic compositions (reported as $\delta^{18}O$ SMOW) of major phenocrysts (quartz and plagioclase) were measured via an integrated laser fluorination-MAT-253 mass spectrometer system at the University of Oregon (Bindeman, 2008), using BrF_5 as the fluorinating reagent. Samples were controlled for reproducibility via intercalibration with a UOG (6.52‰) garnet standard measured relative to a Gore Mountain Garnet standard of 5.8‰ (Valley et al., 1995). Errors on repeat measurements of standards are typically better than 0.2‰ (2 s.d.).

2.4. Results

2.4.1. U–Pb geochronology

Weighted mean $^{238}U/^{206}Pb$ ages with 2σ uncertainties from zircon SIMS spot analyses (Fig. 2.2, Table 2.2) are 14.7 ± 0.37 Ma (n = 14 used out of 14 total ages) for the Johnstons Camp Rhyolite, 14.6 ± 0.42 Ma (n = 10 of 10) for the Lapilli Tuff of Sheep Creek, 15.3 ± 0.38 Ma (n = 10 of 11) for the Rough Mountain Rhyolite, and 15.3 ± 0.66 Ma (n = 6 of 9) for the Jarbidge Rhyolite. For the Jarbidge Rhyolite, three older crystals with ages up to 18.9 ± 1.8 Ma (xenocrysts or antecrysts) were excluded until the MSWD met the criterion for a single population at the 95% confidence level as tabulated in Mahon (1996), in order to isolate the youngest zircon age population. The 15.3 Ma zircon age is in good agreement with a 15.30 ± 0.18 $^{40}Ar/^{39}Ar$ age reported

by Brueseke et al. (2014) for sanidine from Jarbidge Rhyolite outcropping near our sampling site. Although their errors overlap, the age progression is consistent with the observed stratigraphy of the J-P Desert units.

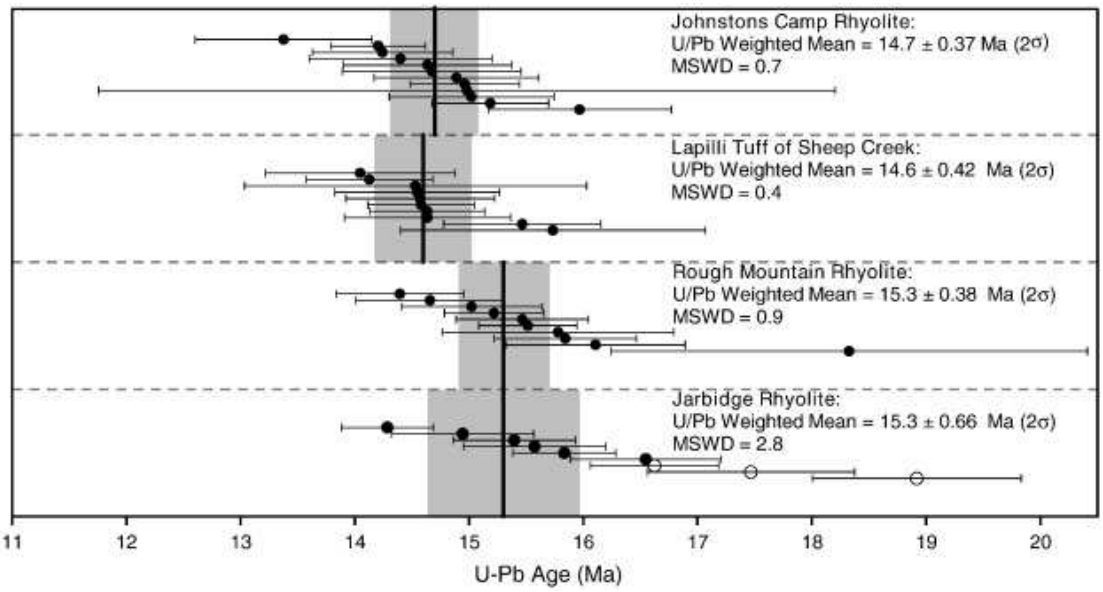

Fig. 2.2. $^{238}U/^{206}Pb$ ages of J–P Desert rhyolites and the Jarbidge Rhyolite. Points represent individual SIMS spot analyses, with error bars representing 1σ confidence intervals. Zircon ages not used in the mean age calculation for the Jarbidge Rhyolite, which are suspected of being antecrysts, are indicated by open circles. Vertical solid bars are U–Pb weighted mean ages, with shaded areas representing 95% confidence intervals.

2.4.2. Major phenocryst O isotopes and whole rock Hf and Nd isotopes

Nearly all major phenocryst $\delta^{18}O$ values from J-P Desert or Jarbidge rhyolites (Fig. 2.4, Table 2.1) fall within 2‰ of the "normal" quartz $\delta^{18}O$ ($\delta^{18}O_{qz}$) value of ~+ 6.5‰ SMOW for quartz, the "normal" plagioclase $\delta^{18}O$ ($\delta^{18}O_{plag}$) of ~+ 5.0 to 5.8‰ (depending on Ca content of plagioclase), or their equivalents for other minerals expected for a 900 °C rhyolitic differentiate of a mantle-derived basalt (Chiba et al., 1989; Bindeman, 2008). Magmatic quartz phenocrysts from the Jarbidge Rhyolite sample have an above-normal $\delta^{18}O_{qz}$ value of + 8.4‰, similar to other $\delta^{18}O_{qz}$ values of Jarbidge Rhyolite reported in Brueseke et al. (2014). In contrast, quartz grains from the Rough

Mountain Rhyolite and the Lapilli Tuff of Sheep Creek have slightly below normal $\delta^{18}O_{qz}$ values, of + 5.0‰ and + 5.2‰, respectively. The sample of Johnstons Camp Rhyolite was quartz-undersaturated but produced a reliably reproduced $\delta^{18}O_{plag}$ value of + 5.8‰. By contrast, a sample of the Cedar Creek Tuff member of the Eocene Bieroth volcanics has $\delta^{18}O_{qz}$ as high as + 9.5‰. We also measured the $\delta^{18}O_{plag}$ of the lowest exposed member of the younger Cougar Point Tuff sequence of the BJTF complex at + 1.3‰ (Table 2.1).

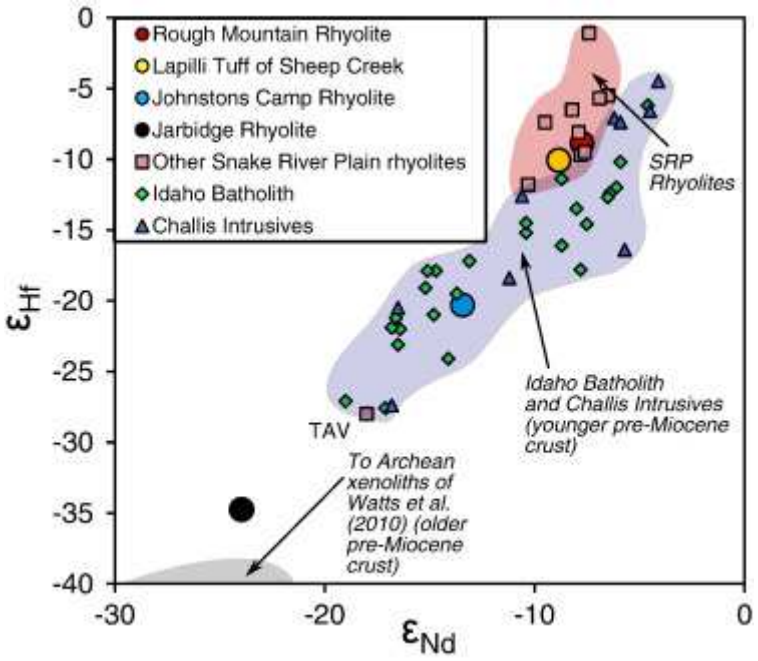

Fig. 2.3. Whole-rock Hf and Nd isotope values for the Jarbidge Rhyolite and J-P Desert Rhyolites and of other rocks in the region, including Challis intrusives and Idaho Batholith (Gaschnig et al., 2011), and younger Snake River Plain (SRP) rhyolites (Drew et al., 2013; Nash et al., 2006); see Nash et al. (2006) for additional SRP data. All SRP rhyolites fall within a narrow compositional range, with the notable exceptions of the Johnstons Camp rhyolite, and the Tuff of Arbon Valley (TAV), an anomalously unradiogenic rhyolite from the Picabo volcanic center, possibly similar to the Jarbidge Rhyolite in its formation. Two-sigma errors are typically of the size of the data points or smaller (± 0.2–0.3 ε units). The "Archean xenolith" field exists outside of the plot area and has an average ε_{Nd} value of − 36 (and estimated equivalent ε_{Hf} = − 60) from Watts et al. (2010) discussed in the text.

The hafnium and neodymium isotopic compositions of bulk rock samples (Fig. 2.3, Table 2.1) are all unradiogenic when compared to chondrite universal reservoir (ε_{Nd} and $\varepsilon_{Hf} = 0$), ranging from ε_{Nd} of − 7.7 and ε_{Hf} of − 8.9 for the Rough Mountain Rhyolite to ε_{Hf} of − 34.7 and ε_{Nd} of − 24.0 for the Jarbidge Rhyolite, the latter in close agreement with the − 24.8 ε_{Nd} value reported by Nash et al. (2006). ε_{Nd} and ε_{Hf} values were calculated using the CHUR composition of Bouvier et al. (2008) and the decay constants of DePaolo (1981) and Söderlund et al. (2004). The Johnstons Camp Rhyolite, which has an ε_{Nd} of − 13.4 and an ε_{Hf} of − 20.3, has a radiogenic isotopic composition which, like its oxygen isotopic composition, is intermediate between the Rough Mountain Rhyolite and Lapilli Tuff of Sheep Creek compositions and that of the Jarbidge Rhyolite.

2.4.3. Zircon isotopic and trace element compositions

Zircon cores from the Jarbidge Rhyolite were homogeneous in $\delta^{18}O$, clustering around + 6‰. In contrast, zircons from the J-P Desert units are diverse in $\delta^{18}O$ values, from low-$\delta^{18}O$ to high $\delta^{18}O$ (− 0.6‰ to + 6.5‰) (Fig. 2.5, Table 2.2). The Rough

---

Fig. 2.4 (next page). Plot of $\delta^{18}O$ (‰ SMOW) values for units from this study (red) and measurements of Cougar Point Tuffs of the BJTF center from Boroughs et al. (2005, 2012) (green) and Bindeman and Simakin (2014) (orange). A single plagioclase analysis of Jarbidge Rhyolite (pink) is from Brueseke et al. (2014). Ages are from this study and Bonnichsen et al. (2008). Ages for the Whiskey Draw Rhyolite and the Browns Basin Tuff, are uncertain (error bars) and have been estimated from stratigraphic position. Low-$\delta^{18}O$ plagioclase grains out of equilibrium with quartz are which are suspected of recording secondary rather than magmatic $\delta^{18}O$ are indicated by dashed outlines. A thick gray line shows the evolution of melt $\delta^{18}O$ values with time, estimated by taking either average measured $\delta^{18}O_{qz}$ value minus 0.5‰, or the average $\delta^{18}O_{plag}$ value if there are no available quartz measurements (see Bindeman, 2008). Large shaded arrows illustrate the two processes governing the evolution of oxygen isotopes in these magmas, which result in different trends. These are gradual alteration of the crust through normal faulting, as in Fig. 2.7, and the recycling of buried and altered intracaldera rhyolites.

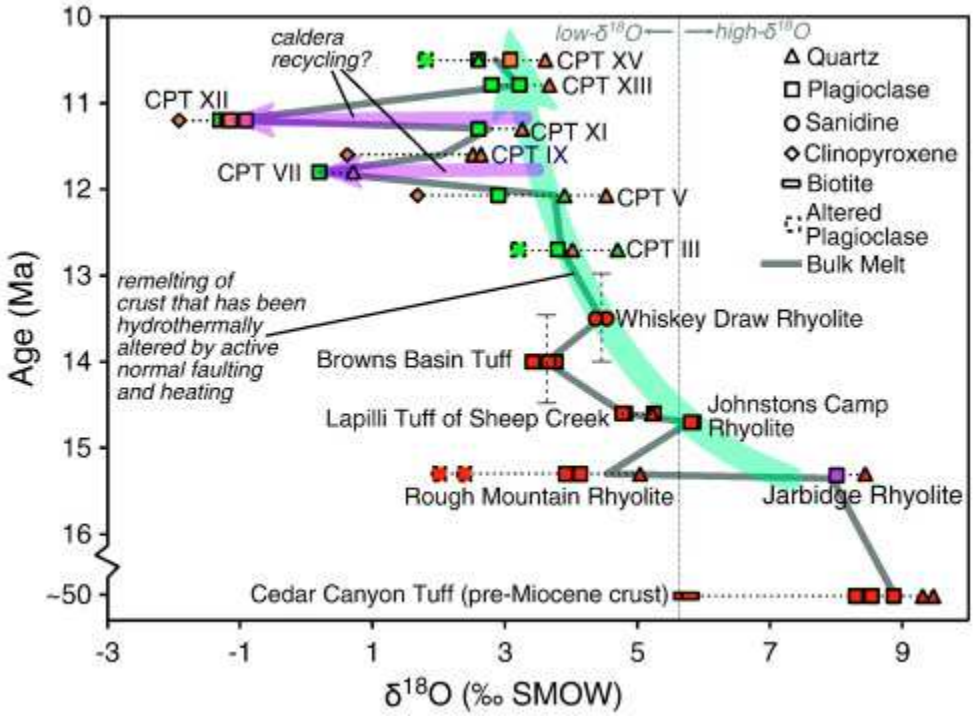

Mountain Rhyolite and Lapilli Tuff of Sheep Creek zircon core $\delta^{18}O$ values range from + 0.5‰ to + 3.5‰, and the Johnstons Camp Rhyolite shows still greater diversity in zircon core $\delta^{18}O$ values, ranging from − 0.6‰ to + 6.5% within a single hand sample. Hf isotope analyses targeting the zircon volume directly underneath the co-registered oxygen isotope and U–Pb geochronology spots also show remarkable variability (ε_{Hf} = − 39.0 to 0.8) (Fig. 2.5, Table A.5). The Jarbidge Rhyolite shows a limited, but very unradiogenic range of ε_{Hf} from − 35 to − 39, mirroring its relative homogeneity in oxygen isotopes. The Rough Mountain Rhyolite and the Lapilli Tuff of Sheep Creek shows greater ε_{Hf} diversity, ranging from ε_{Hf} = − 1 to − 13, and the Johnstons Camp Rhyolite again had the most diverse zircons, with ε_{Hf} values ranging from − 4 to − 29. In all J-P Desert rhyolites, zircons with more unradiogenic Hf also tend to have higher $\delta^{18}O$ values (Fig. 2.5).

Nearly all zircons have Ti concentrations ranging from 5 to 16 ppm (Fig. 2.6);

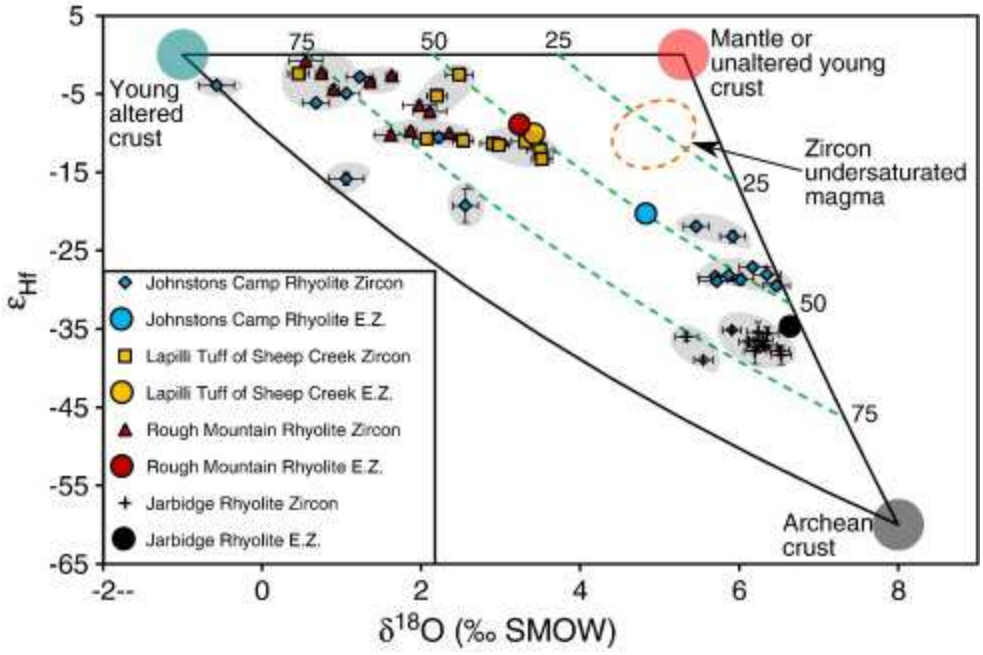

Fig. 2.5. Hf (ε_{Hf}) and O (‰ SMOW) isotopes in individual zircons of the Jarbidge Rhyolite and the J-P Desert rhyolites relative to isotopic end-members. Diamonds are zircon values. Circles are melt compositions represented by equilibrium zircon $\delta^{18}O$ values from major phenocryst $\delta^{18}O$ (quartz—1.8‰ or, if quartz is absent, plagioclase—1.0‰) measurements coupled with whole-rock Hf isotope measurements (Table 2.1); error bars are all 1σ. Green dashed lines show minimum contributions of crustal melts of both sources to the erupted magmas. Note that many zircons are derived from magmas that are > 75% crustal melts. Gray shaded regions on the plot represent one possible interpretation of the compositions of these magma batches, though the distribution of compositions and there accompanying uncertainty allows significant freedom in choosing possible numbers of batches and their compositions. Also shown is the possible composition of the zircon undersaturated melt that must have mixed with the zircon-bearing melts which contributed to the Rough Mountain Rhyolite and the Lapilli Tuff of Sheep Creek, in order to produce the observed bulk composition given from major phenocrysts contributed to the Rough Mountain Rhyolite and the Lapilli Tuff of Sheep Creek, in order to produce the observed bulk composition given from major phenocrysts.

some analyses were higher, but all zircons with elevated Ti also have either extremely high Fe (100s of ppm) concentrations, which indicate that an iron-titanium oxide inclusion may have been sampled, or anomalous concentrations of other rare-earth elements, indicating some other possible contamination. Rare earth element patterns in zircons with diverse

Table 2.1. Whole rock and major phenocryst isotope data.

Unit	Latitude	Longitude	Phenocryst type and $\delta^{18}O$ (‰ SMOW) 2 s.d. = 0.2‰ (major phenocrysts)		Whole Rock ε_{Hf}	2 s.e.	Whole Rock ε_{Nd}	2 s.e.
Cougar Point Tuff (unit unknown)			Plagioclase (s)	1.32	--	--	--	--
			Plagioclase (s)	0.81				
Whiskey Draw Rhyolite	42.00451	-115.91153	Sanidine (s)	4.26	--	--	--	--
			Sanidine (s)	4.37				
Tuff of Browns Basin	41.99738	-115.89178	Plagioclase (s)	3.77	--	--	--	--
			Plagioclase (s)	3.66				
			Plagioclase (m)	3.42				
Johnstons Camp Rhyolite	42.02109	-115.89611	Plagioclase (s)	5.85[a]	-20.3	± 0.2	-13.4	± 0.1
			Plagioclase (s)	5.82[a]				
			Plagioclase (m)	5.81				
			Zircon range	-0.57 to 6.47				
Lapilli Tuff of Sheep Creek	42.03422	-115.91649	Quartz (m)	5.22	-10.1	± 0.2	-8.8	± 0.2
			Plagioclase (m)	4.82				
			Plagioclase (s)	4.77				
			Plagioclase (s)	5.25				
			Zircon range	0.46 to 3.52				
Rough Mountain Rhyolite	42.03152	-115.91373	Quartz (m)	5.04	-8.9	± 0.2	-7.7	± 0.1
			Plagioclase (s)	2.00[b]				
			Plagioclase (s)	3.92				
			Plagioclase (s)	2.39[b]				
			Plagioclase (m)	4.14				
			Zircon range	0.75 to 2.36				
Jarbidge Rhyolite	41.84789	-115.42917	Quartz (s)	8.44	-34.7	± 0.2	-24.0	± 0.1
			Zircon range	5.55 to 6.53				
Cedar Canyon Tuff	41.98953	-115.91016	Quartz (s)	9.31				
			Quartz (s)	9.47				
			Plagioclase (s)	8.87				
			Plagioclase (s)	8.30				
			Plagioclase	8.54				
			Biotite	5.56				
			Biotite	5.67				

[a] Phenocrysts from a different hand sample than studied zircons.
[b] Phenocrysts have low-$\delta^{18}O$ values due to secondary alteration and do not reflect magmatic compositions.

Table 2.2. Zircon $\delta^{18}O$, $^{206}Pb/^{238}U$, and ε_{Hf} of J–P Desert and Jarbidge Rhyolite zircons. "s.d." is standard deviation.

Unit	Grain #	$\delta^{18}O$ (‰ SMOW)	1 s.e.	$^{206}Pb/^{238}U$ Age	1 s.e.	ε_{Hf}	2 s.e.
Jarbidge Rhyolite	1	6.24	0.14	15.4	0.5	-35.4	2.6
	2	6.20	0.14	[a]		-37.8	3.2
	3	5.34	0.14	[a]		-36.0	1.1
	4	6.33	0.14	17.5 [b]	0.9	-37.1	1.0
	5	6.35	0.14	16.6 [b]	0.6	-35.6	1.7
	6	6.12	0.12	18.9 [b]	0.9	-36.6	0.9
	7	5.55	0.12	15.8	0.5	-39.0	0.8
	8	5.91	0.12	14.3	0.4	-35.2	0.7
	9	6.3	0.12	14.9	0.6	-36.5	1.0
	10	6.51	0.12	15.6	0.6	-37.8	1.0
	11	6.53	0.12	16.5	0.7	-38.3	2.4
Rough Mountain Rhyolite	1	1.36	0.07	15.8	1	-3.5	1.1
	2	0.90	0.07	15.5	0.6	-4.5	1.2
	3	0.75	0.07	16.1	0.8	-2.4	1.2
	4	1.63	0.07	15.5	0.4	-2.7	0.9
	5	1.87	0.07	14.7	0.7	-9.8	0.9
	6	1.62	0.21	15.2	0.4	-10.2	0.9
	7	2.11	0.21	15.0	0.6	-7.2	0.8
	8	0.55	0.21	18.3	2.1	-0.8	1.8
	9	1.98	0.21	15.8	0.6	-6.5	1.0
	10	2.36	0.21	14.4	0.6	-10.0	0.9
Lapilli Tuff of Sheep Creek	1	3.31	0.17	14.5	0.7	-11.1	1.1
	2	2.91	0.17	14.6	0.7	-11.4	1.2
	3	2.07	0.17	14.6	0.7	-10.8	0.8
	4	2.48	0.17	14.5	1.5	-2.5	0.9
	5	3.50	0.17	14.0	0.8	-12.2	1.1
	6	0.46	0.13	15.5	0.7	-2.4	1.1
	7	2.53	0.13	14.6	0.5	-11.0	0.9
	8	3.52	0.13	15.7	1.3	-13.3	0.8
	9	2.20	0.13	14.6	0.5	-5.3	1.2
	10	2.98	0.13	14.1	0.6	-11.5	1.1
Johnstons Camp Rhyolite	1	5.92	0.16	13.4	0.8	-23.2	1.6
	2	5.46	0.16	14.2	0.4	-21.9	0.9
	3	5.87	0.16	14.7	0.8	-28.1	0.9
	4	2.56	0.16	16.0	0.8	-19.3	4.3
	5	6.02	0.16	14.4	0.8	-28.7	1.4
	6	6.35	0.17	15.0	0.7	-28.1	2.0
	7	6.47	0.17	15.0	3.2	-29.5	1.1
	8	1.23	0.17	14.9	0.7	-2.8	1.1
	9	6.17	0.17	15	0.5	-27.1	0.6
	10 (core)	0.68	0.17	15.9 [c]	0.8	-6.2	0.8
	10 (rim)	1.06	0.17	16.8 [c]	0.4	-5.0	1.0
	11	-0.57	0.22			-3.9	0.5
	12	2.22	0.22	10.7	15.7	-10.6	1.3
	13	1.06	0.22	15.2	0.5	-15.8	1.7
	14	5.70	0.22	14.6	0.7	-28.3	1.1
	15	5.72	0.22	14.2	0.6	-28.9	0.8

[a]Age is good but excluded from weighted average (suspected antecryst).
[b]Age discarded due to instrumental error.
[c]Age not used in weighted average because of anomalously high U content.

isotopic compositions are broadly consistent with those of continental granitoids, as per the discrimination model of Belousova et al. (2002) (data included in appendix). All zircons from the J-P Desert and the Jarbidge Rhyolite have moderate positive Ce and negative Eu anomalies (calculated by comparing measured Eu and Ce to the expected value determined from linear interpolation on a rare earth element plot when normalized to the chondritic abundances of McDonough and Sun, 1995).

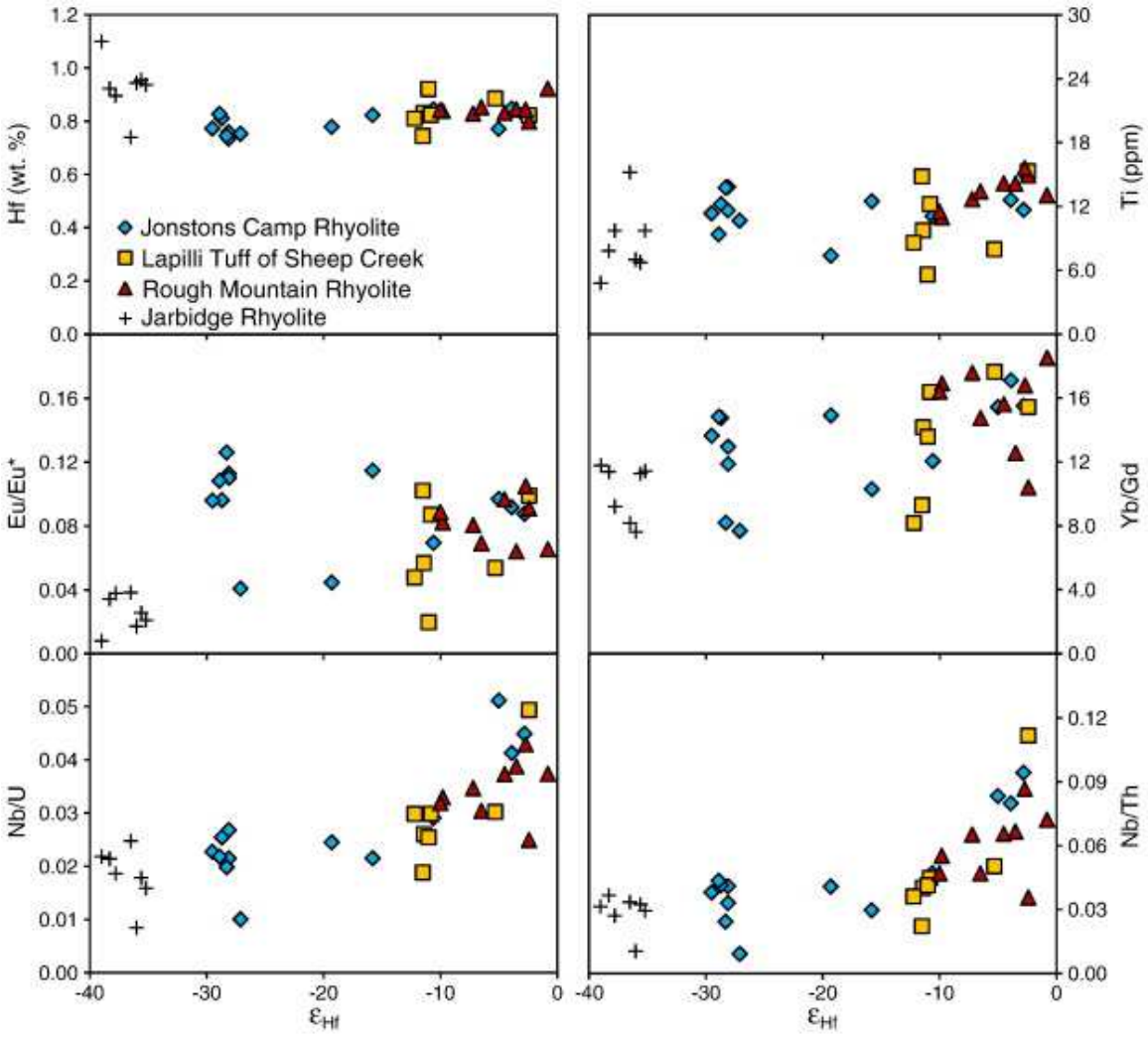

Fig. 2.6. Trace element compositions (ppm and wt.%) of zircons from the Jarbidge Rhyolite and the J-P Desert rhyolites vs. Hf isotopes (ε_{Hf} units).

2.5. Discussion

2.5.1. Linking J-P Desert and Bruneau–Jarbidge/Twin Falls volcanism

New U–Pb dating of zircons from the J-P Desert and the Jarbidge Rhyolite confirm that the two eruptive centers were active at the same time during the waning period of the Columbia River flood basalt eruptions, which were active primarily from 16.7–15.0 Ma (Reidel et al., 2013), and shortly before the eruption of the oldest previously identified member of the BJTF volcanic complex at ~ 13 Ma (Bonnichsen et al., 2008). This also makes the J-P Desert and Jarbidge Rhyolites the oldest Miocene rhyolites yet identified in the vicinity of the Central Snake River Plain. The radiogenic isotopic composition of the Rough Mountain Rhyolite is very similar to those of later erupted Bruneau–Jarbidge Cougar Point Tuffs (e.g. ε_{Nd} of − 8.2 and ε_{Hf} of − 6.5 for the 12.07 Ma Cougar Point Tuff V reported by Nash et al., 2006). Along with very similar major element compositions and mineralogy (Bernt & Bonnichsen, 1982), this suggests that BJTF volcanism was a continuation of the earlier volcanism observed in the J-P Desert.

Perhaps the most convincing link between J-P Desert volcanism and BJTF volcanism, however, is the common presence of low-$\delta^{18}O$ rhyolites at both centers. One of the most enigmatic features of silicic volcanism at Yellowstone and the Snake River Plain in general is the abundance of low-$\delta^{18}O$ rhyolites at all major centers of silicic volcanism (Bindeman & Valley, 2001; Bonnichsen et al., 2008; Boroughs et al., 2005; Drew et al., 2013; Watts et al., 2011). In particular, the rhyolites of the BJTF are exclusively low-$\delta^{18}O$ in character (Boroughs et al., 2005, 2012). Most interestingly,

however, oxygen isotope data for major phenocryst phases in the J-P Desert, while still below normal values (Table 2.1), represent perhaps the highest $\delta^{18}O$ values found among Miocene rhyolites in the region, including all BJTF rhyolites (Fig. 2.4), but excluding normal-$\delta^{18}O$ rhyolites associated with the extension of the Western Snake River Plain (Bonnichsen et al., 2008; Boroughs et al., 2012).

2.5.2. Linking J-P Desert and Jarbidge Mountains rhyolitic volcanism

The Jarbidge Rhyolite is significantly different from the J-P Desert (and by extension BJTF) rhyolites in its Hf and O isotope composition. Additionally, it appears to be nearly exclusively comprised of lava flows, as opposed to the abundant ash-flow tuffs of the J-P Desert and BJTF (Brueseke et al., 2014). However, rhyolitic eruptions in the Jarbidge Mountains and the J-P Desert were both coeval with other syn-CRB rhyolites in the region (Fig. 2.1a) and with the waning stages of the CRBs, all of which are likely derived from the impingement of the Yellowstone mantle plume on the base of the crust (Brueseke et al., 2014; Coble & Mahood, 2012; Cummings et al., 2000; Ferns and McClaughry, 2013; Reidel et al., 2013). Regional tectonic extension may have also contributed strongly to magma production in the study area (Fig. 2.1b), as has been suggested for the Jarbidge Rhyolite by Brueseke et al. (2014), in contrast with BJTF (and the J-P Desert if we indeed group it with BJTF), which is has strong evidence linking it to the mantle plume (Bonnichsen et al., 2008). We argue that this extension was still heavily influenced by the plume, which must have heated and deformed the crust along the margins of its area of impingement (Fig. 2.1) (e.g. Burov & Guillou-Frottier, 2005). In particular, Brueseke et al. (2014) show via cross-cutting relationships that regional faulting post-dates the Jarbidge Rhyolite yet predates the BJTF succession, suggesting

that relaxation of the continental crust associated with extensive crustal melting in Jarbidge-age volcanism may have helped to trigger local faulting, rather than the other way around. Eruptions of the Jarbidge Rhyolite were also coeval with the Seventy Six basalt, minor local eruptions of basalt in the area of the main body of the Jarbidge Rhyolite, that have been dated at 16.5 Ma (Rahl et al., 2002) and are chemically and texturally (plagioclase megaphyric in some outcrops) similar to Steens flood basalts, which are the earliest group of CRB lavas to erupt (Camp et al., 2013; Hart & Carlson, 1985). Callicoat (2010) also showed that the trace element composition of the Seventy Six basalt falls within the range defined by the Steens basalts, and concluded based on this result and the textural similarity between the two that the Seventy Six basalt is a member of the Steens basalts. This suggests a common origin for the heating of the crust that produced rhyolites in the Jarbidge Mountains and in the J-P Desert. The strongest evidence, however, for a closely linked relationship between the Jarbidge Rhyolite and the J-P Desert units, to the extent that there may have been a shared magma plumbing system, comes from the Johnstons Camp Rhyolite in the J-P Desert, which contains zircons that resemble those found in both the Rough Mountain Rhyolite and the Jarbidge Rhyolite in their isotopic and trace element composition (Figs. 2.5, 2.6). At a minimum, the magmas that gave rise to the Jarbidge Rhyolite and the some of the Johnstons Camp Rhyolite zircons had similar, if not identical, origins in the crust.

2.5.3. Origin of extremely unradiogenic Nd and Hf isotope ratios in J-P Desert and Jarbidge magmas

Unradiogenic whole rock and zircon ε_{Hf} and ε_{Nd} values from erupted units in the J-P Desert and from the Jarbidge Rhyolite clearly suggest input of partial melts of ancient Archean crust into erupted magmas (Figs. 2.3, 2.5). Archean basement crust has been documented to exist in the area, in the form of the > 2.5 Ga Grouse Creek cratonic block (Fig. 2.1a, Foster et al., 2006). Watts et al. (2010) found an average ε_{Nd} value of − 36 for silicic Archean xenoliths from the SRP which, when coupled with the roughly linear relationship observed between Hf and Nd isotopes observed among the J-P Desert and Jarbidge Rhyolite samples, would correspond to an approximate ε_{Hf} value of − 60 (Fig. 2.5). Using the two-stage model of Milisenda et al. (1988) for extraction from depleted mantle, this unradiogenic end member has a Nd model age of 3.2 Ga, if we assume a typical silicic crustal Sm/Nd ratio of 0.18, which is typical of our samples (this is converted to $^{147}Sm/^{144}Nd$ using the isotope abundances of Berglund and Weiser, 2011). We caution that this number almost certainly does not represent the true age of the crustal rocks in the area, and is likely and average of the true age and those of older contaminants (Arndt & Goldstein, 1987), and that the xenoliths from Watts et al. (2010) were not collected in the immediate area of the rhyolites from this study. Along similar lines, we consider obtaining Nd or Hf model ages of the most radiogenic zircons to be impossible because the calculated uncertainties dwarf the ages. Nevertheless the crust which melted to form the Jarbidge Rhyolite is certainly very old. A ~ 50% mix of a rhyolitic differentiate of the CRBs, which has ε_{Nd} of 0 to + 10 (Wolff et al., 2008), and ε_{Nd} = − 34 Archean crust is therefore capable of generating magmas with similarly unradiogenic Hf and Nd to the Jarbidge Rhyolite, assuming these end-members have comparable Hf and Nd concentrations. The latter assumption is plausible in the light of

minimal differences in Hf concentrations in zircons in different units of the J-P Desert and Jarbidge rhyolites (Fig. 2.6). Such a high degree of Archean crustal input to a magma is uncommon but not unique to the Jarbidge Rhyolite along the Yellowstone hotspot track; similar rhyolites include the 10.44 Ma Tuff of Arbon Valley, which has ε_{Nd} of − 17.7 and ε_{Hf} of − 28.0 (and normal $\delta^{18}O$) (Fig. 2.3) (Drew et al., 2013), and Member C of the Huckleberry Ridge Tuff of Yellowstone, which has an $^{87}Sr/^{86}Sr$ ratio of 0.726 (Doe et al., 1982). Collaborating the unradiogenic ε_{Hf} and ε_{Nd} values in the rocks, Nb/Th and Nb/U ratios, which have been used by Collerson and Kamber (1999) as an indicator of mantle evolution, with larger ratios corresponding to crust derived from younger mantle, show a positive correlation with ε_{Hf} ratios in all zircons (Fig. 2.6), providing further evidence that zircons with more unradiogenic ε_{Hf} values were derived from melting of older crust. Melting of the Archean crust can only have been accomplished by extensive underplating of middle or upper crustal rocks by intruding basaltic magmas or their silicic differentiates, in volumes far surpassing those of the erupted rhyolites (see below). A very small amount of this magma may have erupted in the form of the Seventy Six basalt, and if this basalt is indeed related to Steens basalts, it provides further evidence of a link between Jarbidge Rhyolite volcanism and the Yellowstone mantle plume.

2.5.4. Significance of low-δ18O magmas

Meteoric water imprints its low-$\delta^{18}O$ oxygen isotopic values on crustal rocks via high-temperature hydrothermal alteration of crustal lithologies in the presence of circulating meteoric waters (Taylor, 1974). This isotope exchange must occur with large

water/rock ratios at relatively shallow depths, as deeply penetrating meteoric water can be reasonably expected to lose its low-$\delta^{18}O$ signature via equilibration with shallower high to normal-$\delta^{18}O$ rocks on the way down (Drew et al., 2013; Gottardi et al., 2013; Menzies et al., 2014). Furthermore, these depths are limited by the brittle–ductile transition, which occurs at depths of 5 to 12 km in the Basin and Range province (Gans, 1987), which should serve as a floor for the vast majority of meteoric water circulation in the crust. For J-P Desert, Jarbidge, and BJTF volcanism, we consider the shallow end of that 5–12 km range to be more likely due to the anomalously high geothermal gradient due to the intruding basalts in the area. This is in contrast to the model of Leeman et al. (2008), which suggests an optimal depth of hydrothermal alteration of 15 km. In the absence of pre-existing deep calderas or large throw normal faults which can deeply bury initially shallow protoliths, low-$\delta^{18}O$ volcanism is conclusive evidence of extensive melting of crustal rocks in rhyolite genesis and of the shallow nature of this process.

Intracaldera volcanics, altered by meteoric water in systems analogous to the present day activity at Yellowstone and then deeply buried by the collapse of additional overlapping calderas, have been suggested to be the source of low-$\delta^{18}O$ magmas at Yellowstone and at the Heise and Picabo systems of the East Snake River Plain (Bindeman & Valley, 2001; Drew et al., 2013; Watts et al., 2011, 2012). This means that low-$\delta^{18}O$ rhyolites at these centers are the remelted and "recycled" products of earlier eruptions of the same volcanic center. To be the sole source of low-$\delta^{18}O$ magmas, this mechanism requires that the first eruptive products of a volcanic center have a normal $\delta^{18}O$ composition which is later altered to low values by hydrothermal activity, which is

what is observed at the Picabo, Heise, and Yellowstone centers (Bindeman & Valley, 2001; Drew et al., 2013; Watts et al., 2011). In light of this, the origin of voluminous (~ 10,000 km^3) low-$\delta^{18}O$ rhyolites (Bonnichsen et al., 2008; Boroughs et al., 2005) at the BJTF eruptive center (Fig. 2.1) that lack exposures of the precursory normal-$\delta^{18}O$ units found at Picabo, Heise, and Yellowstone is less certain and more controversial (Ellis et al., 2013). The search for normal-$\delta^{18}O$ rhyolites in the vicinity of BJTF is therefore of great importance. If no initial normal-$\delta^{18}O$ unit from BJTF can be identified (cf. Watts et al., 2011), then the BJTF low-$\delta^{18}O$ units must have then been derived from some relatively shallow pre-existing low-$\delta^{18}O$ crustal source.

2.5.5. The origins of low-$\delta^{18}O$ volcanism at the J-P Desert and Bruneau–Jarbidge/Twin Falls

We have shown that the oldest known Miocene rhyolite in the vicinity of the central SRP, the Rough Mountain Rhyolite, is in fact depleted in $\delta^{18}O$, though this depletion is relatively minor relative to those of younger BJTF units (Fig. 2.4). This is despite the fact that $\delta^{18}O_{plag}$ values in this unit are diverse and range to very low values, because we interpret the highest single crystal $\delta^{18}O_{plag}$ values in the Rough Mountain Rhyolite and in other units as the ones most closely reflecting magmatic $\delta^{18}O$ values, as they are in equilibrium with quartz phenocrysts (which resist alteration) analyzed from the same sample. Conversely, we consider the lower $\delta^{18}O_{plag}$ values to reflect post-emplacement alteration equivalent to that required for the first stage of the caldera recycling model of low-$\delta^{18}O$ magma formation, as plagioclase is highly susceptible to resetting of its $\delta^{18}O$ value by secondary alteration (these values are dashed boxes in Fig.

2.4 and noted in Table 2.1). The best evidence of early (predating any Miocene calderas) low-$\delta^{18}O$ magma formation in the region, however is the fact that zircons in the Rough Mountain Rhyolite have $\delta^{18}O$ values as low as 0.5‰ (Fig. 2.5, Table 2.2). Zircons in hydrothermally-altered rocks such as the J-P Desert rhyolites or those being formed today at Yellowstone survive hydrothermal alteration intact and retain their magmatic $\delta^{18}O$ values (e.g., Bindeman & Simakin, 2014), even when most other minerals and glass are altered to low-$\delta^{18}O$ compositions. The presence of low-$\delta^{18}O$ zircons in the J-P Desert rhyolites therefore allows us to confidently say that their composition reflects the composition of their parent magma, rather than post-emplacement alteration. There therefore must have been low-$\delta^{18}O$ crust present beneath the J-P Desert prior to the formation of the first Miocene rhyolites there at ~15 Ma. This allows us to discard the caldera recycling model as an explanation for the emergence of low-$\delta^{18}O$ in the neighborhood of the central SRP.

Continued widespread low-$\delta^{18}O$ volcanism in the BJTF (13–8 Ma) center after the earlier J-P Desert volcanism suggests that the low-$\delta^{18}O$ crust that melted to form the J-P Desert magmas is regionally abundant, though its identity is uncertain. One possibility is that earlier Cenozoic volcanic such as the Cretaceous granitoids and Eocene volcanic and intrusive rocks which outcrop in the area (Fig. 2.1) underwent hydrothermal alteration coeval with their formation and later melted to form the low-$\delta^{18}O$ magmas observed in the J-P Desert and the BJTF center. This is the view advocated by Boroughs et al. (2005, 2012) and favored by Ellis et al. (2013).

We prefer another possible source of low-$\delta^{18}O$ rocks in the region: that shallow crust in the region was hydrothermally altered only shortly before the eruption of the J-P

Desert rhyolites. Basin and Range faulting became active in northern Nevada at 16–15 Ma, coincident with the eruption of the CRBs (Brueseke et al., 2014; Colgan, 2013; Colgan & Henry, 2009), although the exact (i.e. within 1 Ma resolution) timing of extension will require further field work to be constrained. tectonic regimes provide numerous opportunities for meteoric water to intrude to depths as deep as the brittle–ductile transition in volumes of many km^3 (Gottardi et al., 2013; Muir-Wood & King, 1993). Geological evidence for active faulting during volcanism in the region consists of faults that cut the 15.3 Ma Jarbidge Rhyolite but do not cut the overlying 10–13 Ma Cougar Point Tuffs (Brueseke et al., 2014). This active faulting, perhaps accentuated by the stresses associated with the underplating and intrusion of the CRBs into the crust, combined with a significantly enhanced geothermal gradient (as at Yellowstone, but perhaps even more so considering the vigor of the Columbia River Basalt eruptions) to create potentially ideal conditions to extensively hydrothermally alter the shallow crust (Fig. 2.7). A variation of this scenario has been advocated for the production of some low-$\delta^{18}O$ rhyolites near the Picabo eruptive center (Drew et al., 2013; Konstantinou et al., 2013), through the heat and extension associated with metamorphic core complex formation. Gottardi et al. (2013) recently modeled the isotopic depletion of the crust along normal faults, showing that significant $\delta^{18}O$ depletion along these faults and the associated detachment zones at the brittle–ductile transition is possible when the permeability of these areas is high and depths are shallow. Importantly, the roughly horizontal zone of intense alteration along these detachments may also represent a significant rheological barrier to later intruding magmas, which leads to the strongest

crustal melting occurring in the areas of the greatest hydrothermal alteration, favoring the production of low-$\delta^{18}O$ magmas.

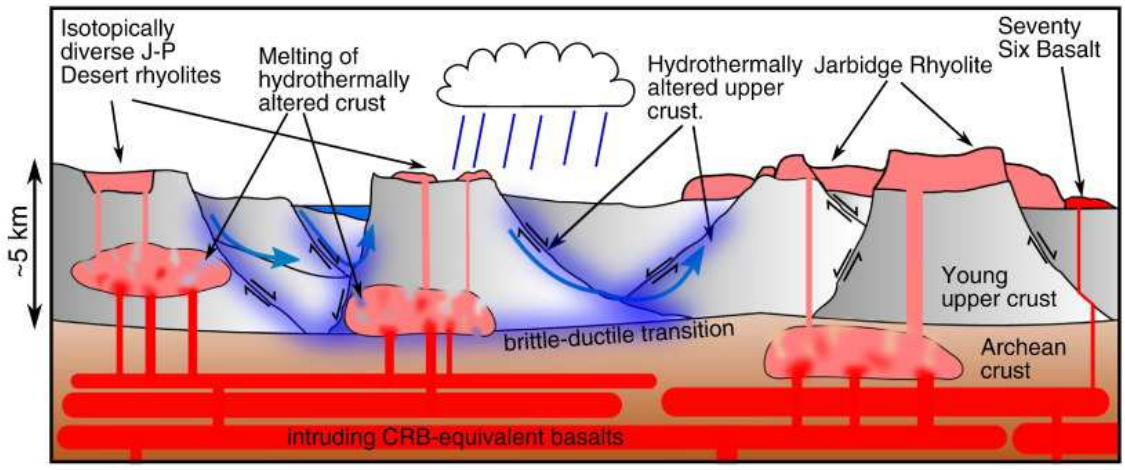

Fig. 2.7. Schematic sketch illustrating the model for production of low-$\delta^{18}O$ and low-ε_{Hf} rhyolites in an area of extension and plume-driven intrusion of basalt. Meteoric water (blue arrows) intrudes along normal faults, where it interacts with shallow country rocks which have ε_{Hf} of approximately zero (gray) to produce low-$\delta^{18}O$ crust (shaded blue). Meanwhile, thick basalt sills (red) accumulate in deep Archean-age crust (brown), a very small quantity of which erupts as the Seventy Six basalt. Heat from these sills drives the hydrothermal alteration of the upper crust, and is responsible for crustal melting to produce the erupted rhyolites of the Jarbidge area and the J-P Desert. The Jarbidge rhyolite erupted first, and as such is cut by systems of faults that do not cut products of younger volcanism at BJTF (and possibly also the intermediate-age J-P Desert rhyolites). In this illustration, we have shown the crust below the brittle–ductile transition as being exclusively Archean in age, and vice versa, a likely oversimplification that nonetheless explains the data well.

Finally, combining our new data from the J-P Desert and Jarbidge rhyolites with previous studies of the BJTF, we note a general trend of decreasing magmatic $\delta^{18}O$ with time (Fig. 2.4). This suggests that whatever process was responsible for the lowering of the $\delta^{18}O$ values of the crustal rocks which gave rise to the J-P Desert and BJTF rhyolites was active coeval with the magmatic activity. We therefore suggest that the first low-$\delta^{18}O$ rhyolites in the J-P Desert and greater central SRP region did not inherit their low-$\delta^{18}O$ composition from pre-Miocene hydrothermal events, as suggested by Boroughs et al. (2005, 2012). Instead, hydrothermal circulation driven by the same magmatic system

that produced the rhyolites altered the local crust only shortly before continued heating and magma intrusion lead to melting of the resulting low-$\delta^{18}O$ crust. This initial hydrothermal "priming" of the crust did not lead to complete oxygen isotope equilibration of the crust with meteoric water as the earliest J-P Desert rhyolites have relatively small $\delta^{18}O$ depletions relative to later BJTF rhyolites (Fig. 2.4). By comparison, the Jarbidge Rhyolite (at least in the area of our sample) predated most extensional faulting where it erupted, meaning the local crust was not yet altered at all. High $\delta^{18}O$ values in the Eocene Cedar Canyon Tuff (Fig. 2.4) further suggest that the initial crust prior to Miocene volcanism was not low-$\delta^{18}O$ in character. After the eruption of the first low-$\delta^{18}O$ rhyolites in the J-P Desert, a combination of heating and extension of the crust led to increasing $\delta^{18}O$ depletion of the shallow crust, creating the decreasing $\delta^{18}O$ trend seen in major phenocrysts in rhyolites in the region. Further stronger $\delta^{18}O$ depletions in the younger and more dramatically depleted in ^{18}O BJTF volcanic complex can then be explained by the caldera collapse and rifting burial-remelting models previously suggested to explain low-$\delta^{18}O$ rhyolites in the East Snake River Plain and Yellowstone (e.g. Bindeman & Valley, 2001; Drew et al., 2013; Watts et al., 2011). In particular, dramatic excursions towards very low-$\delta^{18}O$ values in the 11–12 Ma Cougar Point Tuffs VII and XII (Fig. 2.4) may be explainable by the alteration and remelting of caldera fill material that was already low-$\delta^{18}O$ because of the more regionally extensive normal fault-driven alteration that had been active since at least 15.3 Ma (Fig. 2.7). Our model thus calls for pre-Miocene crustal rocks to be the initial source of low-$\delta^{18}O$ rocks in the area, as in Boroughs et al. (2005, 2012), but with the significant difference that alteration of these rocks was accomplished by the extensional tectonics and the

Yellowstone plume during the Miocene only shortly before the production of rhyolite. We prefer this latter model because of the observation of time-progressive depletion in $\delta^{18}O$ of the erupted magmas.

2.5.6. Constraining crustal melting end-members and magmatic evolution using trace elements and isotopes in zircons

We discovered considerable diversity of Hf and O isotopic compositions between individual zircons in the J-P Desert units, including what is, to our knowledge, the largest range of zircon Hf isotope compositions reported in a single eruptive unit (the Johnstons Camp Rhyolite). The J-P Desert units have disequilibrium $\Delta^{18}O$ values in zircon–zircon, zircon–quartz, and zircon–plagioclase mineral pairs, and only a few zircons are in equilibrium with melt values suggested by major phenocrysts (Figs. 2.4, 2.5). Zircon Hf isotope compositions were also out of equilibrium with each other and whole rock values. By contrast, the Jarbidge Rhyolite zircons are much less diverse in both $\delta^{18}O$ and $\varepsilon_{Hf.}$ Some disequilibrium in O and Hf isotopes between zircon–zircon and zircon–whole rock pairs in the Jarbidge Rhyolite does exist, but to a much lesser extent than in the J-P Desert units (Fig. 2.5). Despite this, the zircons within each J-P Desert unit all had U–Pb ages within error of each other (Fig. 2.2), suggesting that they each formed during a single magmatic event. While there are no obviously xenocrystic zircons in the Jarbidge Rhyolite, the MSWD value associated with the U–Pb ages for the Jarbidge Rhyolite zircons exceeds the limits for a homogeneous population. Pending high-precision zircon geochronology by isotope dilution thermal ionization mass spectrometry(ID-TIMS; e.g., Wotzlaw et al., 2014), this is tentatively interpreted to indicate the presence

of possible antecrystic zircons and/or zircon crystallization over a period of a ~ 2 million years before erupting. Such protracted magmatic activity would agree with persistent volcanism in the vicinity of the main body of the Jarbidge rhyolite from 16.1 to 15.0 Ma (Brueseke et al., 2014).

Trace element variability in zircons of the J-P Desert and Jarbidge rhyolites is decidedly less dramatic than the diversity of isotopic compositions (Fig. 2.6). The range of Ti compositions in zircons from all units corresponds to magmatic temperatures of 790 °C to 925 °C (Ferry & Watson, 2007), assuming a Ti activity of 0.5 for all units, analogous to measured values for similarly hot hotspot rhyolites at Heise and Yellowstone (Rivera et al., 2014; Watts et al., 2011), because titanium–iron oxide compositions are almost certainly compromised by secondary alteration. Variations between units are insignificant and correlations between Ti-in-zircon and hafnium or oxygen isotopic compositions are absent. Due to significant alkali loss and secondary silicification in the J-P Desert and Jarbidge rhyolites (Bernt & Bonnichsen, 1982) we were unable to reliably determine zircon saturation temperatures for the studied units. The Jarbidge Rhyolite zircons show a slightly stronger negative Eu anomaly than the J-P Desert units (Fig. 2.6), but no relationship between the Hf isotope composition of the zircons and the magnitude of the Eu or Ce anomalies was otherwise found. As observed above, we note correlations between Hf isotope composition and Nb/U and Nb/Th ratios, which likely reflects the age of crust that melted to form the initial magmas (Collerson & Kamber, 1999). Finally, a weak correlation exists between the steepness of the heavy element curve (expressed in Fig. 2.6 by the Yb/Gd ratio) and the ε_{Hf} value of the zircons in the Jarbidge and J-P Desert units (Fig. 2.6). We propose that this also

reflects subtle differences in the source rocks of different ages that may prove useful in further constraining the identity of the crustal end-members that melted to produce these rhyolites (see below).

The diversity of the isotopic and trace element compositions exhibited by the zircons in the J-P Desert rhyolites clearly suggests that they crystallized in separate isotopically diverse batches of magma. This has been invoked to explain a similar diversity of zircon $\delta^{18}O$ values also observed in units from the Heise (Watts et al., 2011), Picabo (Drew et al., 2013), Yellowstone, and elsewhere (Bindeman & Simakin, 2014) centers (Fig. 2.1a), along the SRP track. Miocene zircon U–Pb crystallization ages and a lack of evidence of inheritance of Archean or Eocene-age zircons (Fig. 2.2) implies that any crust that melted to form these magmas must have been heated above zircon saturation temperatures, resorbing any pre-existing zircons into the melt (excluding the possibility that source rocks were all zircon-free, which we view as unlikely given their apparent compositional diversity). These batches then crystallized new zircons that recorded the Hf isotope compositions of the parent melt, because Hf is very compatible in zircon, but recorded new U–Pb ages, because Pb is very incompatible in zircon. The subsequent thermal and crystallization histories of these batches is less known, but must have mingled together to form the final melt which erupted and cooled before the zircons could equilibrate with each other and their host melt (e.g. Watts et al., 2011; Wotzlaw et al., 2014). This could have been accomplished by continued addition of heat causing the magma bodies to grow and merge, or perhaps via the formation of dikes or sills that connected the disparate batches of magma. Mixing of at least as many separate initial magma batches as there are distinguishable groups of zircon compositions (shaded

in Fig. 2.5) is required to account for the spread of zircon compositions observed. Such batch assembly is common in the record of the Snake River Plain, and has also been observed at every major eruptive center in the Snake River Plain in either zircons or major phenocrysts (Bindeman & Simakin, 2014; Drew et al., 2013; Ellis & Wolff, 2012; Watts et al., 2011, 2012).

The observed heterogeneity of the zircons in the studied rhyolites suggests that the individual magma batches were derived from melting of at least two continental crust end-members with different Hf and O isotopic compositions followed by mixing with variable amounts of rhyolitic differentiates of mantle-derived basalts. This $\delta^{18}O$-ε_{Hf}relationship is in contrast to systems with variable O isotopes but homogeneous Hf (e.g. the Picabo volcanic field, Drew et al., 2013) which have been explained as the product of melting variably hydrothermally altered crust of pre-homogenized ε_{Hf} composition. The hypothesized crustal end members are: (1) Archean crust that has not experienced high-temperature hydrothermal alteration in the presence of meteoric water, with $\delta^{18}O_{qz} \approx 8‰$ and $\varepsilon_{Hf} \approx -60$ (the crustal xenolith average of Watts et al., 2010), and (2) higher-ε_{Hf} (≈ 0) and low-$\delta^{18}O$ ($\approx -1‰$) crust which we identify as much younger rocks that have experienced shallow hydrothermal alteration by meteoric water shortly prior to rhyolite production, as is discussed above. Potential candidates for crustal end member (2) are Eocene volcanic rocks and Cretaceous granitoids exposed at the surface in the J-P Desert area (Fig. 2.1). We hypothesize remelting of these Eocene volcanic rocks and Cretaceous granitoids to create the Miocene-age, low-$\delta^{18}O$ magmas and zircons observed in the J-P Desert units (Fig. 2.7). If we take the lowest $\delta^{18}O$ and highest ε_{Hf} zircons as indicative of the approximate composition of end member (2), we

estimate that it has $\varepsilon_{Hf} \approx \varepsilon_{Nd} \approx 0$ and $\delta^{18}O \approx 0‰$. All zircon compositions for the rhyolites studied here fall between these two crustal end-member compositions and a third, mantle-like composition with a $\delta^{18}O$ of + 6‰ and an ε_{Hf} value of roughly 0 (Fig. 2.5). This component is most likely a rhyolitic differentiate of intruding CRBs, which also provided the heat for melting of the crustal end-members. Notably, the Archean crustal end-member seems to have escaped any hydrothermal alteration. We suggest that this simply means that the Archean rocks that melted to form the Miocene magmas were physically removed from the zones of hydrothermal alteration, perhaps by being deeper (Fig. 2.7), though we concede that this could be interpreted to support the model of Boroughs et al. (2012) which suggests that the low-$\delta^{18}O$ crust in the region has pre-Miocene age and also acquired its isotopic composition in a separate hydrothermal event coeval with their formation.

Among the zircon compositions observed in the J-P Desert and Jarbidge rhyolites, only a few appear to be derived from nearly pure crustal melts, and while many are derived significantly more from crustal melt than mantle differentiate, and no zircons record the composition of pure uncontaminated mantle differentiates (Fig. 2.5). This is actually unsurprising as the introduction of large volumes of hot intrusive mantle magmas should cause significant melting of the surrounding silicic crust (Annen et al., 2006; Dufek & Bergantz, 2005; Huppert & Sparks, 1988), and the resulting contrasting silicic melts derived from the mantle and the crust should then rapidly mix. The process that creates the final hybrid magma must fall between two end-member scenarios: 1) mafic magma melts the surrounding crust in an approximately one-to-one ratio, producing batch melts of an intermediate composition which then differentiate to rhyolite, 2) mafic

magma provides heat for crustal melting but differentiates into a more silicic composition in isolation; this differentiate is hotter than the crustal melt and remains zircon-undersaturated, and once it reaches rhyolitic composition it mixes with the crustal melts (Simakin and Bindeman, 2012). Supporting scenario 2 is Fig. 2.5, which illustrates that the majority of zircons in the Rough Mountain Rhyolite and the Lapilli Tuff of Sheep Creek are lower in $\delta^{18}O$ than equilibrium zircon values of ~ 3.3‰ predicted by major phenocrysts, which best represent the composition of the final erupted magma. This suggests that a zircon-undersaturated normal-$\delta^{18}O$ melt mixed with the zircon-bearing, low-$\delta^{18}O$ crustal melts, raising the $\delta^{18}O$ value of the whole mix without contributing high-$\delta^{18}O$ zircons (Fig. 2.5). This magma crystallized quartz whose isotopic composition reflects the new bulk magma $\delta^{18}O$ value, but few to no new zircons, suggesting that eruption was very rapid after this final mixing event. The zircon-undersaturated magma was also likely rhyolitic as a more mafic magma would have dissolved the pre-existing zircons in the mixing event. We suggest that this magma is a hot differentiate of the intruding basalts, with relatively minor crustal contamination, as in scenario 2. The average composition of erupted CRB magmas is also basaltic andesite, rather than primitive basalt (Hooper & Hawkesworth, 1993); if that composition is primary, it markedly reduces the amount of initial intrusive material needed to produce rhyolitic differentiates via fractional crystallization prior to mixing with crustal melts. Finally, the relative lack of zircons with compositions mirroring the whole-rock compositions of the Rough Mountain and Johnstons Camp Rhyolites suggests that eruption occurred rapidly after assembly, before additional new zircons could form in the final melt, further

suggesting that the assembly process may quickly lead to the eruption of the final mingled melt.

2.5.7. Total basaltic input into the crust

High-temperature hydrothermal alteration of the crust, the production of crustal partial melts with rhyolitic composition, and the production of isotopically mantle-like rhyolites via fractional crystallization of basaltic magma indirectly and directly require input of basalt into the crust, either as a heat source or as a direct source of material. The total volume of rhyolite erupted in the central SRP and the Jarbidge Mountains during the mid-Miocene, nearly all of which is low-$\delta^{18}O$, was at least 10,000 km^3(Bonnichsen et al., 2008). We estimate that to produce these rhyolites, subequal volumes of crustal melts and rhyolitic differentiates of mantle-derived basalts are required, in line with our calculations concerning the J-P Desert rhyolites (Fig. 2.5), and with a similar ratio of crustal to mantle input for SRP rhyolites of up to 0.4 determined by McCurry and Rodgers (2009). Under these conditions, the addition of ~ 14 km thick mid-crustal sills of gabbro derived from the mantle are required underneath the entire Snake River Plain to account for the basalt needed for fractionation(McCurry & Rodgers, 2009), a suggestion borne out by geophysical observations (Peng & Humphreys, 1998; Rodgers & McCurry, 2009).

Here, we add new constraints on the amount of basalt based on our model of abundant low-$\delta^{18}O$ magmatism that results from extensive hydrothermal alteration of pre-existing crust: 1 kg of basalt cooling from 1200 °C to 500 °C provides 1.1 MJ (cumulate heat content including latent heat of crystallization, based on a specific heat of 1.34 J/g and a latent heat of crystallization of 418 J/g; Huppert & Sparks, 1988) is

necessary to raise the temperature of 1.5 kg of meteoric water from 25 °C to 200 °C. If we take 4‰ as the typical $\delta^{18}O$ enrichment of a 200 °C hydrothermal fluid after water–rock interaction, such as in Yellowstone's Upper Geyser Basin (Fournier, 1989; Hurwitz et al., 2012), and assume a 6‰ $\delta^{18}O$ depletion of the crustal rock over the duration of the alteration episode (the full range of zircon diversity we observe, Figs. 2.5, 2.6), we arrive at a water/rock ratio of 1.5. This is equivalent to a basalt/altered shallow crust volume ratio of approximately 0.55, suggesting that to alter 15,000 km^3 of crust in the central SRP (which we consider to be conservative given the 10,000 km^3 of low-$\delta^{18}O$ rhyolite), some 8200 $km^3$of basalt must have intruded and solidified to provide the necessary heat (Fig. 2.8). This figure is supported by earlier thermal estimates in Taylor (1974), who suggested that to an order of magnitude approximation, hydrothermal alteration of a certain volume of shallow crust requires thermal input from a similar volume of intruded magma. This number is not implausible if one takes into account that this intrusion may have occurred gradually over 3.5 Ma from the start of CRB eruptions to the start of BJTF eruptions, equivalent to an influx of only 0.002 km^3/yr on average. Much larger fluxes of intruding basalt are suggested for Yellowstone today, and Fournier (1989) suggests that 0.08 km^3 per year of basalt is needed to drive the present hydrothermal system at Yellowstone, suggesting that the process of alteration of the crust is not efficient in terms of heat transferred from basalt to water altering new crust. If we estimate the area underlain by these basalt intrusions to be 120 km by 120 km (14,400 km^2), the required basaltic sill complex to drive all of the observed hydrothermal alteration need not be more than approximately 0.6 km thick to account for the calculated 8500 km^3 of intruded basalt. In comparison to the ~ 15 km thickness of basaltic intrusions required by other

studies (e.g. Leeman et al., 2008; McCurry & Rodgers, 2009) needed to account for the physical production of the erupted rhyolites by melting and fractionation, this number represents a small fraction of the total available basalt (and therefore heat) available in the system. It is thus easily plausible, and perhaps inescapable, for the voluminous syn-volcanic hydrothermal alteration that we propose for the BJTF system in general to be accomplished by excess intruded basalts in the overall system.

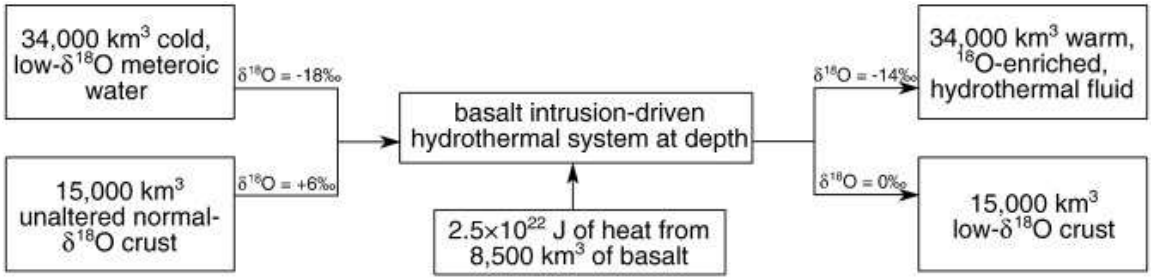

Fig. 2.8. Block diagram showing the requirements of meteoric water and intruding basalt to hydrothermally alter 15,000 km^3 of shallow crust in the central SRP to provide a source for the widespread low-δ^{18}O volcanism that occurred there.

2.6. Conclusion

We present a detailed study of the first rhyolites to erupt in the neighborhood of the central Snake River Plain in the Miocene. These early rhyolites include voluminous low-δ^{18}O (but not so low as the main phase Bruneau–Jarbidge magmas) rhyolitic magmas with diverse ε_{Hf} and ε_{Nd} which erupted southwest of the Bruneau–Jarbidge volcanic center at ~ 15 Ma, coeval with the termination of the main phase of CRB eruptions. These early silicic eruptions derived their oxygen, hafnium, and neodymium isotopic compositions from 1) Archean crust, characterized by normal oxygen isotopes and extremely unradiogenic Hf and Nd isotopes, and 2) younger hydrothermally altered silicic crustal crust with more radiogenic Hf and Nd, which is likely equivalent

to Eocene volcanic and subvolcanic intrusive rocks or Cretaceous intrusions outcropping in the area. U–Pb crystallization ages of zircons from these units are with a few exceptions indistinguishable from the inferred eruption ages given by the youngest zircon ages, and xenocrystic zircons are entirely absent. These zircons, however, show remarkable diversity in $\delta^{18}O$ (− 0.6‰ to + 6.5‰) and ε_{Hf} (− 39 to − 1), suggesting that these magmas were assembled in the shallow crust from many batches of compositionally distinct magma derived from mixtures of melts of the above two crustal-end members and a mantle-derived component. The lowering of magmatic $\delta^{18}O$ values from the oldest J-P Desert rhyolites the younger Bruneau–Jarbidge rhyolites is a result of the remelting of crust that was being hydrothermally altered coeval with rhyolite production.
This hydrothermal alteration was most likely driven by a combination of normal faulting, which provides pathways for meteoric water to penetrate the shallow crust, and increased geothermal gradients caused by voluminous intrusions of the basalt similar to the main phase Columbia River Basalt erupted lavas. These basaltic intrusions were also responsible for local rhyolite production by providing a heat source for crustal melting and by fractional crystallization. We suggest that this mantle plume-induced hydrothermal alteration and later crustal melting may characterize other areas of intraplate volcanism in an extensional environment.

2.7 Bridge

The study presented in Chapter II showed a surprising relationship between the Hf and O isotope compositions of zircon crystals in early Snake River Plain Rhyolites. Also, the discovery of low-$\delta^{18}O$ rhyolites dating back to the very earliest stages of central

Snake River Plain volcanism suggests a possible role for Columbia River flood basalt volcanism in generating the in low-$\delta^{18}O$ signal, possibly via deformation and faulting of the crust. In Chapter III, I investigated these possibilities by performing a wide regional survey of oxygen isotopes in rhyolites that erupted coeval with the Columbia River basalts, and analyzed the radiogenic isotope compositions of a subset of those rhyolites from eastern Oregon, USA. My coauthors and I found further evidence for the crucial role that normal faulting may play in the formation of low-$\delta^{18}O$ crust which remelts to form low-$\delta^{18}O$ rhyolites and show that this faulting and alteration appears to have been concentrated along the boundary of the ancient North American continent.

CHAPTER III

ISOTOPICALLY DIVERSE RHYOLITES COEVAL WITH THE COLUMBIA RIVER FLOOD BASALTS: EVIDENCE FOR MANTLE PLUME INTERACTION WITH THE CONTINENTAL CRUST

This chapter is taken from a paper published in *Terra Nova* in 2015. I was the lead author for this study, which included field work, sample preparation, and writing the manuscript. Again, Ilya Bindeman (University of Oregon) served in an advisory role, and helped with sample collection and manuscript preparation. Richard Stern (University of Alberta) performed the in-situ oxygen isotope analyses in zircon, and Christopher Fisher (Washington State University) performed the Hf isotope analyses. Stern and Fisher also aided in writing the methods sections seen in the appendix. The published manuscript is available at doi:10.1111/ter.12156.

3.1. Introduction

Continental bimodal large igneous provinces are widely considered to be the product of interaction between mantle plumes and the crust (Bryan & Ferrari, 2013 and references therein). The youngest of these, the Columbia River Basalts (CRB), was produced by the Yellowstone mantle plume (e.g. Camp & Ross, 2004; Duncan, 1982; Glen & Ponce, 2002; Schmandt et al., 2012). The first eruptions of the CRB occurred in thin accreted oceanic crust at Steens Mountain at 16.7–16.5 Ma (Camp et al., 2003, 2015; Reidel et al., 2013), and were quickly followed by the earliest syn□CRB silicic volcanism: the 16.55 Ma Tuff of Oregon Canyon at the McDermitt centre (Fig. 3.1, Coble & Mahood, 2012). As with the basalts, silicic volcanism was widespread (Fig. 3.1)

until 14.5 Ma, when it became focused on the Snake River Plain hotspot track. Syn-CRB rhyolitic volcanism occurred in compositionally diverse accreted oceanic terranes west of the $^{87}Sr/^{86}Sr = 0.706$ isopleth (Fig. 3.1, Dorsey & LaMaskin, 2008; Leeman et al., 1992) and in older cratonic crust to the east. In this study, we use oxygen and radiogenic isotopes to determine the origin of these rhyolites and to further understand how the Yellowstone mantle plume modified the composition and structure of this complex crust during the flood basalt event.

3.2. Samples and analytical methods

We collected and analysed ~50 samples of CRB and syn-CRB rhyolites (details in the Supporting Information). Major phenocrysts were picked from whole rock samples

---

Figure 3.1 (next page). Map of the volcanism that occurred over the Yellowstone plume head from 17 to 14 Ma. Syn-CRB rhyolite eruptive centres are solid circles: DeLamar-Silver City (DS), Dinner Creek Tuff eruptive centre (DC), Dooley Mountain (DM), Hawks Valley-Lone Mountain (HV), High Rock (HR), Horsehead Mountain (HH), Jackass Butte (JA), J-P Desert (JP), Jarbidge Rhyolite (JR), Juniper Mountain (JM), Lake Owyhee (LO), Little Juniper Mountain (LJ), Malheur Gorge (MG), McDermitt (MD), Santa Rosa-Calico (SR), Sheep Creek Range (SC), Snowstorm Mountains (SS), Strawberry Mountains (SM), Swamp Creek (SW) and Whitehorse (WH) (estimates of erupted volume from Coble & Mahood, 2012). Younger Snake River Plain caldera complexes at Owyhee-Humboldt (OH), Bruneau-Jarbidge (BJ) and Twin Falls (TF) are shown in light purple. All $\delta^{18}O$ data are from this study, with the exception of values for the High Rock (Mallis et al., 2014) and Santa Rosa-Calico centres (Amrhein et al., 2013) and the J-P Desert and Jarbidge rhyolites (see Colón et al., 2015a, for a discussion of these rhyolites' inclusion with the syn-CRB group), which are emphasised by asterisks in the figure. Syn-volcanic grabens that make up the north–south trending zone of extension that parallels the edge of the craton include the Baker Graben (BG), the La Grande graben (LG), the Northern Nevada Rift, and the Oregon–Idaho graben (OIG). The latter sits on the edge of the suture zone of transitional crust between oceanic and continental lithosphere defined by the $^{87}Sr/^{86}Sr = 0.706$ and 0.704 isopleths, emphasised by the locations of Archean crustal blocks just to the east, explaining the isotopically diverse magmatism there (Fig. 3.2). See the Supporting Information for detailed sample locations.

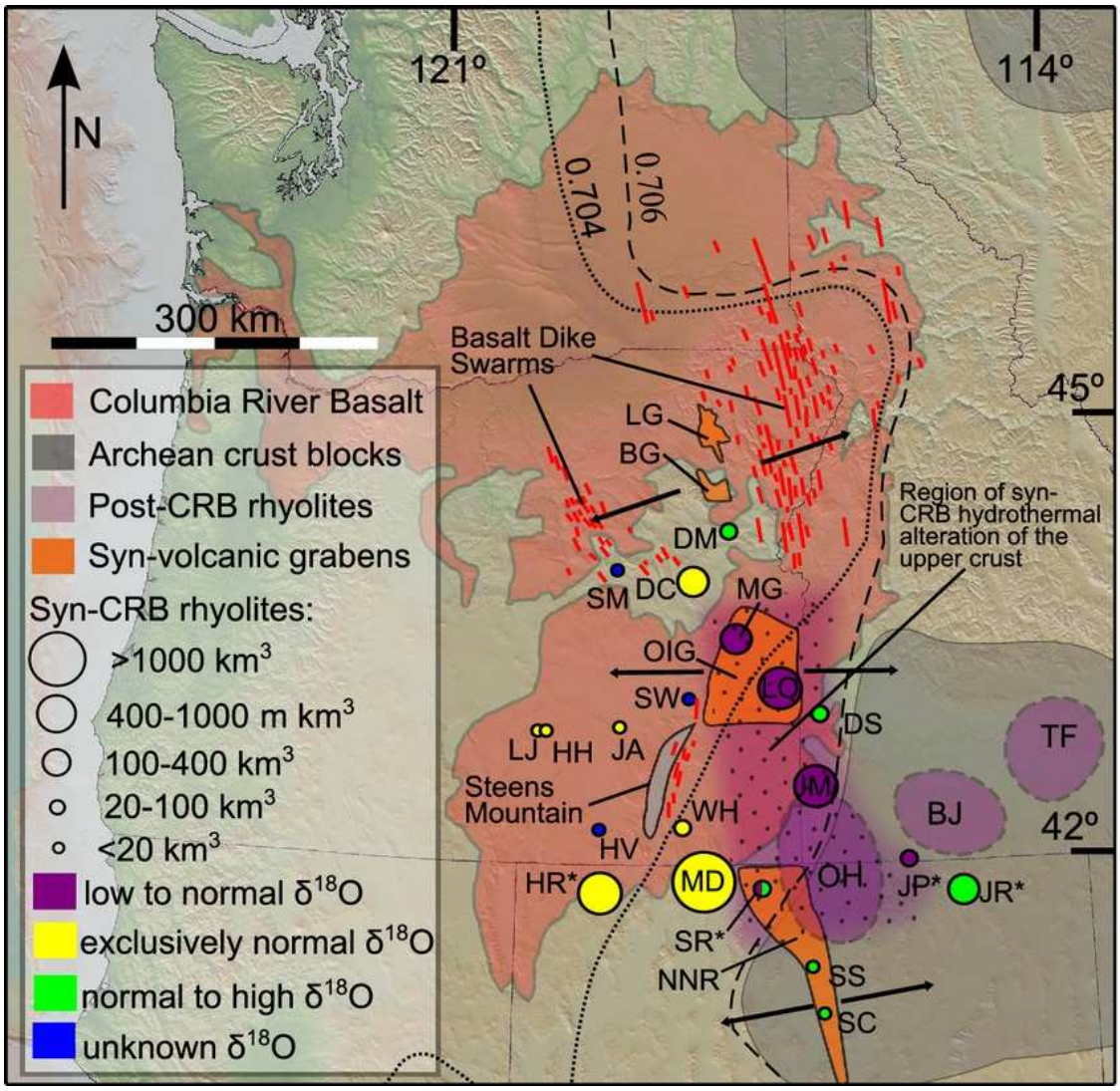

that were crushed and treated with cold hydrofluoric acid (HF) for 80–100 min to remove glass and its alteration products. Zircons were also hand□picked from a subset of syn□CRB rhyolites after dissolving most other material in HF over a period of 2 days. Zircon is particularly useful as it is highly resistant to weathering that may alter the chemical and isotopic composition of the whole rock and major phenocrysts. The $\delta^{18}O$ values of major phenocrysts in basalts and rhyolites were measured via laser fluorination at the University of Oregon (Bindeman, 2008) with 2□sigma precision better than ± 0.1‰. Zircon $\delta^{18}O$ was measured in situ using the CAMECA 1280R ion microprobe at

the University of Alberta (± 0.1–0.2‰), and a subset of these were analysed in overlapping spots for Hf isotope compositions by laser ablation ICP□MS at Washington State University (± 1–2 ε units). XRF and ICP□MS analyses of major and trace elements were also performed for selected units. Detailed methods appear in the Supporting Information.

3.3. Results

We report the first mineral $\delta^{18}O$ analyses for olivine and plagioclase from the CRB, with values ranging from slightly below to normal mantle□like values (average $\delta^{18}O_{olivine}$ = +4.9 to +5.1‰ and average $\delta^{18}O_{plagioclase}$ = 5.5–6.0‰ SMOW) in the Picture Gorge basalts to somewhat higher (average $\delta^{18}O_{olivine}$ = 5.7‰ and $\delta^{18}O_{plagioclase}$ = +5.7 to +6.6‰) values for Steens, Imnaha, and Grande Ronde basalts (Fig. 3.2a). Computed equilibrium melt $\delta^{18}O$ values (bulk including phenocrysts, see Supporting Information) for these phenocrysts broadly overlap with whole rock measurements by Carlson (1984). The ash flow tuffs of the High Rock ($\delta^{18}O$ from Mallis et al., 2014; all other values this study) and McDermitt caldera complexes, the Dinner Creek Tuff, lava domes west of Steens Mountain, and many large□volume lava flows of the Lake Owyhee Volcanic Field have normal to slightly high $\delta^{18}O$ values ($\delta^{18}O_{melt}$ = +6.0 to +8.0‰). In contrast, we observe low□$\delta^{18}O_{melt}$ values in syn□CRB rhyolites that erupted in and near the Oregon–Idaho graben along the terrane–craton boundary (Fig. 3.1), including the major caldera□forming ignimbrites of the Lake Owyhee volcanic field, the Tuff of Spring Creek ($\delta^{18}O_{melt}$ = +4.0‰) and the Tuff of Leslie Gulch ($\delta^{18}O_{melt}$ = +4.8‰), and the Littlefield and Cottonwood Mountain Rhyolites of the Malheur Gorge region ($\delta^{18}O_{melt}$ = +2.6–2.7 and +1.9–2.8‰, respectively), all of which have volumes of 100–

400 km^3 (Fig. 3.1, Coble & Mahood, 2012). High $\delta^{18}O$ values (>+8.0‰) are observed in syn□CRB rhyolites from the Silver City, Northern Nevada Rift and Dooley Mountain centres (Fig. 3.1), with the latter having $\delta^{18}O_{melt}$ values as high as +10.5‰ (Fig. 3.2), some of the highest $\delta^{18}O$ values measured in volcanic rock (e.g. Bindeman, 2008). The range in $\delta^{18}O$ values in the syn□CRB rhyolites therefore greatly exceeds the range measured in the Columbia River Basalts themselves (Fig. 3.2) as well as the range in the basalts and rhyolites of the Snake River Plain (Bindeman & Simakin, 2014), reflecting similar observations of $\delta^{18}O$ diversity in the syn□CRB rhyolites of central Oregon by Jenkins et al. (2013).

Zircons in syn□CRB rhyolites display an even greater range of $\delta^{18}O$ values than the associated major phenocrysts, with values as low as −0.6‰ in the J- P Desert (Colón et al., 2015a) and as high as +10.8‰ at Dooley Mountain (Fig. 3.2). Furthermore,

---

Figure 3.2 (next page). Isotopic and chemical trends in syn□CRB rhyolites. (a) Silica content vs. $\delta^{18}O_{melt}$ for CRB and syn□CRB rhyolites. The curve showing the expected evolution of $\delta^{18}O_{melt}$ during fractional crystallisation is from Bindeman (2008). The spread of $\delta^{18}O$ values away from this curve is the result of extensive melting of diverse□$\delta^{18}O$ crust into the evolving syn□CRB rhyolite magmas. Two coeval units, the low□$\delta^{18}O$ Cottonwood Mountain Rhyolite and the relatively high□$\delta^{18}O$ Hunter Creek Basalt (both of the Malheur Gorge region), are highlighted to emphasise their contrasting compositions. (b) Zircon $\delta^{18}O$ and ε_{Hf} values for a subset of the syn□CRB rhyolites. Data for zircons in rhyolites that erupted through the craton are from Colón et al. (2015a). These zircons show much greater diversity in ε_{Hf} values due to the influence of very old and unradiogenic Archaean crust (**Fig**. 3.1). (c) Detail of zircon compositions of syn□CRB rhyolites that erupted through accreted terranes west of the craton boundary, including zircons from Dooley Mountain (DM), the Dinner Creek Tuff (DC), the Tuffs of Spring Creek (TSC) and Leslie Gulch (TLG) and the Mahogany Mountain Rhyolite (MMR) (the latter three from the Lake Owyhee volcanic field, LO). The three Lake Owyhee units erupted through the transition zone between the craton and the younger accreted terranes to the west, reflected by lower $\delta^{18}O$ values (Fig. 3.3). By contrast, the units that erupted farther from the edge of the craton (DM and DC) have normal to high $\delta^{18}O$ values and generally higher ε_{Hf} values, reflecting the melting of younger accreted crust.

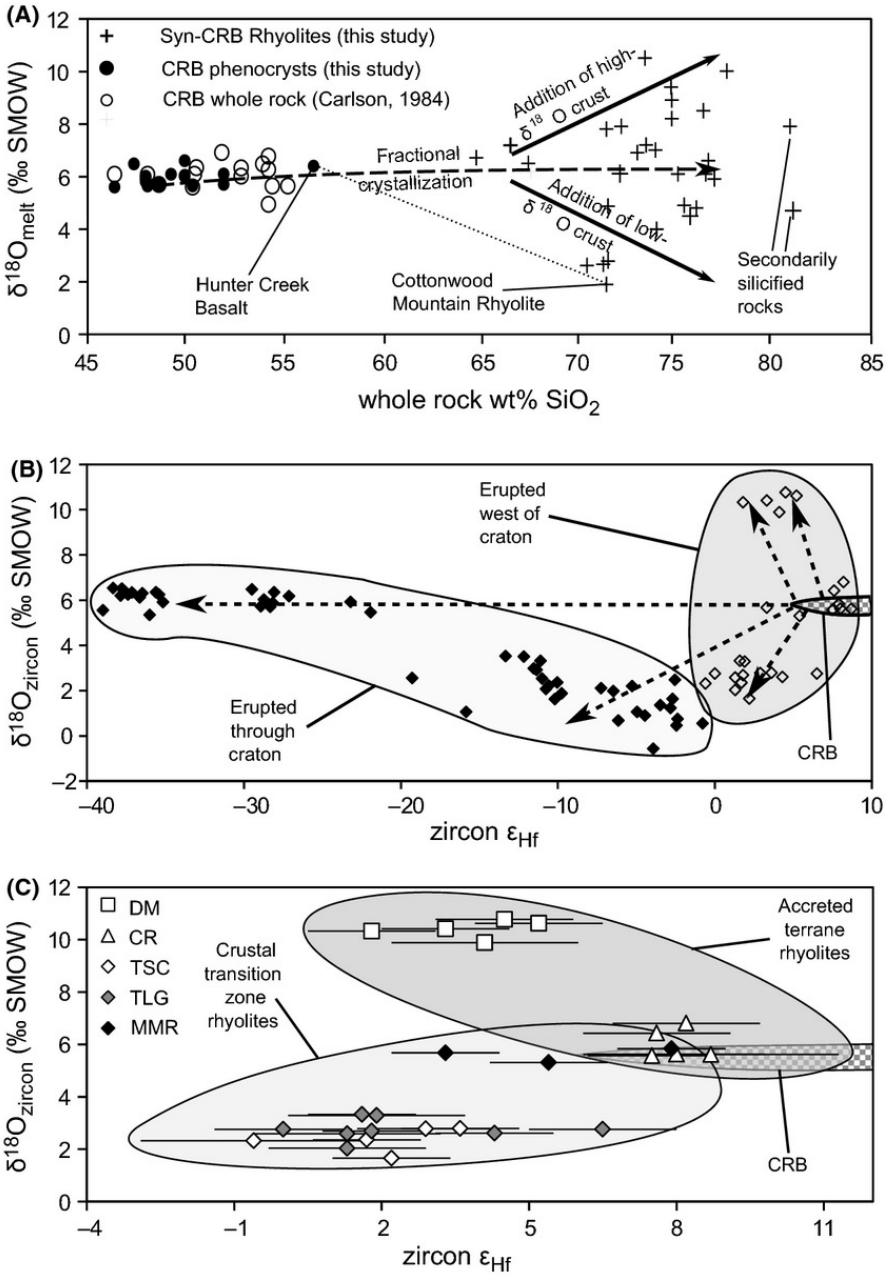

zircons in syn□CRB rhyolites exhibit a variability of >1‰ in $\delta^{18}O$, well in excess of analytical uncertainties for single spots (Fig. 3.2), implying disequilibrium $\Delta^{18}O_{melt\square zircon}$ values for many grains (such as the +1.65‰ zircon in the Tuff of Spring Creek, with $\Delta^{18}O_{melt\square zircon}$ = +2.3‰, or the +10.8‰ zircon from a rhyolitic dike in Dooley Mountain, with $\Delta^{18}O_{melt\square zircon}$ = −0.3‰, both compared to an equilibrium $\Delta^{18}O_{melt\square zircon}$ of ~+1.7‰ for typical 900 °C rhyolite, Bindeman, 2008). One particularly

extreme example of zircon diversity comes from the J□P Desert locality (Fig. 3.1), described in Colón et al. (2015a). There, individual eruptive units contain zircons with a range of up to 6‰ $\delta^{18}O$ and 30 ε_{Hf} units, with severe $\Delta^{18}O_{melt-zircon}$ disequilibrium. Finally, zircons from rhyolites erupted through or near to the cratonic crust east of the $^{87}Sr/^{86}Sr = 0.706$ line (including the J□P Desert) have lower ε_{Hf} values than those from rhyolites erupted through accreted terranes to the west (Fig. 3.3, e.g. Nash et al., 2006 for whole rocks).

3.4. Discussion

3.4.1 High and low-$\delta^{18}O$ rhyolites: evidence for large-scale plume-driven crustal remelting

The scatter in $\delta^{18}O_{melt}$ values away from the normal mantle value of 5.7‰ in

---

Figure 3.3 (next page). Plume influence on the continental crust through tectonism and melt production at the suture between the thick craton and thin, young accreted terranes. (a) The plume asymmetrically flattens against the steep edge of the thick continental lithosphere, causing extensive deformation and crustal heating to be concentrated along this boundary. (b) Surface uplift is concentrated where the lithosphere is thin and is minimal in the thick lithosphere, creating a flexure zone at the suture where the two crustal types and uplift regimes meet. Meteoric water intrudes into the crust via normal faults in this flexure zone, which can also serve as conduits for erupting rhyolitic magmas. Rising magmas melt crust that is hydrothermally altered by the interaction of meteoric water and country rock driven by heat from deeper intrusions, producing low-$\delta^{18}O$ rhyolites (parts (a–b) are modified from the models of Burov et al., 2007). (c) The transition between old crust and young accreted crust is recorded by Hf isotopes in syn-CRB rhyolites in the area, consistent with similar step-function behaviour in radiogenic isotopes in rhyolites observed by Nash et al. (2006). (d) Finally, the concentration of heating and deformation at the transition zone near the crustal boundary leads to the proliferation of hydrothermal alteration of the crust and low-$\delta^{18}O$ rhyolite production in that area. By contrast, syn-CRB rhyolites that erupted to the west of the zone of normal faulting and hydrothermal alteration have normal to high $\delta^{18}O$ values. The plus symbols are from Amrhein et al. (2013) and Mallis et al. (2014), and parts (c–d) also contain data from Colón et al. (2015a).

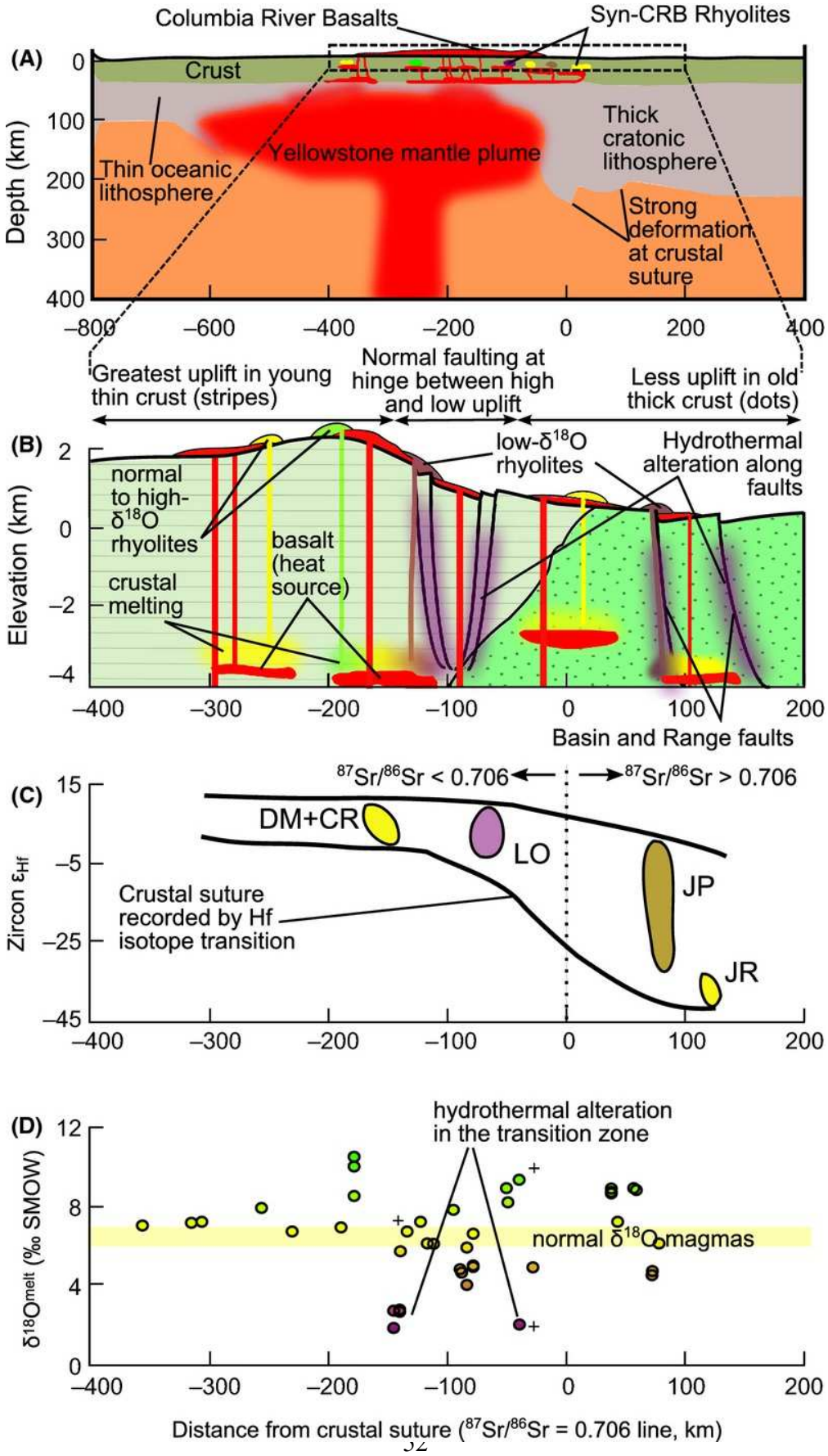
Columbia River Basalts
Syn-CRB Rhyolites
(A)
Crust
Depth (km)
Thick cratonic lithosphere
Yellowstone mantle plume
Thin oceanic lithosphere
Strong deformation at crustal suture
Greatest uplift in young thin crust (stripes)
Normal faulting at hinge between high and low uplift
Less uplift in old thick crust (dots)
(B)
Elevation (km)
low-δ18O rhyolites
Hydrothermal alteration along faults
normal to high-δ18O rhyolites
basalt (heat source)
crustal melting
Basin and Range faults
(C)
87Sr/86Sr < 0.706
87Sr/86Sr > 0.706
DM+CR
LO
JP
JR
Zircon εHf
Crustal suture recorded by Hf isotope transition
(D)
hydrothermal alteration in the transition zone
normal δ18O magmas
δ18Omelt (‰ SMOW)
Distance from crustal suture (87Sr/86Sr = 0.706 line, km)

much of the CRB is consistent with models that implicate the contribution of remelts of lithospheric material in the formation of the CRB (e.g. Camp & Hanan, 2008; Hooper & Hawkesworth, 1993; Wolff et al., 2008; Wolff & Ramos, 2013). Similarly, the much larger variation in major phenocryst $\delta^{18}O$ values in the syn□CRB rhyolites suggests that they are derived from remelting of pre□existing continental crust. Both the syn□CRB rhyolites and the Snake River Plain rhyolites require a minimum crustal melt contribution of 15–40% by volume (Leeman, 1982; McCurry & Rodgers, 2009; Nash et al., 2006) and many are likely up to 80% crustal melt (Bindeman & Simakin, 2014; Colón et al., 2015a). The syn□CRB rhyolites extend into higher $\delta^{18}O$ values than those of the Snake River Plain (e.g. Bindeman & Simakin, 2014), and many high□$\delta^{18}O$ rhyolites, such as those erupted at Dooley Mountain, are likely derived from melting regionally abundant high□$\delta^{18}O$ sedimentary or metasedimentary protoliths. By contrast, at Silver City, Idaho, high□$\delta^{18}O$ rhyolites (δ18Oqtz = +8.6 to +10.2‰) are likely derived from melting of local high□$\delta^{18}O$ Cretaceous granitoids (δ18Oqtz = +10.4‰), implying up to 80% crustal melt in their formation (Supporting Information). Low□$\delta^{18}O$ rhyolites, on the other hand, are derived from the remelting of precursor rocks that have been hydrothermally altered by hot meteoric water at large water/rock ratios (e.g. Taylor, 1974). Like their high□$\delta^{18}O$ counterparts, low□$\delta^{18}O$ rhyolites (+1.8 to +5.5‰) require 10–50% contributions of crustal remelts for their formation, based on the lower bound of $\delta^{18}O$ values observed for typical hydrothermally altered rocks (~0‰) that could melt to form them (e.g. Bindeman & Simakin, 2014, and references therein).

Hf isotopes in zircon from rhyolites that erupted through cratonic crust (Figs. 3.1 and 3.2) are frequently highly unradiogenic, indicating the involvement of melts of

Precambrian crust (Colón et al., 2015a). Hf in zircon from rhyolites that erupted through young accreted terranes is less diagnostic of crustal melting, but the abundance of low-$\delta^{18}O$ values in high-ε_{Hf} crust (this study, Colón et al., 2015a; Seligman et al., 2014) suggests that hydrothermal alteration affects young porous rocks more than older and presumably impermeable metamorphic rocks, similar to what is observed at the Skaergaard intrusion (Norton & Taylor, 1979). The so-called 'Nd–O paradox' observed in the Snake River Plain (McCurry & Rodgers, 2009; Ellis et al., 2013), in which normal-$\delta^{18}O$ rocks have high ε_{Hf} and ε_{Nd} values, and vice versa, can be explained by this simple relationship. Finally, the diversity in zircon isotopic compositions in single units reflects the eruption of mixtures of crustal melt batches before the zircons can reset to equilibrium values (e.g. Bindeman & Simakin, 2014; Colón et al., 2015a).

3.4.2 Plume-driven crustal hydrothermal alteration

The production of low-$\delta^{18}O$ rhyolites is generally constrained to shallow depths, as meteoric water will lose its low-$\delta^{18}O$ composition due to equilibration with the country rocks before reaching depths of 5–10 km (Drew et al., 2013; Bindeman & Simakin, 2014; Seligman et al., 2014). Meteoric water is also unlikely to penetrate the brittle/ductile transition in sufficient volumes to alter the $\delta^{18}O$ value of the country rocks (e.g. Menzies et al., 2014). This transition is at a depth of 5–10 km in the Basin and Range province today (Gans, 1987), and we consider this, or perhaps even shallower depths (due to very high heat flow), to likely reflect conditions in CRB times as well. We prefer this to the model of Leeman et al. (2008), which proposes a deeper 'sweet spot' for low-$\delta^{18}O$ magma generation at 15 km depth.

The low-$\delta^{18}O$ syn-CRB rhyolites erupted in regions that were experiencing syn-volcanic extension, particularly along a north–south trending series of grabens that includes the Oregon–Idaho graben and the Northern Nevada Rift (Fig. 3.1, Ferns & McClaughry, 2013). This east–west extension is also recorded by the orientation of the majority of CRB dikes. The oldest low-$\delta^{18}O$ syn-CRB rhyolite dated so far – the 15.9 Ma (Benson et al., 2013) Tuff of Leslie Gulch ($\delta^{18}O_{melt}$ = +4.8‰, and with zircon as low as +1.95‰) – erupted coevally with the early stages of normal faulting in the Oregon–Idaho graben. More $\delta^{18}O$-depleted rhyolites, such as the Rhyolite of Cottonwood Mountain ($\delta^{18}O_{melt}$ = +1.9‰ in one sample), erupted along the western graben-bounding faults after more subsidence had taken place (Cummings et al., 2000). Another low-$\delta^{18}O$ area, the J-P Desert, discussed in detail in Colón et al. (2015a), also erupted coevally with Basin and Range extension, which started in the region at ~16 Ma (Brueseke et al., 2014; Colón et al., 2015a; and references therein). These extensional faults provided conduits for meteoric water to penetrate the crust and produce low-$\delta^{18}O$ rocks that were then melted to form syn-CRB rhyolites (Fig. 3.3, Gottardi et al., 2013), and there is evidence for the presence of lakes in the Oregon–Idaho graben while these faults were active (Cummings et al., 2000). The heat needed to drive the exchange of oxygen isotopes between the rock and the invading meteoric water would have been provided by the intrusion of the CRB magmas, the waning stages of which erupted coeval with the Oregon–Idaho graben rhyolites (Cummings et al., 2000; Coble & Mahood, 2012; Ferns & McClaughry, 2013). This normal-faulting-based mechanism for low-$\delta^{18}O$ rhyolite formation was also proposed in studies made individually for the Lake Owyhee, Santa Rosa-Calico and J-P Desert syn-CRB rhyolite centres, and the Picabo centre in

the Snake River Plain (Amrhein et al., 2013; Blum et al., 2013; Drew et al., 2013; Colón et al., 2015a). The lack of voluminous low-$\delta^{18}O$ rhyolites at the Northern Nevada Rift, despite syn-volcanic normal faulting there, may have been a result of less available heat for hydrothermal alteration there compared with the Oregon–Idaho graben, which was closer to the putative axis of the mantle plume. Instead, relatively unaltered crust melted to produce the predominantly high-$\delta^{18}O$ rhyolites of the Northern Nevada Rift.

By compiling deviations from mantle values towards different crustal end-members, our isotopic study of the syn-CRB rhyolites 'maps' pre-existing crust types, and particularly maps those areas that experienced syn-volcanic hydrothermal alteration. The Oregon–Idaho graben, which is the site of the most voluminous low-$\delta^{18}O$ rhyolite volcanism, is on the edge of the suture zone between accreted Palaeozoic terranes and the ancient North American craton (Leeman et al., 1992; Dorsey & LaMaskin, 2008; Shervais & Hanan, 2008). Similarly, the other sites of low-$\delta^{18}O$ volcanism are located in or near this transition zone, which is marked on the surface by the $^{87}Sr/^{86}Sr = 0.706$ and 704 isopleths (Fig. 3.1), and reflected by diverse Hf isotopes in zircons in rhyolites from this transition zone (Fig. 3.3).

These isotopic observations corroborate numerical models of plume interactions with continental lithosphere. In particular, Burov et al. (2007) showed that lithospheric warping and gradients in surface uplift above a mantle plume will be concentrated by a lithospheric thickness transition, as the plume stalls against the thicker lithosphere and causes greater uplift in the thin lithosphere (**Fig**. 3.3). This concentration of deformation, which can produce conduits for magma and hydrothermal fluids via shallow faulting, is illustrated by the eruption of a majority of the syn-CRB rhyolites, including the great

majority of low-$\delta^{18}O$ rhyolites, through the crustal transition zone that represents the transition between thin accreted terranes and the North American craton (Figs. 3.1 and 3.3). In addition, it appears that broader regional extension in the northwest Basin and Range province, which began nearly simultaneously with the eruption of the CRB (Colgan & Henry, 2009), was triggered by the heat from the mantle plume underplating and thermally weakening the overthickened and pre-stressed continental lithosphere (e.g. Burov & Gerya, 2014; Camp et al., 2015a). Hence, the Yellowstone mantle plume produced the normal faulting in the suture region, the heat to drive hydrothermal alteration in those faults, and the further heat to melt the crust and produce both high- and low-$\delta^{18}O$ rhyolites in compositionally diverse crust. This interplay between a mantle plume, extensional tectonics and the production of low-$\delta^{18}O$ rhyolites with diverse zircons has been observed today in Iceland (e.g. Bindeman et al., 2012). This suggests that mantle plumes may have played a significant role, via hydrothermal preconditioning and melting, in the evolution of continental crust throughout geological history.

3.4. Bridge

The next chapter in this dissertation, Chapter IV, represents the culmination of my investigation into the isotopic story recorded by zircon in the Yellowstone hot spot track. My coauthors and I turned from the Columbia River basalts back towards the younger central Snake River Plain rhyolites, which were the most voluminous concentration of silicic magmas to erupt in the Yellowstone hot spot track's discovered history. Using a rich data set of many hundreds of zircon, we combined measurements of $\delta^{18}O$ and ε_{Hf},

with extremely precise U-Pb ages, allowing us to add a temporal component to the study that was unavailable in the studies outlined in Chapters II and III. We show clear documentation through zircon ages of the magma batch assembly process, recorded in different core and rim isotopic compositions and ages in zircon, and combined our dataset with other recent studies of Yellowstone hot spot track zircon to demonstrate that there are common trends in both the O and Hf isotopic evolutions of each volcanic center along the Snake River Plain and Yellowstone.

CHAPTER IV

ORIGINS AND EVOLUTION OF RHYOLITIC MAGMAS IN THE CENTRAL SNAKE RIVER PLAIN: INSIGHTS FROM COUPLED HIGH-PRECISION GEOCHRONOLOGY, OXYGEN ISOTOPE, AND HAFNIUM ISOTOPE ANALYSES OF ZIRCON

This chapter is taken from a paper published in *Contributions to Mineralogy and Petrology* in 2018, of which I was the lead author, which included sample processing, manuscript writing, and figure design. Again, Ilya Bindeman (University of Oregon) served as an advisor, provided some samples, and assisted with manuscript revisions. Jörn Wotzlaw (ETH Zürich) performed the ID-TIMS dating of zircon. Eric Christiansen (Brigham Young University) provided samples from the Kimberly borehole and assisted with interpreting their provenance. Richard Stern (University of Alberta) performed the in-situ measurements of oxygen isotopes in zircon. Wotzlaw and Stern also helped with writing the methods section for this paper. The published manuscript is available at doi:10.1007/s00410-017-1437-y.

4.1. Introduction

The Columbia River Basalt–Snake River Plain–Yellowstone system is the world's premiere example of a continental hotspot track (Fig. 4.1). It is the site of many of the most voluminous volcanic eruptions in the Neogene Period (Christiansen 2001; Hildreth et al., 1991; Pierce & Morgan 2009), and comprises one of the largest suites of anorogenic (A-type) rhyolites worldwide (Christiansen & McCurry 2008; Pearce et al., 1984). The Yellowstone hotspot track additionally includes the largest known

concentration of low-$\delta^{18}O$ rhyolites in the world, with a cumulative volume of over 10^4 km^3 (Bindeman & Simakin 2014; Bonnichsen et al., 2008). Low $\delta^{18}O$ values in fresh igneous rocks were once considered to be geologic oddities (e.g. Hildreth et al., 1984), but they have since been found around the world, particularly in association with extensional tectonics and large igneous provinces (both present at Yellowstone). Examples include rhyolites and basalts in Iceland (Bindeman et al., 2012; Gautason & Muehlenbachs 1998; Zierenberg et al., 2013), Archean extensional granites in Greenland (Hiess et al., 2011), rhyolites in the Karoo Volcanic Province in Africa and Antarctica

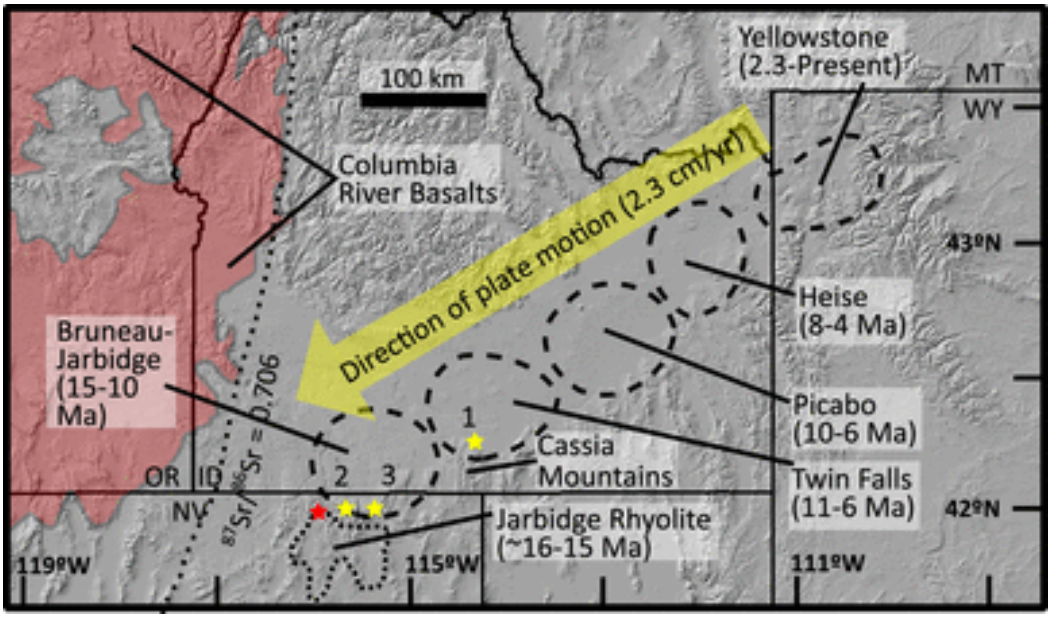

Fig. 4.1. Map of the Yellowstone hotspot track, showing the major volcanic centers that formed after the onset of the eruption of the Columbia River Flood Basalts (red). Three yellow stars are sampling locations for this study: (1) the Kimberly borehole, (2) along the Bruneau River, and (3) along the Jarbidge River. The red star is the site of the J-P Desert locality discussed in the text and in Colón et al., (2015b). Outlines of volcanic centers are from Bonnichsen et al. (2008) and Colón et al. (2015b). Plate velocity is from Anders et al. (2014). Map background is from Ryan et al. (2009) via GeoMapApp (http://www.geomappapp.org/).

(Harris & Erlank 1992), younger rifted-margin granites in South Africa (Curtis et al., 2013), Jurassic granites of the North China Craton (Wang et al., 2017a), Proterozoic granites of east-central and south China, Seychelles, and Madagascar (Archibald et al., 2016; Fu et al., 2013; Harris & Ashwal 2002; Zheng et al., 2007), and rhyolites of the Proterozoic Malani Igneous Suite in India (Wang et al., 2017b).

The Snake River Plain–Yellowstone system is the youngest and likely the best-preserved of these suites globally, making it the ideal laboratory for the detailed study of the origin of these types of magmas worldwide. In this study, we make measurements of the O and Hf isotopic compositions of zircon grains from central Snake River Plain rhyolites and combine them with precise U–Pb ages of those same crystals. The relative youth of Snake River Plain volcanism compared to many other low-$\delta^{18}O$ anorogenic igneous suites allows us to make detailed measurements of the time-dependent changes in both O and Hf isotope compositions of its magmas, and recently developed high-precision dating techniques allow us to study variations in the ages of zircon from a single eruption (e.g. Rivera et al., 2016; Wotzlaw et al., 2013, 2014, 2015). Finally, we combine our results with data from several other recent studies of Yellowstone hotspot track O and Hf isotopes in zircon to identify isotopic trends common to the entire hotspot track, as opposed to those dependent on local geology, allowing us to determine which processes may be properties of similar igneous suites around the world.

4.2. Geologic setting

Previous work on Yellowstone hotspot zircon has identified considerable isotopic diversity (Fig. 4.9) which has been interpreted as the result of variable mixing between a

mantle-like end-member ($\delta^{18}O \approx +5.7‰$ VSMOW; $\varepsilon_{Hf} = 0$ to $+5$) considered to be isotopically identical to basalts from the Snake River Plain/Yellowstone (e.g. Stelten et al., 2017) and up to 60% of some combination of end-member crustal compositions (Colón et al., 2015b; Drew et al., 2013; Wotzlaw et al., 2015). These crustal end-members are visible in Fig. 4.9, which combines previous measurements of Hf and O isotopes along the hotspot track with data from this study. We intentionally leave out rhyolites from west of the $^{87}Sr/^{86}Sr = 0.706$ line (Fig. 4.1) which defines the edge of the Precambrian core of North America (Leeman 1992; Nash et al., 2006), as these rhyolites were produced in significantly different crust and with very different rates of basaltic intrusion from the mantle (Blum et al., 2016; Coble & Mahood 2012; Colón et al., 2015a; Ferns & McClaughry 2013). The first crustal end-member has been interpreted as ancient Proterozoic or even Archean crust with exceptionally unradiogenic (low-ε_{Hf}) hafnium isotopic compositions, and relatively normal $\delta^{18}O$ values (+ 5–8‰); xenoliths of such material have been observed throughout the Snake River Plain, despite the relative paucity of surface outcrops (Leeman et al., 1985; Shirley 2013; Watts et al., 2010). The unit on the hotspot track containing the most of this end-member is the Jarbidge Rhyolite (Colón et al., 2015b), which has zircon with ε_{Hf} values as low as − 39, the lowest value observed in a non-xenocrystic zircon in the entire region (Fig. 4.9).

The second crust type is very low-$\delta^{18}O$ and only moderately unradiogenic in terms of Hf isotopes, and is well-represented among Snake River Plain and Yellowstone zircon grains (Fig. 4.9). This material must have been hydrothermally altered in the presence of meteoric water, and has previously been proposed to be (1) deeply buried and syn-volcanically altered caldera-filling ignimbrites, (Bindeman & Valley 2001; Colón et

al., 2015b; Drew et al., 2013; Watts et al., 2011), (2) shallow crustal rocks that were hydrothermally altered during some magmatic event that significantly predates Yellowstone volcanism, such as the emplacement of the Idaho and Challis batholiths (Boroughs et al., 2012; Drew et al., 2013; Ellis et al., 2013), or (3) shallow country rocks or juvenile (Yellowstone hotspot-age) intrusions altered by hydrothermal circulation driven by heat produced by intrusions of basalt coeval with the Columbia River Basalts and early Snake River Plain volcanism (Blum et al., 2016; Colón et al., 2015a, b). The first explanation is inadequate on its own at the central Snake River Plain (Bruneau–Jarbidge and Twin Falls, Fig. 4.1) because the erupted rhyolites there are exclusively low-$\delta^{18}O$ (Colón et al., 2015b), uniquely among the rhyolitic centers of the region (Bindeman & Simakin 2014), precluding a role for buried young ignimbrites from the same system in the production of the first low-$\delta^{18}O$ eruptions. The earliest low-$\delta^{18}O$ rhyolites of the central Snake River Plain are thus likely derived from some combination of the latter two mechanisms, with a possible role for caldera burial in producing the later, even lower-$\delta^{18}O$ rhyolites (Colón et al., 2015b). We note that the second two options assume the hydrothermal alteration of some pre-existing crust, but option (3) assumes that this happened only shortly before rhyolite production, and includes juvenile intrusions with older crust in the collection of material that is hydrothermally altered.

To date, only limited work on zircon isotope geochemistry has been published for the Bruneau–Jarbidge and Twin Falls centers (Blum et al., 2016; Cathey et al., 2011; Couper 2016; Seligman 2012; Fig. 4.1), even though they are both the most voluminous and the only exclusively low-$\delta^{18}O$ rhyolitic centers on the entire hotspot track (Bonnichsen et al., 2008; Ellis et al., 2013). This fact makes their study critical to any

broader investigation of the origins of low-$\delta^{18}O$ magmas at Yellowstone, and any extrapolation to other volcanic provinces worldwide. In this study, we measured coupled O and Hf isotope compositions of zircon grains from four large-volume ignimbrites from the Bruneau–Jarbidge center and from three units from the Twin Falls center, filling in this crucial gap. This data is complemented by laser ablation U–Pb geochronology and further dating via chemical abrasion isotope dilution thermal ionization mass spectrometry (CA-ID-TIMS) performed on the same crystals after removing them from the mounts used for spot analyses. These techniques provide new insights into the volcanic centers of the central Snake River Plain, building on earlier petrologic work by Cathey and Nash (2004) and Ellis and Wolff (2012).

4.3. Sampling of Bruneau–Jarbidge and Twin Falls rhyolites

At the Bruneau–Jarbidge center, we collected one sample each from four large welded ignimbrite outflow sheets. At a locality along the southern Jarbidge River in Nevada, we collected the 11.81 ± 0.06 Ma Cougar Point Tuff (CPT) VII and the 10.79 ± 0.14 Ma CPT XIII ($^{40}Ar/^{39}Ar$ ages of Bonnichsen et al., 2008; Fig. 4.1). The other two units were collected at the Bruneau River Canyon, approximately 20 km west of the first site, and are the 12.07 ± 0.08 Ma CPT V ($^{40}Ar/^{39}Ar$ age of Perkins et al., 1998) and a previously unnamed tuff unit at the base of the section. The latter unit predates CPT III, the previously oldest described member of the Cougar Point Tuff sequence, and we will refer to it as the tuff of Bruneau Canyon, though a name of Cougar Point Tuff I or Cougar Point Tuff II (no existing units have these names) may eventually prove to be more

appropriate (Bonnichsen & Citron 1982). These samples were chosen to encompass both the early and late stages of the eruptive sequence.

At the younger Twin Falls center (Figs. 4.1, 4.2), we sampled the three rhyolitic units intersected by the Kimberly borehole of Project Hotspot (Knott et al., 2016; Shervais et al., 2014). The uppermost of these is the Shoshone Rhyolite, dated by Knott et al. (2016) by single-grain laser fusion $^{40}Ar/^{39}Ar$ at 6.37 ± 0.44 Ma using plagioclase. This unit is buried by about 100 m of young basalt flows, and is itself just over 100 m thick. It appears to be a lava flow with a well-developed basal breccia. The second rhyolite unit, which has no other known exposures, is separated from the Shoshone Rhyolite by another ~ 170 m of basalt and sediment, and is referred to as the Kimberly Member of the Cassia Formation. It has been dated at 8.11 ± 0.05 and 7.95 ± 0.11 Ma (single grain sanidine $^{40}Ar/^{39}Ar$; Knott et al., 2016). This unit is approximately 180 m thick, and may be a densely welded ignimbrite (Knott et al., 2016), though we tentatively identify it as another lava flow because of its well-developed lower and upper breccias and lack of pyroclastic shards. Only a thin sediment horizon separates it from the lowermost unit, the Castleford Crossing Member (7.93 ± 0.48 Ma, single grain plagioclase $^{40}Ar/^{39}Ar$; Knott et al., 2016), which is interpreted as a welded ignimbrite. The Castleford Crossing Member has a minimum thickness of ~ 1400 m, and its base was not reached in the borehole (Fig. 4.2). Considering this thickness, we interpret this unit as a caldera-filling ignimbrite. Knott et al. (2016) estimate based on regional exposures of the outflow facies of this unit that it represents an eruption of a minimum of 1900 km^3 of magma (dense rock equivalent), making it among the largest identified silicic eruptions produced by the Yellowstone hotspot. Finally, it should be noted that at least 10

additional ignimbrite outflow units underlie the Castleford Crossing Member in the Cassia Mountains just south of Twin Falls (Fig. 4.1); these range in age from 8.1 to 11.3 Ma, and likely originate from the Bruneau–Jarbidge and Twin Falls centers as well (Ellis et al., 2012; Knott et al., 2016), which means that the three rhyolitic deposits encountered by the Kimberly Borehole and sampled for our study probably represent only the later stages of the Twin Falls eruptive sequence.

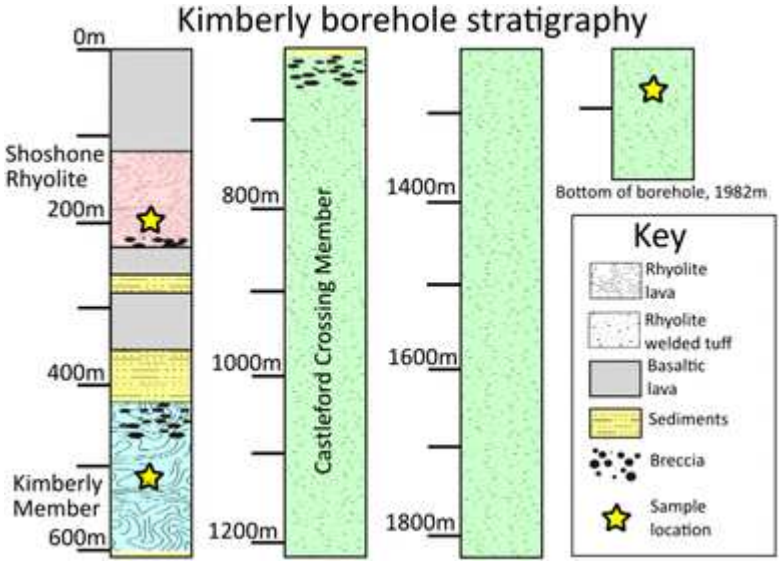

Fig. 4.2. Stratigraphy of the Kimberly Borehole, location shown in Fig. 4.1. The locations of sections of core used for this study are given by yellow stars, and are at depths of 218.2, 547.4, and 1888.8 m. For more detailed stratigraphy of the borehole and the surrounding region, see Knott et al., (2016).

4.4. Sample preparation and methods

4.4.1 Measurement of major phenocryst $\delta^{18}O$ values via laser fluorination

Major mineral phenocrysts (plagioclase, quartz, pyroxene) were extracted from crushed hand samples of welded ignimbrite using the methods described in Colón et al. (2015b). Zircon was isolated by either dissolution of the surrounding glass and phenocrysts in a 40% solution of hydrofluoric acid for the Bruneau–Jarbidge units or by

separation in 3.2 g/cm^3 methylene iodide for the Twin Falls units. Oxygen isotopes in major phenocrysts were measured with an integrated laser fluorination-MAT-253 mass spectrometer system at the University of Oregon (Bindeman 2008), using BrF_5 as the fluorinating reagent. Samples were controlled for reproducibility via intercalibration with a UOG (+ 6.52‰ VSMOW) garnet standard measured relative to a Gore Mountain Garnet standard of + 5.8‰ (Valley et al., 1995). Reproducibility of repeat measurements of standards was typically better than 0.2‰ (2 s.d.). When possible, measurements were made on multiple types of phenocrysts from each sample to rule out secondary alteration as a source of deviation from original magmatic $\delta^{18}O$ values.

4.4.2. Ion microprobe measurement of zircon $\delta^{18}O$ values

Zircon mount preparation was carried out at the Canadian Centre for Isotopic Microanalysis at the University of Alberta (CCIM, Twin Falls zircon, mount M1408) and at the Australian National University (Bruneau–Jarbidge zircon, mount M1402 = BF041), and secondary ion mass spectrometry (SIMS) measurements of zircon $\delta^{18}O$ were made at CCIM. Polished zircon mid-sections (though not necessarily the exact center of each grain) of unknowns and zircon reference materials were exposed within two 25-mm diameter epoxy mounts using diamond grits. The mounts were cleaned with a lab soap solution and de-ionized H_2O. The mounts were coated with 10 nm of high-purity Au prior to scanning electron microscopy (SEM) utilizing a Zeiss EVO MA15 instrument equipped with high-sensitivity, broadband cathodoluminescence and backscattered electron detectors. Beam conditions were 15 kV and 2–3 nA sample current. A further 40 nm of Au was subsequently deposited on the mount prior to SIMS analysis.

Oxygen isotopes (^{18}O, ^{16}O) in zircon were analyzed using a Cameca IMS 1280 multicollector ion microprobe. A $^{133}Cs^{+}$ primary beam was operated with impact energy of 20 keV and beam current of 2.0–2.5 nA. The ~ 10-µm diameter probe beam was rastered (20 × 20 µm) for 60–90 s prior to acquisition, and then 10 × 10 µm during acquisition, forming rectangular analyzed areas ~ 15 × 18 µm across and ~ 2 µm deep. The normal incidence electron gun was utilized for charge compensation. Negative secondary ions were extracted through 10 kV into the secondary (transfer) column. Transfer conditions included a 122-µm entrance slit, a 5 × 5-mm pre-ESA (field) aperture, and 100× sample magnification at the field aperture, transmitting all regions of the sputtered area. No energy filtering was employed. The mass/charge separated oxygen ions were detected simultaneously in Faraday cups L'2 ($^{16}O^{-}$) and H'2 ($^{18}O^{-}$) at mass resolutions (m/Δm at 10%) of 1950 and 2250, respectively. Secondary ion count rates for $^{16}O^{-}$ and $^{18}O^{-}$ were typically ~ 2.2×10^{9} and 4.5×10^{6} counts/s utilizing 10^{10} Ω and 10^{11} Ω amplifier circuits, respectively. Faraday cup baselines were measured at the start of the analytical session. A single analysis took 275 s, including pre-analysis rastering, automated secondary ion tuning, and 75 s of continuous peak counting.

Instrumental mass fractionation was monitored by repeated analysis of the zircon primary reference material (RM) after every four unknowns, either TEM2 ($\delta^{18}O_{VSMOW} = +8.2‰$; Black et al., 2004) for the Bruneau–Jarbidge samples, or S0081 (UAMT1; $\delta^{18}O = +4.87$; R. Stern, unpublished laser fluorination data, University of Oregon) for the Twin Falls zircon. TEM2 was also analyzed as a secondary RM on M1408 after every eight unknowns. The $^{18}O^{-}/^{16}O^{-}$ data set for the primary RM was processed collectively for each of three sessions (N = 51, 21, 40 for the Bruneau–Jarbidge

and the two Twin Falls sessions, respectively), yielding standard deviations of 0.09‰–0.10‰, following correction for systematic within-session drift (≤ 0.4‰); overall instrumental mass fractionation was 1.1–1.8‰. The individual spot uncertainties for the unknowns at 95% confidence for $\delta^{18}O$ are derived from considering errors relating to within-spot counting statistics, between-spot (geometric) effects, and correction for instrumental mass fractionation, and average ± 0.19‰, ± 0.25‰, and ± 0.20‰ for the three sessions, respectively. For the Bruneau–Jarbidge zircon, twelve analyzes of FC1 zircon (lacking a conventional reference value) yielded a weighted mean $\delta^{18}O = +5.81 \pm 0.06$ (MSWD = 1.19). For the two sessions with the Twin Falls zircon, results for multiple spots on multiple grains of the secondary RM (TEM2) gave mean values for $\delta^{18}O = +8.21 \pm 0.11$ (MSWD = 1.3; N = 9, standard deviation = 0.14‰) and $+8.20 \pm 0.04$ (MSWD = 0.96; N = 30, standard deviation = 0.10‰), consistent with the reference value of + 8.2‰ stated above (Black et al., 2004).

4.4.3. Laser ablation U-Pb dating and Hf isotope analysis of zircon

Zircon grains were then analyzed at the University of California Santa Barbara via laser ablation multi-collector inductively coupled plasma mass spectrometry (LA-MC-ICP-MS) analysis (Kylander-Clark et al., 2013); these were selected to encompass the full diversity of zircon $\delta^{18}O$ values observed by SIMS. Grains were first dated via U–Pb spot analyses 15 μm wide and 5 μm deep (Fig. 4.3), using the TEM2 standard. 2σ uncertainties averaged 0.6 Ma for single spot analyses (see appendix). $^{206}Pb/^{238}U$ ages were corrected by measuring ^{207}Pb and using the correction for common Pb in ISOPLOT (Ludwig 2003).

Spots closely adjacent to the U–Pb age spots were then separately analyzed by LA-MC-ICP-MS in another session (to achieve better precision than a split-stream

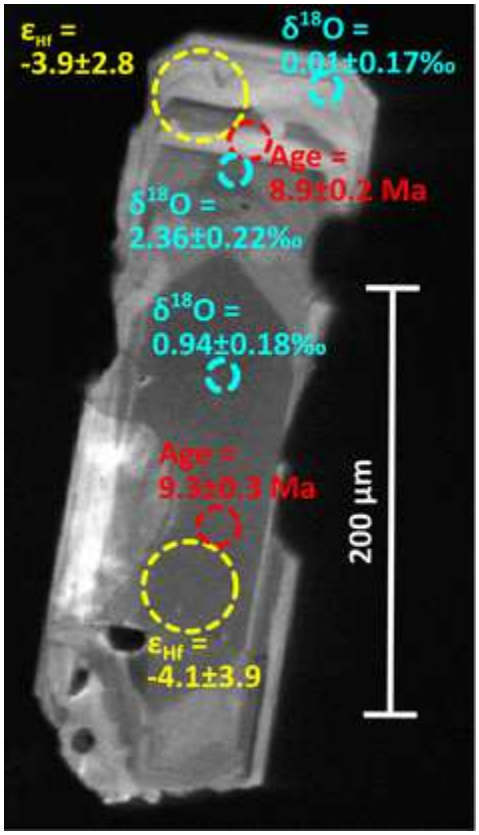

Fig. 4.3. Cathodoluminescence image of a complexly zoned zircon grain (#44, see appendix) from the Shoshone Rhyolite from the Kimberly borehole. Dashed circles show spot sizes of various analyses, including SIMS for $\delta^{18}O$ (~ 15 µm), U–Pb dates by LA-MC-ICP-MS (~ 15 µm, though they appear to have been slightly larger than SIMS spots on average), and 50 µm spot diameters for LA-MC-ICP-MS measurements of ε_{Hf} values. This grain was not dated by CA-ID-TIMS.

analysis) for their Hf isotope composition, using 50 µm wide and 30 µm deep spots (Fig. 4.3) and using UAMT1 standards. 2σ uncertainties for each Hf isotope measurement averaged 3.6 ε units. Care was taken to keep laser ablation spots for both Hf and U–Pb spots as close as possible to the SIMS $\delta^{18}O$ spots so that analyses of the same zone of a single crystal could be compared (Fig. 4.3), which is especially important considering the intra-crystal variability in both isotopic compositions and ages

(Figs. 4.4, 4.5). For this reason, we are able to pair zircon O and Hf isotope compositions of zircon cores and rims with the ages of those same regions of the crystal.

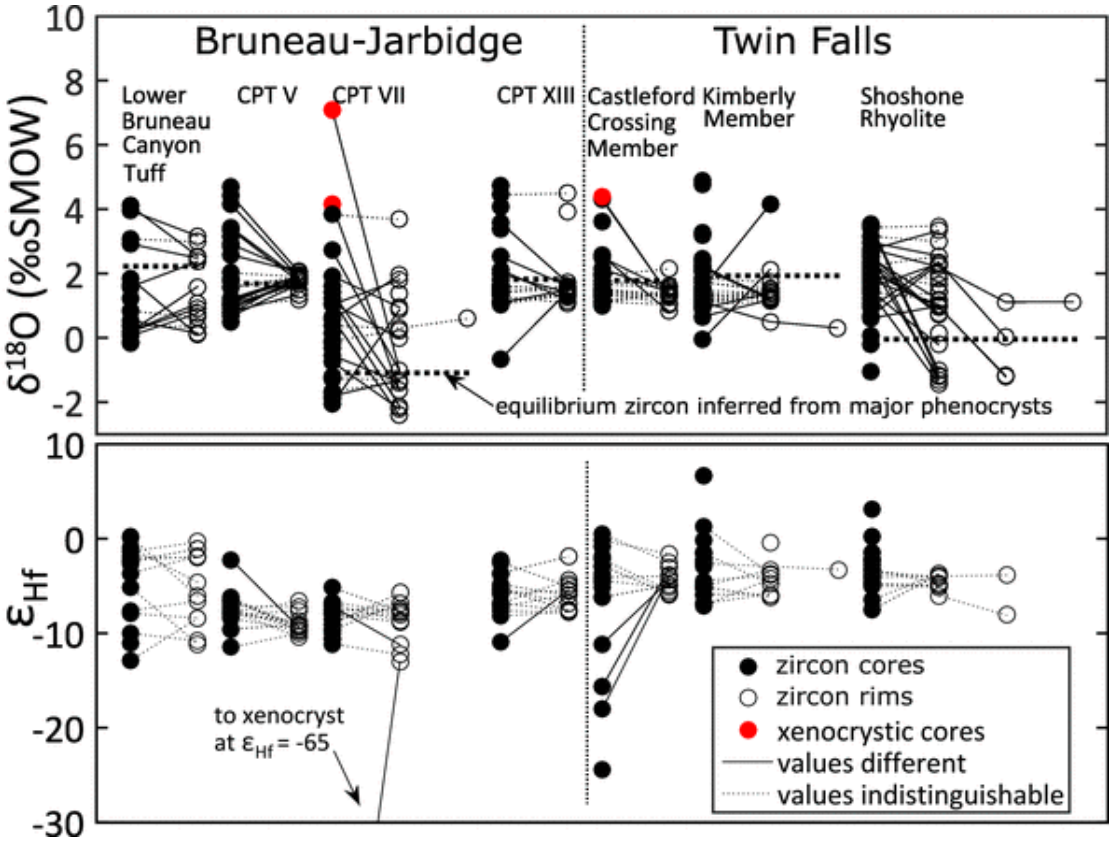

Fig. 4.4. Diversity in both hafnium and oxygen isotopes in zircon from all studied rhyolites. Core-rim pairs are connected by lines, solid where the two values do not overlap within their 2σ uncertainties, and are therefore resolvably different, and dashed otherwise. When more than one rim analysis was performed, the analyses farthest from the rim are plotted to the right. Zircon equilibrium compositions computed from major phenocrysts were inferred by subtracting 1.8‰ from quartz $\delta^{18}O$ values, 0‰ from pyroxene, or 1.0‰ from plagioclase (using fractionations from Loewen and Bindeman 2016), with the former minerals preferred when available. Note the much less diverse rims in CPT V which we interpret to be the result of batch mixing and overgrowth of rims in a well-mixed pre-eruptive magma chamber.

4.4.4 Thermal ionization mass spectrometry measurements of zircon

Finally, selected zircon crystals from the three Kimberly borehole units were extracted from epoxy grain mounts using stainless steel tools for high-precision dating via CA-ID-TIMS. Crystals were selected to encompass the entire range of laser ablation

U–Pb ages and O and Hf isotopic compositions measured by the above methods, and care was taken (with one exception, see below) to avoid grains with noticeably different core and rim ages. As such, the distribution of ages derived from the TIMS data should be taken as representative of the ranges of ages of zircon grains in an individual eruption, but not as representative of the relative abundances of those ages (Fig. 4.5). Individual grains were annealed at 900 °C for 48 h, ultrasonically cleaned in 3N HNO_3 and loaded into Savillex microcapsules with a microdrop of 7N HNO_3 and 80 µl of concentrated HF for chemical abrasion (Mattinson, 2005). Microcapsules were assembled in Parr bombs and zircon crystals were chemically abraded for 13 h at 180 °C. After chemical abrasion, zircon grains were transferred into 3 ml Savillex beakers, fluxed in 6N HCl and ultrasonically cleaned in 3N HNO_3. Cleaned single crystals were loaded back into their microcapsules with a microdrop of 7N HNO_3 and 60 µl of concentrated HF, spiked with 5 mg of EARHTIME ^{202}Pb-^{205}Pb-^{233}U-^{235}U tracer solution (Condon et al., 2015) and dissolved for 60 h at 210 °C in Parr bombs. After dissolution, samples were dried down and re-dissolved in 6N HCl at 180 °C overnight in Parr bombs. Samples were again dried down and re-dissolved in 3N HCl for anion exchange chemistry. Uranium and lead were separated from major and other trace elements using an HCl-based single-column anion-exchange chemistry modified from Krogh (1973) and U–Pb fractions were dried down with a drop of 0.02M H_3PO_4. Dried U–Pb fractions were loaded onto outgassed single Re-filaments with 1 µl of Si-Gel activator (Gerstenberger & Haase 1997). All analyses were performed at ETH Zürich employing a Thermo Scientific TRITON Plus thermal ionization mass spectrometer. Pb was analyzed using a dynamic peak-hopping routine on the axial secondary electron multiplier and U was measured as UO_2 using a static Faraday

collection routine employing 10^{13} ohm resistors. Details concerning mass spectrometry and associated corrections are given in von Quadt et al. (2016) and Wotzlaw et al. (2017). U–Pb dates were calculated relative to the published calibration of the ET2535 tracer solution (Condon et al., 2015) and using the U-decay constants of Jaffey et al. (1971). $^{206}Pb/^{238}U$ dates were corrected for initial ^{230}Th-^{238}U disequilibrium using a constant Th–U partition coefficient ratio of 0.2 (see Wotzlaw et al., 2014 for details). We achieved average 2σ uncertainties of ~ 0.025 Ma with analytical uncertainties largely correlating with Pb^*/Pb_c (i.e., the ratio of radiogenic lead over common lead) and thus with uranium concentration. These uncertainties do not include systematic uncertainties associated with the tracer calibration and decay constants.

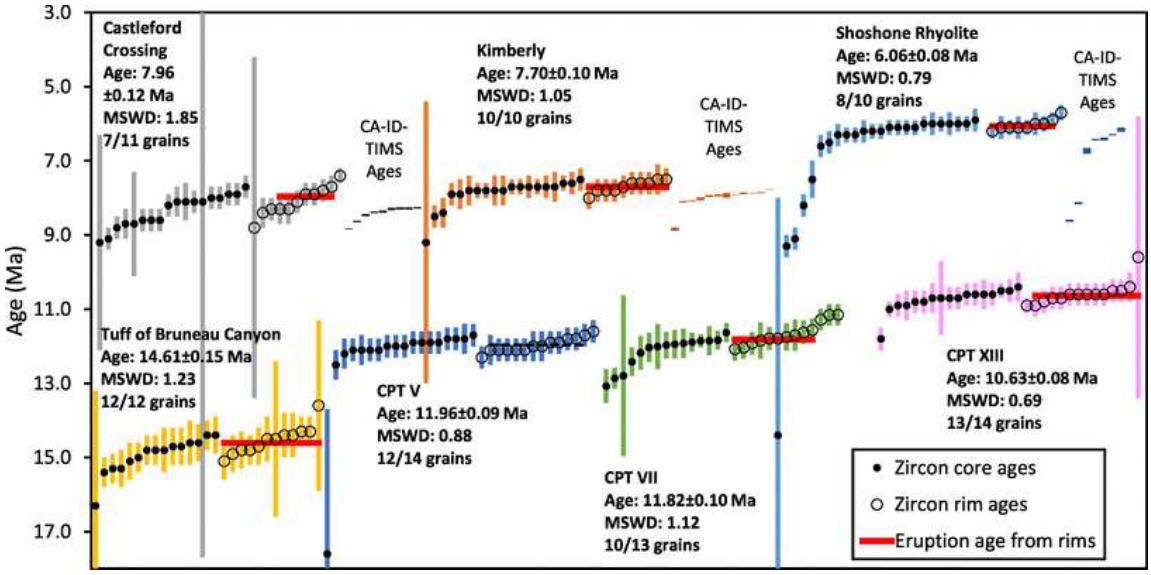

Fig. 4.5. Collection of all age data from this study. CA-ID-TIMS ages are all from the Twin Falls Kimberly borehole units (Fig. 4,2), and have much less uncertainty than the laser ablation ages (smaller vertical bars). Note that laser ablation-measured zircon rim ages are both younger and more homogeneous than the core ages. Horizontal red lines show the inferred eruption ages based on the rims, and cover the vertical error bars of the ages of the zircon used to compute those ages. All vertical age error bars are 2σ.

4.5. Results

4.5.1. Zircon ages

We obtained maximum estimates for eruption ages by taking the weighted mean of the largest population of statistically equivalent zircon rim LA-MC-ICP-MS ages from each sample (Fig. 4.5). All individual spot ages that differ by more than 95% confidence from the average age were excluded from the weighted averages, to remove the influence of antecrysts or zircon affected by Pb loss (Fig. 4.5, appendix). We only consider rim ages as many zircon cores are measurably older than the associated rim ages (Fig. 4.5, appendix), and thus cannot possibly reflect eruption ages. At Bruneau–Jarbidge, we propose an eruption age of 14.61 ± 0.15 Ma for the newly identified tuff of Bruneau Canyon, and ages of 11.96 ± 0.09 Ma for CPT V, 11.82 ± 0.10 Ma for CPT VII, and 10.68 ± 0.08 (all reported uncertainties are 2σ) for CPT XIII. The latter three are all indistinguishable from the $^{40}Ar/^{39}Ar$ ages previously reported by Bonnichsen et al. (2008, see above). At Twin Falls, we find zircon rim U–Pb ages of 7.96 ± 0.12 Ma for the Castleford Crossing Member, 7.70 ± 0.10 Ma for the Kimberly Member, and 6.06 ± 0.08 Ma for the Shoshone Rhyolite. All of these ages agree with the less precise $^{40}Ar/^{39}Ar$ ages given by Knott et al. (2016, see above), and we are able to distinguish the ages of the Kimberly and Castleford Members unlike in that study. This broad agreement with previous $^{40}Ar/^{39}Ar$ eruption ages suggests that our weighted average zircon rim U–Pb ages accurately reflect the time of eruption of the magmas, giving us confidence that our age for the tuff of Bruneau Canyon, for which there is no $^{40}Ar/^{39}Ar$ age, also reflects the time of eruption of that unit.

With the 14.61 Ma tuff of Bruneau Canyon, we find clear evidence for volcanism significantly predating the 12.7 Ma $^{40}Ar/^{39}Ar$ age given by Bonnichsen et al. (2008) for

the onset of volcanism at the Bruneau–Jarbidge center (with CPT III), again assuming that at least some zircon ages from each unit reflect eruption ages. This corroborates earlier results by Colón et al. (2015b), who dated three rhyolitic units exposed near Sheep Creek, some 20 km farther west of the Bruneau Canyon (the J-P Desert locality of Fig. 4.1), with ages ranging from 15.3 ± 0.4 Ma to 14.6 ± 0.4 Ma. The presence of a deposit of similar age in the Bruneau River Canyon to the east in the form of the tuff of Bruneau Canyon extends the mapped extent of units of this age, and corroborates that rhyolitic volcanism in the central Snake River Plain started shortly after the main phase of the Columbia River Basalts (Coble & Mahood 2012; Colón et al., 2015b), and continued for more than 9 Myr until the eruption of the Shoshone Rhyolite.

While the ages of our zircon rims are generally in good agreement with each other (Fig. 4.5), the populations of zircon core ages are not homogeneous in the cases of the three Kimberly borehole units, CPT VII, and the Tuff of Bruneau Canyon (Figs. 4.5, 4.6). Our high-precision TIMS dates of zircon from the Kimberly borehole (Figs. 4.5, 4.7, 4.8) define the age diversity of individual zircon grains within each unit more clearly than the lower-precision laser ablation dates (Fig. 4.5). We cross-checked the CA-ID-TIMS and LA-MC-ICP-MS dates for the zircon grains which were dated via both methods (Fig. 4.7). In nearly all cases, the CA-ID-TIMS and LA-MC-ICP-MS are equivalent within 2σ uncertainty. There are two zircon grains where this is not the case; one Castleford Crossing Member grain has a rim which is much younger than the core of the bulk grain (the only grain known to have significantly different core and rim ages which was dated by total dissolution), and one Kimberly Member grain has a CA-ID-TIMS age which is much older than either the core or rim age measured by LA-MC-ICP-MS.

Despite these small inconsistencies, however, the general match achieved gives us confidence that the age distributions identified by the two methods are consistent. We also measured a few grains via CA-ID-TIMS for which we have $\delta^{18}O$ values but no laser ablation analyses (appendix). The single crystal ID-TIMS dates of isotopically diverse zircon resolve a prolonged history of magma production and recycling of older zircon. They span a range of 2.5 Myr for the Shoshone Rhyolite, 1.1 Myr for the Kimberly Member, and 0.6 Myr for the Castleford Crossing ignimbrite. These ranges far exceed the average 2σ analytical uncertainty which was ~ 0.025 Myr. They are also somewhat smaller than the age ranges obtained from LA-MC-ICP-MS analyses. This is likely the result of the smaller number of zircon grains used for TIMS dates (Fig. 4.5), unintentional blending of core and rim ages, and the fact that we specifically avoided grains with different core and rim ages, and thus all of the zircon grains are identified to have old cores.

4.5.2. Oxygen and hafnium isotopes

Every one of the rhyolitic units analyzed in this study was depleted in $\delta^{18}O$ relative to normal melt values of ~ + 6.2 ± 0.3‰ (VSMOW) expected for a rhyolite derived from fractionation of mantle-derived basalts (e.g. Bindeman 2008). Calculated

---

Fig 4.6 (next page). Probability density curves for the zircon LA-MC-ICP-MS ages given in Fig. 4.5. The CA-ID-TIMS dates are not considered here, as they deliberately targeted non-representative zircon to characterize the full range of zircon ages, and would produce artificially wide peaks. Both core and rim ages contributed to these curves, but the eruption age estimates are calculated only from rims, as in Fig. 4.5. Curves were computed using ISOPLOT (Ludwig 2003). We also plot $^{40}Ar/^{39}Ar$ ages (as red dashed lines) from previous studies for four additional units, the Dry Gulch, Indian Springs, and McMullen Creek Members of the Cassia Formation at Twin Falls (Knott et al., 2016), and CPT III of Bruneau–Jarbidge (Bonnichsen et al., 2008).

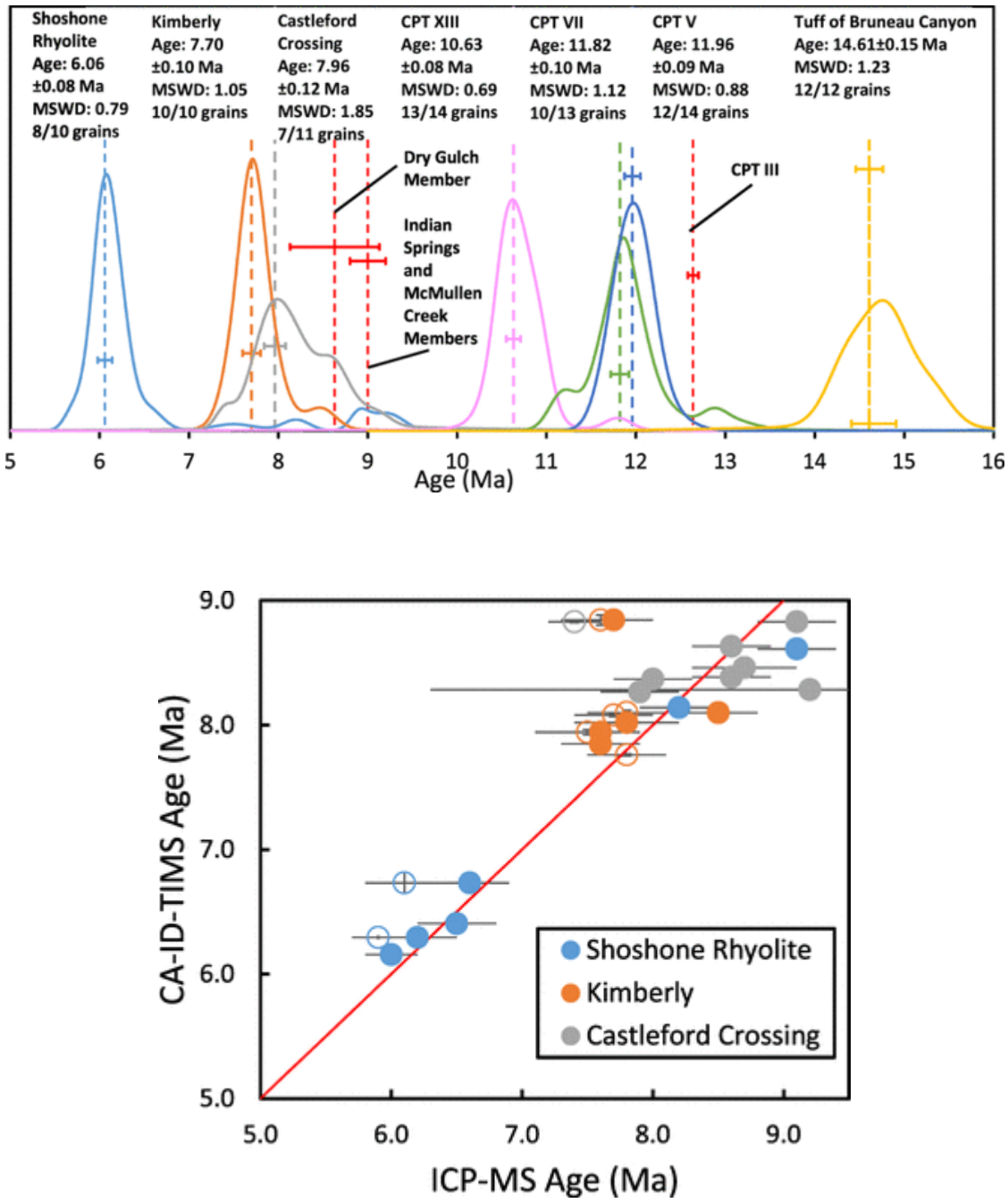

Fig. 4.7. Comparison of the two methods of dating zircon used in this study. Analyses made by laser ablation of rims are open circles, cores are closed. The red line is the 1:1 line; most of the ages fall on or near this line. All error bars are 2σ. This plot does not include five zircon grains that were dated via CA-ID-TIMS (all plotted in Fig. 4.8) that were not also analyzed by laser ablation

magmatic $\delta^{18}O$ values inferred from the compositions of major phenocrysts for the tuff of Bruneau Canyon, CPT V, CPT VII, and CPT XIII are + 3.5, + 3.8, + 0.2, and + 3.2‰, respectively (all uncertainties ± 0.2‰, these analyses were also reported in Bindeman and Simakin 2014, where the newly defined here tuff of Bruneau Canyon is labeled as CPT III, see sample 2005-ID-14). Amongst the Twin Falls units, we find magmatic $\delta^{18}O$ values based on major phenocrysts of + 2.3‰ for the Castleford Crossing Member, + 2.2‰ for the Kimberly Member, and − 0.6‰ for the Shoshone Rhyolite. Notably, the latter is one of the lowest $\delta^{18}O$ values obtained from major phenocrysts measured in any unit along the entire Snake River Plain–Yellowstone system. All seven units studied have significantly diverse oxygen isotope compositions in zircon. In all but the Shoshone Rhyolite, there is a greater range in $\delta^{18}O$ values in zircon cores than in zircon rims (Fig. 4.4), and the more homogeneous rim compositions tend to cluster around the bulk melt compositions inferred from the major phenocrysts, though in CPT VII and the tuff of Lower Bruneau Canyon this difference is admittedly small.

Similar complexity can be seen in the Hf isotope compositions of the zircon, though it is less resolvable than the diversity in the oxygen isotopes due to higher analytical error. We note several comparable trends, however, there are no samples with

---

Fig. 4.8 (next page). Plot of all CA-ID-TIMS dates against the corresponding oxygen isotope measurements of the same zircon. Open circles represent cores and closed circles represent rims, which for a single zircon have matching whole-grain TIMS ages. Note the large range of ages, particularly in the Shoshone Rhyolite, and the large range of oxygen isotope compositions in magmas which were crystallizing zircon simultaneously in the crust, particularly in the rhyolite of the Kimberly Member at about 8 Ma, providing further evidence for the batch assembly process. Diamonds represent eruption ages (our estimates, Figs. 4.5, 4.6) paired with estimated equilibrium zircon values (horizontal lines in Fig. 4.4). All error bars are 2σ

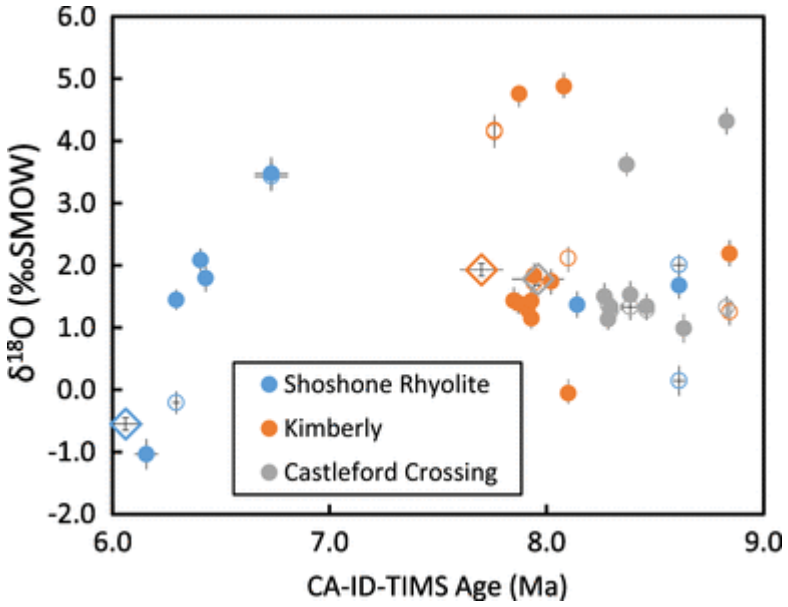

zircon rims that are more diverse than the corresponding cores, and we see significant reductions in diversity between cores and rims overall in the three studied Twin Falls units. This contrast is most pronounced in the Castleford Crossing Member, which has cores as low as ε_{Hf} -24 but no rims with ε_{Hf} less than − 6, and an upper limit of approximately $\varepsilon_{Hf} = 0$ in both cores and rims (Fig. 4.4).

4.5.3. Xenocrystic zircon

We identified only three xenocrystic (pre-Miocene) zircon cores in our entire dataset using laser ablation, all of which had young rims which closely matched the eruption ages of their respective host units (Fig. 4.4). In CPT VII, we found a single zircon core with an age of 86 ± 1.4 Ma, a $\delta^{18}O$ value of + 7.1 ± 0.18‰, and an ε_{Hf} value of − 9.7 ± 1.4, which we interpret based on its age and Hf isotopic composition as being derived from the Idaho Batholith (Gaschnig et al., 2010). The other two xenocrysts are Precambrian in age. One, which was also found in CPT VII, has an age of 1672 ± 24 Ma, a $\delta^{18}O$ value of + 4.14 ± 0.19‰, and an ε_{Hf} value of − 64 ± 1.7. The second Precambrian

age comes from the Castleford Crossing Member, and has an age of 631 ± 21 Ma, a $\delta^{18}O$ value of + 4.37 ± 0.26‰, and an ε_{Hf} value of -18 ± 2.3. These cores all contrast significantly from their young rims in cathodoluminescence images, with the two Precambrian grains being exceptionally dark, with the Cretaceous core showing very fine oscillatory zoning which is absent in all the younger grains and is typical of intrusive zircon (e.g. Corfu et al., 2003).

4.6. Discussion

4.6.1. Recycling and inheritance of zircon grains

We find significant diversity in both LA-MC-ICP-MS and CA-ID-TIMS ages in the zircon from the three Kimberly borehole units, and, at Bruneau–Jarbidge, in the laser ablation ages from CPT VII and the tuff of Bruneau Canyon (Figs. 4.5, 4.6, 4.7, 4.8). Zircon grains which occur in the 6.06 Ma Shoshone Rhyolite range in age from the time of eruption to 9 Ma, a greater time span than the entire history of volcanism at the Yellowstone Plateau (Christiansen 2001). We additionally find that many zircon grains have rim LA-MC-ICP-MS spot ages that are measurably younger than the cores of those same crystals (Figs. 4.5, 4.7).

We identify three potential sources for this zircon age diversity. The first is that these zircon grains are merely incorporated into the volcanic deposit during the eruptive process, either from the sides of the conduits feeding the eruption or from the ground during the emplacement of pyroclastic flows. While we cannot rule this out for all zircon, we consider this explanation to be unlikely as the deposits we sampled lack significant visible xenoliths, and because several of the older zircon cores that we analyzed have

rims that more closely mirror the eruption ages of the units that contain them (Fig. 4.5). This means that the zircon grains with older cores must have spent enough time in a younger magma to grow substantial rims, ruling out the possibility that they may have been derived from destroyed lithic fragments during an eruption.

The second possibility is that the older zircon grains were derived from previously erupted material which was deeply buried and partially remelted without destroying all the original zircon cores. The ≥ 1.5 km thickness of the 7.96-Ma Castleford crossing member in the Kimberly borehole (Fig. 4.2), coupled with the existence of many older ignimbrite units that may be associated with the Twin Falls volcanic center (Knott et al., 2016), suggests that the cumulative depth of burial of the deepest intracaldera deposits of the earliest eruptions may be as much as 5 km. This puts these oldest ignimbrites and their constituent zircon well inside estimated depth range of the magma bodies which fuel the large ignimbrite eruptions throughout the Yellowstone hotspot track (e.g. Almeev et al., 2012; Bolte et al., 2015; Huang et al., 2015). This implies that the products of early caldera-forming eruptions at each volcanic center are recycled by processes of repeated caldera collapse, burial, melting, and re-eruption, perhaps even more than once in the case of the oldest eruptive deposits. The faulting associated with caldera collapse may also bring not just volcanic rocks, but also buried older intrusions into contact with hot intrusions that can melt them. This process has been implicated in the production of the low-$\delta^{18}O$ rhyolites which are ubiquitous throughout the Snake River Plain–Yellowstone system (Bindeman & Simakin 2014; Bindeman & Valley 2001; Colón et al., 2015b; Drew et al., 2013; Watts et al., 2011), as was discussed above.

The third possible source for the zircon age diversity is inheritance from older intrusions of the same volcanic center. Such grains would be antecrysts and are distinct from the much older and rarer xenocrysts discussed above. Given the long times between some of the zircon crystallization ages and their eruption ages, these source intrusions were probably mostly if not completely solidified prior to their remelting and incorporation into a younger magma chamber. This process is also the only possible source of antecrystic zircon found in the oldest ignimbrites at each locality, which formed before any deeply buried young volcanic rocks even existed (Fig. 4.10). All of these processes would tend to make the crystal cargo of each successive eruption more isotopically diverse, but it is also important to note that large scale melting and mixing of the magmatic system could destroy and effectively "reset" much of this variation, and we do not see any trend towards greater age diversity in later eruptions, with the sole possible exception of the Shoshone Rhyolite at Twin Falls (Figs. 4.5, 4.6).

Determining whether an individual zircon with a crystallization age that is resolvably older than an eruption age was inherited from an older intrusion or from buried volcanic rocks can be difficult. That said, we note a tantalizing correlation between the ages of antecrystic zircon grains at both Bruneau–Jarbidge and Twin Falls and the ages of prior eruptions. In Fig. 4.6, we plot four additional $^{40}Ar/^{39}Ar$ ages for eruptions not sampled in this study, the Dry Gulch, McMullan Creek, and Indian Springs Members of the Cassia Formation from Twin Falls, dated at 8.63 ± 0.50 Ma, 9.0 ± 0.3 Ma, and 9.0 ± 0.2 Ma, respectively (Knott et al., 2016), and CPT III from Bruneau–Jarbidge, dated via $^{40}Ar/^{39}Ar$ at 12.64 ± 0.08 by Bonnichsen et al., (2008). We see in Fig. 4.6 that the Shoshone Rhyolite has a notable antecrystic age peak that

correlates with the 9.0 Ma age of the Indian Springs and McMullen Creek eruptions, and that the Castleford Crossing and Kimberly Members have zircon that also appear to match both the Dry Gulch and Indian Springs/McMullen Creek eruption ages. These peaks are represented by at least three core ages for each unit for each peak. Similarly, at Bruneau–Jarbidge we can see that CPT XIII has a secondary age peak (which is only one grain) which matches the ages of CPT XII and CPT V perfectly, and that CPT VII, in turn, has a secondary peak (corresponding to three grains) that matches the eruption age of CPT III.

Together, these observations build a compelling case that most zircon growth in the subvolcanic magma chambers occurs near the times of the eruptions, suggesting that magma production in the Snake River Plain is a punctuated rather than continuous process, and that eruptions are associated with these periods of increased magma production. To come to this conclusion, we assume that times of greater magma production are almost always recorded by populations of zircon ages, because the heating pulses associated with new intrusions and the growth of melt bodies should be associated with growth of zircon (either new crystals or adding to existing rims) during the subsequent cooling (Bindeman & Melnik 2016). Not all zircon ages match known eruption ages, however, and our very precise CA-ID-TIMS ages that we obtain for the Twin Falls units show that there are many zircon ages which are clearly older than their host eruptions but younger than the previous identified eruption (Figs. 4.5, 4.8), particularly in the case of the Shoshone Rhyolite. It is of course possible that these ages match those of small lava flows that are entirely concealed by younger deposits, but we argue that it is at least as likely that at least some of them represent periods of intrusion

which were not linked to any eruption. However, the fact that the overwhelming majority of zircon core and rim ages overlap with the ages of already identified eruptions suggests that most of these pulses of melt production were associated with eruptions. This assumes, of course, that intrusions of rhyolitic magma that never erupt are at least partially remolten and their zircon sampled by later intrusions that do produce eruptions. If there is a large body of rhyolitic intrusions at a totally different depth in the crust than the magma bodies that fuel eruptions, we would not expect to infer their compositions in this study. In summary, we expect that antecrystic zircon grains are almost certainly sometimes the result of the digestion of older intrusions which are frequently correlated with the ages of older eruptions, and perhaps sometimes inherited from the buried products of those older eruptions themselves.

The significant age diversity that we observe in several of these erupted units, including in the precise CA-ID-TIMS ages (Figs. 4.5, 4.7, 4.8), stands in contrast to the homogenous ages found in several previous high-precision CA-ID-TIMS studies of zircon from Yellowstone hotspot super-eruptions (Rivera et al., 2016; Szymanowski et al., 2016; Wotzlaw et al., 2014, 2015), where nearly all measured zircon ages from a given eruption are within 0.25 Myr of each other. We tentatively speculate that this is a result of two key differences between rhyolitic volcanism in the central Snake River Plain, and at Heise and Yellowstone. First, repose intervals between large ignimbrite eruptions in the central Snake River Plain (Bonnichsen et al., 2008; Knott et al., 2016; this study), at ~ 0.25 Myr, were much shorter than those at Heise and Yellowstone, where they have been 0.5–2.0 Myr (Christiansen 2001; Morgan & McIntosh 2005). Second, at any point in the 11−6 Ma time period, multiple caldera centers were simultaneously

active (Bonnichsen et al., 2008), while in contrast activity at the Heise and Yellowstone systems since has been much more geographically focused. This suggests that the production of rhyolitic magma bodies in the central Snake River Plain was not only more frequent (e.g. Ellis et al., 2012, 2013) than in more recent times but was also more structurally complex and less centralized, possibly allowing populations of older zircon to survive more readily on the fringes of any new melt body.

4.6.2. Isotopic heterogeneity in zircon and batch assembly of pre-eruptive magma chambers

This greater geometric and temporal complexity in the central Snake River Plain is recorded not only by zircon ages but also by their O and Hf isotopic compositions. The range in zircon $\delta^{18}O$ values that we find in these rhyolitic units is among the greatest ever observed in any igneous rocks (Fig. 4.4) with ranges of up to 6.2‰ within a single unit (CPT VII), only rivaled by the Kilgore tuff of the Heise center (Wotzlaw et al., 2014). We see slightly less dramatic but still notable variability in the Hf isotopic composition of the grains, with most zircon grains having ε_{Hf} values scattered between 0 and − 10. Previous studies have found similar O and Hf isotope diversity at every major center of the Snake River Plain, and interpreted it as having formed through the assembly of "batches" of isotopically distinct melt bodies which existed for varying amounts of time prior to eruption (Bindeman & Simakin 2014; Colón et al., 2015a, b; Drew et al., 2013; Ellis & Wolff 2012; Szymanowski et al., 2016; Watts et al., 2011; Wotzlaw et al., 2014, 2015). We add the caveat that while the zircon crystals eventually reside within the same magma, some may be derived from solidified wall rocks rather than adjacent

melt bodies to the parent magma, particularly in the case of zircon that are much older than the associated eruption ages. We see this in the plot of $\delta^{18}O$ vs. CA-ID-TIMS ages for the Shoshone Rhyolite zircon grains (Fig. 4.8), where the zircon closest to our inferred eruption age has a $\delta^{18}O$ value that overlaps with that estimated for the melt from major phenocrysts while older phenocrysts have very different $\delta^{18}O$ values. However, there are several cases where zircon have different isotopic compositions but have identical CA-ID-TIMS (or laser ablation) ages (Fig. 4.8), suggesting that at least some zircon diversity is derived from the mixing of coeval melt bodies, rather than the partial melting of separate previously solid intrusions.

We find additional evidence for the batch assembly of diverse melts in the core-rim relationships of zircon. In CPT V, we observe a large population of zircon rims and cores of indistinguishable age (Fig. 4.5), but the rims are significantly less diverse with respect to both Hf and O isotopes (Fig. 4.4), and we observe that the rim $\delta^{18}O$ values converge on the $\delta^{18}O$ value inferred for the melt from major phenocrysts, which are assumed to equilibrate with their host melts faster than zircon (Bindeman and Simakin 2014; Wotzlaw et al., 2014). Using the batch assembly model, we interpret these cores as recording the compositions of the early magma batches and the rims as recording the final eruptive melt composition, also reflected by major phenocryst oxygen isotopic composition. We also note that the time required to grow these zircon rims is likely much smaller than the age resolution of any of our dating methods, and was suggested to be on the order of 10^2–10^3 years by the modeling work of Bindeman and Melnik (2016). This convergence towards a common rim isotopic composition, seen most dramatically in CPT V and to a lesser extent in CPT XIII and in the Castleford Crossing Member, is in strong

contrast with the equally diverse rims and cores observed in CPT VII and in the Shoshone Rhyolite, even amongst rims with indistinguishable ages. This suggests that either the zircon in these units mixed so rapidly in the final magma body that they did not have time to grow rims, or simply that there was not a post-mixing cooling (or intrusion of Zr-rich magma) that oversaturated the magma in Zr and produced new zircon rims prior to eruption. In any case, we can constrain the speed of the batch assembly and eruption to be less than the typical 0.25 Myr uncertainty on our laser ablation ages, and we suspect that it may in fact occur much more quickly than that, in line with previous results for other centers along the hotspot track that have constrained it to occur in no more than 50 kyr (Wotzlaw et al., 2014, 2015). Such assembly of disparate melt bodies has been suggested by previous workers (Colón et al., 2015b; Wotzlaw et al., 2014, 2015) to possibly even be the trigger for the eventual volcanic eruption, as linking adjacent magma bodies may significantly alter the stress field of the surrounding crust, or allow volatiles to come out of solution and overpressurize the system. In the context of our study of the central Snake River Plain, this suggests that the pulses of rhyolitic magma production identified by zircon age peaks (Fig. 4.6) initially produce many isotopically distinct separate magma bodies, which then merge and erupt. In contrast, we find no evidence that magma bodies grow as a single isotopically homogeneous reservoir, and propose that the only way to produce large "supervolcanic" magma bodies in this kind of intraplate environment is through the progressive merging and mixing of smaller adjacent magma bodies.

4.6.3. Crustal sources of rhyolitic magmas

We compared the O and Hf isotope compositions that we observed in zircon from the Bruneau–Jarbidge and Twin Falls centers with data from four previous studies of other parts of the post-15 Ma hotspot track (Fig. 4.9, Colón et al., 2015b; Drew et al., 2013; Stelten et al., 2013; Wotzlaw et al., 2015). We find that the central Snake River Plain zircon analyses all fall along the compositional trend between the mantle end-member defined by the compositions of Snake River Plain and Yellowstone basalts, and the high-ε_{Hf} and low-$\delta^{18}O$ end-member discussed earlier, with CPT VII extending the lower bound in measurements of $\delta^{18}O$ from the hotspot track (Fig. 4.9, lowest gray points, appendix). While Colón et al. (2015b) found low-ε_{Hf} and normal-$\delta^{18}O$ zircon in precursor units to the Bruneau–Jarbidge center in the J-P Desert (orange points), we do not find any very low-ε_{Hf} zircon or, more importantly, any normal-$\delta^{18}O$ zircon in any of our Bruneau–Jarbidge or Twin Falls samples, confirming the exclusively low-$\delta^{18}O$ nature of the central Snake River Plain (Fig. 4.9).

This observation would seem to support the model of Boroughs et al. (2012), which asserts that the emplacement of the Idaho Batholith and later the Challis intrusions

---

Fig. 4.9 (next page). Oxygen and hafnium isotopes in zircon from rhyolites throughout the Snake River Plain. Data sources for areas other than those covered in this study are Drew et al. (2013, Picabo), Colón et al. (2015b, Jarbidge and J-P Desert), Stelten et al. (2013), and Wotzlaw et al. (2015, both Yellowstone). The extent of the Mesozoic/Cenozoic Hf isotope range is inferred from Gaschnig et al. (2010), and the size of the Snake River Plain basalt field is from Stelten et al. (2017). We plot the J-P Desert zircon separately from the Bruneau–Jarbidge data from this study for the sake of clarity, though we interpret them as are part of the same system. Note the lack of zircon with low ε_{Hf} and $\delta_{18}O$ values, indicating a lack of mixing between those magma types, and suggesting that they did not form simultaneously, and that Precambrian rocks were not hydrothermally altered to a significant degree. We interpret the low-$\delta^{18}O$ end-member to be the result of syn-magmatic hydrothermal alteration of the young, unradiogenic, porous and hydrologically permeable gabbros and upper crust by a variety of mechanisms, in line with previous studies (e.g., Bindeman and Simakin 2014; Boroughs et al., 2012; Colón et al., 2015b; Drew et al., 2013; Wotzlaw et al., 2015). All error bars are 2σ.

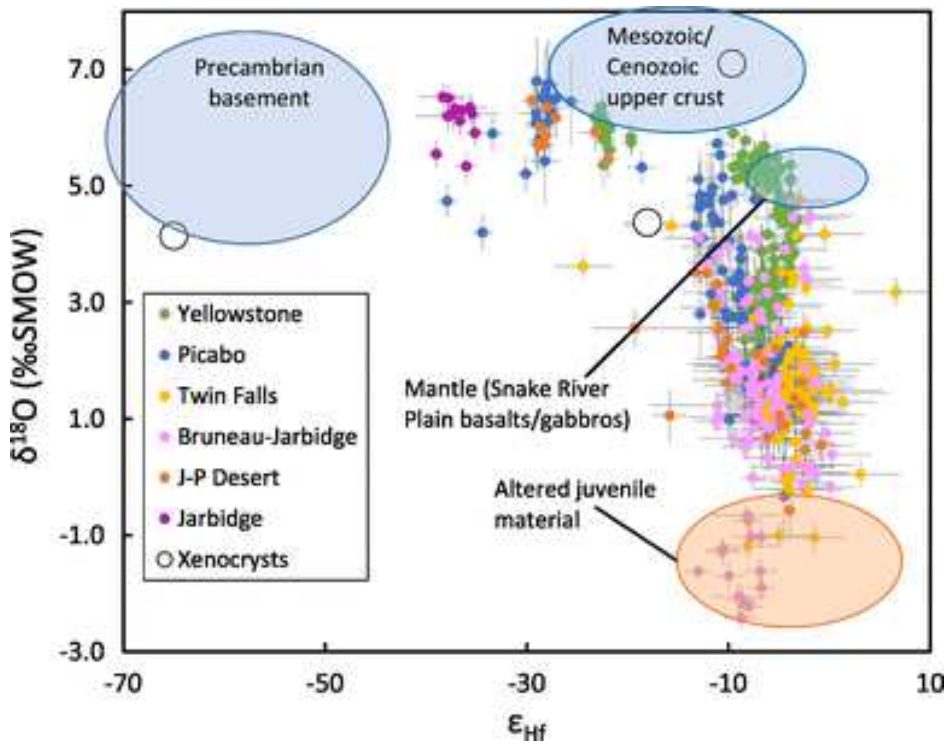

and volcanic rocks drove a regional-scale hydrothermal system which imparted low $\delta^{18}O$ values throughout the crust in the region of the central Snake River Plain, making any rhyolites generated by crustal melting in the central Snake River Plain also low-$\delta^{18}O$ in character. The involvement of Idaho Batholith-age protolith in the production of Bruneau–Jarbidge rhyolites is further suggested by the presence of an 86 Ma xenocryst in our CPT VII sample. This xenocryst has a normal $\delta^{18}O$ value, but we would not expect zircon to be affected by later hydrothermal alteration events. Its ε_{Hf} value, -9.7, is a match with the more radiogenic end of the Hf isotope composition of the low-$\delta^{18}O$ end-member, suggesting that it could be a source rock for many of the low-$\delta^{18}O$ rhyolites.

However, the fact that voluminous low-$\delta^{18}O$ rhyolites are found at every center along the hotspot track from eastern Oregon to Yellowstone strongly suggests that there is a process not dependent on any local geology that is responsible for a large portion of

the low-$\delta^{18}O$ signature. High-ε_{Hf} and low-$\delta^{18}O$ zircon, particularly common at Bruneau–Jarbidge and Twin Falls (Fig. 4.9), are a better match in terms of Hf isotopes with Snake River Plain basalts, which have a minimum ε_{Hf} value of -8 (itself suggesting crustal contamination), than they are with the Idaho Batholith or the Challis, which have ε_{Hf} values which are generally less than − 10 (Colón et al., 2015b; Gaschnig et al., 2010). This suggests that basaltic or rhyolitic intrusions or buried volcanic rocks of central Snake River Plain age were also being hydrothermally altered and melted along with older low-$\delta^{18}O$ material. This would tend to support the explanations for low-$\delta^{18}O$ rhyolites that depend on altered and buried intracaldera material (e.g. Bindeman and Valley; Drew et al., 2013; Watts et al., 2011) or on syn-volcanic alteration along local fault lines (Blum et al., 2016; Colón et al., 2015a, b; Drew et al., 2013).

Determining the relative amounts of hydrothermally altered and melted basalt/gabbro and Idaho Batholith/Challis-like upper crust is very difficult, as they are so isotopically similar with respect to their ε_{Hf} values both before and after alteration, and because variations in xenocryst compositions (Fig. 4.9) show that any simple mixing calculation using fixed end-members will likely be faulty. However, petrologic mass balances put upper limits on the volume of rhyolite that could have been derived from young basalts via fractionation and partial melting. If we assume that something on the order of 15 km of crustal thickening occurred in the Snake River Plain from basaltic intrusions (e.g. McCurry and Rodgers 2008; Peng and Humphreys 1998), and that it requires 90% fractionation (or 10% partial melting) of this material to produce rhyolite, then we arrive at a cumulative rhyolite thickness of 1.5 km in the Snake River Plain. The fact that the combined thickness of rhyolitic units in the Kimberly borehole meets or

exceeds this value (Fig. 4.2), despite being an incomplete record of volcanism in the area, suggests that the cumulative thickness of erupted rhyolites is likely greater than 1.5 km, more than can be produced from basalts. This means that a significant portion of the low-$\delta^{18}O$ rhyolites in the central Snake River Plain can potentially be derived from partial melts of Mesozoic–Cenozoic upper crust that predates the Yellowstone hotspot. We again note, however, that caldera burial is not the only potential mechanism of hydrothermal alteration coeval with Yellowstone hotspot magmatism, and that the faulting and thermal conditions necessary to hydrothermally alter the crust existed in the central Snake River Plain since the time of the Columbia River Basalts (Blum et al., 2016; Colón et al., 2015b).

4.6.4. Time dependence of crustal reservoir contributions to erupted magmas

We observe that there is a distinct lack of zircon with simultaneously low-$\delta^{18}O$ and very low-ε_{Hf} compositions (Fig. 4.9). Wotzlaw et al. (2015) observed this pattern at Yellowstone, and interpreted it as the result of two-stage melting where the production of low-ε_{Hf} melts in the lower crust is followed by melting of shallow low-$\delta^{18}O$ crust in a separate system. We can now extend this observation to the entire hotspot track, which implies that it reflects a fundamental property of the melt generation processes along the hotspot track, and possibly in rhyolites that form in old continental crust in general. This lack of isotopically ancient low-$\delta^{18}O$ rocks is also observed at the Skaergaard intrusion in Greenland, where the fractured and permeable Tertiary gabbros are altered to low-$\delta^{18}O$ values but there is comparatively little oxygen isotopic alteration in the impermeable host Precambrian gneisses (Taylor & Forester 1979). Throughout the hotspot track, we argue

that the lack of simultaneously low-$\delta^{18}O$ and low-ε_{Hf} rhyolites is likely a result of a combination of a two-step process, as proposed by Wotzlaw et al. (2015), and the impermeability-driven lack of alteration of Archean metamorphic rocks. Such rocks rarely outcrop on the surface in the region of the hotspot track (Drew et al., 2013) and, therefore, may not only be hard to alter but are also confined to depths below those typical of hydrothermal systems. Additionally, the low-$\delta^{18}O$ and low-ε_{Hf} magma end-members never appreciably mixed, as is recorded by the lack of hybrid-composition zircon, lending weight to the fact that the production of these magma types took place at different times.

In Fig. 4.10, we plot the ε_{Hf} and $\delta^{18}O$ values of all the zircon from the studies compiled in Fig. 4.9 against the difference between their age and the time of the earliest eruption at their respective source centers. When this difference is negative, it means that the zircon is older than the oldest identified eruption in the system, and reflects the growth of pre-volcanic magma chambers. We note that very low-ε_{Hf} grains only occur in significant numbers near and before the age of the oldest eruption, and quite rare after the first eruption at each volcanic center, especially if we exclude the off-axis Jarbidge rhyolite (distinct from Bruneau–Jarbidge, see Fig. 4.1), whose relationship to the main Snake River Plain sequence is debated (Brueseke et al., 2014; Colón et al., 2015b; Nash et al., 2006). We are not yet able to test for this trend in the Twin Falls zircon because the oldest zircon from that center has yet to be measured for Hf isotopes. While the precise composition of the Precambrian crustal end-member is unconstrained, we can use changes in the hafnium isotopic composition of each center's zircon population with time as a crude proxy for the amount of old crust which was melting to produce the erupted

rhyolites at that time. This leads us to conclude that the melting of Precambrian crust is important for the initial stages of volcanism at each area (e.g. the Arbon Valley Tuff at Picabo; Drew et al., 2013, 2016) and diminishes over time as the zircon in later rhyolites become less like the Precambrian crustal end-member. At the one center not included in Fig. 4.10, Heise, a similar gradual increase in ε_{Nd} values with time has been documented by Nash et al. (2006). Late-stage rhyolites must still have a very large component of crustal melting, as they do not resemble the mantle end-member in their $\delta^{18}O$ values. Therefore, the crust which melts to produce the late-stage rhyolites of the Snake River Plain/Yellowstone volcanic systems is likely some combination of hydrothermally altered shallow crust and volcanic rocks and juvenile basaltic and rhyolitic intrusions, whereas the Precambrian crustal end-member becomes increasingly diluted as the system evolves (Fig. 4.10).

Fig. 4.10 (next page). a Hafnium isotopes vs. time after the oldest eruption at each major volcanic center along the Yellowstone-Snake River Plain hotspot track, using the same data sources as in Fig. 4.9. The Yellowstone, Bruneau–Jarbidge (which includes the J-P Desert), and Picabo centers all have their most unradiogenic (low-ε_{Hf}) zircon at the very beginning the cycle of activity, the only time in each magmatic cycle when the Precambrian crustal end-member is clearly discernable. We see few low-ε_{Hf} zircon crystals at Twin Falls; we speculate that this is because we did not study the earliest units from that center. We only include zircon analyses with age uncertainties less than 2 Myr (2σ). **b** Plot showing the probability that a zircon analysis at each studied eruptive center would give a low- ε_{Hf} (< -15) value as a function of its age, as in part (**a**). Note that in all cases this probability generally decreases with time. The Yellowstone curve is fragmented because the precise young age data (Wotzlaw et al., 2015) has gaps between eruptions. **c** Plot showing the oxygen isotopic compositions of zircon vs. time for the same set of zircon as in (**a**). **d** Plot showing the gradual increase in the likelihood of a zircon analysis being low-$\delta^{18}O$ ($< +4.0$‰) with time at each center. Here and in part (**c**) the combined curve is derived from averaging the other curves with equal weights. We note similar trends are documented in the one center not included here, the Heise center (Fig. 4.1; Drew et al., 2013; Nash et al., 2006; Szymanowski et al., 2016; Watts et al., 2011). All error bars in both panels are 2σ

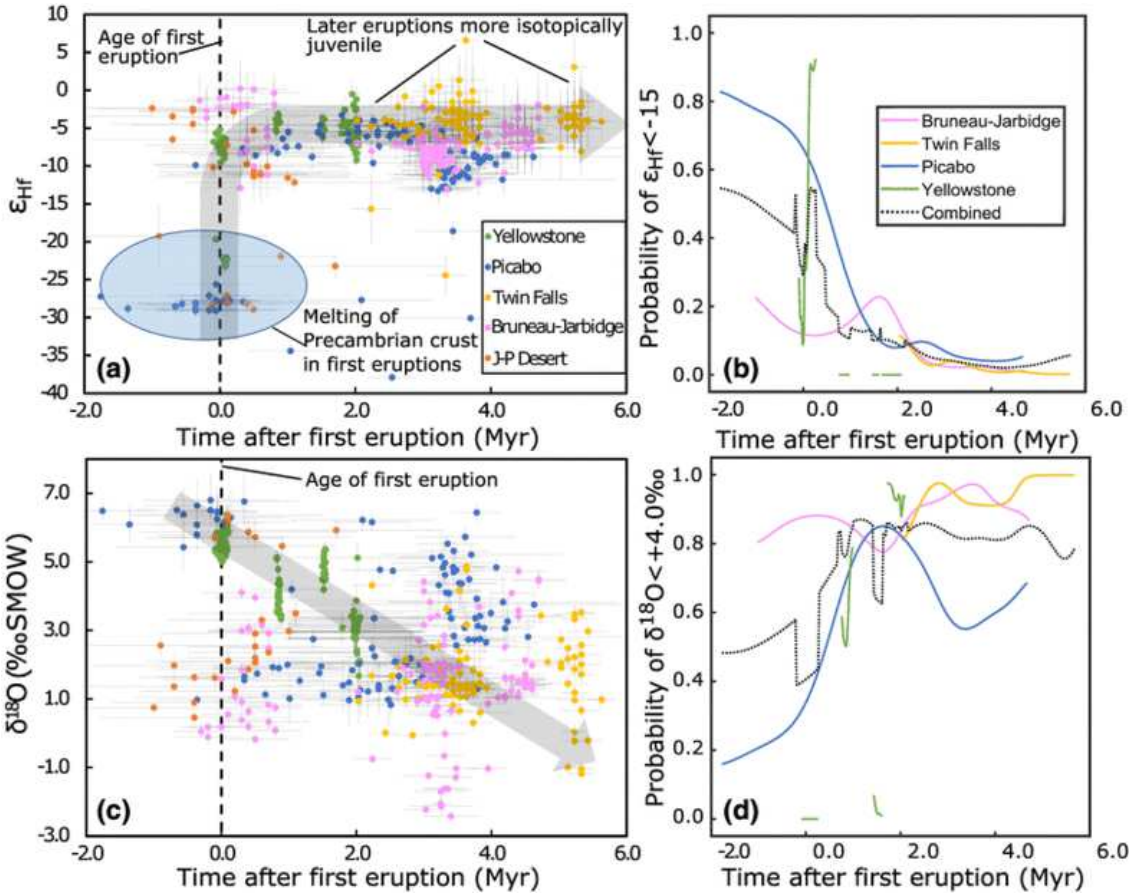

We also note that there is a common trend of evolution towards lower $\delta^{18}O$ values in the zircon from each center over time, most dramatically in those from Yellowstone (Stelten et al., 2013; Wotzlaw et al., 2015). This trend is visible to a lesser degree in the Bruneau–Jarbidge zircon if we include the J-P Desert units in the Bruneau–Jarbidge center, as is suggested by Colón et al. (2015b). This suggests that at least some of the processes that produced low-$\delta^{18}O$ crust that melted to become new rhyolites continued while the system was active, providing additional evidence that some combination of caldera burial-driven recycling and alteration along normal faults continued coeval with

volcanism in the central Snake River Plain and that low-$\delta^{18}O$ values there are not solely the result of pre-existing alteration (Boroughs et al., 2012).

In Fig. 4.11, we illustrate how early intrusions of basalt from the mantle at each center could melt significant quantities of older crust. By contrast, later intrusions encounter an environment filled with these early basaltic intrusions or with rhyolitic material that has been buried by successive volcanic collapses. Once each caldera center becomes more mature, as seen in the lower part of the figure, the density of the early basaltic intrusions allows new basalt intrusions to buoyantly rise into the growing sill complex, or to even reach its top where it meets the rhyolitic magma chamber. If, as we suspect, ancient Precambrian rocks are primarily concentrated in the mid to lower crust (as suggested by Colón et al., 2015b; Drew et al., 2013, 2016; Foster et al., 2006), this means that later basalt intrusions will likely be isolated from it and will not melt it efficiently (Fig. 4.11). Furthermore, any melts of ancient Precambrian crust that do form in the late stages of the system may be too hot to be crystallizing zircon, and may also not be able to rise through the mid-crustal sill system without hybridizing with more radiogenic melts to the point where their Archean-like Hf isotope composition is lost.

Fig. 4.11 (next page). Conceptual model of Snake River Plain caldera volcanism to explain the isotopic evolution seen in Figs. 4.9 and 4.10. Early Snake River Plain-Yellowstone rhyolites at each center are produced with large amounts of assimilation of old pre-existing crust, giving the products of the first eruptions normal $\delta^{18}O$ values and low ε_{Hf} values. By the late stage, new partial melting is mostly confined to the upper crust, and old solidified sills isolate the Precambrian crust from the melt bodies, which have been displaced to slightly shallower levels. Late stage ignimbrites and rhyolite lavas are isotopically juvenile and low-$\delta^{18}O$

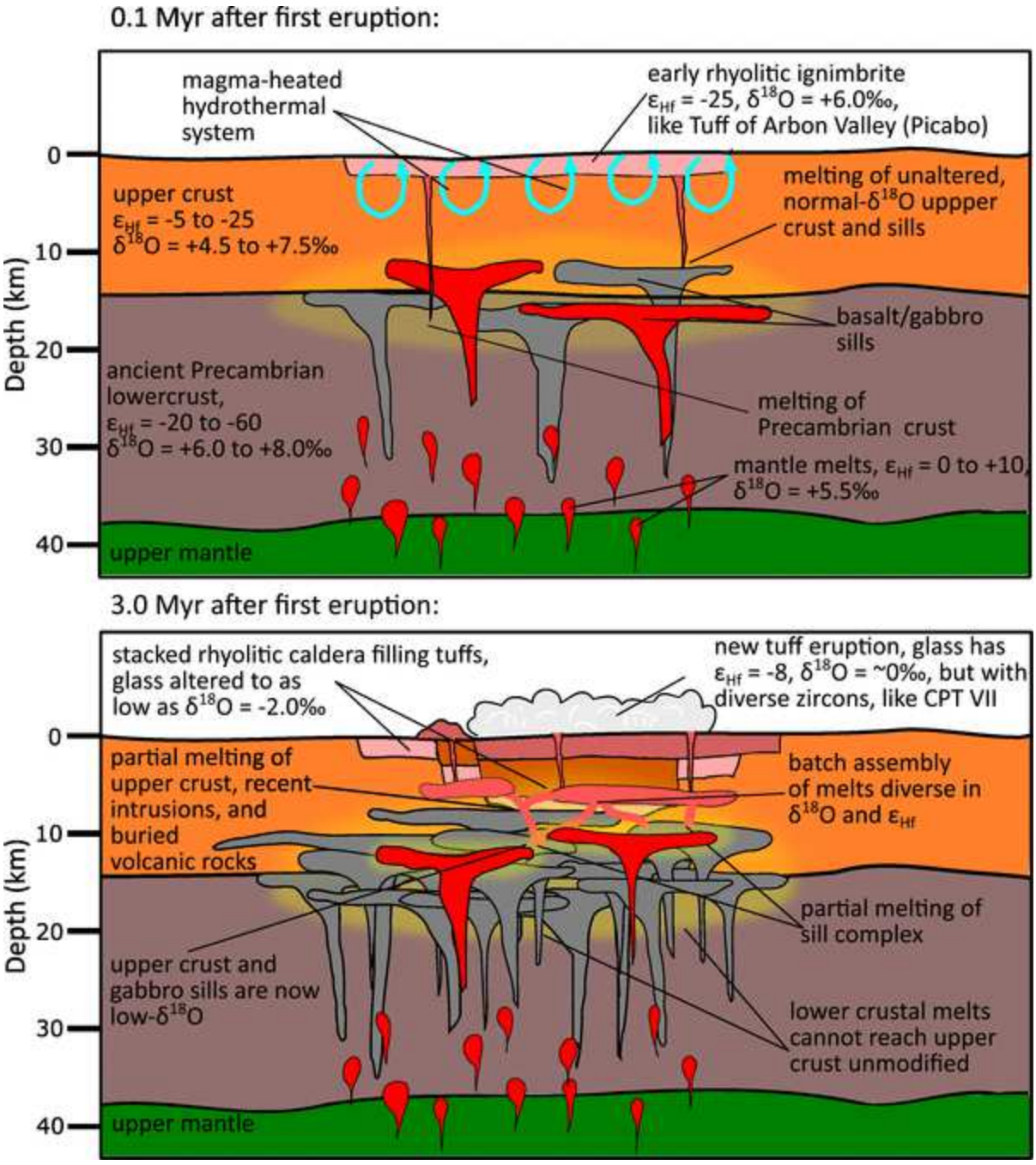

4.7. Conclusions

(1) We find considerable ranges in the ages and isotopic compositions of zircon from the Bruneau–Jarbidge and Twin Falls volcanic centers of the central Snake River

Plain, implying that their source magmas were a diverse combination of partial melts of coeval basalt intrusions and their differentiates, of buried volcanic rocks from the same system, and of pre-existing crust. (2) This pre-existing crust can be roughly separated into two isotopically distinct end-members which are the ancient Precambrian basement rock, and the intrusions and volcanic rocks of the Idaho Batholith and Challis formations. (3) Combinations of the latter and young basaltic intrusions were progressively altered to lower $\delta^{18}O$ values by hydrothermal systems driven by heat from hotspot magmatism. Mixing between these crustal end-members was characterized by an early stage of magmatism where isotopically mantle-like melts hybridized with both ancient Precambrian crust and isotopically younger but mostly normal-$\delta^{18}O$ upper crust and a later stage where melting is dominated by shallow hydrothermally altered low-$\delta^{18}O$ material and the Precambrian end-member becomes nearly undetectable. (4) We also find no evidence that the Precambrian crust itself became significantly hydrothermally altered, presumably because it occurs at greater depths and/or has a much lower permeability that prevents it from being accessed by hydrothermal fluids. (5) Populations of zircon ages from these units are diverse, and suggest that magma production in the central Snake River Plain was an intermittent process characterized by pulses of rhyolite production which appears to have usually led to eruption, preserving zircon O and Hf isotopic diversity. These pulses of magma production were characterized first by the formation of many closely spaced but isotopically distinct batches of melt which later merged into a single magma body prior to eruption. In some cases, particularly CPT V at Bruneau–Jarbidge, this final magma body's composition is recorded by the rims of the zircon, which like the rim ages, are much more homogeneous than the associated zircon cores.

(6) We suggest that these two processes of (i) rapid batch assembly of separate bodies of melt prior to supervolcanic eruptions and increasingly shallow melting and (ii), vigorous syn-magmatic hydrothermal alteration leading to the coeval production of low-$\delta^{18}O$ rhyolites characterizes similar low-$\delta^{18}O$ anorogenic, intraplate, rift, and hot-spot rhyolitic provinces worldwide, because we can now confirm that these processes occur throughout the Yellowstone hotspot track, suggesting that they not solely function of the variable local geology.

4.8. Bridge

After this detailed study of the Yellowstone hot spot track's isotope geochemistry, I was drawn to further investigate the magmatic structures which drive the isotopic evolution of Yellowstone rhyolites in the crust, hinted at in Fig. 4.11 if this last chapter. In Chapter V, I take an entirely different approach to investigating the origins of Yellowstone's magmas. I used Taras Gerya's I2VIS thermomechanical modeling code, and added new functionality to allow the intrusion of multilevel magmatic systems in the crust above the mantle plume. With the insight that it is primarily rheological discontinuities that trap magma in the crust, I was able to successfully reproduce many of the structures that had previously been observed at Yellowstone via geophysical imaging. This suggests that this approach is likely to be a fruitful one for further investigation of Yellowstone and other large igneous systems, and I further develop this method in Chapter VI.

CHAPTER V

THERMOMECHANICAL MODELING OF THE FORMATION OF A MULTILEVEL, CRUSTAL-SCALE MAGMATIC SYSTEM BY THE YELLOWSTONE PLUME

This chapter is taken from a paper published in *Geophysical Research Letters* in 2018. This paper was coauthored with Ilya Bindeman (University of Oregon), who served as an advisor and assisted with manuscript edits, and Taras Gerya (University of Oregon), who also served in an advisory role and provided instruction on use of the I2VIS modeling code. I was the lead author of this study, which included new code development, and preparing figures and text. The published manuscript can be found at doi:10.1029/2018GL077090.

5.1. Introduction

Recent geophysical imaging of the Yellowstone volcano (Farrell et al., 2014; Huang et al., 2015) shows a magma body at 4□ to 14□km depth and a separate, larger melt body at 20□ to 45□km depth, with estimated melt fractions of 9% and 2%, respectively (estimated from *P* wave velocities, Fig. 5.1). While geochemical and petrological studies provide "snapshots" of the state of the shallow system at the time of past eruptions (e.g., Almeev et al., 2012; Myers et al., 2016), they cannot tell us how the structures visible in Fig. 5.1 came to be. We therefore use thermomechanical forward modeling to investigate the large□scale and long□term emplacement and evolution of the Yellowstone magmatic system (by contrast, inverse models produce nonunique solutions using the method

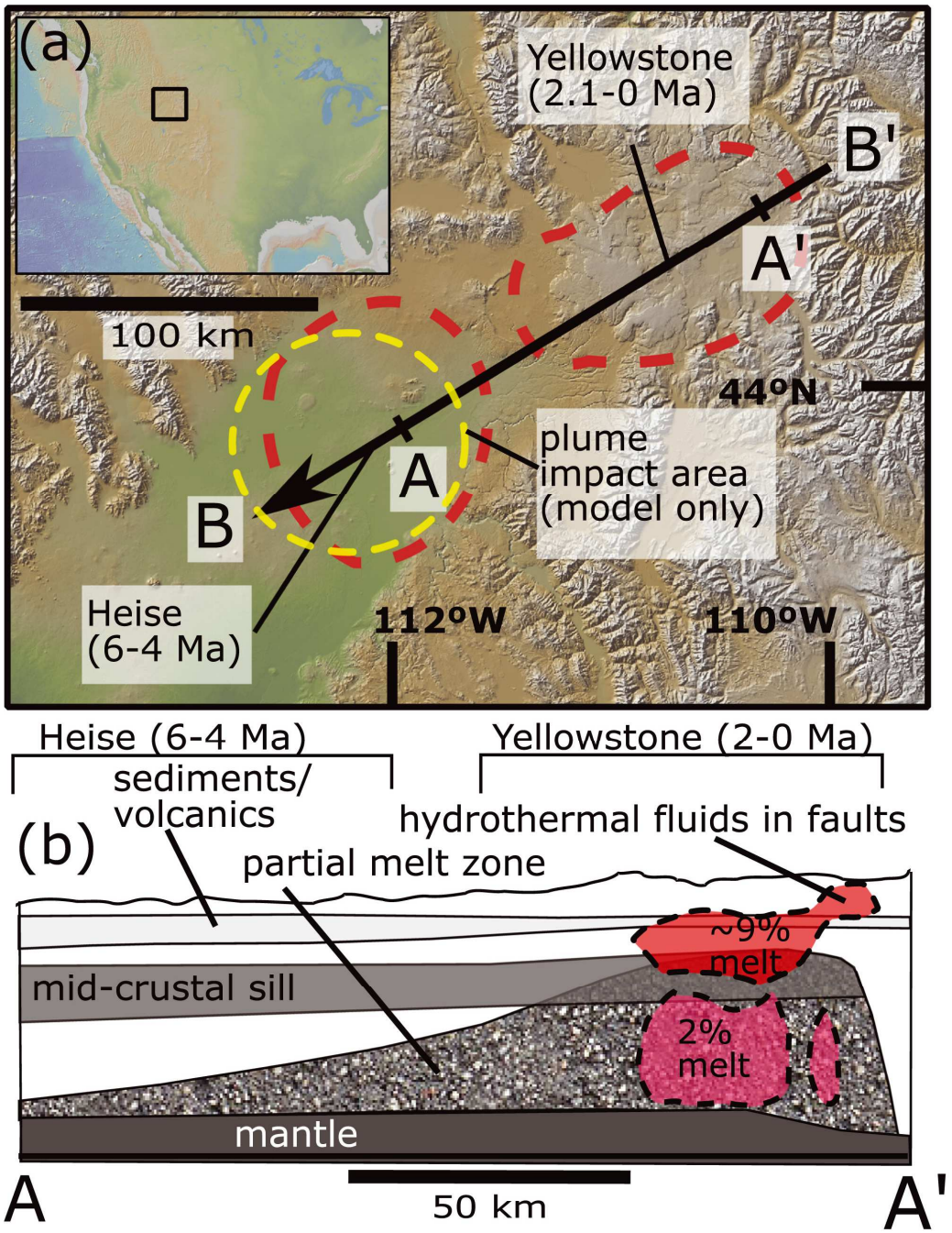

Fig. 5.1. (a) Map showing Yellowstone and the youngest part of the Snake River Plain hot spot track (Ryan et al., 2009; GeoMapApp). Arrow represents the orientation of the cross sections in Figs. 5.2-5.4 and the direction of plate motion over the mantle plume. Inset shows the location of this system in western North America. (b) Cross section of the Snake River Plain□Yellowstone system as imaged by the studies of Peng and Humphreys (1998, black and white materials) and Huang et al. (2015, color). Note zones of partial melt and the midcrustal sill complex that dominate the depth range from 10 to 20 km.

outlined below). Recreating the emplacement of the intrusions that fuel continental hot spot volcanism not only is important for understanding the dynamics of Yellowstone but also informs our knowledge of the impact that mantle plumes can have on the evolution and structure of continental crust.

5.2. Model Setup

We performed several dozen 2□D numerical experiments exploring a broad parameter space using a 1,000 × 300□km finite difference grid with a resolution of 2 km, with 16 or more Lagrangian markers per cell, a time step of 5 kyr, and a total duration of 7–8 Myr. We are interested in the behavior of the crustal magmatic system which develops over a relatively stable mantle plume tail, rather than over the plume head which is commonly assumed to be responsible for the eruption of the Columbia River large igneous province (Camp & Ross, 2004; Pierce & Morgan, 2009). However, it is very difficult to begin a model with an initial condition of a dynamically stable plume tail, so we allow a plume tail to develop naturally in the wake of a rather small initial plume head which quickly disperses (Fig. 5.2). For simplicity, we assume laterally homogeneous continuous continental crust (Fig. 5.2), with no major tectonic boundaries like the edge of the accreted terranes that host the Columbia River basalts (Nash et al., 2006; Pierce & Morgan, 2009); hence, the initial stages of our models cannot be considered a direct analog of the Columbia River basalts. In our models, the plume begins as a hemisphere of hot material 160 km in diameter at the bottom of the model, replenished from below by a fixed advective boundary condition with the same temperature, a radius of 40 km, and an upward velocity of 4.7 cm/year, consistent with

recent buoyancy flux estimates for the modern Yellowstone plume (Stachnik et al., 2008). The overlying lithosphere moves right to left at 25 km/Myr. For further details, see the supporting information.

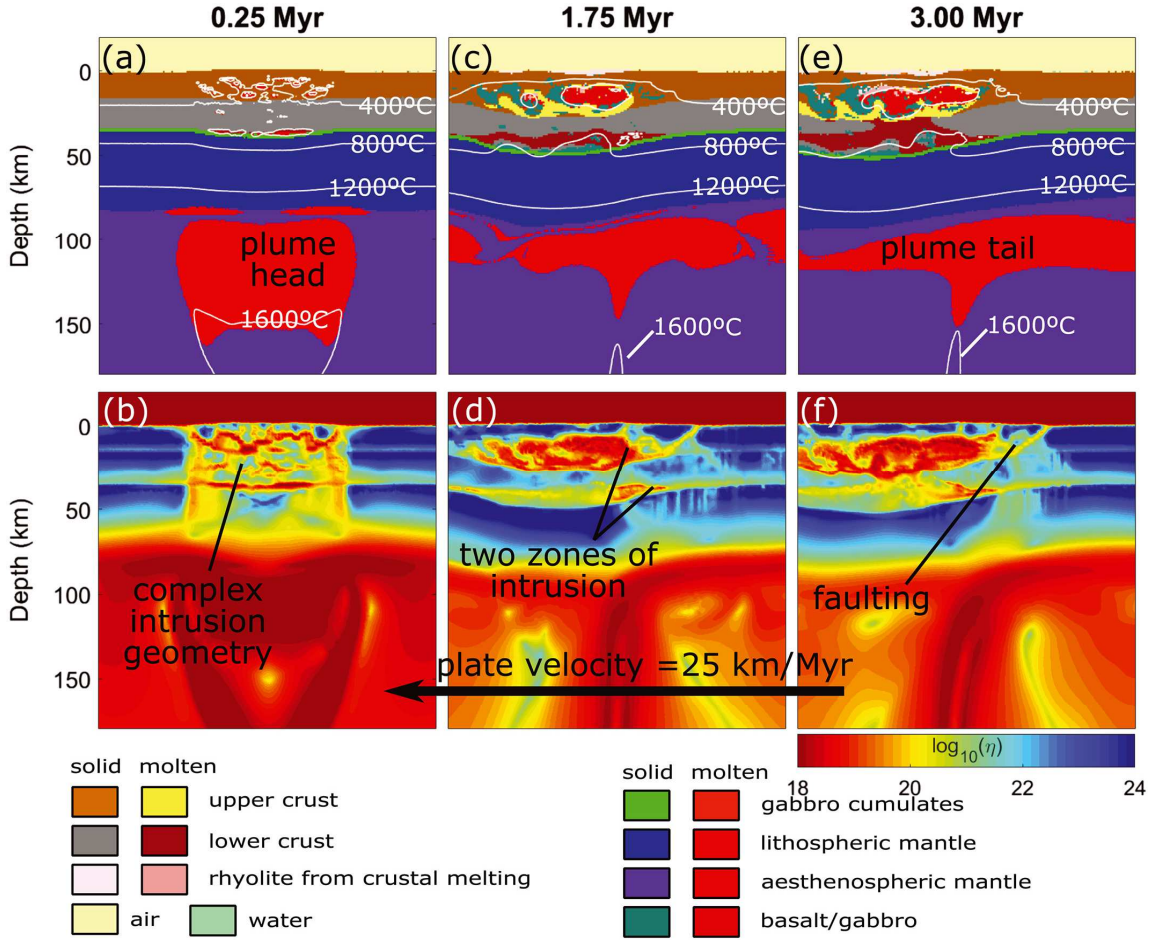

Fig. 5.2. Evolution of our reference model. Panels in the upper row, which show materials and temperatures, represent identical views to the panels below them, which plot effective viscosity. (a) About 0.25 Myr after the plume head is initiated from a depth of 280 km, it reaches the base of the lithosphere at a depth of 80 km and melts extensively. (b) These melts accumulate in a complex pattern of interconnected lenses visible as weak zones in the crust. (c) By the time the plume tail is established as a steady flow of material at 1.75 Myr, this complex intrusion geometry gives way to two zones of intrusion, one at the Moho and one in the middle to upper crust, which is much larger. (d) Together, these two depths of intrusion represent the points of greatest contrast between local weak zones in the crust and the surrounding more rigid rocks. (e and f) By 3.00 Myr, we see that this regime has stabilized and that intrusions into the upper crust begin to produce the extensive zones of partial melt which will eventually cool to produce the midcrustal basaltic sill complex seen in Fig. 5.2.

5.3. Melt Emplacement Method

Our numerical modeling approach (detailed treatment in the supporting information) is based on the I2VIS code of Gerya and Yuen (2003), which we have coupled with a new, computationally efficient way of predicting where melts will accumulate in the crust depending on local melt overpressure and the crustal rheology profile. For this regional□scale, long□term approach, we define the nondimensional melt emplacement efficiency parameter D:

$$D = \frac{\Delta P}{\eta} \cdot \Delta t \qquad 5.1$$

where ΔP is the buoyancy□driven overpressure, defined as the difference between ambient pressure and hydrostatic pressure in the dike, η is the effective viscosity of the host material surrounding the dike (which may be solid or partially molten), and Δt is the time step. Dikes are assumed to rise vertically, and 20% of a dike's melt is assumed to cool in an even distribution on its length, and remaining melt stalls at places where D has a local maximum. The fraction of all melt available in a rising dike that will stall at a given local maximum in D is determined by assuming that it is large contrasts in D that will cause melt to stall, such as would be found when a dike rising through dense or rheologically weak crust encounters less dense and/or more rigid crust. We thus assume that

$$locally\ intruding\ melt\ fraction = (1-f) * \frac{1}{L} \cdot \left(\left(\frac{D_{max}}{D_{min}} \right)^{n} - 1 \right) \qquad 5.2$$

where D_{max} is the D value at the point of intrusion, D_{min} is the value of the next relative minimum along the dike path, f is the evenly distributed melt percentage (20%), and n and L are empirically determined constants (0.5 and 15, respectively). If the sum of

the above values and *f* for a given dike is above unity, they are normalized; otherwise, the remaining melt is erupted at the surface if it is sufficiently buoyant.

5.4. Emplacement of the Two-Level Magmatic System

The evolution of the reference model can be divided into three main stages: (i) the emplacement of the plume head from 0.2 to 1.0 Myr after the start of the model (Fig. 5.2a), (ii) the transition period from 1.0 to 2.0 Myr where the plume tail arrives and stabilizes under the lithosphere and the structure of the midcrustal intrusions is established (Fig. 5.2b), and (iii) a steady state emplacement of a midcrustal sill complex with accompanying volcanism within the crust moving over the fixed plume tail after 2.0 Myr (Fig. 5.2c).

About 0.25 Myr after the model starts (Fig. 5.2a), the plume head impacts the base of the lithosphere, and basaltic melts intrude the crust, primarily along weakened shear zones formed by the buoyancy of the plume and the growing intrusions themselves. By the time the plume tail arrives 1.5 Myr after the start of the model (Fig. 5.2b), this complex melt geometry gives way to two distinct zones of intrusion, one just above the Moho and one at a depth of 7–15 km in the upper crust, corresponding to the rheological discontinuities at the Moho and at the brittle□ductile transition (Figs. 5.2c and 5.3). Notably, the rheological and density transition at the lower crust□upper crust boundary does not trap significant amounts of rising melt, as the associated *D* ratio (equation 5.2) is much smaller than in the two dominant discontinuities. This rapid maturation of the crustal magmatic system is analogous to the establishment of hot spot track volcanism in the central Snake River Plain at 14–15 Ma after the eruption of the Columbia River

basalts at 16.5–15.5 Ma (e.g., Camp & Ross, 2004; Coble & Mahood, 2012). This progression and overall geometry occurs regardless of the composition of the crust and of the basalt intrusion rate (Fig. 5.4 and supporting information), suggesting that they likely represent the actual situation at the Yellowstone hot spot track even if our assumptions of these parameters are flawed.

After 7 Myr (after which boundary effects weaken the plume), the lithosphere has traveled ~150 km since the stabilization of the plume tail, leaving a long wake of cooling intrusions to the southwest of the plume center and the major melt bodies (Fig. 5.1 and left of Figs. 5.2-5.4). The plume tail has been stable for at least 5 Myr at this point, which means that we can compare this stage of the model's development with the present situation at the Yellowstone and Heise volcanic centers (Figs. 5.1 and 5.3). The rheological discontinuity at the brittle□ductile transition remains critically important, while the one at the Moho is comparatively smoothed out (Fig. 5.3), meaning that most basalt from the mantle intrudes into a midcrustal sill complex at depths of 10–20 km, broadly matching the geophysical images of Peng and Humphreys (1998; Fig. 5.1b). At the far eastern side of the midcrustal sill, where it is still growing, there is a zone of molten crust and cooling basalts directly above the plume tail that is approximately 40□km wide and spans a depth range of 7–17 km, in close agreement with the previously imaged upper crustal melt body (Huang et al., 2015) which spans a depth range of 4–14 km. West of this hottest region, the midcrustal sill cools and solidifies, separating the shallow melt zone into two bodies above and below it. The uppermost magma body consists of rhyolitic intrusions formed by basaltic differentiation and crustal melting and is up to 5□km thick. These are the sources of a pile of erupted rhyolite on the surface

locally up to 3□ to 4□km thick. This is analogous to the caldera□filling ignimbrites of the Snake River Plain, where a minimum cumulative depth of rhyolite of 1.5 km has been established by drilling at one locality (Knott et al., 2016), and the presence of older eruptions not penetrated by the drill core suggests that the total depth may be much greater (Bonnichsen et al., 2008; Colón et al., 2018b). The lower melt body is produced by heating of the crust from above by the main sill complex and by many smaller intrusions of basalt, which accumulate in the lower crust and particularly at the Moho, and consists of mostly solidified basalt and crustal rocks that are just above their solidus temperature and are typically <4% molten, again in line with geophysical observations (Fig. 5.3c).

Plotting the viscosity of the system (Fig. 5.3b) reveals that the upper magma bodies are connected to the surface by faults, visible as lines of shear□weakened crust, and are most common on the far east side of the intrusive complex. They are caused by the deformation of the brittle upper crust around the tip of the growing midcrustal sill complex and likely provide a pathway for both magmatic and meteoric fluids. This matches with the observation of a seismically slow zone northeast of and above of the

---

Fig. 5.3 (next page). (a) View of the modeled Yellowstone system after 7 Myr of runtime for the same reference model depicted in Fig. 5.2. Note the midcrustal basaltic sill complex that corresponds well with the seismic observations in Fig. 5.1b, as well as the concentration of melt under the current center of activity at Yellowstone. (b) View of the effective viscosities of melts and rocks in the model, showing the heated and weakened magmatic system overlain by the cold and brittle upper crust, which forms the lid that traps rising basalts to produce the midcrustal sill. (c) View of the distribution of melt in the model. Large melt fractions over 20% are plotted as the same color for clarity. Note a broad swath of partial melt under the Snake River Plain "downstream" from the center of activity with a very similar geometry to that observed by Peng and Humphreys (Fig. 5.1b). Also, note the separation between the upper magma body with a very high melt fraction and the larger and more diffuse lower crustal melt body by the cooling sill at a depth of ~15 km.

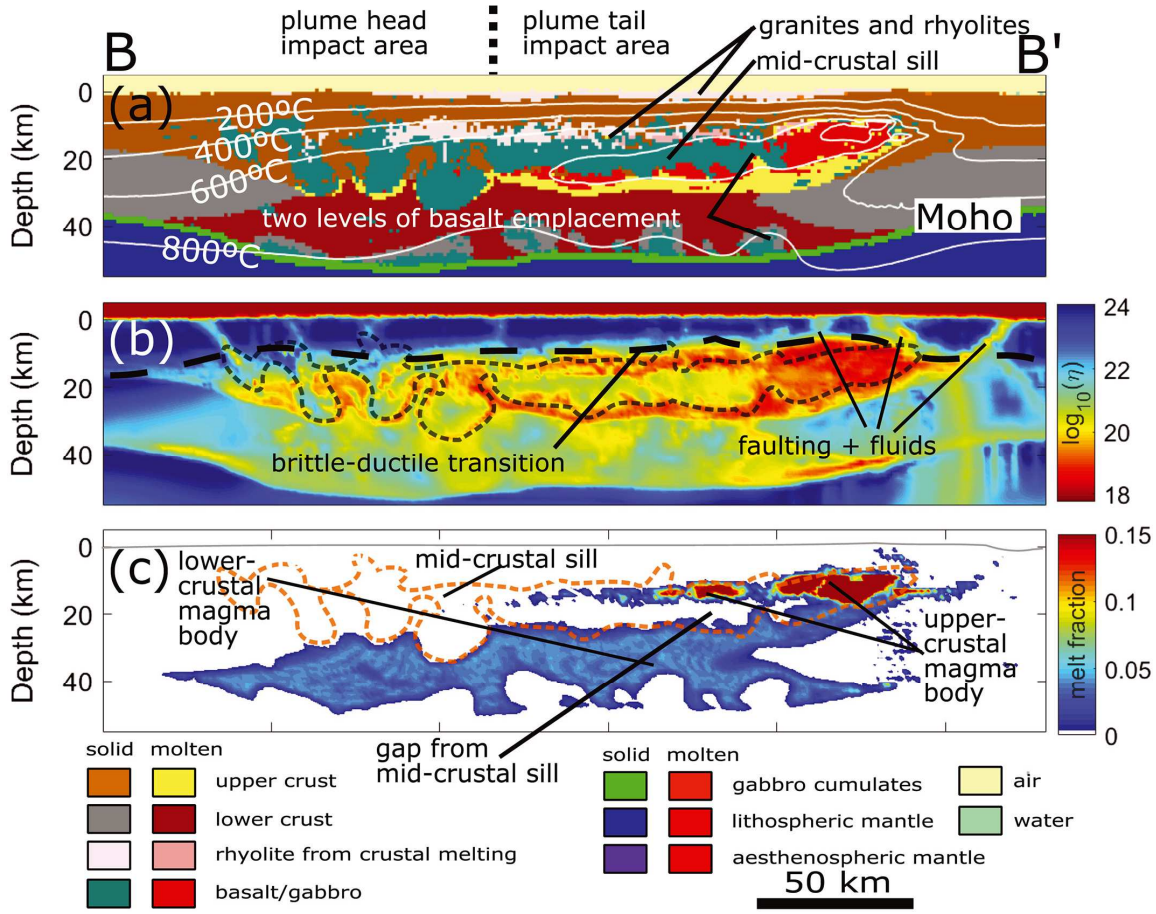

main shallow Yellowstone magma body and has been interpreted as a fluid□filled fault zone (Fig. 5.3, Farrell et al., 2014; Huang et al., 2015). These fluids are likely the source of the hydrothermal alteration which produces the distinctly low□$\delta^{18}O$ character of rhyolites along the hot spot track (Bindeman & Simakin, 2014; Colón et al., 2018b).

5.5. Influence of Model Parameters

5.5.1. Constraining Crustal Structure

Experiments varying the composition of the crust show that the primary depths of intrusion do not significantly change with realistic changes in crustal density, suggesting

that magma overpressure makes density contrasts within the crust subordinate to rheological contrasts when it comes to trapping rising melts, as has been suggested from observations of intrusive field relationships (Annen et al., 2015; Menand, 2011), numerical modeling (Maccaferri et al., 2011), and analog modeling (Kavanagh et al., 2006). In Figs. 5.4a and 5.4b, we see that changing the depth of the boundary of the upper and lower crust changes the amount of melt in the crust but only weakly affects the

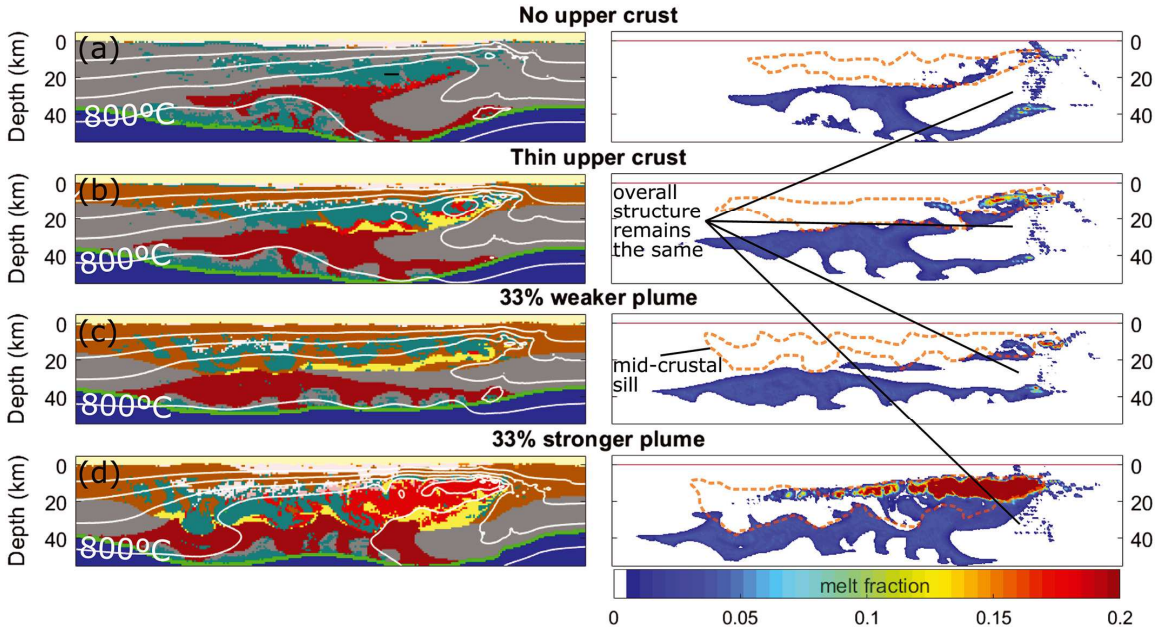

Fig. 5.4. Views of models with differing crustal composition and plume power from the reference model in Figs. 5.2 and 5.3. Temperature contours are 200°C, and all colors are the same as in Fig. 5.3. (a) Making the entire crust has the same mafic and rigid character as the lower crust in the reference model fails to significantly change the intrusion geometry of basalt but nearly eliminates crustal melting. (b) Making the upper crust thin produces a situation intermediate between that of part (a) and the reference model. Note that in parts (a) and (b) the structure and depth of the midcrustal sill is relatively stable even though the buoyancy of basalt relative to the surrounding crust is significantly changed (basaltic liquids have a density of 2,800 km/m^3, lower crust is 2,900 km/m^3, and upper crust is 2,700 km/m^3). (c) Result of using a plume that produces 33% less melt. Crustal melting is severely suppressed due to the reduced available heat, but the position of the smaller midcrustal sill remains the same as in the reference model. (d) Result of using a plume with 33% greater melt production. There is a much larger and more melt□rich midcrustal sill, which is more disturbed by Rayleigh□Taylor instabilities than in the reference model. The large shallow magma body hosts melt fractions approaching 100% in its center.

overall structure of the basalt intrusions seen in Fig. 5.3. Extreme changes such as making the entire crust consist of dry mafic material disrupt this structure, but we can safely rule these out based on our knowledge of regional geology (supporting information; Pierce & Morgan, 2009).

5.5.2. Constraining Plume Parameters

The rate of melting in the mantle is strongly dependent on the plume's temperature and on the thickness of the overlying lithosphere. Figs. 5.4c and 5.4d show the result of changing the amount of basalt rising from the plume by ±33% from the standard model, equivalent to changing the plume temperature by ~±25°C or to changing the thickness of the lithosphere by ±10 km (Fig. 5.5a), as can be seen in Fig. 5.5a. These variations in turn produce large differences in the degree of crustal melting and in the melt fraction in the upper crustal magma body. Again, however, we note that the overall structure of the basalt intrusions seen in Fig. 5.3 persists, even if the shallow magma body varies greatly in size. In Fig. 5.5b, we observe a surprisingly robust linear relationship between mantle melting rates and the resulting rhyolite eruption rates. These eruption rates, while certainly on the high end of estimates for Yellowstone (Christiansen, 2001), are not out of line with those for other parts of the hot spot track (Bonnichsen et al., 2008) and are directly proportional to the total rhyolite production rate in the crust. We may also simply be overestimating the volcanic□plutonic ratio for rhyolites here, which is related to the constant L (equation 5.2) and averages about 0.6 in our standard model (see supporting information). Increases in basalt flux into the crust increase rhyolite production by melting of the upper crust with a larger and hotter midcrustal sill and to a

lesser extent via additional fractionation of juvenile basalts. In contrast, lower crustal melting is comparatively unaffected; all new melt mostly accumulates in the middle–upper crust. Changing the composition of the crust also alters rates of rhyolite production, with crust with purely upper crustal or lower crustal compositions changing rhyolite production rates by ±25–30%, but we consider these changes to be unrealistic end-members relative to our reference model compared to more plausible changes in mantle conditions. We finally note that significant crustal melting ceases when basalt

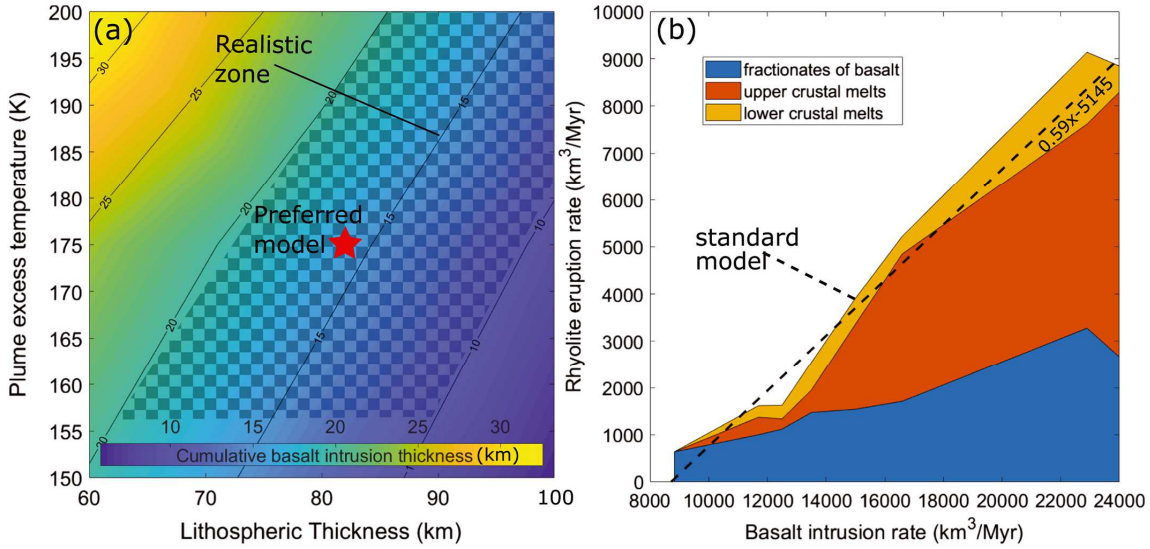

Fig. 5.5. (a) Effect of varying lithospheric thickness and mantle plume temperature above the background mantle with a potential temperature of 1350°C. We plot the combined thickness of all basalt intrusions that form between 5 and 7 Myr after the start of the model. In practice, this number is close to but slightly larger than the thickness of the midcrustal sill complex because that intrusion is the ultimate destination of most, but not all, basalts intruding from the mantle. We see that our preferred model with 80-km thick lithosphere and a plume with a potential temperature of 1425°C produce approximately 15 km of crustal thickening via basalt intrusion, in line with previous estimates (McCurry & Rodgers, 2009). (b) Plot of rhyolite eruption rates as a function of basalt intrusion rate, which is calculated by taking the thicknesses in part (a) and multiplying them by a presumed hot spot track width of 40 km and the plate velocity of 25 km/Myr. Contributions to the total volume of rhyolite from melts of the upper crust, lower crust, and basalt fractionation are shown with different colors. Our standard model produces approximately 3,800 km^3/Myr of rhyolite (corresponding to a cumulative depth of 3.8 km, though this is strongly dependent on volcanic–plutonic ratios, which we do not strongly constrain) from a basalt intrusion rate of 15,000 km^3/Myr.

intrusion rates fall below approximately 8,000 km^3/Myr, as the crust is advected away from such a weak plume before significant melting can occur.

We prefer a Yellowstone plume temperature of 175°C above ambient mantle temperatures and a lithospheric thickness of 80 km (assuming the dry peridotite melting model of Katz et al., 2003), which produces model results that match existing geophysical observations of both the mantle and the crustal magmatic system (Hopper et al., 2014; Huang et al., 2015) as well as the rates of eruption observed along the hot spot track (Christiansen, 2001; Knott et al., 2016). This implies some 15,000 km^3/Myr of basalt from the mantle (Fig. 5.5b), in line with previous estimates for Yellowstone based on gas emission fluxes (Lowenstern & Hurwitz, 2008; Werner & Brantley, 2003). Variations in the eruption rate over the last 13 Ma (Pierce & Morgan, 2009) are most easily reproduced by minor changes in lithospheric thickness from this baseline.

5.6. Conclusion

Our models illustrate that the entire continental crust along the Yellowstone hot spot track is strongly reworked by melting and intrusion centered on a 10□ to 15□km thick midcrustal sill complex, which forms as a result of the trapping of melts by the brittle□ductile transition and which separates a melt□rich upper crustal magma body from a larger but melt□poor lower crustal magma body. The good match between observations and numerical results seen here suggests that our relatively simple large□scale and long□term magma emplacement model captures the first□order physical controls of the tectono□magmatic plume□lithosphere interaction system and could be potentially applied to other continental igneous settings worldwide.

5.7. Bridge

Where Chapter V represented the first use of the I2VIS magmatic-thermomechanical modeling program to assess the problem of the origin of Yellowstone's crustal magmatic system, Chapter VI represents the continuation of that effort. This chapter, in many ways, brings the dissertation full circle, as it uses further developments of the modeling program to test some of the ideas presented in Chapters II-IV concerning the origins of the isotopic trends observed in Yellowstone hot spot track rhyolites and zircon crystals in particular. This work is preliminary for now, but should represent a useful advance in wedding isotope geochemistry and geophysical modeling, tying together the conclusions Chapter IV and Chapter V of this dissertation.

CHAPTER VI

MAGMATIC, CHEMICAL, AND ISOTOPIC EVOLUTION OF YELLOWSTONE HOT SPOT MAGMATISM BY MAGMATIC-THERMOMECHANICAL MODELING

This chapter contains material co-authored with Ilya Bindeman, who served in an advisory role, and Taras Gerya, who provided the original I2VIS code which was modified by me for this study. I was the lead author of this paper, including experiment design, code writing, and writing the manuscript. Ilya Bindeman provided feedback on manuscript structure and writing, and Taras Gerya provided the original unmodified code. These results are preliminary, but will eventually be submitted to the Journal of Volcanology and Geothermal Research.

6.1. Introduction

6.1.1 Motivation

Silicic magma genesis plays a critical role in processes ranging from the evolution of continental crust to explosive volcanic eruptions. The post-Columbia River Basalt part of the Yellowstone hot spot track, which is one of the most voluminous concentrations of erupted rhyolite in the Cenozoic (Bonnichsen et al., 2008; Pierce and Morgan, 2009), has received renewed interest in recent years due to advances in microanalytical techniques and high-precision geochronology, seismic imaging, and numerical modeling (e.g. Colón et al., 2018a, 2018b; Huang et al., 2015; Wotzlaw et al., 2015). These studies have provided critical constraints on the source materials for the rhyolitic melts which fuel the majority of volcanism in the region, investigating the relative contributions of melts of

the Cenozoic upper crust, the Precambrian lower crust, and material ultimately derived from the Yellowstone mantle plume (e.g. Colón et al., 2018a; Drew et al., 2013; Wotzlaw et al., 2015). A key observation has been the near-universal presence of diverse crystal and glass chemical and isotopic compositions within individual eruptive deposits, which indicates that the erupted magmas from throughout the Yellowstone hot spot track were derived from diverse batches of eruptible magma which assembled and mixed prior to/during eruption. (Bindeman and Valley, 2001; Boroughs et al., 2012; Colón et al., 2018a; Nash et al., 2006; Stelten et al., 2017; Swallow et al., 2018; Watts et al., 2011). Concurrently, there has been rapid progress in constraining the timescales over which these magmatic systems develop prior to erupting, which have shown that the giant pre-eruptive magma bodies with volumes of 10^3 km^3 or more can be assembled in as little as a few kyr, but may also inherit materials, particularly zircon phenocrysts, which date back millions of years earlier in the systems' history (Colón et al., 2018a; Rivera et al., 2016, 2017; Stelten et al., 2013; Szymanowski et al., 2016; Watts et al., 2012; Wotzlaw et al., 2014, 2015;). These scenarios are in strong contrast with the cooler, wetter, and more slowly assembled voluminous silicic magmas associated with arc magmatism (Christiansen & McCurry, 2008; Wotzlaw et al., 2013). Together, these observations suggest that the magmatic systems that fuel Yellowstone hotspot track "super eruptions" are both geometrically and temporally complex, with further investigation continuing to reveal ever finer details.

6.1.2. Numerical modeling insight into magma petrogenesis

The modern subsurface structure of the Yellowstone volcanic system has been recently constrained by geophysical imaging (Farrell et al., 2014; Hopper et al., 2014; Huang et al., 2015; Yuan et al., 2010), which has revealed a large shallow magma body at depth of 5 to 15 km, underlain by a larger and more diffuse magmatic system at depths of 25 to 45 km. Further insight into the origins of this structure are best provided by numerical modeling, which has the potential to study the physical evolution of a hotspot magmatic system in both space and time in a way that is inaccessible to the above methods.

Computer modeling of magmatic systems has been an active field of research for several decades now, with important insights provided by models of varying levels of sophistication. Much has been learned from one-dimensional and quasi-one-dimensional (e.g. axisymmetric cylindrical) models of magma genesis (Annen et al., 2002, 2006, 2015; Dufek & Bergantz, 2005; Huppert & Sparks, 1988), the latter of which we employ in this study. These models continue to yield new results (e.g. Karakas et al., 2017) especially when coupled with analytical solutions for the stress fields controlling transport into and out of magma bodies by dikes (Jellinek & DePaolo, 2003; Karlstrom et al., 2009; Simakin & Ghassemi, 2010) in a stress field. More complex thermomechanical treatments of specific magmatic processes at various scales and resolutions including convection of melts and the elastic response of the surrounding crust have also been performed (e.g., Cao et al., 2016; Gerya & Burg, 2007; Gregg et al., 2015; Schubert et al., 2013; Keller et al., 2013; Simakin & Bindeman, 2012). These approaches provide high spatial and temporal resolution and allow good control in an investigated parameter space, but also only consider intrusive or eruptive events over scales of 1000s of years or

less. At the other end of the spectrum, there have been several recent regional-scale thermomechanical models of mantle plumes and plume-crust interactions that do operate on the scale of many Myr (e.g., Burov et al., 2007; Burov & Gerya, 2014; Burov & Guillou-Frottier, 2005; Gerya et al., 2015; Sobolev et al., 2011), but have lacked or used very simplified magmatic processes treatments.

The rapid development of computational resources has allowed the combination of these regional-scale models with models of magma genesis in the crust. A recent such attempt was our previous study (Colón et al., 2018a), which used magmatic-thermomechanical modeling code modified from the I2VIS code of Gerya and Yuen (2003). This study is the result of an attempt to bridge the gap between small and detailed models of individual phenomena such as heat transport (e.g. Annen et al., 2002; Karakas et al., 2017) or dike propagation (e.g., Jellinek & DePaolo, 2003) with regional scale models of which include tectonomagmatic systems such as mantle plumes but lack a detailed treatment of crustal magmatic processes (e.g. Gerya et al., 2015). In that study, we assume that the primary mechanism by which rising magmas stall and accumulate in the crust is the trapping of dikes by rheological discontinuities in the crust, particularly the brittle-ductile transition which occurs at depths of 5-10 km. We further showed that the dominant control on the distribution of magma in the crust under Yellowstone is the presence of a large mafic sill complex that forms at depths of 10-20 km in response to this brittle-ductile transition, providing both heat and material to the magma bodies above and below it, corroborating observations of a similar feature under the eastern Snake River Plain which presumably dates back to the age of eruptions there (Peng & Humphreys, 1998). In this study, we seek to expand upon that result by taking that

modeling scheme, improving its treatment of melt propagation through the crust by adding a very simple scheme for melt density stratification via porous flow in regions of partial melt, and by allowing it to make simple predictions about the chemical and isotopic compositions of the erupted melts. We check some of these results by using a simple modification of the cylindrical axisymmetric Heat2D code of Annen et al. (2015) which allows crustal melts to be erupted at the surface. Finally, we compare these results to observed geochemical trends in the eruptive products of Yellowstone hot spot volcanoes, testing previous hypotheses concerning the origin of the enigmatic low-$\delta^{18}O$ and low-$\varepsilon_{Hf}/\varepsilon_{Nd}$ magmas which are found throughout the hotspot track (Colón et al., 2018a; Boroughs et al., 2012; Hildreth & Christiansen, 1984; Nash et al., 2006; Watts et al., 2011).

6.2. Geologic background: Geochemical trends in Yellowstone hot spot silicic calderas

We seek to understand the origins of the rhyolites which fueled the giant eruptions which have taken place along the Yellowstone hot spot track over the last 15 Myr (Fig. 6.1; Pierce and Morgan, 2009). To properly constrain our models, we turn to

---

Fig. 6.1 (next page). Map of the Yellowstone hot spot track in continental North America, showing 15 Myr of magmatic activity. Red dashed ovals are the major named eruptive centers of the hot spot track (Bonnichsen et al., 2008), culminating in the site of modern activity at Yellowstone, which has been active since the last ~2.3 Myr. The green shaded area is the area where hot, seismically slow mantle has been imaged under the continental lithosphere (Wagner et al., 2010), and interpret as the remnant of older parts of the plume currently located under Yellowstone. Solid orange and red represents areas of exposed Precambrian rocks in the region, of Proterozoic and Archean age, respectively, which are likely the source for the rare extremely low-ε_{Hf} magmas which occur on parts of the hot spot track. By contrast, voluminous low-$\delta^{18}O$ magmas have been found at every single part of the hot spot track.

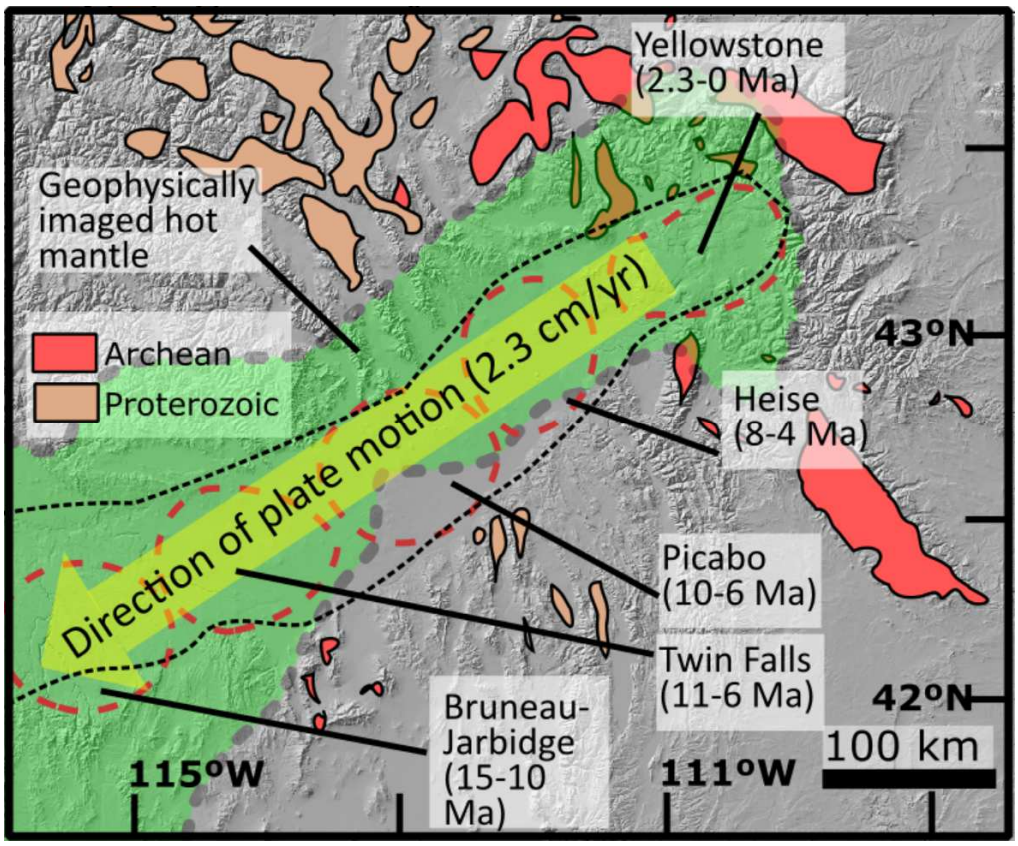

several important trends which have been identified by previous workers in both the isotopic and chemical compositions of the erupted magmas. Understanding these geochemical trends is important for evaluating our different models of the sources of erupted magmas, so we describe them here in some detail.

6.2.1 Chemical and thermal evolution of erupted rhyolites

The Yellowstone hot spot track is characterized by a pronounced Daly Gap, with all erupted lavas and tuffs during the main phase of activity being either basaltic or rhyolitic in composition, with intermediate melts nearly absent (Christiansen 2001; McCurry et al., 2008; Szymanowski et al., 2015). Furthermore, the caldera systems themselves are almost exclusively rhyolitic, with basaltic eruptions limited to the margins of the system or the post-caldera phase of activity after the silicic magma bodies have

presumably cooled and crystallized (Christiansen 2001; McCurry et al., 2008). The highly welded nature of most Yellowstone hot spot tuffs, along with their lack of hydrous phenocrysts, suggests that Yellowstone rhyolites are frequently very hot and dry compared to arc magmas (e.g. Almeev et al., 2012; Branney et al., 2008). Hydrous phases such as amphibole and biotite are almost always absent, and calculated temperatures based on zircon saturation, and oxygen isotope equilibrium are typically in excess of 800°C at Yellowstone (Loewen & Bindeman 2016; Troch et al. 2017). This is even more pronounced in the central Snake River Plain, where Ti-in-quartz thermometers in very crystal-poor magmas suggest temperatures approaching 1000°C (Cathey & Nash, 2009; Honjo et al., 1992), and melting experiments suggest that observed mineral assemblages are produced at temperatures in excess of 900°C with H_2O contents not exceeding 2% (Almeev et al., 2012). In contrast, rare rhyolites contain up to 6% water with temperatures as low as 720°C, most notably the Arbon Valley Tuff, which is coincidentally also one of the most low-ε_{Hf} magmas in the hot spot track, erupted at the start of the Picabo cycle (Drew et al., 2013, 2016). Silica content and temperature trends in Yellowstone hotspot magmas are not consistent across the hotspot track, with both cooling trends with increases in silica (Watts et al., 2012, Yellowstone) and heating trends with increasingly mafic magmas (Bonnichsen et al., 2008, Bruneau-Jarbidge and Twin Falls) observed at different eruptive centers. By contrast, there are common systematic changes in both the radiogenic and stable isotope compositions of the erupted rhyolites.

6.2.2. Radiogenic isotopes

Sr, Pb, Nd, and Hf isotopes clearly differentiate ancient Precambrian crust from material which has been extracted from the mantle more recently. Most rhyolitic magmas on the Yellowstone hotspot track are much more mantle-like in their radiogenic isotope compositions than the ancient crust, indicating the strong involvement of differentiates of basalt in producing erupted magmas (McCurry & Rodgers, 2009; Nash et al., 2006; Shervais et al., 2006). Rhyolitic magmas in the Yellowstone hotspot track are the product of widely varying proportions of mantle differentiate and melts of both young and ancient crust, so their whole rock radiogenic isotope compositions are similarly diverse (Colón et al., 2015a; Doe et al., 1982; Drew et al., 2013; Nash et al., 2006; Shervais et al., 2006; Watts et al., 2012; Wolff et al., 2011). The largest dataset is available for Hf isotopes, as Hf partitions strongly into zircon and is easily measured by in situ methods (e.g. Fisher et al., 2014; Kylander-Clark et al., 2013). In the past five years, multiple in situ and dissolution studies of zircon in the Yellowstone hot spot track have found significant diversity in their hafnium isotopes within single eruptive units, indicating their derivation from multiple separate batches of magma themselves derived from varying amounts of mantle-derived fractionates and melts of different types of crust (Drew et al., 2013; Colón et al., 2015a, 2015b, 2018a; Stelten et al., 2013, 2017; Wotzlaw et al., 2015). Most magmatic zircon from the hotspot track have Hf isotope compositions reflecting moderate involvement of unradiogenic crustal melting, clustering around ε_{Hf} values of -10 (Colón et al., 2018a), in line with the bulk-rock values of most major tuffs from the Snake River Plain (Colón et al., 2015a; Nash et al., 2006). More rarely, some units have extremely unradiogenic Hf isotopes, with ε_{Hf} values ranging from -25 to as low as -38, including the Arbon Valley Tuff at the Picabo Center (Drew et al., 2013; 2016)

Huckleberry Ridge Tuff C at Yellowstone (Doe et al.,1982; Wotzlaw et al., 2015), and the Johnstons Camp Rhyolite at Bruneau-Jarbidge (Colón et al., 2015b)). Notably, only one rhyolite with a significant population of these very unradiogenic zircon has been found at each major eruptive center, and they always occurred very early in the eruptive sequence at each center (Colón et al., 2018).

The sources of diversity in the Hf isotope compositions of individual zircons are in the different types of crust that melt to produce the erupted rhyolites. Extremely low-ε_{Hf} magmas can only be produced by the melting of Precambrian crust, which has been well-documented in the Snake River Plain rhyolites in the form of xenoliths and xenocrysts with ε_{Hf} values as low as -60 (Colón et al., 2018a; Leeman et al., 1985; Watts et al., 2010). There is also significant evidence for the melting of much younger rocks such as the Idaho Batholith and the Challis volcanics, which have significantly more mantle-like radiogenic isotopes (Boroughs et al., 2012; Colón et al., 2018a; Gaschnig et al., 2011). Finally, the highest-$\varepsilon_{Hf}/\varepsilon_{Nd}$ magmas of the hot spot track can only be produced by significant input of mantle material (McCurry et al., 2008; Nash et al., 2006; Stelten et al., 2017).

Previous studies have documented a trend of gradually increasing ε_{Nd} and ε_{Hf} values with time at each center, moving towards more radiogenic (mantle-like) compositions (Colón et al., 2018a; Hildreth et al. 1991; Nash et al., 2006; Stelten et al., 2017). Recently Stelten et al. (2017) noticed that the Central Plateau Member rhyolite lavas at Yellowstone became gradually more radiogenic in their Hf isotopes with time, which they interpret as the result of the continuous input of isotopically primitive material from the mantle into a magma body which becomes more radiogenic with time

as a result. The trend of extremely low-ε_{Hf} material being erupted early in each volcanic center's evolution has been interpreted by Colón et al. (2018a) as possibly being the result of early melting of ancient deep crust followed by the isolation of the shallow crustal magma reservoir that fuels the large rhyolitic eruptions by a growing cumulate pile and mafic sill complex which separates it from the isotopically ancient deeper rocks. In this study, we seek to test these models and to consider which crustal compositions and structures yield the observed trends.

6.2.3. O isotopes

The Yellowstone hot spot track has long been recognized as the largest known concentration of low-$\delta^{18}O$ rhyolites in the world, with at least 10^4 km^3 of low-$\delta^{18}O$ tuffs and lavas having erupted in the last 14 Myr (Bindeman, 2008; Bonnichsen et al., 2008; Boroughs et al., 2012; Watts et al., 2011). Low-$\delta^{18}O$ magmas can only be derived from the melting of shallow, hydrothermally altered crust, with low-$\delta^{18}O$ being defined as anything less than the mantle value of +5.5-6.0‰ (VSMOW), with rhyolites ranging toward the higher values because of minor isotopic effects during fractional crystallization (Taylor & Sheppard, 1986). Every major center in the Snake River Plain contains low-$\delta^{18}O$ rhyolites with $\delta^{18}O$ values reaching as low as -2.6‰ in zircon phenocrysts, and whole-rock values as low as 0‰ (Colón et al., 2018a; Bindeman & Simakin, 2014). The caldera centers of the hotspot track in the Snake River Plain and Yellowstone (Fig. 6.1) also all exhibit a crude trend towards lower $\delta^{18}O$ values in erupted rocks through time, with the Picabo, Heise, and Yellowstone centers in particular opening with normal-$\delta^{18}O$ rhyolites and finishing at low-$\delta^{18}O$ values (Bindeman & Valley, 2001;

Drew et al., 2013; Watts et al., 2011, 2012). By contrast, the central Snake River Plain caldera centers (Bruneau-Jarbidge and Twin Falls, Fig. 6.1) have initial eruptions which are low-$\delta^{18}O$, though still-lower values appear later in time, suggesting that the same trend of lowering $\delta^{18}O$ is at work there, if less clearly (Boroughs et al., 2012; Bindeman & Simakin, 2014; Colón et al., 2015a).

Attempts to understand the origin of the voluminous low-$\delta^{18}O$ rhyolites at the Yellowstone hot spot track have been a source of considerable recent debate. In summary, there have been 3 main proposed mechanisms for the production of low-$\delta^{18}O$ rhyolites: (1) intracaldera tuffs and lavas are hydrothermally altered through systems similar to that seen at Yellowstone today, making them low-$\delta^{18}O$, and further overlapping caldera collapses bring this material down to depths where it can be melted, and this material first acquires a low-$\delta^{18}O$ composition through a shallow hydrothermal system analogous to the one present at Yellowstone today (Drew et al., 2013; Watts et al., 2011), (2) hydrothermal alteration along fault lines associated with tectonic extension related to the early stages of magmatism at each center produced low-$\delta^{18}O$ alteration of some combination of buried volcanic rocks, preexisting crust (such as Idaho Batholith or Challis volcanics), and earlier hot spot-derived mafic intrusions, which later melted and produce low-$\delta^{18}O$ magmas (Blum et al., 2016; Colón et al., 2015a, 2015b; Drew et al., 2013), and (3) older low-$\delta^{18}O$ alteration of the upper crust associated with earlier magmatism unrelated to the Yellowstone plume, such as the emplacement of the Idaho Batholith, provides pre-existing sources of low-$\delta^{18}O$ material for melting and eruption during Yellowstone plume magmatism (Boroughs et al., 2012, Ellis et al., 2013), potentially explaining the fact that central Snake River Plain rhyolites are exclusively

low-$\delta^{18}O$ in their composition. We evaluate these models, particularly (1) and (3), by considering means of producing and melting low-$\delta^{18}O$ crust in an active continental hot spot setting. In any case, the trend towards increasingly not mantle-like $\delta^{18}O$ values in erupted rhyolites at each caldera center stands in marked contrast with the evolution towards primitive values in radiogenic isotopes, which would suggest a role for some kind of crustal melting even at the latest stages of each system, but that the type of crust which is melting changes distinctly. Finally, we note that that the extreme crust-like end-members in both oxygen and radiogenic isotopes do not occur together in the Yellowstone hot spot track, resulting in a distinct L-shaped pattern in plots of O and Hf isotopes for Yellowstone hot spot zircon (Colón et al., 2018b; Fig. 6.15). Understanding these trends is a key goal of this study.

6.3. Methods

6.3.1 I2VIS magmatic-thermomechanical models

We employ large-scale 2D Lagrangian marker-in-cell-based magmatic-thermomechanical finite difference models of the Yellowstone system modified from those of Colón et al. (2018a) to consider the evolution of a single part of the Yellowstone hot spot track. In Colón et al., (2018a), we modeled the interaction between a deeply-sourced mantle plume and overlying lithosphere which moves at 25 km/Myr relative to the plume. These models solve slow Stokes flow, continuity and heat equations:

$$\frac{\partial \sigma'_{ij}}{\partial x_j} - \frac{\partial P_i}{\partial x_i} = -\rho g_i \qquad 6.1$$

$$\frac{\partial v_i}{\partial x_i} = \Gamma \qquad 6.2$$

In these equations v is velocity, P pressure, σ' is the deviatoric stress tensor, ρ is density, g is (purely vertical) gravitational acceleration, x_i are the spatial coordinates, and Γ is a source term that accounts for local melt extraction and emplacement. We couple these fluid-flow equations with a Lagrangian heat equation that includes shear heating and radiogenic heating:

$$\rho C_p \left(\frac{DT}{Dt}\right) = \frac{\partial}{\partial x_i}\left(k\frac{\partial T}{\partial x_i}\right) + H_r + H_s + H_a \qquad 6.3$$

where T is temperature in kelvin, C_p is the heat capacity, k is thermal conductivity, H_r is radiogenic heating, which is a predefined constant, H_s is shear heating, and H_a is adiabatic heating. These equations are solved on a two-dimensional fully staggered finite difference grid and temperature advection is performed with markers. For this model, we use a 2×2 km square finite difference grid with 16 Lagrangian markers per cell at the start of the run (subject to change during material advection and melt extraction). For full discussion of the methods via which these equations are solved see Gerya and Yuen (2003) and Gerya (2010).

6.3.2. Melt transport in the I2VIS model

We consider four main methods by which melt is transported in the crust and upper mantle, after Solano et al. (2012). (1), melt may be transported through via dikes. This requires a relatively large volume of melt and rigid, mostly solid crust that can fracture. (2), areas of partial melt with sufficient permeability may allow the extraction and transport of melt through them via porous flow. The melt fraction threshold at which porous flow can occur varies depending on the rock composition and grain size, but we assume for these models that it can occur at melt volume fractions as low as 2% (Solano

et al., 2012). (3), melt can move about freely when it is surrounded by other mostly molten material which is above the solid-liquid rheological transition which tends to occur at melt fractions of approximately 50%, depending on the shape and size of the solid grains (Solano et al., 2012). Finally (4), entire melt bodies or areas of partial melt may rise or sink as buoyant diapirs in thermally weakened lower crust and mantle (Keller et al., 2013).

Previous workers have mostly attempted to model these types of melt transport one at a time, as they take place on extremely different length and timescales (e.g., Kavanagh et al., 2006; Keller et al., 2013; Maccaferri et al., 2011; Ramberg 1971; Simakin & Bindeman, 2012; Solano et al., 2012,). In order to encompass the full behavior of the magmatic system under hot spot volcanoes, undertook the task of considering each one of these phenomena simultaneously within a single computational run. The movement of diapirs is slow enough that it is captured by the bulk physics of our models (equations 6.1-6.3), but the former three require modeling techniques beyond the simple Stokes flow equations discussed above, as they occur on much time and spatial scales which are much smaller than the 5 kyr timestep and 2 km grid size of our model. For simplicity, we assume that all melt that originates in the mantle intrudes in the crust as dikes, as we are not concerned with the structure of any intrusions in the upper mantle for this study. We also assume that all melt transport of the first three types is purely vertical, to make the physics much more tractable.

For melt extraction, we consider the melt fraction of each Lagrangian marker in the model based on their composition, temperature, and pressure. For markers with greater than 50% melt fraction, we consider two melt transport regimes, which are

defined by whether or not eruptions are permitted. Eruption triggering mechanisms in large caldera-forming systems are poorly understood and very complex (e.g. Allen et al., 2012; Gregg et al., 2015, 2017; Karlstrom et al., 2012), so we consider their occurrence to be random for the purposes or our models. A random number generator gives each time stop an equal probability of having an eruption, and we adjust the probabilities to give the desired average recurrence interval. If an eruption is determined to be occurring by this method, we transport all markers in the crust that are at least 50% molten to the surface if they are buoyant enough for this to be possible (we consider all rhyolitic magmas to have densities of 1000 kg/m^3 during eruptions due to volatile exsolution for this purpose, making them almost always buoyant enough to erupt). If eruptions are not occurring, markers with a melt fraction that exceeds 50% initiate a dike which proceeds vertically upward and produces a distribution of new melt markers via the method described in detail in Colón et al. (2018a) and the appendix accompanying this paper. If eruptions are not occurring, we find local maxima in the non-dimensional value D:

$$D = \frac{\Delta P}{\eta}\Delta t \tag{6.4}$$

where ΔP is the magma overpressure in the dike, η is the viscosity of the host material, and Δt is the time step, computed in the entire vertical column over the source melt marker where ΔP>0 (where the magma is buoyant). Dikes give rise to sills at these local maxima with relative volumes computed as follows:

$$intrusion\ fraction \propto \left(\frac{D_{max}}{D_{min}}\right)^{0.5} \tag{6.5}$$

where D_{max} is the value of D at the local maximum in question, and D_{min} is the value of D at the overlying local minimum. In addition to intrusion at local maxima of D, 20% of all

available melt along a dike is also evenly distributed along the entire length of the dike (see Colón et al., 2018a). Finally, one difference in our model here from the work of Colón et al. (2018a) is that dikes can have a crystal cargo, and both the melt and crystal parts of Langrangian marker are transported in dikes.

If the melt fraction of the marker is between 2% and 50%, it cannot feed eruptions, but can still be transported via porous flow up or down vertically, as long as the average melt content in its local 2×2 km cell is above 2%, and the melt cannot propagate into cells which contain less than 2% partial melt. In this case only the liquid part of the original marker moves and it seeks its level of neutral buoyancy. Rising dikes that encounter zones of at least 4% partial melt will also only continue if they are still buoyant relative to the surrounding material, allowing bodies of evolved magma to from buoyancy traps for underplating dense mafic magmas. This behavior is unique to this study and is not considered in the results of Colón et al. (2018a). For a detailed treatment of the methods by which melt extraction is treated in the model see the appendix.

6.3.3. Isotopic modeling

We also track the isotopic compositions of Lagrangian markers, both molten and solid. Given the large $\delta^{18}O$ ranges of different components in our systems, we assume for simplicity that there is no noticeable fractionation in oxygen isotopes during fractional crystallization, at least relative to the large changes in $\delta^{18}O$ values which can be derived from hydrothermal alteration of the crust (Bindeman, 2008). Similarly, Hf isotopes are completely unchanged during melting and melt extraction. We initially set all material to have a normal $\delta^{18}O$ value of +7‰, which while higher than the mantle value of 5.7‰,

accounts for fractionation-driven increases in $\delta^{18}O$, which we do not directly compute (at the end we only track the $\delta^{18}O$ of erupted rhyolites anyway). We also assume all upper crust to have an ε_{Hf} value of -10 (see Colón et al., 2018a; Gaschnig et al., 2011), all lower crust to have an ε_{Hf} value of -60, and all mantle to have a relatively depleted ε_{Hf} value of +10. The Hf isotope distribution of the crust is only changed by physical movement of material through melting and melt transport. These processes also affect O isotopes, but they are also changed by hydrothermal alteration.

We assume that all hydrothermal alteration (lowering the $\delta^{18}O$ of rocks/markers) occurs in the uppermost crust in heated areas, which have been additionally mechanically disturbed in some way, presumably opening fractures which allow the circulation of fluids. We consider areas in the upper crust which have been weakened by strain to and effective viscosity of less than 10^{22} Pa·s to be vulnerable to penetration by meteoric waters and thus hydrothermal alteration (e.g., Gottardi et al., 2013; Colón et al., 2015b). We also require heat, and only allow hydrothermal alteration to occur in a temperature window of 100-300°C, above which we assume the ductile behavior of hot rocks and silica precipitation from solution closes pores and limits permeability. Finally, we require that hydrothermal alteration only occur in areas of enhanced geothermal gradient, with values of at least 40°C/km. Without this final requirement, we observe extensive hydrothermal alteration of the crust in areas where it is likely inappropriate, such as faults in relatively cold crust with no magmatic activity of any kind nearby. If these criteria are satisfied, we automatically reset the $\delta^{18}O$ value of a marker to -3‰, in line with the lowest $\delta^{18}O$ zircon observed anywhere in the Snake River Plain (Colón et al., 2018a), though occasional lower values are not unlikely (e.g. Troch et al., 2018).

6.3.4. Heat2D modeling

We modify the Heat2D code of Annen et al. (2002, 2006, 2015) to allow eruptions at periodic fixed intervals. This is a pseudo-2D axisymmetric model designed to mimic the conditions of the I2VIS models (see below). During time steps where there are eruptions, crustal material which is at least 50% molten is evacuated to the surface, while partial melts of mafic intrusions are not erupted, due to the difficulty of separating the liquid and solid parts of partially molten rocks in the purely thermal model. We use these models to test some of the observations made in the thermomechanical models in a simpler geometry, particularly observations of the relationship between eruption repose times and total cumulative eruptive volumes (Figs. 6.6-6.7, see below).

6.4. Goals of the present study and model setup

Unlike in the previous Colón et al. (2018a) study primarily focused on interpreting/recreating geophysical images of the Yellowstone system, we here are interested in the isotopic and chemical evolution of magmas at a single eruptive center in a continental hot spot track such as Yellowstone. Therefore, we remove the confounding factor of tectonic lithospheric velocity relative to the plume, and instead consider the effect of intrusions of basalt into fixed crust. This additionally allows for closer comparison with the Heat2D models, which have no crustal movement aside from the vertical movement associated with intrusions and eruptions. Mafic melts are emplaced evenly over a 50 km-wide zone of crust for 2 Myr, consistent with the lifespan of the two most recent caldera centers on the Yellowstone hotspot track at Yellowstone and Heise

(Christiansen, 2001; Morgan & McIntosh, 2005). This results in a crustal thickening of 18-19 km, which is in excess of most estimates for the hotspot track which suggest a value closer to 15 km (McCurry & Rodgers, 2009; Yuan et al., 2010), but we consider the fact that this is compensated for by adjacent gaps in apparent magmatism, such as between Yellowstone and Heise, which can be filled in by lower crustal flow as the system evolves in a more realistic 3D model, allowing us to remain within existing geophysical and geochemical constraints on the Yellowstone system. This is in marked contrast with the situation in the models of Colón et al., (2018a), where a ~25 km wide zone of intrusion and crustal melting moves at a velocity of 25 km/Myr, creating a very clear and uninterrupted trend in position versus eruption time on the surface of the hot spot track.

We use the same 1000 km × 300 km model space with a regularly-spaced 2 km square finite difference grid as in Colón et al. (2018a), with a mantle plume generated by a thermal and advective boundary condition anomaly at the base of the model. In our standard model, the crust is initially 35 km thick with 6 km of upper crust and 29 km of lower crust. The upper crust (Fig. 6.2, brown) is assumed to be rheologically weak (wet quartzite rheology of Ranalli, 1995), to have a very low melting point characteristic of wet granites or sediments (Johannes, 1985; Poli & Schmidt, 2002), have a silica content of 70%, a density of 2700 kg/m^3 (all densities reported for atmospheric temperature and pressure and may increase with depth), and an ε_{Hf} value of -10. The top 2 km of lower crust (orange) is identical except for the fact that it has an ε_{Hf} value of -60, matching the most isotopically ancient xenoliths and xenocrysts found in the Snake River Plain so far (Colón et al., 2018a; Watts et al., 2010). The rest of the lower crust (gray) has a wet

mafic melting curve (Hess, 1989; Schmidt & Poli, 1998), the An75 rheology of Ranalli (1995), a silica content of 50%, a density of 2900 kg/m^3, and an ε_{Hf} value of -60. The lowermost 5 km of crust above the Moho is a mafic cumulate assumed to have the same properties as the main part of the lower crust, but is slightly denser (3000 kg/m^3), has only 45% silica, and follows a dehydrated mafic rock melting curve (Hess, 1989). The mantle also has 45% silica and a density of 3000 kg/m^3, and follows the dry olivine rheology of Ranalli (1995) and the dry melting scheme of Katz et al., (2003), and has an ε_{Hf} value of a +10. For further information on material properties see Colón et al. (2018a).

The initial Moho temperature is 700°C, with a geothermal gradient of 35°C/km in the top 15 km of the crust overlying a much shallower geothermal gradient in the initial model setup. This rapidly equilibrates to a linear 20°C/km gradient over the entire crustal column in the 2 Myr period during which the model is made to run before magmatism begins, even in the presence of radiogenic heating in the upper crust, forming the initial condition before magmatism begins (Fig. 6.2). Below the crust is 45 km of mantle lithosphere, producing a lithosphere-asthenosphere boundary at 80 km depth, as constrained by the modeling of Colón et al. (2018a). The mantle has a potential temperature of 1350°C, and the mantle plume is 175°C hotter than the surrounding mantle, which leads to basalt production rates of between 19,000 km^3/Myr and 25,000 km^3/Myr, which we calculate by multiplying 2D melt areas with a presumed model thickness of 50 km. The model is allowed to progress for 2 Myr to allow the plume head and the crustal geothermal gradient to come to equilibrium, after which point all melt from the plume is redirected via what essentially amounts to several hundred kilometers

of horizontal teleportation to an area of crust which is previously entirely unaffected by the plume head. Melts then intruded into the lithosphere in an even distribution which in our standard model is 50 km in diameter, matching the Heat2D models (Fig. 6.13). The height to which melts rising into the crust is determined by the melt extraction protocol detailed below.

6.5. Results

6.5.1. Development of the mid-crustal sill complex

In the new series of models employed here, we confirm the main result of Colón et al. (2018a), showing that basalts rising from the mantle primarily accumulate in a mid-crustal sill complex which occupies depths of 8-20 km by the time it has fully developed after 2.0 Myr of intrusions (Fig. 6.2). Combined with other more diffuse intrusions in the lower crust, these produce a total of 15-20 km of crustal thickening, in line with previous estimates for the Yellowstone hot spot track (McCurry & Rodgers, 2009; Yuan et al., 2010). The depth of the top of this intrusive system corresponds to the brittle-ductile transition, which as the site of the greatest contrast in D (equations 6.4, 6.6) traps the most rising melts. The mafic magmas of the sill complex drive rhyolite production through their fractionation to form rhyolitic residual liquids, and by heating and melting of the surrounding crust, which begins approximately 0.75 Myr after the start of basalt intrusion in our standard model (Figs. 6.2, 6.3, 6.5). Despite the relatively low solidus temperatures used for the lower crust (Fig. 6.3), we find that the lower crust does not melt in significant quantities compared to the upper crust, and mafic intrusions in the lower

crust do not heat it to the point of melting except at the Moho and at the base of the sill complex (Fig. 6.2, 6.3).

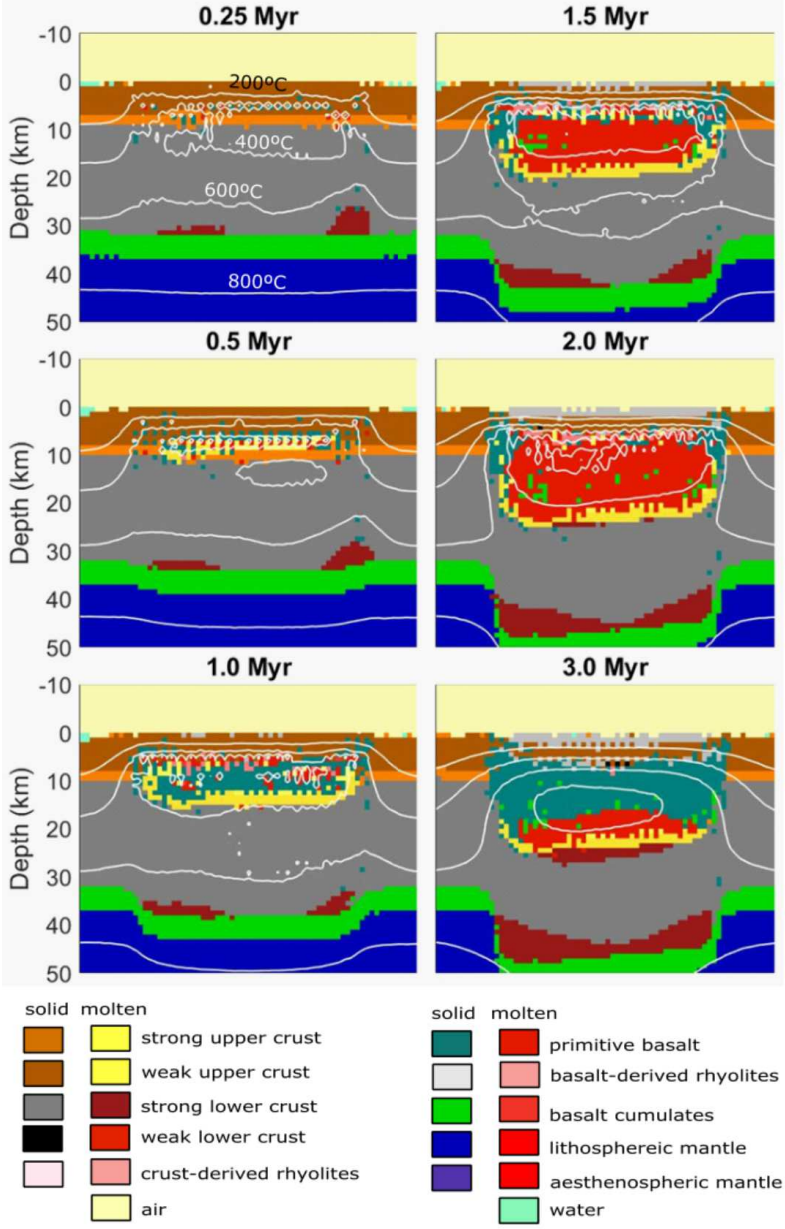

Fig. 6.2. Development of the Yellowstone magmatic system in the I2VIS model. Intrusions gradually build a large mafic sill complex, which remains partially molten while basalt intrusions continue, though it rapidly solidifies by 3 Myr after these intrusions cease after 2 Myr. Note that the position of the top of the intrusive complex remains relatively constant at 5-6 km, while its bottom reaches progressively deeper depths as new magma intrudes, advecting the lower crust downward and thickening the crust. By 2.0 Myr, just over 15 km of crustal thickening has occurred. Upper crustal boundaries move downward and surface material is getting buried by eruptions. White lines represent 200°C contours. Describe rhyolite vs basalt.

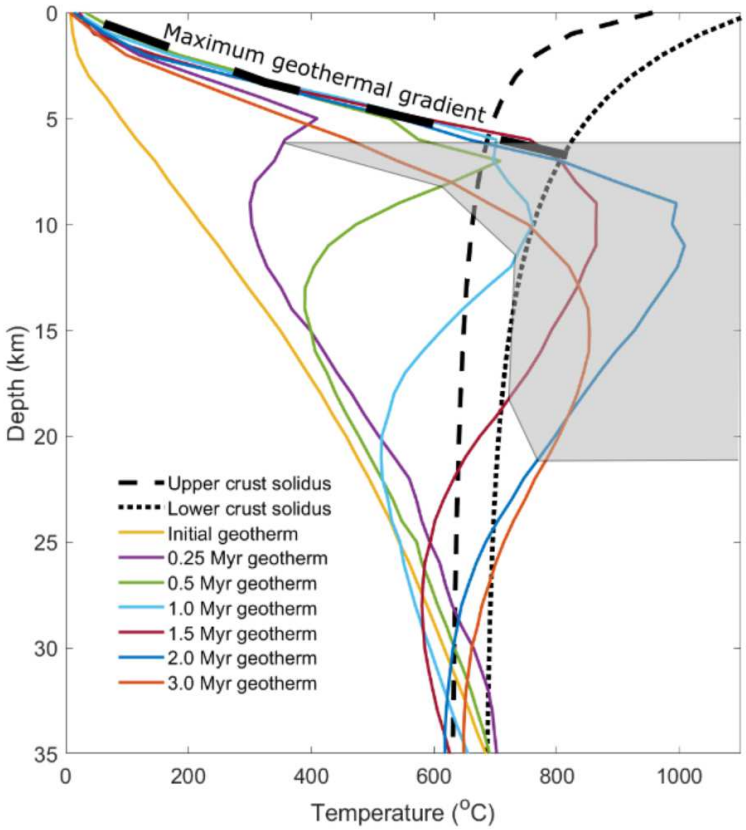

Fig. 6.3. Evolution of the geothermal gradient in the growing magmatic system shown in Fig. 6.2, showing the thermal effect of 3 Myr of basalt intrusion at a rate of 0.08 m/yr, resulting in 15 km of crustal thickening. The initial geothermal gradient (yellow) is approximately 20°C/km, and produces a Moho temperature of 700°C at a depth of 35 km. The shaded region encompasses the parts of each curve which are inside the mafic sill complex. Basaltic magma intrusion at 7-8 km depth rapidly raises the temperature of the upper crust, initiating melting there after 0.5 Myr of heating. Peak temperatures of approximately 1000°C are reached inside of the differentiating mafic sill complex at depths of approximately 10 km after 2.0 Myr, after which basalt intrusion from the mantle ceases and the system begins to cool. This cooling is slow, however, and peak temperatures 1 Myr after basalt intrusions cease are still in excess of 850°C. Finally, we note that the geothermal gradient in the upper crust does not seem to ever exceed ~150°C/km and that 2 Myr of crustal heating instead simply increases the maximum depth of this gradient.

6.5.2. Evolution of the geothermal gradient

The addition of mafic melts with temperatures of up to 1350°C from the mantle plume into the crust causes extremely rapid heating of the upper crust, as is documented in Fig. 6.3. We start with a steady-state crustal geothermal gradient of ~20°C/km in both the upper and lower crust, which stabilizes as such in our model despite having upper

crust which is ~10 times as radioactive as the lower crust. This gradient arises naturally even if we start with a stronger 35°C upper crustal gradient relaxing to be a straight line to the Moho. 0.25 Myr after the beginning of basalt intrusion, we see that the upper crust has been heated to a sharp local maximum temperature of 400°C at a depth of about 5 km. This corresponds to the depth of the incipient sill complex formed by the earliest intrusions (Fig. 6.2a). At the same time, the lower crust begins to melt as it is also being heated by basalt intruding there, but the melt fraction is too low for melt to migrate out of this region via dikes. The upper crustal local maximum in temperature grows and deepens slightly as time progresses, and first reaches the upper crustal solidus curve at 0.5 Myr, marking the start of upper and mid-crustal melting at a depth of 7-8 km, which can also be seen in Fig. 6.4. Because this is approximately at the boundary of the upper and lower crust, the first crustal melts are a roughly even mixture of upper crustal melts (solid counterpart is brown in Fig. 6.2) and lower crustal melts (orange in Fig. 6.2). By 1.0 Myr after the start of intrusion, a broad region of crust from depths of 5-14 km depth is heated above its solidus temperature, releasing large quantities of melt, some of which erupts (gray material at the surface in Fig. 6.2c). The peak in crustal melting occurs when intrusions cease at 2.0 Myr, and a very large and broad magma body occupies the upper crust spanning depths of 5-20 km, fueling voluminous volcanism at the surface. A noteworthy result is that the upper crustal geothermal gradient stabilizes at approximately 150°C/km for all depths above the melt zone, after an initial steeper ramping up in the top kilometer of crust. This geothermal gradient does not increase over time, and instead merely extends itself to greater depths as the system matures, eventually reaching peak temperatures of over 1000°C at depths of approximately 10 km. The fact that the peak in

temperature at the base of this gradient always occurs near the top of the developing basaltic sill complex suggests that most intrusions of new basalt overplate the older ones and intrude near the top of the sill complex.

When intrusion ceases after 2 Myr, the system immediately begins to cool, and further crustal melting and rhyolite fractionation ceases almost instantly aside from a very small amount of melting which continues in the lower crust (Fig. 6.5). The melts which have formed, however, are able to persist for a long time, including, somewhat counterintuitively, the shallowest magma reservoir where the most evolved rhyolitic magmas with the lowest melting temperatures naturally accumulate in our models. The mid-crustal sill complex rapidly solidifies as it is depleted of fertile silicic melts (that migrated upward) by fractionation, producing a noticeable amagmatic gap between the partially molten crust above and below it, as was previously observed in the models of Colón et al. (2018a).

6.5.3. Production of rhyolitic liquids

Rhyolitic liquids begin forming in the upper crust 0.5 Myr after basalt intrusions begin when the temperature at the upper crust-lower crust boundary reaches the solidus.

Fig. 6.4 (next page). Evolution of the melt bodies in the model depicted in Fig. 6.2. The views here are identical to Fig. 6.2, except for part **(f)**, where the time is 2.25 Myr instead of 3.0 Myr, which we select to show the early part of the cooling history of the system. **(a)** At 0.25 Myr there are very small amounts of melt throughout the crust that represent rapidly cooling basaltic dikes, along with incipient melting at the Moho, and the earliest beginnings of the mid-crustal sill complex at ~6 km depth. **(b)** Crustal melting begins in the upper crust at 0.5 Myr, and accelerates until basaltic intrusions cease at 2.0 Myr **(c-e)**. After basalt intrusion ceases at 2.0 Myr, the basaltic sill complex rapidly solidifies, but the lower crust below it remains partially molten where warm enough (see Fig. 6.3), and the rhyolitic magma body between 5 and 10 km depth also takes up to a million years to fully solidify.

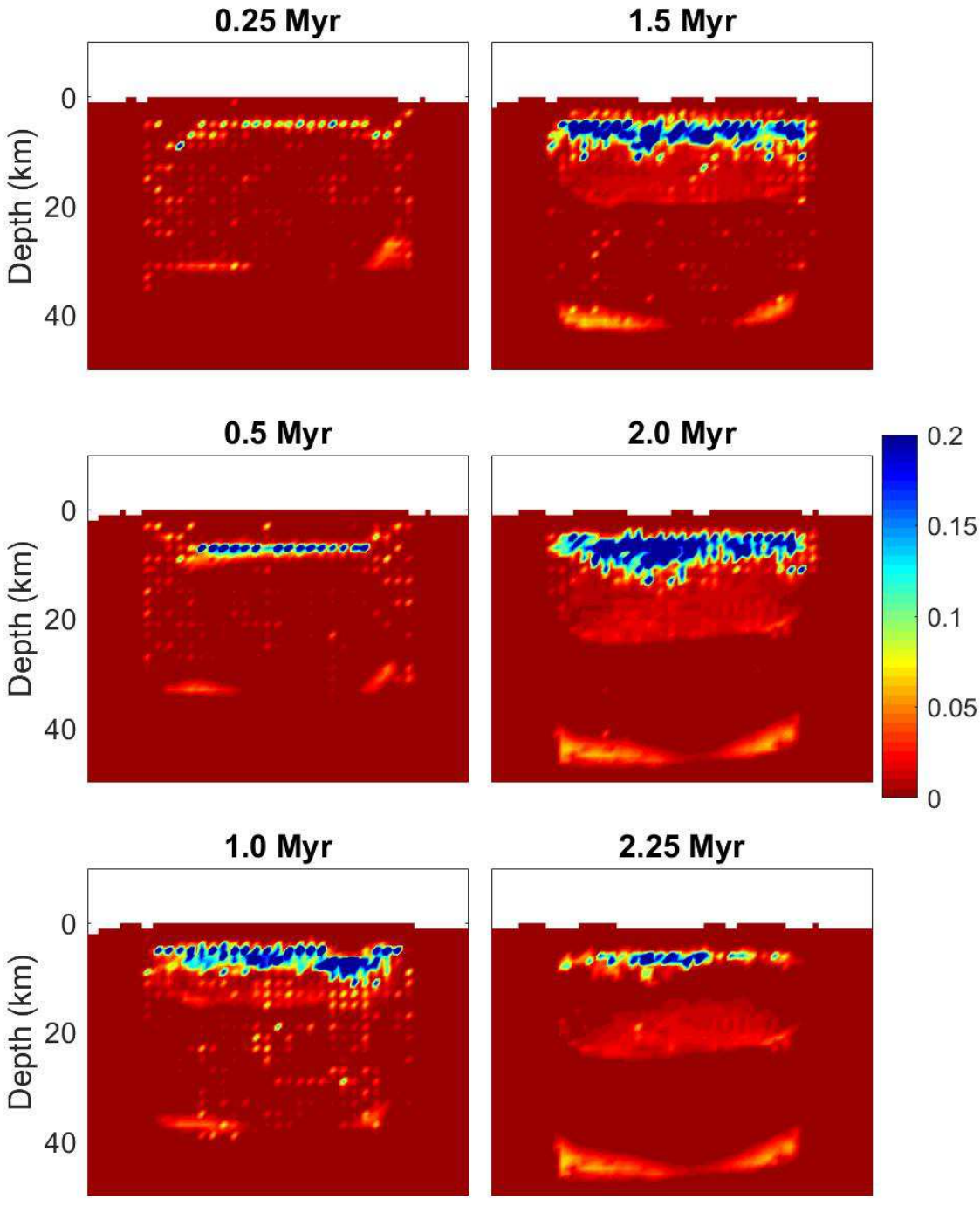

Melting of the upper 2 km of the lower crust, which melts according to the upper crustal solidus curve (Fig. 6.3), rapidly increases and peaks at ~0.8 Myr after the start of basaltic intrusions (Fig. 6.5). Lower crustal melting then rapidly declines as the material is depleted by the extraction of silicic melts. This rapid pulse of melting of

the upper fertile part of the lower crust dominates all lower crustal melting over the lifetime of the system, and melting of the main part of the lower crust (gray) is always comparatively minor, largely in part because of its relative isolation from the sill complex. Upper crustal melting follows lower crustal melting, and remains vigorous until basalt intrusions stop at 2.0 Myr (Fig. 6.5), with several large swings associated with the disruptions to the system caused by eruptions. Production of rhyolite through basalt fractionation starts at approximately the same time as crustal melting at 0.5 Myr after basalt intrusion begins, and steadily increases until rapidly ceasing when basalt intrusion stops at 2.0 Myr. Basalts that intrude the upper crust prior to 0.5 Myr cool and solidify too quickly to produce extractable rhyolitic liquids.

6.5.4. Rhyolite production vs. eruption rates as a function of frequency of eruption

We find that volumetric rhyolite eruption rates depend heavily on the number of individual eruptions, the depth of basalt intrusion, and the longevity of the system. Modifying the base model shown in Figs. 6.2-6.6 to change the average interval between eruptions from our standard model where eruption repose times average 200 kyr demonstrates a robust trend in which longer repose times between eruptions are associated with significantly less total erupted volume of rhyolite over the lifetime of

---

Fig. 6.5 (next page). Production rates of rhyolitic liquids from lower crustal melting, upper crustal melting, and fractionation of intruding basalts (this includes remelting of solidified basalt). Basalt intrusion starts at 0 time and ends at 2.0 Myr. Lower crustal melting is characterized by a large spike at just before 1.0 Myr, whereas upper crustal melting and basalt fractionation steadily increase until basalt intrusion stops. The system is too cool prior to 0.5 Myr to produce rhyolites by any means. The large spike at the start of the system's history is the result of a numerical problem which will be corrected in future work; it does not change the overall behavior significantly.

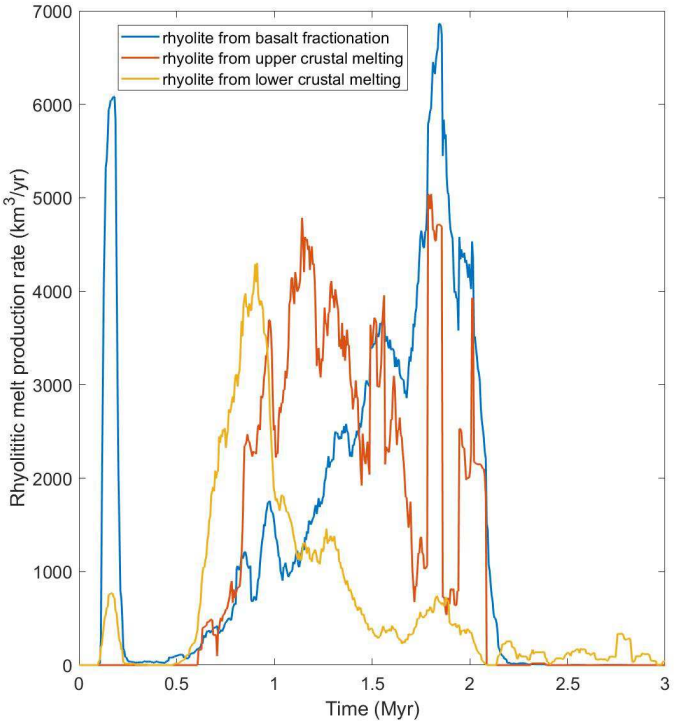

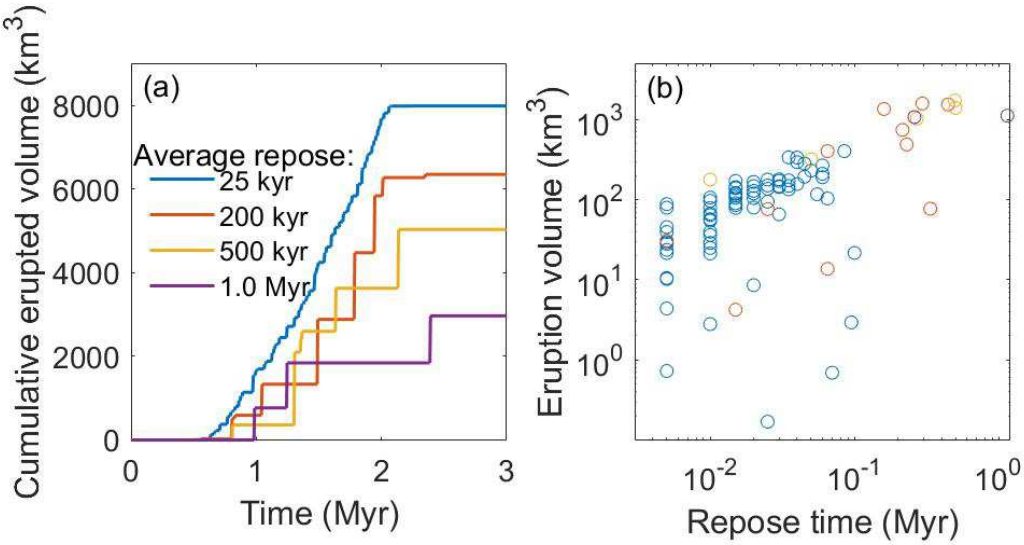

Fig. 6.6. (a) Comparison of cumulative erupted volumes over time for the four different I2VIS models using different average eruption repose times. Models with fewer eruptions produce noticeably less total erupted material over their lifetimes, despite having larger eruptions. **(b)** Plot of all individual eruption volumes for the models plotted in part **(a)** as a function of the repose time, here defined as the time gap between each eruption and the previous eruption. We note a crude trend towards larger eruptive volumes (up to ~1300 km^3 in these models) being associated with longer repose times. Discrete behavior on the left side of part **(b)** is a result of the 5000-year model timestep.

the system (Fig. 6.6a). This is despite the fact that longer repose times between eruptions are, intuitively, associated with greater eruptive volumes; this trend is more than counterbalanced by the greater number of smaller eruptions which occurs with smaller repose times. We further note that while total cumulative eruptive volumes strongly vary with eruption rates, the total volume of felsic melts produced (including intrusions) is less significantly affected by changing the eruption rate, with slightly higher total melt production occurring with longer repose times.

To further test this observation, we employ the Heat2D models which, because of their relative simplicity, are easier to interpret. As described above, these models involve intrusions of basalt to a fixed depth (7 km in this case) with melting of the crust occurring purely via conductive heating from the sill. We erupt all crustal material with melt fractions of at least 50% at regular intervals, but do not erupt partially molten basalt sills (see above). To achieve the best match with the I2VIS models, 15 km of basaltic sills was intruded over a 2 Myr period, with all new intrusions overplating the previous intrusions at a depth of 7 km, similar to what we observe in the model detailed in Figs. 6.2-6.4. Intruding basalts are assumed to have temperature of 1200°C. Tracking the total volume of melt in the crust over time, we find that longer repose times are associated with significantly greater volumes of melt in the crust, including melt in both the basaltic intrusions (Fig. 6.7a), and in the partially molten surrounding crust (Fig. 6.7b). Again, we find that larger repose times are followed by larger volcanic eruptions, with a maximum erupted volume of pure crustal melt of 1500 km^3 occurring in the case of a single giant eruption after 2 Myr (Fig. 6.7c). This increase in eruption size with repose time is not enough, however, to counter the decreased total number of volcanic eruptions in terms of

eruptive volume, and produce the same strong inverse correlation between total erupted volume over the lifetime of the system and the repose time between eruptions (Fig. 6.7d). We also compare the trend that we observe for intrusions at 7 km depth and find it nearly perfectly replicated when the basaltic intrusions accumulate at 4 km or 15 km depth, but with the expected increase in melting when the intrusions are at greater depths with higher ambient crustal temperatures (e.g. Annen et al., 2006; 2015).

6.5.5. Width of the zone of intrusion

We also investigate the effect of varying the width of the intrusive zone in the crust from the 50 km that we assume for the model represented in Fig. 6.2. This is important because the width of the crust that is subject to basalt intrusions at any given time is not very well constrained. We suspect it is comparable in size to the calderas along the hot spot track, but even those

---

Fig. 6.7 (next page). Melt production in Heat2D assuming an initial geotherm of 20°C/km, a sill accumulation rate of 7.5 km/Myr for 50 km diameter circular intrusions, which intrude overplating previous intrusions at 7 km depth (except for part **d)**. **(a)** Total melt volume in the mid-crustal sill, not including crustal melts. This material is not allowed to be erupted in these simulations, unlike in the I2VIS models. The total volume of melt steadily increases until 2 Myr, when new basalt intrusions are stopped and the system begins to cool. This increase is much greater in the models with less frequent eruptions. **(b)** Total volume of crustal melts in the system. This begins to rise approximately 0.3 Myr after the start of intrusions, as heating is more focused and efficient than in the I2VIS models because basalt intrusions always occur at exactly the same level. The total melt volume drops when there are eruptions, but not to zero because partially molted areas with less than 45% melt cannot erupt. As with mafic melts, there is much more crustal melt at any given time in the models with infrequent eruptions. **(c)** Total erupted volume as a function of time, analogous to Fig. 6.6a. When eruptions occur more rapidly, they are smaller, but the total volume is larger. **(d)** Plot of total erupted volume, the final value in the part **(c)** curves, vs. the repose time, demonstrating the trend or greater total eruptive volume with more frequent eruptions. This trend is not affected by changing the intrusion depth, though the total volume is.

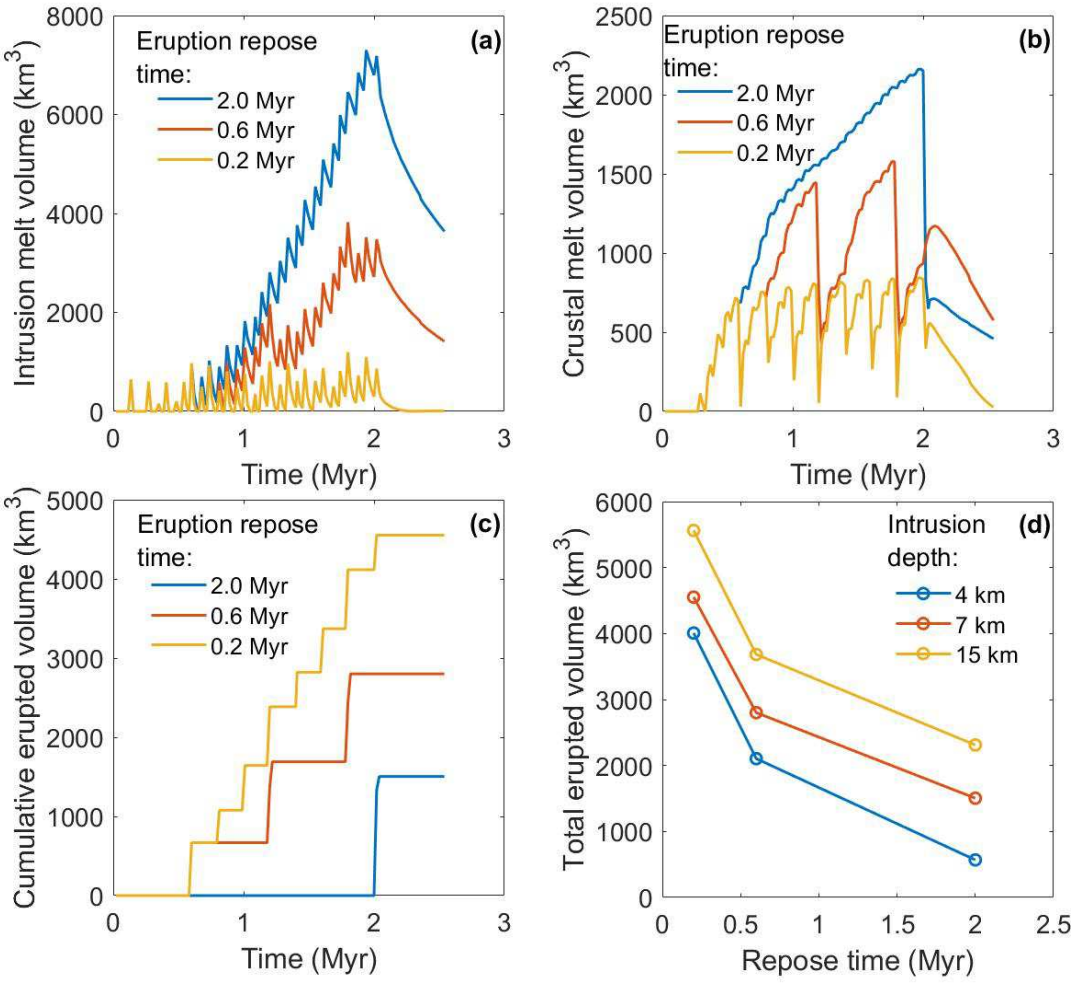

vary from 30 to 90 km in length (Christiansen, 2001; Morgan & McIntosh, 2005; Pierce & Morgan, 2009). In these cases, we keep the total volumetric flux of basaltic melts from the mantle the same, but instead spread it out over a greater length and allow the wider intrusions to grow for longer so that the same amount of crustal thickening and total mafic intrusion volume is achieved in all models. This tests for uncertainty in the width of the plume, its footprint in the crust, while preserving the volumetric intrusion rate which was constrained in Colón et al. (2018a) for the modern Yellowstone system.

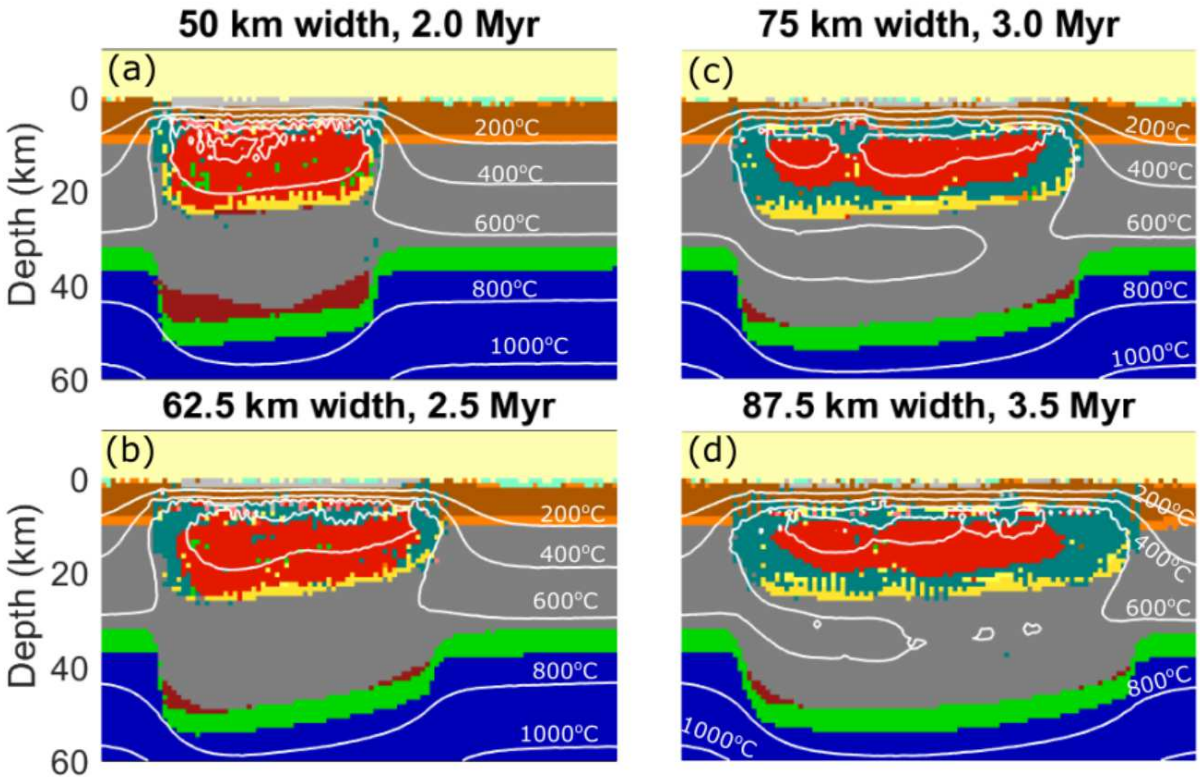

Fig. 6.8. Comparison of different intrusion widths. Models are compared at the end of the mafic intrusion time (varying between 2 and 3.5 Myr), which lasts longer for wider intrusions in order to obtain the same degree of crustal thickening given a fixed volumetric basalt flux. Part **(a)** is identical to Fig. 6.2e. Note that with increasing width, the temperature in the center of the intrusion decreases. In part **(a)** it is over 1000°C, while in part **(d)** the temperature at the center of the intrusion (>800°C unlabeled contour) is barely over 800°C. These cooler temperatures correspond with lower total eruptive volumes (less gray material at the surface) in parts **(c)** and **(d)** relative to parts **(a)** and **(b)**, as well as in Fig. 6.9 below.

We find that widening the zone of intrusion dramatically reduces the temperature of the crustal magmatic system (Fig. 6.8) and decreases the volume of erupted material (Fig. 6.9), even when controlling for the fact that the wider intrusions are allowed to accumulate for more time. This effect is nearly as dramatic as the dependence of total erupted volume on the eruption repose time, and allows us to put constraints on the width of the crust which is likely being heated at any given time by the Yellowstone plume. Additionally, this is likely evidence that in systems that are very laterally extensive, such

as the roughly 90 km-long Yellowstone caldera complex, melt input from the mantle cannot be evenly distributed and must be focused under different subsections of the volcano at any given time.

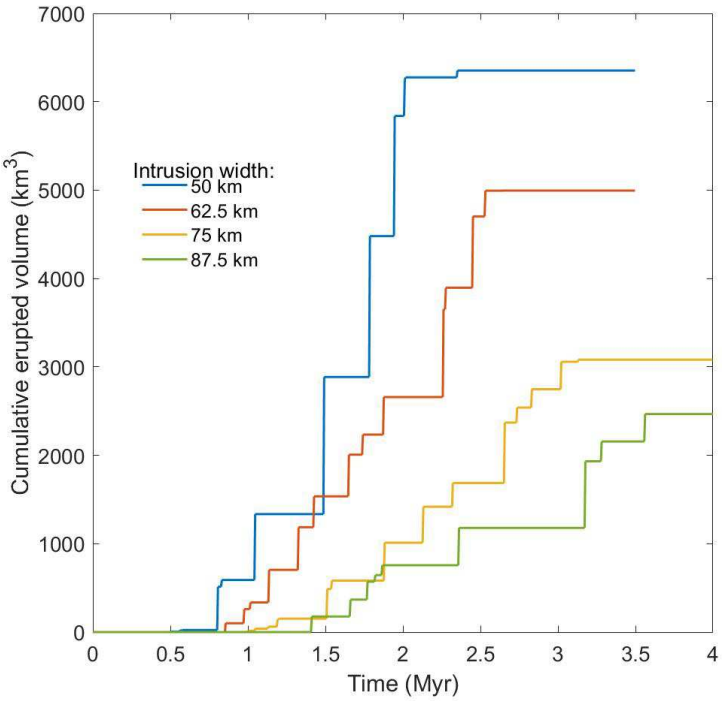

Fig. 6.9. Comparison of eruptive rates for the different intrusion width scenarios seen in Fig. 6.8. Significantly more rhyolite eruptions occur when mafic intrusions are concentrated in the narrower region of the crust. Note that eruptions cease earlier for the narrow intrusion zone models, this is because the crustal thickening is achieved earlier, as the total mafic intrusion rate remains constant.

6.5.6. Isotopic trends in erupted rhyolites

The isotopic compositions of the erupted rhyolites in the I2VIS models vary significantly over time, and broadly match many of the observations summarized by us above that have been made by previous workers working on the volcanic products of the hot spot (Colón et al., 2018a; Drew et al., 2013; Nash et al., 2006; Shervais et al., 2008; Watts et al., 2012; Wotzlaw et al., 2015). We see that the first major rhyolite eruptions have Hf isotope compositions which reflect the extensive melting of the lower crust (Fig.

6.10a), and that that signal later gradually recovers towards mantle-like values. We also find that the first rhyolitic melts to be produced and erupt are normal in their $\delta^{18}O$ values, but that these are quickly followed by eruptions of low-$\delta^{18}O$ rhyolites. This is in turn followed by a return towards normal mantle-like values in the oxygen isotopes, in step with the Hf isotpes. Fig. 6.11 shows us an alternate view of the isotopic trends, showing the stratigraphy of Hf and O isotopes as well as eruption ages for the 3 km-deep nested caldera system which develops at the surface in our standard model, which is visible as a thin gray layer at the surface in Fig. 6.2a. Fig. 6.10a shows the evolution of the Hf isotopes both of the melts being produced in the crust at any given time (solid line) and of the eruptions themselves (open circles, scaled by eruptive volume). We see that there is a good match between the crustal melts being produced at any given time and the compositions of contemporaneous eruptive products. With O isotopes (Fig. 6.10b, however, we note a significant mismatch, where the erupted compositions are considerably more normal-$\delta^{18}O$ than the melts which appear to be gereated at the same time. This plot may be somewhat misleading, however, because we have no way of directly tracking the isotopic compositions of all new melts in the crust, just what erupts, so we must compare the amounts of different types of material that are melting at any given time using the fluxes given in Fig. 6.5. This works well for Hf isotopes, which are well constrained for each rock type, but less so for oxygen, as we don not know for sure the degree of alteration of any given piece of upper crust. Since we assume all upper crust is hydrothermally altered in certain heated areas (see above), this may contribute to our underestimating the $\delta^{18}O$ value of the crustal melts, possibly explaining the disparity in Fig. 6.10b. We do note, however, that very low- $\delta^{18}O$ values do characterize many of the

zircon in rhyolites with only moderately low-$\delta^{18}O$ bulk compositions (Bindeman and Simakin, 2014; Colón et al 2015a, 2018a), confirming the involvement of very low-$\delta^{18}O$ magma batches, and thus crust, in the formation of these erupted magmas.

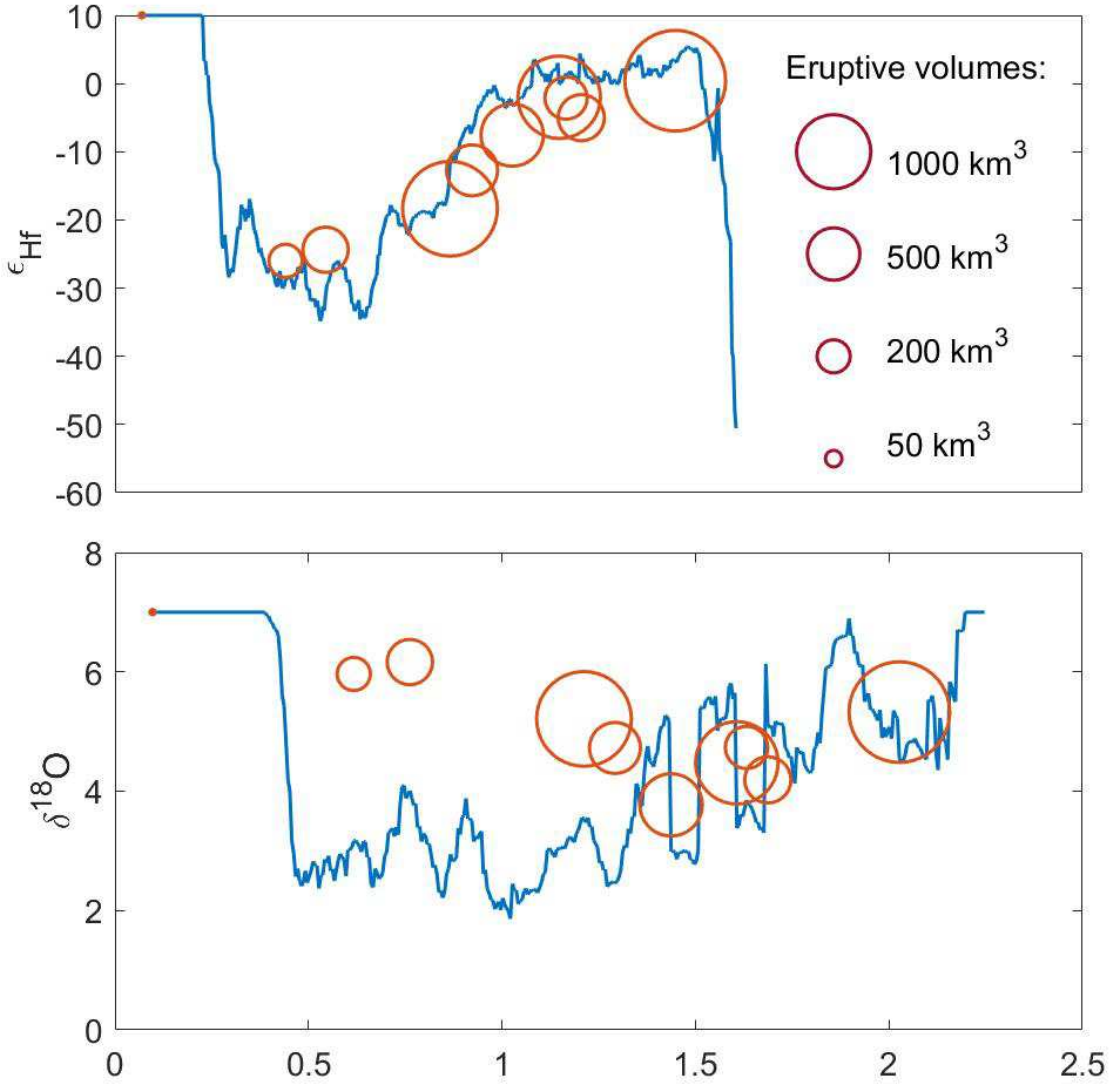

Fig. 6.10. Isotopic values of melts forming in the crust (solid lines) and the bulk values of eruptions (open circles). In the first 1 Myr, Hf isotpes are extremely unradiogenic, indicating the melting of Precambrian crust, and O isotpes of the erupted rhyolkits are normal. As the system matures, Hf isotpes become much more mantle-like, while $\delta^{18}O$ values become more depleted, indicating the involvement of hydrothermal alteration of the crust followed by melting of that same crust.

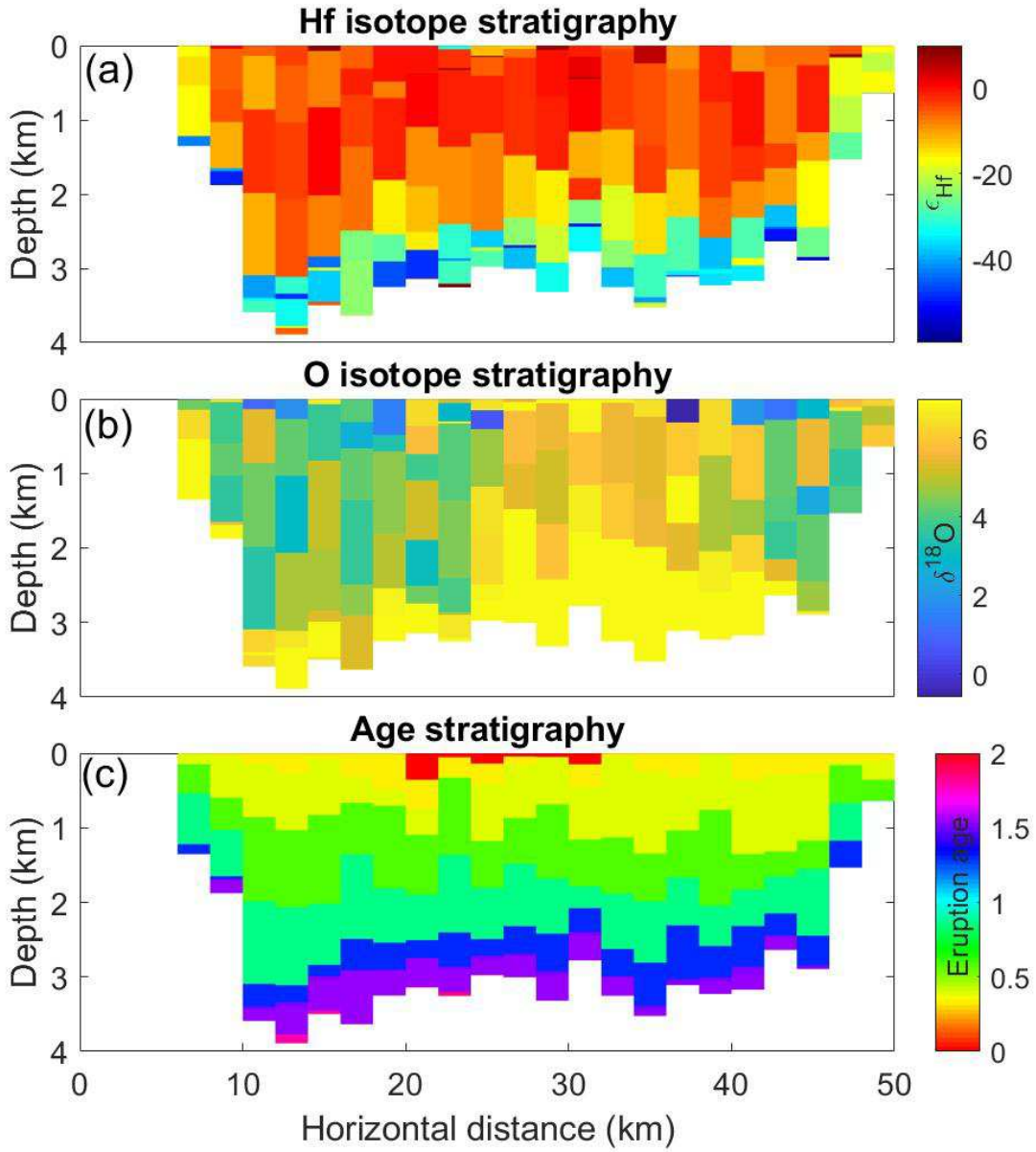

Fig. 6.11. Intracaldera isotopic stratigraphy from the I2VIS model depicted in Fig. 6.2. Values for each eruption are homogenized along vertical columns to reflect magma mixing, but not horizontally, to better show the diversity one might expect in erupted zircon phenocrysts (e.g. Colón et al., 2018a; Drew et al., 2013; Watts et al., 2011). **(a)** Hf isotope stratigraphy showing that the earliest two major eruptions had a strong imprint of Precambrian lower crustal melting, while younger rhyolites are much more mantle-like in their composition. **(b)** The O isotope stratigraphy shows less of a clear trend but low-$\delta^{18}O$ magmas are certainly more common in later eruptions. **(c)** Ages of erupted material, with the age of the youngest eruption set to zero. We can distinguish 9 eruptions, each one of which is mapped as a unique color. Notice diversity of $\delta^{18}O$ and ε_{Hf} at each level, consistent with the zircon diversity seen in the rock record (Bindeman and Simakin, 2014; Colón et al., 2018a).

6.5.7. Chemical and eruptive temperature trends in erupted rhyolites

We investigate the eruptive temperatures and silica contents for magmas erupted in our base model (Fig. 6.2), and show some preliminary results in Fig. 6.12. We find that eruptive temperatures are relatively low in our models compared to the extremely hot estimates for Yellowstone hot spot rhyolite temperatures found in Almeev et al., (2012) and Loewen et al., (2016), both of which estimate temperatures in excess of 900°C for the hottest rhyolites. This appears to be the result of an inappropriately low solidus temperature for the most evolved rhyolites, which will be corrected in future work. There is a clear trend, however, towards both hotter and more mafic magmas with time, similar to the trend observed in the central Snake River Plain by Hirt (2002) and Bonnichsen et al. (2008).

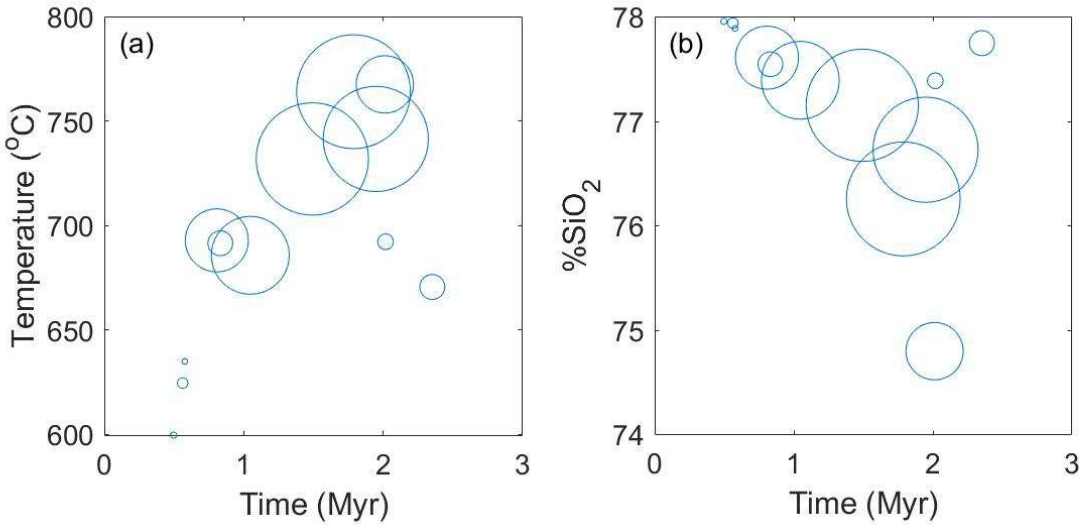

Fig. 6.12. Temperature and SiO_2 content of erupted magmas over time for a model with 50 km intrusion width and an average eruption repose time of 200 kyr. We note towards increasing eruptive temperature and decreasing silica content as the system matures. Circle sizes are as in Fig. 6.10.

6.6. Discussion

Our coupled thermomechanical magmatic models provide valuable insight into the possible origins of the compositional trends that we observe in Yellowstone hot spot track rhyolites, and provide an important new test on existing models. We investigate multiple possible methods of generating low-$\delta^{18}O$ rhyolites, and provide a possible explanation for the existence of isotopically ancient rhyolites early in the eruptive cycle of some caldera centers. We also make some preliminary observations of the types of chemical and thermal trends that occur in erupted magmas, anticipating possible further research. First, however, we reexamine some of the controls on the total volume of melt which erupts at all.

6.6.1 Eruption rate control on erupted volume

In both the I2VIS and Heat2D models, we observe that models with smaller and more frequent eruptions yield significantly greater total eruptive volume than a few extremely large eruptions (Figs. 6.6, 6.7) separated by long repose intervals. From looking at our Heat2D results in Fig. 6.7, this phenomenon might be explicable by thinking in terms of the most efficient way to produce and erupt melt. As soon as any crust is melted, additional heat to bring it above its melting temperature can be considered "wasted" heat that could be instead devoted to melting more crust. To avoid this, erupting crustal melts to the surface shortly after they form allows new cold crust to come into contact with the hot mafic intrusions. Doing this more often, as occurs in models with shorter eruption repose times, allows a greater total volume of crust to melt. By this interpretation, the largest total eruptive volumes (aka continuous eruptions) seen

in Fig. 6.7c-d may represent a thermodynamic limit to the amount of crust that can be melted by a 15-km sill complex of basalt intruded to 7 km depth over 2 Myr. In Fig. 6.7a, we note that there is much less mafic melt in the crust at any time in the scenario with more eruptions, even though it cannot erupt, suggesting that the enthalpy of the mafic intrusion is being carried away by the many eruptions, and cold subsolidus crust is constantly being brought into contact with the sill complex and cooling it.

This view is complicated, however, by the fact that in the I2VIS models there is actually slightly more crustal melt produced over time in the models with fewer eruptions; this melt simply fails to erupt. Models in I2VIS with longer repose times are characterized most clearly by smaller volcanic to plutonic ratios rather than large changes in the total volume of melt. Additionally, eruption temperatures are slightly hotter in the models with shorter repose times, but have significantly lower average temperatures in the mid-crustal sill, as well as less melt in the crust at any given time, reflecting cooling and melt removal by frequent eruptions. These observations may be reconciled by considering that basalts intruding into the crust in the I2VIS model can have temperatures well in excess of 1300°C, meaning that initial crustal melts and their fractionates can be quite hot. Long repose times between eruptions allow these melt bodies to cool, even as they consolidate and grow, allowing them to drop below the 50% melt fraction that is needed for eruptability. These large, cool crystal mushes insulate the upper crust in particular from the intruding basalts, allowing for large melt volumes but limiting eruptions. In both models, the reduction in total eruptive volume with increased repose time can be framed as a problem in efficiency, where the most eruptions can be produced by extracting rhyolitic melts to the surface as soon as they form.

Cooling rates provide the key explanation for why the wider intrusions shown in Fig. 6.8 are so much less magmatically productive, despite the total enthalpy being delivered to the crust per kilometer of horizontal model space being the same. At the very shallow depths where melting primarily takes place in these models, cooling from the surface is a critical control on the amount of rhyolite melt that can form, and reducing the rate of basalt accumulation severely limits crustal melting. Despite this, many of the eruptive centers along the Yellowstone hot spot track produced several 1000's of km^3 of rhyolite over durations significantly longer than those required by Fig. 6.9 to produce volumes of 4000 km^3 or more. This suggests that to have significant rhyolite volumes erupted over as many as 4 Myr (e.g. Bonnichsen et al., 2008; Drew et al., 2013; Knott et al., 2016), basalt intrusion rates were not the long, slow and steady rates used to make the Fig. 6.9 models, but were likely either punctuated by brief periods of much more intense intrusion and heating or where characterized by multiple separate focused areas of intrusion.

6.6.2. The origin of isotopically ancient rhyolites

The Yellowstone hot spot track is characterized by several extremely low-ε_{Hf} eruptions which require the melting of large volumes of Precambrian crust, most notably the Johnstons Camp Rhyolite in the central Snake River Plain (Colón et al., 2015), the Arbon Valley Tuff at the Picabo center (Drew et al., 2013, 2016), and Huckleberry Ridge Tuff Member C at Yellowstone (Wotzlaw et al., 2015). These eruptions all occurred within 1.0 Myr of the start of activity at their respective volcanic centers (Fig. 6.1; Colón et al., 2018a). In our models, we successfully replicate a trend of initially low-ε_{Hf}

eruptions at the start of the cycle of activity which eventually give way to more mantle-like eruptions later on (Fig. 6.10a). The crustal melts which fuel these low-ε_{Hf} eruptions are nearly entirely derived from the melting of the 2 km-thick fertile layer (orange, Fig. 6.2) which forms boundary between the upper crust and lower crust but which is isotopically ancient. If we remove this layer and replace it with more refractory "normal" lower crust (gray, Fig. 6.2), or with more upper crust, this effect vanishes and all erupted rhyolites are relatively radiogenic with respect to Hf isotopes. We therefore propose that the necessary precondition for producing an initial Precambrian crust-like eruption is a relatively fertile piece of Precambrian crust which melts before the bulk of the upper crust, largely as a function of its greater depth (Fig. 6.5, discussion below). Such rocks should be relatively rare, as the long history of Cenozoic volcanism and intrusive magmatism in the region (Chadwick, 1985; Gaschnig et al., 2011) should have provided many opportunities for such crust to be heated, melted, and stripped of its fertile components. This is likely the reason that low-ε_{Hf} magmas are not more common along the Yellowstone hot spot track, and they appear to be nearly entirely absent amongst rocks described so far from the Heise and Twin Falls centers (Fig. 6.1, Bindeman & Simakin, 2014; Colón et al., 2018a). We emphasize that we are not requiring that the lower crust be especially dry/refractory in order to avoid extensive melting, just that especially fertile material (upper crustal solidus, Fig. 6.3) be relatively scarce.

6.6.3. Caldera collapse-driven crustal melting and the production of low-$\delta^{18}O$ magmas

The fact that voluminous low-ε_{Hf} magmas only occur early in the evolution of Yellowstone volcanic centers, and the fact that low-$\delta^{18}O$ magmas become more common

with time suggests that the mix of crustal rocks that melt to produce erupted rhyolites changes with time, which we confirm in our models (Fig. 6.5). Previous workers have suggested that low-$\delta^{18}O$ rhyolites were formed by the burial and remelting of the earliest rocks in the eruptive cycle, which were hydrothermally altered shortly after emplacement by a hydrothermal system similar to the one at Yellowstone today (Bindeman and Simakin, 2014; Colón et al., 2018a; Drew et al., 2013; Watts et al., 2011). We test this model with both the Heat2D and I2VIS codes, and find that, in our models, that the first erupted rhyolites are never buried deeply enough beneath the products of later eruptions to be remelted, which likely rules out the direct remelting of large volumes of older volcanic rocks, but not of their deeper subvolcanic intrusive equivalents, which may also include such features as significantly low-$\delta^{18}O$ hydrothermally-derived porphyry deposits.

We do, however, find a clear potential role for caldera collapse in generating these isotopic trends. As is demonstrated in the illustration of a Heat2D model in Fig.

Fig. 6.13 (next page). Evolution of a Heat2D model where 15 km of basalt intrudes at a depth of 7 km over a duration of 2.0 Myr. Four eruptions occur at intervals of 0.5 Myr. Gray areas are the growing sill complex, and red areas are areas of partial melt, in both the sill and the surrounding crust. The color scheme in the surrounding crust simply corresponds to depth, but could be thought of as an analog for any isotopic tracer such as O or Hf isotopes. We see that a ~3 km-deep nested caldera complex forms, with the earliest eruptions having the "yellow" composition characteristic of the 7 km depth where melting begins, followed by eruptions with the progressively shallower crust that is advected down towards the heat source of the sill by repeated magma evacuation and caldera collapse. If shallower rocks are more low-$\delta^{18}O$, this caldera advection provides a mechanism by which erupted material could go from being normal to low-$\delta^{18}O$, despite the fact that erupted material does not reach the zone of remelting in these models.

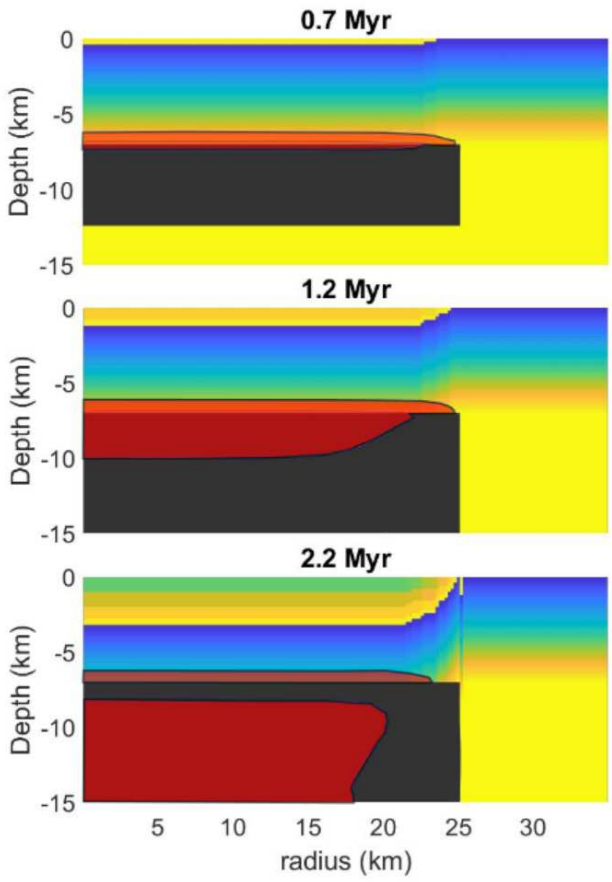

6.13, magma evacuation and caldera collapse above a mid-crustal basaltic sill complex with stable depth results in progressively shallower crust melting and erupting at the surface. The resulting 3-4 km-thick nested caldera complex will thus have the same isotopic stratigraphy as the 3-4 km of crustal material which lies above the initial depth of the growing sill complex. If the top of the mid-crustal sill lies just below the boundary between low-ε_{Hf}, but fertile, lower crust and more isotopically primitive upper crust, this transition will also manifest in the overlying eruptive stratigraphy. Similarly, if the upper crust becomes more depleted in ^{18}O with decreasing depth, the later eruptions, which result from the melting of progressively more shallow crust, should have a more low-$\delta^{18}O$ composition as well.

We see similar patterns when examining the I2VIS models. In Figs. 6.14a and 6.14b, we show the isotopic stratigraphy resulting from the I2VIS model seen in Figs. 6.2-6.4, specifically recreating the trends seen in Fig. 6.10. We see the progression towards progressively more low-$\delta^{18}O$ values and more mantle-like ε_{Hf} values with decreasing depth and age, for a series of 9 eruptions which can be clearly identified by plotting the stratigraphy of eruptive ages in Fig. 6.11c. Comparing this view to Fig. 6.13, we see that the story of progressively shallower depths of crustal melting is less clear-cut than in the Heat2D models, but the Hf isotope stratigraphy again strongly suggests that crust at deeper levels melts first (orange material in Fig. 6.2). Adding further credence to the importance of caldera collapse to producing low-$\delta^{18}O$ magmas, we note that the I2VIS model with short repose times, much greater cumulative eruptive volume (Fig. 6.9), and therefore a greater total caldera subsidence depth, produces lower-$\delta^{18}O$ eruptions towards the end of its eruptive cycle than the standard model with less total eruptive volume (Fig. 6.15). Finally, we note that we cannot entirely rule out the remelting of buried intracaldera rocks, as caldera collapse structures in nature can be much more complex than the relatively flat-bottomed, piston-like structures we see in our models, including funnel like, trapdoor, and other shapes which can produce locally very thick sections of intracaldera material (Lipman et al, 1997). These may be produced by concentrating upper crustal melts into less laterally-extensive structures through horizontal melt migration to a more roughly spherical melt body, possibly driven by an incipient magma body's effect on local dikes (e.g. Karlstrom et al., 2009). The existence of such thick intracaldera tuffs in the geologic record is also confirmed by some of the tilted and dissected sections seen in the older Basin and Range province south of the

Yellowstone hot spot track, most notably in the ~4 km thick Caetano Tuff (John et al., 2008).

6.6.4. Origin of low-$\delta^{18}O$ magmas by sill-induced splitting and burial

We here discover and describe an additional possible explanation for the origin of low-$\delta^{18}O$ magmas by examining the distribution of oxygen isotopes in the I2VIS models. In Fig. 6.14, we map the $\delta^{18}O$ values of the upper and mid crust in the standard model seen in Fig. 6.2. Recall that the I2VIS models use a very simplified scheme for hydrothermal alteration, where crust is "reset" to low-$\delta^{18}O$ values if it is weakened below an effective viscosity of 10^{22} Pa·s, has a temperature between 100 and 300°C, and exists in a geothermal gradient of greater than 40°C/km. This results in the rapid development of a zone of low-$\delta^{18}O$ crust above the mafic sill complex which is fairly mature as early as 0.25 Myr after the start of intrusions into the crust. As this layer of low-$\delta^{18}O$ material is heated from below, it can melt and erupt at the surface, as in Fig. 6.13. However, we also observe that some of this initial low-$\delta^{18}O$ crustal layer is overplated by further intrusions of basalt, and gradually advected down to depths of as great as 20 km by continued overplating of basalt over the next 2 Myr. There, it is heated to temperatures approaching the liquidus temperature of upper crust (~1000°C), where it melts and releases low-$\delta^{18}O$ material to the surface as eruptions. Tellingly, comparing Figs. 6.14 and 6.15 shows that the two areas of low-$\delta^{18}O$ material in the lower crust correspond to two equivalent areas in the overlying caldera with more low-$\delta^{18}O$ material, suggesting that this overplating and deep burial mechanism may be important for producing low-$\delta^{18}O$ rhyolites in the Yellowstone hot spot track and elsewhere. In particular, the hot and

voluminous low-$\delta^{18}O$ magmas in the central Snake River Plain may have been partially produced in this way, regardless of whether the initial alteration of the shallow crust was coeval with early hot spot magmatism (Boroughs et al., 2012; Colón et al., 2015a).

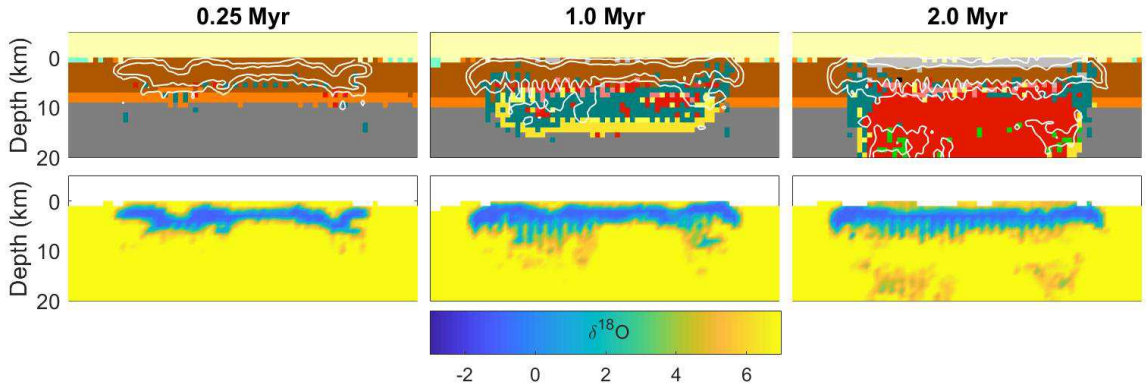

Fig. 6.14. Map of oxygen isotopes in the upper and mid crust in our standard I2VIS model. White lines are $\delta^{18}O$ contours of +4‰ and 0‰. We note that a robust layer of low-$\delta^{18}O$ crust manifests above the incipient intrusions by as early as 0.25 Myr after intrusions begin, but cannot advance to greater depths because they are too hot for hydrothermal circulation to occur. Instead, we observe that the developing mafic sill complex "bites off" part of the shallow low-$\delta^{18}O$ layer, and subsequent repeated overplating by basalt advects that material down to depths of as great as 20 km, where it is heated to temperatures of over 900°C, allowing it to melt extensively.

The eventual depletion of this material may cause a temporary "recovery" towards normal $\delta^{18}O$ values in the erupted material, as is observed in Fig. 6.5 and has been documented in both the central Snake River Plain and in the post-caldera lavas at Yellowstone (Colón et al., 2015a; Loewen and Bindeman 2015; Watts et al., 2012).

6.6.5. Combining the Hf and O isotopic records

In Fig. 6.15, we show the bulk eruption Hf and O isotope compositions from our standard (Fig. 6.2) I2VIS model and from the model with a 25 kyr average eruption

repose time (Fig. 6.6). The numerical data is superimposed on compiled zircon data from

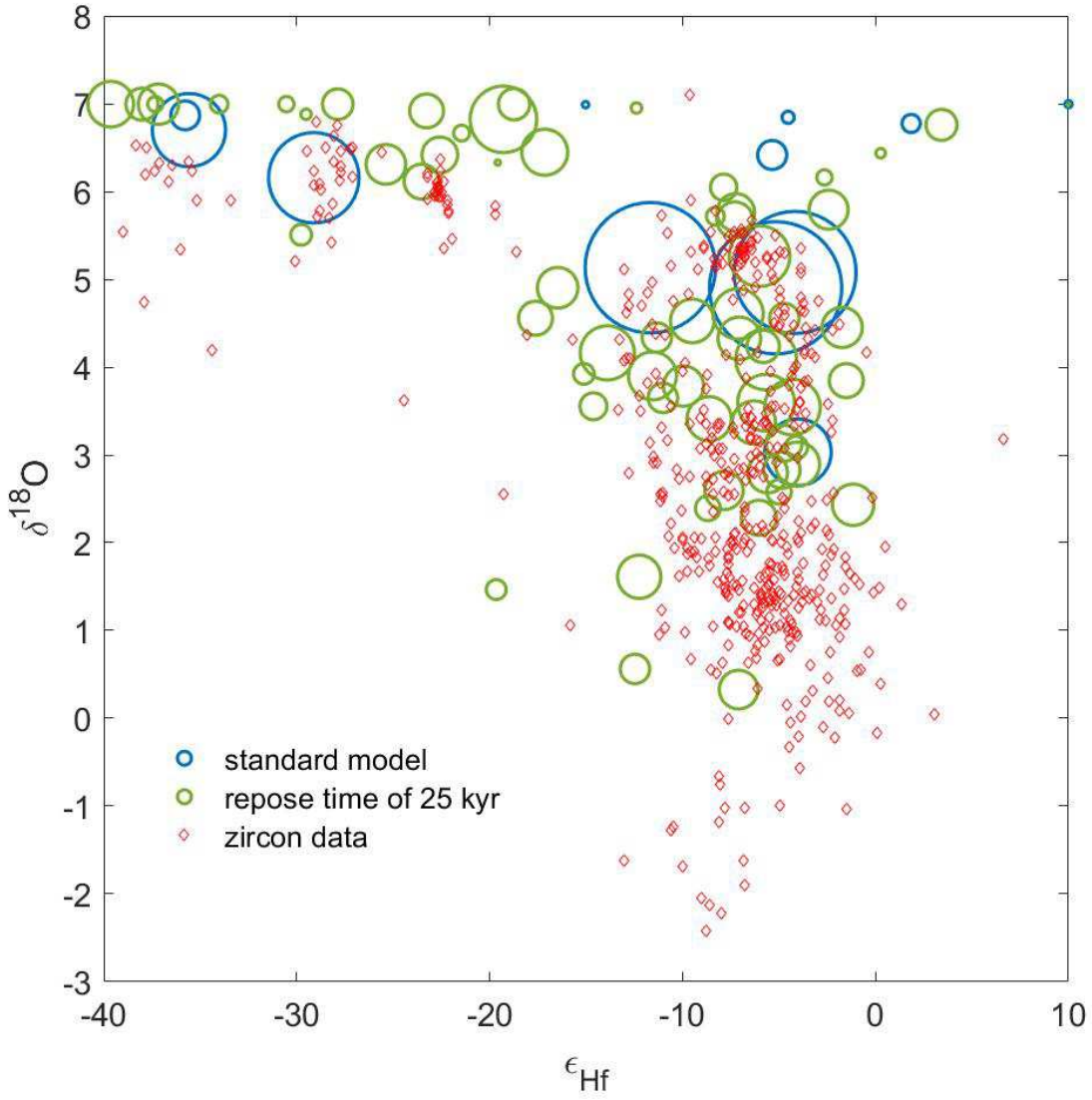

Fig. 6.15. Plot of bulk eruption $\delta^{18}O$ and ε_{Hf} values from two I2VIS model runs compared to the actual isotopic record from zircon from the Yellowstone hot spot track (Colón et al., 2018a, all centers in Fig. 6.1 except Heise represented here). The size of circles correlates to the volume of individual eruptions, as in Fig. 6.10 (same scale). We note a reasonable match between the modeled and real data, particularly for the model with the smaller repose time. We suspect that this is partially because the greater total volume erupted in a short eruption repose model (Figs. 6.6, 6.7) results in a deeper nested caldera and more opportunities to melt low-$\delta^{18}O$ crust (Figs. 6.13, 6.15), and also because the shorter eruption reposes may coincidentally result in a more realistic constant reorganization of the rhyolitic magma body above the mid-crustal sill, aiding in upper crustal melting. Finally, we observe that simultaneous eruption of low-ε_{Hf} and low-$\delta^{18}O$ magmas does not occur in our models, as it does not in the real world. Circle sizes are as in Fig. 6.10.

throughout the post-Columbia River Basalt Yellowstone hot spot track (summarized in Colón et al. 2018a), that has a characteristic L-shape, requiring three component mixing, but with a distinct lack of mixing between the low-ε_{Hf} and low-$\delta^{18}O$ end-members. Our models crudely recreate this trend, suggesting that our assumptions about magma transport and the structure of the crust are broadly correct. We can test other schemes, which result in greater accumulation of magma in the crust, or such as our models with much wider and slower-accumulating intrusions, as in Fig. 6.8, and find that they produce different shapes in Hf-O isotope space, including the production of simultaneously low-ε_{Hf} and low-$\delta^{18}O$ rhyolites, further allowing us to rule them out.

6.7. Conclusions

We use a modification of the I2VIS code of Gerya and Yuen (2003) and Colón et al. (2018a) and the Heat2D heat equation solver of Annen and Sparks (2002) and Annen et al. (2005, 2015) to investigate the controls on the compositions of erupted rhyolites at the nested caldera complexes of the Yellowstone hot spot track. We model intrusion of basalt in 50 km-wide areas for 2 Myr, resulting in a thickening of the crust by approximately 15 km. Intruding basalts primarily accumulate in a large mid-crustal sill complex at depths of 8-20 km, as described in Colón et al. (2018a), resulting in the complete reworking of the crustal column and the eruption of as much as 7000 km^3 of rhyolite. We make several new observations about the chemical and isotopic evolution of the erupted rhyolites. (1) We find that making volcanic eruptions more frequent improves the efficiency of the delivery of heat to the crust, melting more of it and significantly increasing total eruptive volumes. (2) The modeled evolution of the chemical and

isotopic compositions of the erupted rhyolites, replicate natural trends towards less isotopically ancient Hf isotopes over time. We interpret this as reflecting a regime in which early eruptions are dominated by melts of the uppermost lower crust, which we assume is isotopically ancient but fertile like the overlying younger rocks, and later eruptions are more dominated by melts of the upper crust and fractionates of the basaltic magma chamber. In all of these ways, the erupted rhyolites gradually more closely resemble the chemical and isotopic composition of the basalts from the mantle that enable their eruption, reflecting the isotopic "mantleization" (basaltification) of the entire lower and mid crust during continental hot spot volcanism.

(3) The sole exception to this trend is in the $\delta^{18}O$ values of the erupted rhyolites, which become progressively lower than the mantle-like values over time. We test models for the origin of this trend, which is well-documented in the actual volcanic products of the hot spot track (Bindeman & Simakin, 2014). Heat balance modeling suggests that remelting of already-erupted caldera-filling ignimbrites may be quite minor in the real world but melting of coeval and deeper synvolcanic low-$\delta^{18}O$ porphyries placed inside into the sill complex from above, is a viable possibility. Finally, (4), we find and describe an additional robust role for caldera collapse in generating low-$\delta^{18}O$ rhyolites, through advecting shallow pre-existing crust down to depths of 20 km or more by repeated overplating of basalt, eventually extensively melting it and producing low-$\delta^{18}O$ rhyolites, a previously unrecognized means of producing such magmas.

CHAPTER VII

SUMMARY

This dissertation investigates the origins of the voluminous rhyolite magmas from throughout the Yellowstone hotspot track, using the tools of isotope geochemistry, high-precision geochronology, and magmatic-thermomechanical computer modeling. Over the course of this research, which has resulted in four published papers with an additional paper in preparation, I come to the following main conclusions:

(1) The voluminous rhyolitic eruptions of the Yellowstone hot spot track were derived from multiple separate batches of magma which assembled into a larger common melt bodies prior to eruption, allowing homogenous rims to grow around isotopically diverse zircon cores in many cases.

(2) Erupted magma chambers are assembled rapidly, but may retain zircon crystals dating to as much as 3 Myr prior to eruption, indicating a complex history of repeated magma production, solidification, and remelting prior to its eventual eruption.

(3) The isotopic diversity in Yellowstone hot spot rhyolites can be traced to their derivation from varying proportions of four compositional end-members. These are (i) ancient Precambrian crust with normal to high-$\delta^{18}O$ values, (ii) shallow younger crust which is also normal in $\delta^{18}O$ but does not have the extreme radiogenic isotope compositions of the first composition, (iii) fractionates of mantle-derived basalt with mantle-like radiogenic and stable isotope compositions, and (iv) combinations of (ii) and (iii) which become

hydrothermally altered and remelted. Notably, we find little evidence that the Precambrian rocks undergo the same hydrothermal alteration and remelting process.

(4) At each caldera center, erupted magmas typically start out with normal $\delta^{18}O$ values and highly unradiogenic Hf isotope compositions. After this they rapidly become mantle-like in their radiogenic isotopes, as the Precambrian crustal source becomes overwhelmed by the others or is depleted. There is also a more erratic trend towards lower $\delta^{18}O$ values over time.

(5) The production of low-$\delta^{18}O$ magmas can be explained by four mechanisms: (i) pre-existing crust is already hydrothermally altered before magmatism begins, (ii) syn-magmatic fault rocks become hydrothermally altered and later melt as magmas use those same faults as conduits to the surface, (iii) caldera collapse advects upper crustal rocks down to the depth of melting, and (iv) overplating of shallow hydrothermally altered rocks by basalt sills causes them to be eventually buried at depths where they melt.

(6) Magmatism on the hot spot can be explained in terms of a 10-15 km-thick mid-crustal mafic sill complex which develops in response the trapping of rising melts by the brittle-ductile transition in the crust. Changes in the sources of crustal melts bordering this sill as is grows and melts are removed by eruption drive much of the isotopic and chemical variability of Yellowstone rhyolites.

APPENDIX A

MATERIAL FOR CHAPTER II

Contents:

A.1. Supplementary figures and tables

A.1. Supplementary figures and tables

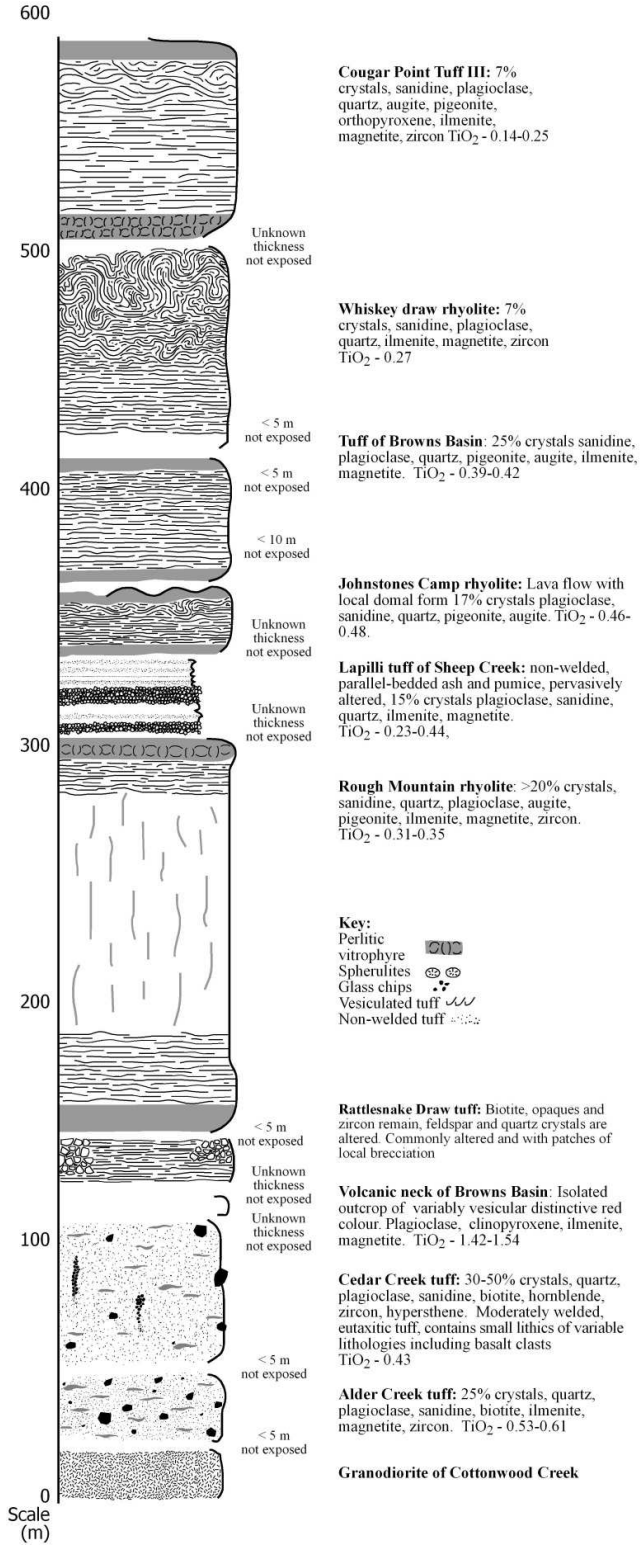

Fig. A.1. Miocene volcanic stratigraphy of the J-P Desert

Fig. A.2. This is a view of Sheep Creek Canyon with exposures of the Rough Mountain Rhyolite (foreground), with flat exposures of Cougar Point Tuff in the background.

Fig. A.3. Detail of columnar jointing in the Rough Mountain Rhyolite.

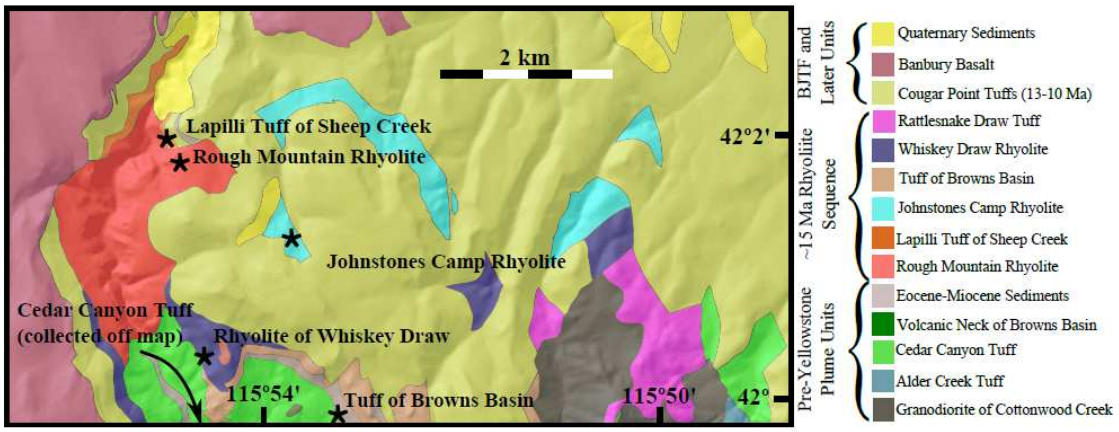

Fig. A.4. Map of J-P Desert field area**.** This map is simplified from Bernt and Bonnichsen (1982).

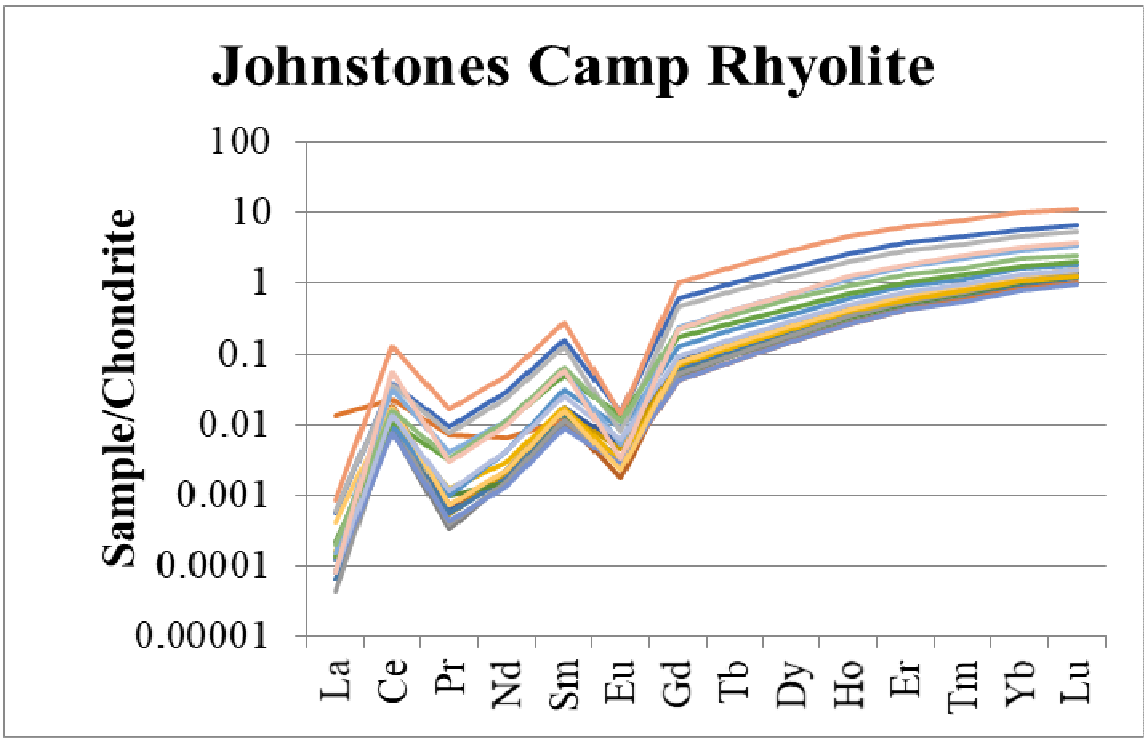

Fig. A.5. Rare earth element compositions of the Johnstons Camp Rhyolite.

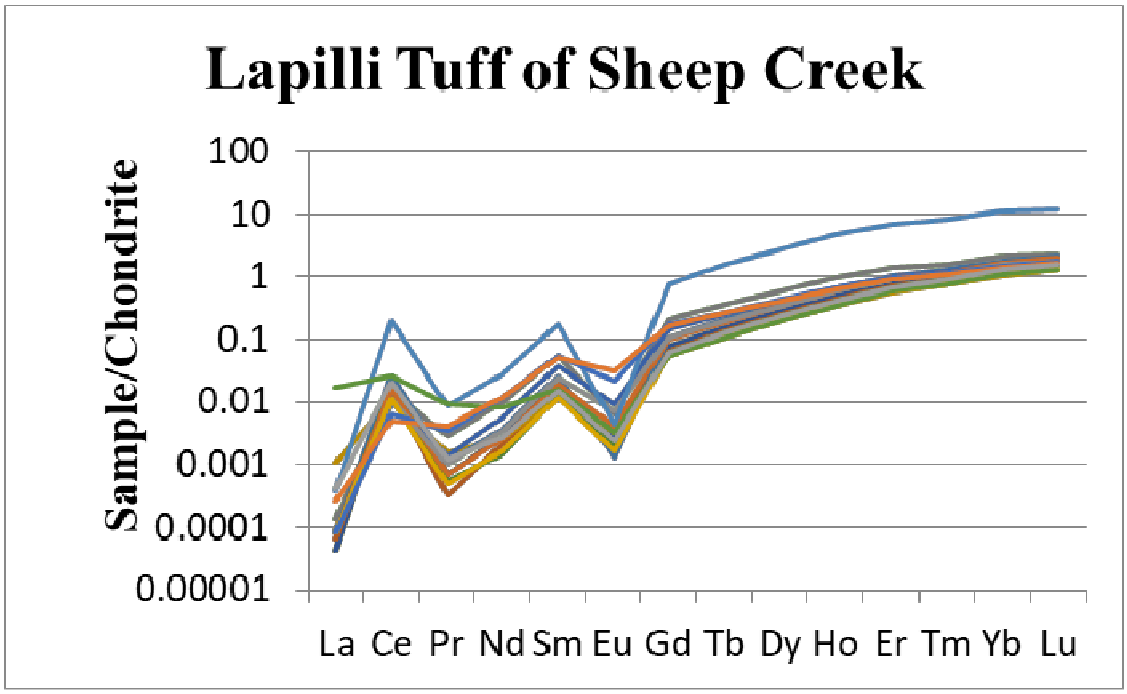

Fig. A.6. Rare earth element compositions the Lapilli Tuff of Sheep Creek.

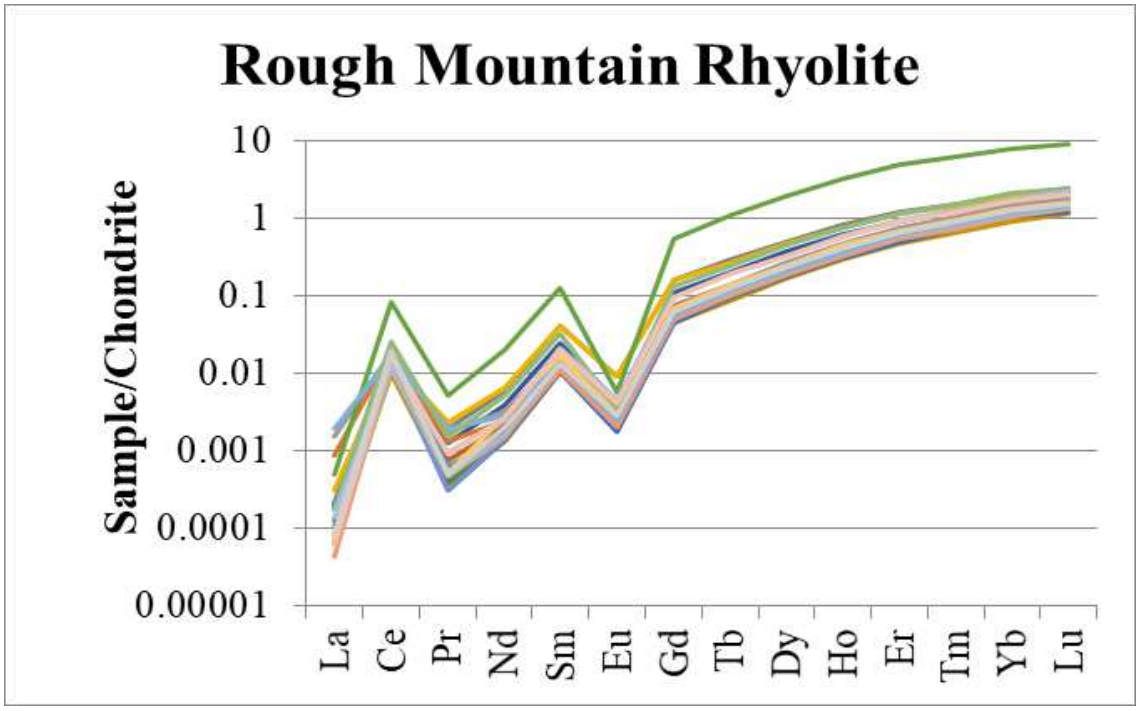

Fig. A.7. Rare earth element compositions the Rough Mountain Rhyolite.

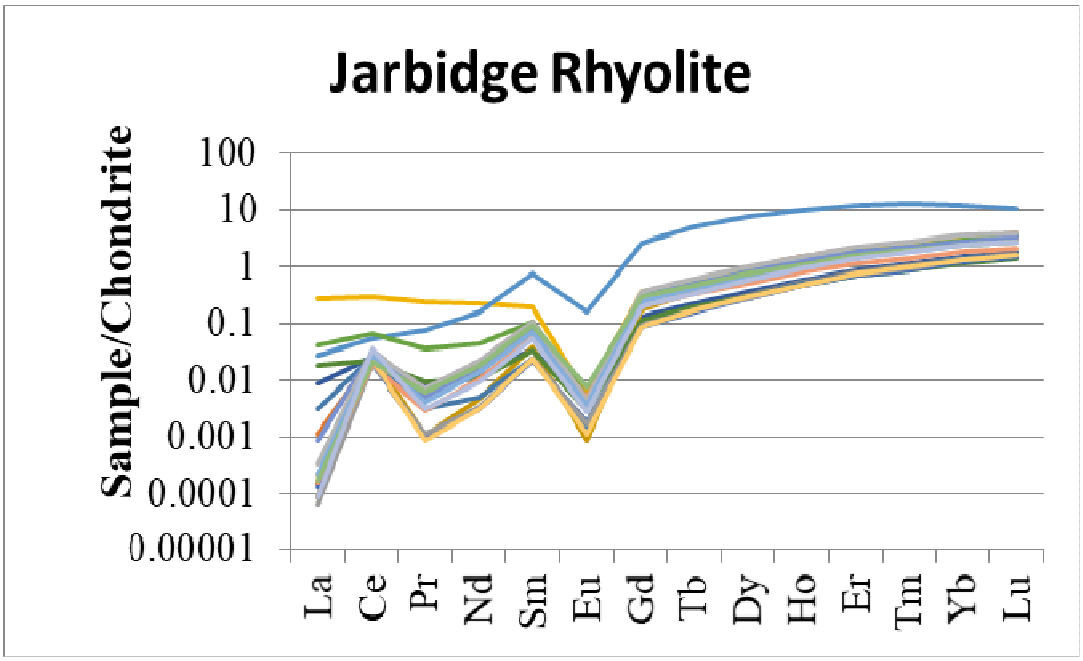

Fig. A.8. Rare earth element compositions the Jarbidge Rhyolite.

Table A.1. Zircon and GSD-1D Standard Trace Element Compositions (ICP-MS, ppm)

	Lapilli Tuff of Sheep Creek (LTSC)						
Grain #	2	3	5	6	7	9	10
^{7}Li	<1.12	<1.06	<1.17	<1.22	<1.11	<1.09	<1.37
^{24}Mg	<0.610	<0.623	<0.660	<0.684	<0.617	<0.620	<0.721
^{27}Al	<3.37	<3.32	<3.38	<3.53	<3.23	<3.25	<4.02
^{29}Si	147000	147000	147000	147000	147000	147000	147000
^{31}P	193	182	120	179	253	154	153
^{39}K	<4.93	<4.90	<5.05	<5.27	<4.87	<4.86	<6.01
^{43}Ca	<188	<197	<200	<195	<190	<189	<231
^{49}Ti	9.73	12.2	8.57	15.3	5.58	7.95	14.8
^{51}V	<0.113	<0.119	<0.128	0.255	<0.116	0.109	<0.133
^{53}Cr	<1.92	<1.93	<1.84	<1.98	<1.89	<1.92	<2.39
^{55}Mn	<0.713	<0.706	<0.743	<0.777	<0.721	<0.720	<0.912
^{57}Fe	<23.9	<23.0	<23.3	<25.6	30.6	<22.8	<28.3
^{59}Co	<0.328	<0.315	<0.349	<0.349	<0.330	<0.354	<0.438
^{85}Rb	0.166	0.127	0.326	0.146	0.184	0.138	0.176
^{88}Sr	0.324	0.226	0.340	0.224	0.376	0.332	0.298
^{89}Y	757	691	1410	532	1030	664	1020
^{90}Zr	432000	437000	443000	434000	427000	428000	423000
^{93}Nb	4.25	3.34	3.67	3.00	7.78	3.88	1.54
^{95}Mo	1.33	1.21	1.55	1.35	1.51	1.30	1.34
^{133}Cs	<0.0550	<0.0565	<0.0603	<0.0590	<0.0543	<0.0598	<0.0725
^{137}Ba	<0.155	<0.178	<0.218	<0.207	<0.184	<0.174	<0.229
^{139}La	<0.0122	<0.0154	0.0319	0.249	<0.0186	<0.0185	<0.0199
^{140}Ce	11.9	9.28	9.25	6.71	16.1	10.5	6.05
^{141}Pr	0.0656	0.0299	0.258	0.142	0.103	0.0508	0.127
^{146}Nd	1.26	0.939	4.54	1.15	1.73	0.671	2.60
^{147}Sm	2.80	2.02	7.90	1.84	3.78	1.89	5.47
^{151}Eu	0.157	0.193	0.350	0.187	0.0736	0.111	0.509
^{157}Gd	15.9	13.0	41.2	10.9	21.3	12.1	27.9
^{159}Tb	5.44	4.87	12.9	3.77	7.31	4.48	8.98
^{163}Dy	68.6	59.7	142	47.6	92.1	57.5	99.8
^{165}Ho	26.0	23.3	51.0	18.3	34.9	22.4	36.3
^{167}Er	123	111	217	87.0	163	109	158
^{169}Tm	24.6	22.8	39.3	18.3	32.1	23.0	30.4
^{173}Yb	225	212	337	168	289	213	259
^{175}Lu	41.5	39.5	57.1	31.6	52.8	39.7	47.7
^{178}Hf	8300	8230	8090	8220	9200	8850	7440
^{181}Ta	1.34	1.08	1.07	1.01	2.58	1.50	0.548
^{206}Pb	1.61	0.989	1.32	0.628	3.01	1.24	0.909
^{208}Pb	0.201	0.0868	0.161	0.119	0.441	0.151	0.150
^{232}Th	106	74.7	102	26.9	188	77.2	69.6
^{238}U	163	112	123	60.8	306	129	81.9

Table A.1 (continued).

	LTSC						
Grain #	11	12	13	15	16	17	18
^{7}Li	<1.08	<1.09	<1.20	<1.06	1.65	<1.12	<1.11
^{24}Mg	<0.772	<0.744	<0.804	<0.697	12.7	<0.724	<0.717
^{27}Al	<3.58	<3.51	<3.77	<3.39	3750	<3.63	<3.47
^{29}Si	147000	147000	147000	147000	147000	147000	147000
^{31}P	165	150	179	535	153	157	171
^{39}K	<4.70	<4.72	<5.17	<4.68	2550	<5.05	<4.89
^{43}Ca	<196	<186	<206	<182	344	<198	<195
^{49}Ti	11.3	14.2	7.60	9.55	91.2	18.8	27.6
^{51}V	0.176	<0.120	<0.127	0.776	0.171	<0.125	<0.123
^{53}Cr	<1.82	<1.82	<2.13	<1.79	<1.66	<2.00	<1.93
^{55}Mn	<0.696	<0.680	<0.744	<0.697	10.7	<0.751	<0.727
^{57}Fe	<21.9	<22.4	<24.4	29.5	619	<24.3	<23.8
^{59}Co	<0.345	<0.338	<0.385	<0.344	<0.351	<0.374	<0.370
^{85}Rb	0.232	<0.123	<0.137	1.44	11.3	0.192	0.275
^{88}Sr	0.281	0.220	0.235	0.932	1.16	0.235	0.278
^{89}Y	944	916	568	6980	557	1000	956
^{90}Zr	433000	426000	422000	430000	372000	422000	428000
^{93}Nb	2.99	1.82	3.92	95.3	4.09	1.02	0.856
^{95}Mo	1.09	1.29	1.51	1.29	1.05	1.16	1.46
^{133}Cs	<0.0572	<0.0587	<0.0631	<0.0571	0.263	<0.0544	<0.0586
^{137}Ba	<0.220	0.106	<0.224	<0.147	18.4	<0.205	<0.144
^{139}La	<0.0175	<0.0206	<0.0190	0.0903	4.00	<0.0199	0.0627
^{140}Ce	9.91	6.89	6.57	123	15.5	3.82	3.14
^{141}Pr	0.0650	0.0962	0.0441	0.783	0.877	0.313	0.380
^{146}Nd	1.16	1.56	0.738	12.6	3.81	5.32	5.43
^{147}Sm	2.84	3.66	1.76	25.2	2.34	7.95	7.36
^{151}Eu	0.233	0.398	0.0919	0.242	0.186	1.25	1.72
^{157}Gd	19.5	21.7	11.4	151	11.0	33.7	33.2
^{159}Tb	6.84	7.26	4.10	55.1	3.92	9.69	9.48
^{163}Dy	84.3	84.3	50.5	681	47.8	104	101
^{165}Ho	31.8	31.6	19.8	250	18.8	36.0	34.3
^{167}Er	150	142	94.2	1110	91.8	150	141
^{169}Tm	29.2	27.0	19.0	208	18.6	27.6	26.4
^{173}Yb	268	248	176	1770	173	239	226
^{175}Lu	49.2	44.6	32.2	292	32.3	42.6	40.6
^{178}Hf	8600	7820	8790	9270	7070	6910	6500
^{181}Ta	0.936	0.542	1.38	15.8	1.05	0.308	0.244
^{206}Pb	1.08	0.792	1.11	30.1	2.60	0.465	0.314
^{208}Pb	0.102	<0.0700	<0.0859	4.89	1.64	<0.0781	<0.0700
^{232}Th	80.7	68.0	49.9	3430	59.9	40.6	31.2
^{238}U	118	86.9	93.8	3160	92.2	45.6	35.8

Table A.1 (continued).

	LTSC	Johnstons Camp Rhyolite (JCR)					
Grain #	19	3	4	5	6	7	8
^{7}Li	<1.15	<1.10	<1.86	<1.12	<1.11	<1.10	<1.09
^{24}Mg	<0.741	<0.675	<1.08	<0.673	<0.620	<0.627	<0.652
^{27}Al	<3.49	<3.40	17.5	<3.31	<3.32	<3.32	<3.29
^{29}Si	147000	147000	147000	147000	147000	147000	147000
^{31}P	206	187	202	170	197	166	203
^{39}K	<4.97	<4.98	31.6	<4.91	<5.03	<5.01	<5.00
^{43}Ca	<200	<197	<298	<194	<191	<195	<194
^{49}Ti	7.49	13.8	7.38	12.2	11.6	11.3	11.7
^{51}V	0.235	<0.123	0.357	<0.121	<0.124	<0.121	0.145
^{53}Cr	<1.93	<1.95	<2.90	<1.88	<1.92	<1.73	<1.96
^{55}Mn	<0.738	<0.736	<1.19	<0.732	<0.730	<0.736	<0.739
^{57}Fe	<23.6	<24.1	85.6	<23.6	<24.3	<23.9	<24.0
^{59}Co	<0.350	<0.344	<0.578	<0.352	<0.359	<0.355	<0.365
^{85}Rb	0.193	0.127	0.242	<0.120	0.129	0.137	<0.122
^{88}Sr	0.320	0.224	0.244	0.210	0.178	0.288	0.232
^{89}Y	687	647	637	451	605	543	513
^{90}Zr	429000	441000	391000	467000	435000	436000	428000
^{93}Nb	3.72	2.15	3.80	1.72	1.99	1.89	3.09
^{95}Mo	1.13	1.16	1.04	1.24	1.40	1.28	1.28
^{133}Cs	<0.0566	<0.0559	<0.0933	<0.0579	<0.0575	<0.0537	<0.0554
^{137}Ba	0.225	<0.194	0.368	<0.179	<0.173	<0.169	<0.204
^{139}La	0.0955	<0.0151	<0.0384	<0.0241	<0.0216	<0.0161	0.0535
^{140}Ce	12.2	5.66	11.2	4.96	6.83	6.11	6.40
^{141}Pr	0.114	0.0559	0.0680	0.0321	0.0513	0.0530	0.0957
^{146}Nd	1.27	1.04	0.830	0.739	1.01	0.810	0.711
^{147}Sm	2.19	2.55	1.85	1.57	2.25	1.90	1.78
^{151}Eu	0.131	0.300	0.0994	0.156	0.260	0.192	0.157
^{157}Gd	12.4	15.4	13.3	9.39	13.7	11.6	10.3
^{159}Tb	4.57	5.01	4.78	3.44	4.58	3.97	3.56
^{163}Dy	58.1	60.1	58.9	38.7	53.8	47.9	45.1
^{165}Ho	22.9	22.6	22.4	15.3	21.0	18.5	17.7
^{167}Er	110	102	105	71.0	94.1	83.8	82.5
^{169}Tm	22.6	20.4	21.3	14.9	19.3	17.4	17.2
^{173}Yb	207	183	198	138	177	159	160
^{175}Lu	39.2	33.7	37.1	25.2	32.7	29.3	29.9
^{178}Hf	8790	7340	7780	8100	7580	7720	8220
^{181}Ta	1.40	0.668	1.25	0.500	0.662	0.614	1.03
^{206}Pb	1.27	0.773	1.67	0.530	0.930	0.725	0.682
^{208}Pb	0.120	0.108	<0.140	<0.0761	0.111	0.0899	<0.0680
^{232}Th	71.0	52.4	93.2	41.6	60.3	49.7	32.8
^{238}U	126	80.1	155	67.7	93.0	83.2	68.8

Table A.1 (continued).

	JCR						
Grain #	9	11	12	13	14	15	16
^{7}Li	1.36	5.23	<1.12	<1.14	<1.43	<1.15	<1.35
^{24}Mg	<0.631	6.00	<0.812	<0.824	<0.986	<0.781	<0.931
^{27}Al	<3.22	2480	<3.69	3.87	<4.51	<3.65	<4.12
^{29}Si	147000	147000	147000	147000	147000	147000	147000
^{31}P	429	176	243	161	167	220	135
^{39}K	<4.96	2060	5.91	5.59	<6.37	<5.19	<5.93
^{43}Ca	<186	<196	<197	<198	<249	<199	<232
^{49}Ti	10.7	36.0	12.6	11.1	12.5	13.8	9.37
^{51}V	1.85	<0.127	<0.124	0.523	<0.160	<0.126	<0.156
^{53}Cr	<1.77	<1.74	<1.94	<1.82	<2.59	<1.72	<2.26
^{55}Mn	<0.740	5.33	<0.713	<0.710	<0.921	<0.740	<0.841
^{57}Fe	<24.2	530	<24.5	<24.1	<29.8	<23.2	<26.4
^{59}Co	<0.354	<0.372	<0.377	<0.362	<0.465	<0.377	<0.435
^{85}Rb	0.822	8.36	<0.115	0.155	0.184	0.162	<0.147
^{88}Sr	0.601	0.919	0.213	0.258	0.305	0.376	0.214
^{89}Y	3950	424	548	597	967	1090	413
^{90}Zr	455000	404000	443000	448000	491000	446000	442000
^{93}Nb	6.79	3.17	2.87	2.44	1.87	1.97	1.37
^{95}Mo	1.32	1.42	1.25	1.30	1.29	1.41	1.04
^{133}Cs	<0.0618	0.253	<0.0577	<0.0572	<0.0715	<0.0576	<0.0631
^{137}Ba	<0.171	19.1	<0.201	<0.180	<0.313	<0.192	<0.229
^{139}La	0.133	3.17	<0.0118	0.0388	<0.0327	0.0325	<0.0248
^{140}Ce	22.9	13.7	7.17	6.00	6.16	6.91	4.71
^{141}Pr	0.889	0.682	0.0367	0.115	0.0924	0.297	0.0408
^{146}Nd	13.3	2.96	0.739	1.41	1.95	5.00	0.621
^{147}Sm	22.7	1.76	1.67	2.57	4.62	7.21	1.31
^{151}Eu	0.869	0.150	0.163	0.173	0.505	0.772	0.158
^{157}Gd	120	8.55	10.3	14.1	24.9	33.6	8.56
^{159}Tb	36.2	2.91	3.60	4.59	7.94	10.2	2.87
^{163}Dy	400	35.6	45.8	56.2	88.6	109	36.2
^{165}Ho	141	14.6	18.7	21.2	33.0	38.4	14.2
^{167}Er	590	67.0	88.8	92.7	142	166	66.0
^{169}Tm	112	14.1	18.8	19.1	28.0	31.8	13.6
^{173}Yb	921	132	176	170	257	275	127
^{175}Lu	160	24.7	33.1	31.2	44.2	49.3	23.9
^{178}Hf	7530	7700	8470	8440	8220	7450	8270
^{181}Ta	1.79	0.788	1.07	0.827	0.560	0.654	0.447
^{206}Pb	6.36	1.95	0.679	0.883	0.659	0.881	0.565
^{208}Pb	0.979	1.43	<0.0741	0.139	0.131	0.107	<0.0836
^{232}Th	739	38.1	35.9	51.8	62.9	80.9	31.4
^{238}U	679	62.1	69.6	83.9	86.9	99.3	62.7

Table A.1 (continued).

	JCR						
Grain #	17	18	19	20	21	22	23
^{7}Li	20.9	<1.13	<1.26	3.99	<1.21	<1.38	<1.13
^{24}Mg	<0.719	<0.691	<0.800	<0.832	<0.749	<0.863	<0.720
^{27}Al	5.21	<3.39	<3.74	<3.90	<3.54	<4.07	<3.35
^{29}Si	147000	147000	147000	147000	147000	147000	147000
^{31}P	552	341	168	351	185	201	368
^{39}K	<4.93	<4.96	<5.57	<5.77	<5.30	8.13	<5.09
^{43}Ca	<201	<196	<212	<234	<203	<242	<203
^{49}Ti	7.60	10.6	11.7	10.7	9.67	11.3	10.1
^{51}V	0.571	0.335	0.167	0.520	0.167	0.178	0.295
^{53}Cr	<1.91	<1.76	<2.06	<2.08	<2.03	<2.29	<2.00
^{55}Mn	<0.723	<0.719	<0.806	<0.841	<0.765	<0.899	<0.753
^{57}Fe	<21.1	<21.1	<23.5	<23.7	<22.1	<25.1	<20.5
^{59}Co	<0.355	<0.364	<0.398	<0.417	<0.383	<0.438	<0.370
^{85}Rb	1.19	0.562	0.185	0.351	0.256	0.260	0.448
^{88}Sr	0.851	0.492	0.333	0.308	0.270	0.212	0.418
^{89}Y	6830	3030	677	1770	1410	749	1840
^{90}Zr	467000	454000	452000	431000	446000	422000	443000
^{93}Nb	17.6	6.61	2.44	5.34	1.98	1.88	11.0
^{95}Mo	1.56	1.21	1.19	1.30	1.24	1.17	1.49
^{133}Cs	<0.0538	<0.0585	<0.0684	<0.0656	<0.0552	<0.0744	<0.0534
^{137}Ba	<0.214	<0.194	<0.250	<0.247	<0.222	<0.199	<0.187
^{139}La	0.200	0.142	0.0968	0.0372	0.0475	<0.0205	<0.0175
^{140}Ce	77.0	21.8	11.0	18.8	9.68	8.41	33.1
^{141}Pr	1.54	0.726	0.0696	0.380	0.314	0.107	0.280
^{146}Nd	22.8	11.1	1.08	5.38	5.22	2.00	4.60
^{147}Sm	40.1	18.4	2.40	8.63	9.71	3.78	8.70
^{151}Eu	0.818	0.456	0.130	0.296	0.630	0.355	0.186
^{157}Gd	203	92.8	15.0	48.0	45.2	18.8	44.8
^{159}Tb	62.4	27.9	4.97	14.9	13.2	6.01	15.0
^{163}Dy	692	309	60.6	170	146	71.8	175
^{165}Ho	245	110	23.4	62.9	50.8	26.1	66.4
^{167}Er	1020	469	107	270	213	116	294
^{169}Tm	193	89.2	22.3	54.3	40.8	23.9	59.0
^{173}Yb	1570	747	202	457	355	207	514
^{175}Lu	267	130	37.0	82.9	61.0	38.0	91.6
^{178}Hf	9430	7820	8890	7740	8100	7760	8820
^{181}Ta	4.30	1.92	0.803	1.82	0.591	0.606	3.60
^{206}Pb	14.8	5.38	1.13	4.54	1.43	1.28	9.20
^{208}Pb	2.49	0.759	0.0793	0.674	0.186	0.105	1.68
^{232}Th	1910	577	68.3	508	128	79.5	1190
^{238}U	1700	596	131	517	154	119	946

Table A.1 (continued).

	JCR	Rough Mountain Rhyolite (RMR)					
Grain #	24	1	2	3	4	5	7
^{7}Li	<1.35	<1.13	<1.17	<1.10	<1.14	<1.08	<1.60
^{24}Mg	<0.899	<0.716	<0.745	<0.681	<0.694	<0.693	<1.22
^{27}Al	5.39	<3.33	<3.32	<3.26	<3.29	<3.30	<5.00
^{29}Si	147000	147000	147000	147000	147000	147000	147000
^{31}P	165	198	193	223	151	176	175
^{39}K	19.3	<5.13	<5.22	<5.05	<5.15	<5.11	<6.89
^{43}Ca	<251	<202	<197	<188	<209	<201	<287
^{49}Ti	14.2	14.1	14.2	14.9	15.6	10.9	12.7
^{51}V	0.249	0.609	0.280	0.453	<0.127	0.169	<0.188
^{53}Cr	<2.39	<1.80	<1.87	<1.77	<1.89	<1.96	<2.67
^{55}Mn	<0.906	<0.749	<0.772	<0.735	<0.762	<0.760	<0.976
^{57}Fe	<24.5	23.4	<20.4	<18.6	<19.0	<18.5	<26.3
^{59}Co	<0.465	<0.388	<0.404	<0.371	<0.378	<0.399	<0.550
^{85}Rb	0.177	0.197	0.207	0.150	0.163	<0.124	<0.173
^{88}Sr	0.264	0.328	0.295	0.264	0.320	0.263	<0.149
^{89}Y	1100	953	669	1230	458	639	582
^{90}Zr	450000	431000	426000	435000	431000	422000	401000
^{93}Nb	2.02	4.85	3.59	2.78	2.34	3.37	3.16
^{95}Mo	1.42	1.24	1.27	1.45	1.37	1.28	1.21
^{133}Cs	<0.0659	0.0906	<0.0580	<0.0553	<0.0555	<0.0619	<0.0835
^{137}Ba	<0.277	<0.190	<0.193	<0.187	<0.160	<0.132	<0.319
^{139}La	0.141	0.0502	0.0439	0.0251	0.0153	<0.0167	<0.0295
^{140}Ce	9.01	9.60	9.12	8.49	6.11	9.73	8.72
^{141}Pr	0.248	0.117	0.0696	0.179	0.0340	0.0399	0.0365
^{146}Nd	3.71	1.80	0.962	2.73	0.593	0.838	0.678
^{147}Sm	6.51	3.60	1.87	5.98	1.52	2.01	1.84
^{151}Eu	0.492	0.238	0.218	0.508	0.159	0.171	0.147
^{157}Gd	32.9	21.5	13.4	31.4	8.68	11.9	10.4
^{159}Tb	9.80	7.34	4.73	10.3	3.10	4.38	3.78
^{163}Dy	109	89.8	59.6	121	40.2	56.2	53.3
^{165}Ho	38.7	33.2	23.0	43.9	15.7	22.0	20.5
^{167}Er	162	147	110	190	74.7	105	94.2
^{169}Tm	33.2	30.8	22.6	38.0	16.0	22.1	19.7
^{173}Yb	285	269	210	327	146	202	184
^{175}Lu	49.8	50.4	38.6	59.1	28.0	38.9	35.5
^{178}Hf	8000	8440	8300	7990	8430	8390	8280
^{181}Ta	0.624	1.44	1.12	0.922	0.821	1.20	1.11
^{206}Pb	1.14	1.19	0.859	0.992	0.538	1.04	1.15
^{208}Pb	0.148	0.0837	0.115	0.103	<0.0769	0.113	<0.0982
^{232}Th	103	72.8	54.7	78.0	27.0	61.0	48.5
^{238}U	135	125	96.1	112	54.5	102	91.3

Table A.1 (continued).

	RMR						
Grain #	8	9	10	11	12	14	15
^{7}Li	<1.38	<1.14	<1.11	<1.62	<1.13	<1.83	<1.64
^{24}Mg	<1.06	<0.855	<0.837	<1.15	<0.812	7.72	<1.13
^{27}Al	<4.36	<3.62	23.3	<4.93	<3.55	<5.45	<4.98
^{29}Si	147000	147000	147000	147000	147000	147000	147000
^{31}P	144	204	219	228	177	518	164
^{39}K	<6.10	<5.10	14.8	<6.97	<5.08	<7.96	<7.26
^{43}Ca	<249	<200	<205	<294	<200	<323	<310
^{49}Ti	13.0	13.4	11.5	13.5	12.2	24.5	10.5
^{51}V	<0.156	0.254	0.190	0.730	0.141	6.24	<0.174
^{53}Cr	<2.42	<2.08	<1.96	<2.66	<2.03	<3.05	3.32
^{55}Mn	<0.867	<0.745	<0.733	<1.02	<0.765	3.58	<1.09
^{57}Fe	<22.7	<19.4	<20.5	<28.3	<21.1	435	<32.8
^{59}Co	<0.479	<0.418	<0.389	<0.574	<0.403	<0.639	<0.585
^{85}Rb	<0.157	0.170	0.196	0.181	<0.123	1.08	<0.164
^{88}Sr	0.263	0.241	0.422	0.331	0.271	0.691	0.186
^{89}Y	481	708	749	1160	624	4960	592
^{90}Zr	450000	416000	420000	382000	410000	377000	379000
^{93}Nb	3.05	3.56	3.52	2.82	3.27	31.8	2.26
^{95}Mo	1.36	1.05	1.37	0.897	1.13	1.15	1.23
^{133}Cs	<0.0656	<0.0564	<0.0557	<0.0805	<0.0612	<0.0979	<0.0791
^{137}Ba	<0.299	<0.229	<0.226	<0.276	<0.169	<0.413	<0.384
^{139}La	<0.0219	0.207	0.353	0.0722	0.0491	0.117	<0.0194
^{140}Ce	8.96	11.9	11.0	8.79	9.46	49.4	7.57
^{141}Pr	0.0284	0.122	0.161	0.218	0.0572	0.484	0.0290
^{146}Nd	0.645	1.12	1.46	3.02	0.749	9.20	0.672
^{147}Sm	1.51	2.20	2.35	5.88	1.90	18.7	1.83
^{151}Eu	0.100	0.172	0.221	0.507	0.141	0.313	0.135
^{157}Gd	8.83	14.6	14.5	31.4	11.9	106	10.5
^{159}Tb	3.40	5.06	5.08	9.79	4.22	38.9	4.10
^{163}Dy	43.3	62.9	65.9	116	55.1	472	50.1
^{165}Ho	17.1	24.4	25.4	40.7	21.2	176	19.7
^{167}Er	77.3	114	121	180	98.9	779	94.1
^{169}Tm	17.3	23.6	25.2	36.3	21.2	151	19.9
^{173}Yb	164	216	237	305	196	1280	181
^{175}Lu	29.6	41.1	44.4	57.0	36.8	224	35.1
^{178}Hf	9220	8520	8410	7480	8680	8750	8130
^{181}Ta	0.856	1.08	1.20	0.951	1.10	7.94	0.685
^{206}Pb	0.443	1.06	1.15	0.997	1.00	17.2	0.888
^{208}Pb	<0.105	<0.0769	0.188	<0.109	<0.0748	1.91	<0.107
^{232}Th	42.3	75.9	74.9	76.6	54.9	1180	48.6
^{238}U	81.8	117	110	109	93.6	1590	82.5

Table A.1 (continued).

	RMR						
Grain #	16	17	20	21	22	26	27
^{7}Li	<1.14	<1.09	<1.13	<1.11	<1.08	<1.09	<1.10
^{24}Mg	<0.768	<0.786	<0.788	<0.780	<0.731	<0.963	<0.959
^{27}Al	<3.42	<3.38	<3.37	<3.33	9.29	7.04	<3.71
^{29}Si	147000	147000	147000	147000	147000	147000	147000
^{31}P	168	168	189	192	219	209	187
^{39}K	<5.08	<5.05	<5.07	<5.06	6.45	13.9	<4.97
^{43}Ca	<213	<204	<204	<209	<196	<212	<211
^{49}Ti	13.7	16.4	13.0	11.3	10.8	11.5	15.9
^{51}V	<0.119	0.330	0.339	0.193	0.551	0.748	0.532
^{53}Cr	<1.85	<2.08	<1.95	<1.92	<1.87	<1.88	<2.02
^{55}Mn	<0.760	<0.756	<0.775	<0.771	<0.757	<0.742	<0.736
^{57}Fe	<23.0	<23.0	<25.5	<27.0	28.5	44.3	<35.0
^{59}Co	<0.415	<0.374	<0.408	<0.412	<0.378	<0.430	<0.427
^{85}Rb	0.116	<0.123	0.199	0.208	0.329	0.206	0.129
^{88}Sr	0.287	0.294	0.320	0.290	0.329	0.302	0.308
^{89}Y	518	561	693	607	1150	941	923
^{90}Zr	408000	403000	420000	399000	425000	393000	404000
^{93}Nb	3.21	2.36	3.59	3.09	5.12	6.42	3.15
^{95}Mo	1.20	1.42	1.34	1.42	1.34	1.23	1.38
^{133}Cs	<0.0516	<0.0547	<0.0591	<0.0565	<0.0508	<0.0577	<0.0565
^{137}Ba	<0.192	<0.201	<0.175	<0.229	<0.249	0.325	<0.165
^{139}La	<0.0136	<0.0159	<0.0207	0.454	0.0420	0.0332	<0.0152
^{140}Ce	8.54	7.04	10.1	10.3	15.5	8.39	10.1
^{141}Pr	0.0436	0.0438	0.0475	0.177	0.142	0.0877	0.0851
^{146}Nd	0.702	0.722	1.31	1.30	2.35	1.17	1.23
^{147}Sm	1.60	1.94	2.43	1.97	4.84	3.07	3.00
^{151}Eu	0.115	0.209	0.162	0.143	0.197	0.250	0.235
^{157}Gd	9.57	11.2	13.3	11.3	25.9	18.5	19.0
^{159}Tb	3.57	3.90	4.90	4.26	8.89	6.76	6.77
^{163}Dy	44.7	48.7	60.1	52.5	107	80.4	79.8
^{165}Ho	17.5	19.3	24.3	20.5	40.7	31.8	31.0
^{167}Er	86.2	92.4	110	99.5	183	149	146
^{169}Tm	17.8	18.8	22.7	20.9	37.3	30.2	29.3
^{173}Yb	164	173	207	191	329	280	266
^{175}Lu	31.9	33.0	39.3	36.0	59.9	52.8	49.7
^{178}Hf	8780	8120	8970	8890	9070	8560	8750
^{181}Ta	1.10	0.730	1.17	1.10	1.80	1.79	0.970
^{206}Pb	0.737	0.695	1.02	0.760	1.85	1.61	1.07
^{208}Pb	0.0828	<0.0827	0.0891	<0.0718	0.255	0.144	<0.0802
^{232}Th	41.7	41.9	73.1	51.3	160	81.1	67.8
^{238}U	77.7	65.9	108	91.9	208	126	101

Table A.1 (continued).

	RMR	Jarbidge Rhyolite (JR)					
Grain #	28	1	2	5	7	8	9
^{7}Li	<1.10	<1.13	<1.08	<1.17	<1.12	<1.10	<1.23
^{24}Mg	<0.897	<0.907	<0.824	<0.889	<0.831	12.0	2.37
^{27}Al	<3.67	<3.67	<3.60	<3.54	<3.48	120	3490
^{29}Si	147000	147000	147000	147000	147000	147000	147000
^{31}P	190	242	173	166	190	220	117
^{39}K	<4.95	<4.99	<4.93	<4.98	<4.91	99.8	2340
^{43}Ca	<198	<217	<211	<221	<212	<214	<232
^{49}Ti	12.8	9.73	7.00	6.72	4.78	9.73	15.2
^{51}V	0.194	<0.127	<0.125	<0.121	0.143	<0.117	<0.138
^{53}Cr	<1.78	<1.99	<2.00	<1.84	<2.06	<2.04	<2.09
^{55}Mn	<0.746	<0.774	<0.762	<0.776	<0.773	1.15	1.68
^{57}Fe	<34.4	<34.3	<33.7	<35.1	<33.6	161	154
^{59}Co	<0.420	<0.422	<0.404	<0.422	<0.428	<0.418	<0.427
^{85}Rb	0.140	0.177	0.418	0.148	0.310	0.662	11.0
^{88}Sr	0.347	0.325	0.498	0.380	0.466	0.390	1.60
^{89}Y	650	934	2210	831	1560	800	756
^{90}Zr	408000	402000	418000	397000	412000	405000	364000
^{93}Nb	3.87	3.94	4.44	6.13	21.2	5.29	3.49
^{95}Mo	1.04	1.62	1.38	1.35	1.09	1.18	1.01
^{133}Cs	<0.0568	<0.0559	<0.0537	<0.0565	<0.0575	<0.0583	0.150
^{137}Ba	<0.221	<0.193	<0.231	<0.233	<0.196	<0.213	18.4
^{139}La	<0.0198	2.03	0.0338	<0.0189	<0.0174	0.732	4.33
^{140}Ce	12.0	16.1	18.7	15.6	19.0	15.2	14.0
^{141}Pr	0.0461	0.710	0.601	0.0894	0.0956	0.283	0.883
^{146}Nd	0.941	5.23	9.54	1.49	2.21	2.34	4.77
^{147}Sm	1.95	5.31	15.6	3.49	5.79	3.64	4.98
^{151}Eu	0.158	0.177	0.218	0.0907	0.0487	0.0732	0.161
^{157}Gd	12.2	25.8	68.6	20.3	35.2	19.7	23.0
^{159}Tb	4.53	8.02	20.5	6.78	12.7	6.39	6.98
^{163}Dy	55.8	89.9	224	78.8	151	74.1	74.4
^{165}Ho	22.0	32.5	79.8	29.0	55.4	27.8	26.7
^{167}Er	104	141	347	133	246	125	116
^{169}Tm	21.7	27.5	62.4	26.2	48.7	25.1	21.9
^{173}Yb	200	238	522	229	415	225	187
^{175}Lu	37.7	44.1	94.3	42.4	73.7	40.3	34.5
^{178}Hf	9000	8960	9440	9550	11000	9370	7390
^{181}Ta	1.17	1.39	1.82	2.12	5.82	1.85	0.846
^{206}Pb	1.04	2.01	4.95	3.23	9.66	3.60	3.94
^{208}Pb	0.104	0.187	0.596	0.213	0.917	0.369	2.62
^{232}Th	72.9	146	424	189	677	179	104
^{238}U	116	212	529	344	974	333	141

Table A.1 (continued).

	JR						
Grain #	11	12	13	14	16	17	18
^{7}Li	<1.15	<1.12	<1.16	<1.14	1.70	<1.12	<1.18
^{24}Mg	<0.778	<0.780	<0.817	<0.787	0.949	<0.768	<0.942
^{27}Al	<3.49	<3.42	<3.45	82.3	50.0	<3.43	<3.83
^{29}Si	147000	147000	147000	147000	147000	147000	147000
^{31}P	173	178	122	707	4200	286	141
^{39}K	<4.97	<4.95	<4.97	97.5	237	<4.97	<4.88
^{43}Ca	<214	<209	<217	1750	<224	597	<237
^{49}Ti	7.81	8.44	8.57	6.75	79.4	7.63	6.44
^{51}V	<0.121	<0.128	<0.129	<0.121	0.819	0.132	0.203
^{53}Cr	<2.15	<1.96	<2.20	<1.97	<2.21	<2.09	<2.10
^{55}Mn	<0.798	<0.782	<0.802	4.68	<0.836	0.808	<0.782
^{57}Fe	<34.5	<33.7	<34.8	41.5	37.8	<34.8	<33.0
^{59}Co	<0.415	<0.417	<0.426	<0.410	<0.430	<0.434	<0.439
^{85}Rb	<0.126	0.394	0.177	1.11	2.78	0.444	0.232
^{88}Sr	0.282	0.425	0.340	0.883	2.63	0.523	0.396
^{89}Y	724	1900	743	2000	20400	1980	1930
^{90}Zr	415000	411000	413000	418000	425000	437000	426000
^{93}Nb	4.62	4.69	4.41	7.04	4.26	5.13	4.00
^{95}Mo	1.34	1.13	1.08	1.43	1.67	1.23	1.38
^{133}Cs	<0.0556	<0.0535	<0.0592	<0.0565	<0.0604	<0.0535	<0.0616
^{137}Ba	<0.197	<0.202	<0.203	0.180	2.53	<0.198	<0.166
^{139}La	0.0295	0.272	<0.0152	67.1	6.33	9.43	0.198
^{140}Ce	11.8	15.6	12.2	182	33.9	40.0	19.2
^{141}Pr	0.0982	0.533	0.102	21.9	7.08	3.43	0.479
^{146}Nd	1.41	7.35	1.49	101	71.3	20.8	7.66
^{147}Sm	3.32	13.1	3.43	29.2	116	15.7	13.0
^{151}Eu	0.105	0.369	0.0973	0.300	8.74	0.280	0.222
^{157}Gd	17.2	63.4	18.7	73.0	501	60.8	61.8
^{159}Tb	5.73	19.1	6.06	19.5	185	18.5	18.7
^{163}Dy	68.4	199	70.1	209	1960	201	203
^{165}Ho	25.5	69.4	26.0	73.1	569	71.9	70.2
^{167}Er	111	290	119	312	1990	306	291
^{169}Tm	22.3	54.3	23.4	58.8	320	57.2	55.4
^{173}Yb	196	452	207	496	2000	493	460
^{175}Lu	36.2	81.4	38.6	89.5	265	87.2	81.5
^{178}Hf	9220	8750	9160	9140	9010	9220	9330
^{181}Ta	1.37	1.52	1.48	2.44	0.987	2.16	1.62
^{206}Pb	2.39	3.65	2.37	6.00	4.26	5.14	4.72
^{208}Pb	0.173	0.383	0.229	0.963	0.880	0.609	0.498
^{232}Th	126	324	134	487	175	426	355
^{238}U	216	380	240	618	393	558	457

Table A.1 (continued).

	JR						GSD-1G
Grain #	21	22	23	24	25	27	1
^{7}Li	<1.59	<1.20	<1.43	<1.15	<1.14	<1.22	36.4
^{24}Mg	<1.16	<0.919	<1.10	<0.851	<0.906	<0.861	17200
^{27}Al	<4.63	<3.76	<4.47	<3.50	<3.62	<3.64	61600
^{29}Si	147000	147000	147000	147000	147000	147000	245000
^{31}P	266	196	164	184	184	254	707
^{39}K	<5.98	<4.91	<5.90	<4.62	<4.80	<4.81	23200
^{43}Ca	<286	<234	<273	<220	<223	<233	40800
^{49}Ti	7.92	6.85	6.11	6.29	8.07	7.32	6810
^{51}V	<0.164	<0.132	<0.169	<0.133	<0.142	<0.151	35.7
^{53}Cr	<2.57	<2.14	<2.45	<2.08	<2.23	<2.13	32.5
^{55}Mn	<0.955	<0.804	<0.967	<0.776	<0.798	<0.816	179
^{57}Fe	<39.8	<32.3	<38.6	<29.9	<30.4	<29.4	102000
^{59}Co	<0.553	<0.472	<0.545	<0.426	<0.464	<0.447	34.2
^{85}Rb	0.185	0.366	<0.161	0.323	0.264	0.259	32.3
^{88}Sr	0.284	0.401	0.342	0.404	0.418	0.342	56.4
^{89}Y	1230	2270	761	1580	1700	1460	33.5
^{90}Zr	410000	438000	399000	429000	429000	434000	33.5
^{93}Nb	3.42	4.91	5.89	4.31	2.66	8.72	35.1
^{95}Mo	1.15	1.25	1.17	1.14	1.24	1.11	34.0
^{133}Cs	<0.0705	<0.0568	<0.0722	<0.0527	<0.0563	<0.0613	27.7
^{137}Ba	<0.268	<0.210	<0.302	<0.173	<0.257	<0.164	55.1
^{139}La	0.0364	0.0769	0.0472	0.0516	0.0399	0.0207	31.8
^{140}Ce	12.0	20.6	15.1	17.3	13.1	22.4	32.9
^{141}Pr	0.265	0.656	0.0794	0.372	0.563	0.297	36.8
^{146}Nd	4.74	10.5	1.43	6.42	8.20	4.30	35.3
^{147}Sm	8.27	16.1	3.48	10.8	13.6	7.94	38.8
^{151}Eu	0.274	0.245	0.0610	0.196	0.428	0.148	33.0
^{157}Gd	38.3	74.1	17.7	48.9	57.6	38.6	39.1
^{159}Tb	11.8	22.0	6.04	15.1	16.6	12.5	39.1
^{163}Dy	124	247	71.5	166	183	145	42.3
^{165}Ho	43.9	83.7	26.8	56.7	60.2	52.1	41.5
^{167}Er	180	357	119	241	253	228	32.6
^{169}Tm	35.0	68.3	24.7	46.2	47.7	44.6	40.9
^{173}Yb	296	568	212	396	397	386	42.1
^{175}Lu	53.4	98.6	39.6	70.0	69.2	69.5	42.8
^{178}Hf	8560	9250	9240	9490	8750	9190	32.7
^{181}Ta	1.32	2.03	2.08	1.88	1.07	2.88	34.6
^{206}Pb	2.45	5.83	3.25	4.25	2.54	5.14	45.6
^{208}Pb	0.284	0.759	0.268	0.405	0.269	0.579	42.1
^{232}Th	175	486	175	304	227	429	33.5
^{238}U	228	616	317	425	264	566	34.6

Table A.1 (continued).

	GSD-1G						
Grain #	2	3	4	5	6	7	8
^{7}Li	37.4	36.9	40.3	36.9	37.7	39.1	37.8
^{24}Mg	17800	17600	17700	18400	18400	18300	18100
^{27}Al	63400	62000	63600	62700	63500	64300	63900
^{29}Si	245000	245000	245000	245000	245000	245000	245000
^{31}P	676	613	825	667	733	556	777
^{39}K	24300	22500	24100	24400	24100	24100	23000
^{43}Ca	44200	44100	44100	43900	43600	46500	45700
^{49}Ti	7170	7290	7250	7150	7200	7330	7100
^{51}V	36.6	36.2	37.7	36.8	37.7	38.8	38.4
^{53}Cr	40.0	36.5	37.4	39.6	38.1	37.4	40.5
^{55}Mn	183	185	188	185	187	192	190
^{57}Fe	92300	78100	86900	62100	106000	115000	97000
^{59}Co	35.3	35.3	35.1	35.5	35.2	35.9	36.9
^{85}Rb	33.3	33.2	34.0	33.8	33.7	34.3	34.7
^{88}Sr	58.2	57.6	59.2	58.8	57.9	60.1	60.4
^{89}Y	34.9	34.4	35.2	35.3	35.1	35.6	35.5
^{90}Zr	36.4	35.9	38.9	32.1	33.2	34.0	31.5
^{93}Nb	36.6	35.9	37.0	36.7	36.8	37.2	38.0
^{95}Mo	34.9	36.4	33.8	34.1	34.1	36.5	34.8
^{133}Cs	28.7	27.8	28.1	28.5	28.2	28.3	29.0
^{137}Ba	55.4	59.4	57.5	57.3	59.4	59.7	60.7
^{139}La	32.5	31.7	33.2	33.2	32.5	33.4	33.4
^{140}Ce	34.0	33.6	34.8	35.1	33.8	35.4	35.5
^{141}Pr	37.2	36.9	38.0	37.7	37.7	39.2	38.6
^{146}Nd	36.8	36.0	36.7	35.7	36.9	37.5	38.0
^{147}Sm	39.0	39.5	40.2	39.4	40.3	40.7	41.0
^{151}Eu	33.6	33.4	34.4	34.0	34.0	35.3	35.4
^{157}Gd	40.7	39.7	42.1	42.0	40.4	43.0	41.8
^{159}Tb	40.8	40.2	40.4	40.4	41.2	41.5	42.2
^{163}Dy	43.0	42.5	43.6	44.1	43.7	44.6	45.5
^{165}Ho	42.2	42.1	42.8	43.5	42.6	43.4	44.2
^{167}Er	32.5	32.5	32.8	33.7	34.1	33.3	34.4
^{169}Tm	42.5	41.2	43.0	42.6	41.8	44.2	44.2
^{173}Yb	44.4	41.4	44.9	43.6	44.3	45.1	45.8
^{175}Lu	43.7	43.9	44.2	44.9	43.9	46.7	46.2
^{178}Hf	34.2	34.4	34.3	34.4	34.2	36.5	35.6
^{181}Ta	34.9	35.2	35.5	35.8	35.7	36.4	36.9
^{206}Pb	44.5	46.1	46.5	47.7	46.3	49.0	47.5
^{208}Pb	41.9	42.0	42.5	42.9	42.8	44.3	43.8
^{232}Th	32.9	32.6	33.8	34.7	35.1	36.9	35.1
^{238}U	34.3	34.4	35.1	35.7	35.4	35.9	36.0

Table A.1 (continued).

	GSD-1G			Detection Limit
	Average	St. Dev.	% Dev.	(based on 166 runs)
^{7}Li	37.8	1.28	3.38	1.21
^{24}Mg	17900	436	2.43	0.78
^{27}Al	63100	938	1.49	3.75
^{29}Si	245000	3.11×10^{-11}	1.27×10^{-14}	481.92
^{31}P	694	86.5	12.5	21.54
^{39}K	23700	726	3.06	5.41
^{43}Ca	44100	1650	3.74	210.20
^{49}Ti	7160	162	2.26	2.12
^{51}V	37.3	1.09	2.94	0.13
^{53}Cr	37.7	2.58	6.83	2.12
^{55}Mn	186	4.08	2.19	0.79
^{57}Fe	92500	16700	18.1	28.20
^{59}Co	35.4	0.774	2.19	0.39
^{85}Rb	33.7	0.744	2.21	0.13
^{88}Sr	58.6	1.32	2.26	0.10
^{89}Y	34.9	0.711	2.03	0.12
^{90}Zr	34.4	2.45	7.11	2.36
^{93}Nb	36.6	0.879	2.40	0.02
^{95}Mo	34.8	1.09	3.14	0.12
^{133}Cs	28.3	0.454	1.60	0.06
^{137}Ba	58.1	2.06	3.55	0.20
^{139}La	32.7	0.704	2.15	0.02
^{140}Ce	34.4	0.930	2.71	0.02
^{141}Pr	37.8	0.834	2.21	0.01
^{146}Nd	36.6	0.906	2.48	0.08
^{147}Sm	39.9	0.820	2.06	0.15
^{151}Eu	34.1	0.860	2.52	0.04
^{157}Gd	41.1	1.34	3.26	0.12
^{159}Tb	40.7	0.942	2.31	0.01
^{163}Dy	43.7	1.09	2.49	0.06
^{165}Ho	42.8	0.876	2.05	0.01
^{167}Er	33.2	0.764	2.30	0.05
^{169}Tm	42.5	1.24	2.91	0.01
^{173}Yb	44.0	1.51	3.43	0.05
^{175}Lu	44.5	1.33	2.99	0.01
^{178}Hf	34.5	1.09	3.17	0.06
^{181}Ta	35.6	0.739	2.07	0.02
^{206}Pb	46.6	1.39	2.98	0.12
^{208}Pb	42.8	0.861	2.01	0.08
^{232}Th	34.3	1.39	4.05	0.01
^{238}U	35.2	0.667	1.90	0.01

Table A.2. Whole Rock Trace Element Compositions (XRF)

		Bieroth Volcanics (undifferentiated)				Cedar Canyon Tuff (CCT)	
	Sample #	361	395C	395B	371	10-074	10-075
Normalized percentages†	SiO_2	64.41	66.83	66.48	68.84	65.61	65.19
	TiO_2	0.657	0.510	0.506	0.498	0.609	0.526
	Al_2O_3	17.68	16.20	15.96	15.39	16.04	17.14
	FeO^T	4.60	3.59	3.67	3.62	4.36	4.03
	MnO	0.067	0.059	0.063	0.053	0.053	0.081
	MgO	0.89	1.89	2.14	1.25	1.86	1.95
	CaO	4.47	3.99	4.72	3.24	4.16	5.04
	Na_2O	3.75	3.21	3.01	3.33	3.36	3.45
	K_2O	3.28	3.57	3.31	3.59	3.75	2.39
	P_2O_5	0.208	0.153	0.144	0.182	0.192	0.198
ppm	Ni	11	13	12	9	12	9
	Cr	17	23	27	25	26	27
	Sc	11	10	9	9	11	10
	V	98	70	65	67	85	74
	Ba	1182	1188	1115	1053	1226	1162
	Rb	89	105	106	81	110	89
	Sr	654	501	584	526	528	908
	Zr	181	176	173	145	194	156
	Y	46	16	15	11	21	15
	Nb	10.1	11.3	10.5	9.6	11.9	9.8
	Ga	21	18	18	18	18	19
	Cu	15	11	10	38	12	8
	Zn	75	57	54	58	70	60
	Pb	16	21	19	16	20	17
	La	49	44	41	36	47	41
	Ce	76	75	68	60	77	69
	Th	12	20	19	14	19	14
	Nd	44	28	28	25	34	28
	U	3	6	3	1	4	3
	Cs	1					
	Pr						
	Hf						

Table A.2 (continued).

		LTSC		JCR		RMR	
Normalized percentages†	Sample #	10-083*	10-084	10-077	10-078*	10-085	345A
	SiO_2	85.23	73.90	72.93	73.76	80.33	74.38
	TiO_2	0.287	0.237	0.477	0.463	0.272	0.350
	Al_2O_3	7.97	12.95	12.98	12.70	9.94	13.04
	FeO^T	2.08	2.25	3.39	3.53	1.42	2.04
	MnO	0.017	0.028	0.047	0.037	0.010	0.030
	MgO	0.28	0.20	0.29	0.12	0.09	0.16
	CaO	0.46	0.19	1.38	0.92	0.58	0.90
	Na_2O	0.76	0.18	2.57	3.22	1.11	2.60
	K_2O	2.88	10.04	5.86	5.17	6.19	6.44
	P_2O_5	0.030	0.023	0.079	0.076	0.056	0.052
ppm	Ni	4	4	4	4	2	5
	Cr	2	4	3	3	3	4
	Sc	3	3	6	5	3	4
	V	8	3	14	16	7	10
	Ba	562	150	1680	1845	700	953
	Rb	94	257	181	160	120	198
	Sr	44	15	121	118	83	63
	Zr	396	397	485	493	301	384
	Y	29	57	49	52	49	46
	Nb	21.6	34.8	26.5	27.0	21.9	28.7
	Ga	11	16	20	18	16	19
	Cu	3	4	4	6	3	4
	Zn	51	60	76	73	30	50
	Pb	14	10	29	32	22	27
	La	37	50	76	85	54	70
	Ce	70	99	133	137	98	130
	Th	14	30	23	23	20	27
	Nd	30	35	56	63	38	49
	U	5	6	6	5	4	8
	Cs	6	3				6
	Pr						
	Hf						

Table A.2 (continued).

		RMR	JR
Normalized percentages†	Sample #	10-087*	I4306***
	SiO_2	77.18	81.07
	TiO_2	0.305	0.20
	Al_2O_3	11.64	11.69
	FeO^T	1.47	1.21**
	MnO	0.009	0.00
	MgO	0.06	0.02
	CaO	0.21	0.06
	Na_2O	1.94	0.05
	K_2O	7.14	5.67
	P_2O_5	0.037	0.02
ppm	Ni	4	1
	Cr	4	7
	Sc	5	3
	V	17	9
	Ba	760	368
	Rb	207	274
	Sr	39	30
	Zr	344	317
	Y	44	40
	Nb	26.5	37
	Ga	17	21
	Cu	8	0
	Zn	17	36
	Pb	30	12
	La	71	76
	Ce	130	156
	Th	25	32
	Nd	50	55
	U	5	6
	Cs	6	
	Pr		16
	Hf		10

†Weight percentage of major oxide normalized so all major oxides add to 100%.
*Sample used for zircon analyses.
**This value is $Fe_2O_3^T$, rather than Feo^T.
***This analysis performed at Pomona College, all others performed at Washington State University.

Table A.3. Whole Rock Trace Element Compositions (ICP-MS, ppm)

	CCT		**JCR**		**RMR**	
Sample #	10-074	10-075	10-085	10-087*	10-077	10-078*
La	47.38	41.36	56.66	72.85	75.52	86.24
Ce	80.47	72.18	108.4	135.5	142.1	142.3
Pr	9.405	8.087	11.65	15.01	15.93	17.86
Nd	33.33	28.32	40.95	51.18	56.79	63.98
Sm	5.880	4.979	7.981	9.136	10.68	12.10
Eu	1.371	1.354	0.7982	0.8807	1.689	1.781
Gd	4.544	3.701	7.364	7.420	9.183	10.33
Tb	0.6511	0.5279	1.265	1.241	1.500	1.655
Dy	3.649	2.931	7.874	7.551	9.100	9.768
Ho	0.7326	0.5538	1.658	1.549	1.819	1.976
Er	1.934	1.435	4.659	4.357	5.070	5.311
Tm	0.2803	0.2013	0.6885	0.6432	0.7323	0.7806
Yb	1.823	1.288	4.281	4.126	4.634	4.853
Lu	0.2801	0.2021	0.6589	0.6415	0.7080	0.7418
Ba	1226	1183	720.8	775.0	1758	1910
Th	18.61	14.61	19.94	26.22	23.17	23.36
Nb	11.13	9.167	22.17	26.14	26.32	26.26
Y	20.25	14.68	47.44	42.28	47.79	51.27
Hf	5.171	4.067	8.496	9.781	12.48	12.59
Ta	0.8494	0.7636	1.577	1.804	1.684	1.685
U	3.848	2.354	3.925	5.753	4.964	4.535
Pb	19.81	16.91	21.85	29.22	28.44	29.97
Rb	107.2	87.84	123.0	210.9	181.5	158.2
Cs	3.012	3.313	6.420	1.845	2.581	1.919
Sr	526.0	950.9	83.39	39.45	123.2	118.9
Sc	11.00	9.640	4.062	4.963	6.740	7.023
Zr	190.8	148.9	311.4	366.0	512.8	520.4

*This sample used for zircon analyses.

Table A.4. Whole rock Hf and Nd isotope compositions

	Lapilli Tuff of Sheep Creek	**Johnstons Camp Rhyolite**	**Rough Mountain Rhyolite**	**Jarbidge Rhyolite**
$^{176}Hf/^{177}Hf$	0.2825	0.282211	0.282534	0.281802
2 s.e. (%)	5.8	6	5.6	4.6
$^{178}Hf/^{177}Hf$	1.467182	1.467171	1.467183	1.467171
2 s.e. (%)	9.2	9	9.4	8.96
$^{180}Hf/^{177}Hf$	1.886684	1.886696	1.886689	1.886676
2 s.e. (%)	17.6	19.4	18	18
ε_{Hf}	-10.0636	-20.305	-8.87853	-34.7479
2 s.e.	0.205674	0.212766	0.198582	0.163121
$^{143}Nd/^{144}Nd$	0.512177	0.511941	0.512233	0.511402
2 s.e. (%)	7.8	6.998	6.6	6
$^{145}Nd/^{144}Nd$	0.348419	0.34842	0.348421	0.348419
2 s.e. (%)	4	4.54	4.56	4
$^{148}Nd/^{144}Nd$	0.241572	0.241566	0.241574	0.24157
2 s.e. (%)	5.176	3.4	2.88	3.02
$^{150}Nd/^{144}Nd$	0.236437	0.236442	0.236435	0.236433
2 s.e. (%)	5	4.58	4.66	4
ε_{Nd}	-8.84629	-13.4312	-7.73904	-23.9524
2 s.e.	0.152344	0.13668	0.128906	0.117188

Table A.5. Lu-Hf isotope compositions of zircons

	Grain #	$^{176}Hf/^{177}Hf$	2 s.e.	$^{176}Lu/^{177}Hf$	2 s.e.	$^{176}Yb/^{177}Hf$	2 s.e.	$^{178}Hf/^{177}Hf$	2 s.e.	$^{180}Hf/^{177}Hf$	2 s.e.	ε_{Hf}	2 s.e.
Lapilli Tuff of Sheep Creek	1	0.282514	0.000031	0.000802	0.000032	0.026	0.0014	1.467172	0.000029	1.886855	0.00009	-11.1	1.10
	2	0.282507	0.000035	0.00145	0.00011	0.0454	0.0029	1.467185	0.000041	1.88704	0.00011	-11.4	1.24
	3	0.282524	0.000022	0.000557	0.000013	0.0181	0.00066	1.467157	0.000029	1.88689	0.000085	-10.8	0.779
	4	0.282756	0.000025	0.00094	0.000036	0.0313	0.0013	1.467184	0.000035	1.8869	0.000084	-2.55	0.884
	5	0.282484	0.000031	0.000901	0.000053	0.0313	0.0022	1.467172	0.000043	1.88696	0.0001	-12.2	1.10
	6	0.282759	0.000031	0.000779	0.000019	0.02543	0.00066	1.467185	0.000039	1.88688	0.00011	-2.44	1.10
	7	0.282517	0.000026	0.001497	0.000041	0.0513	0.0019	1.467188	0.000035	1.88693	0.0001	-11.0	0.920
	8	0.282451	0.000024	0.000708	0.000042	0.0237	0.0013	1.467188	0.000044	1.886873	0.000088	-13.3	0.850
	9	0.282679	0.000034	0.000766	0.000037	0.0246	0.0013	1.467135	0.000028	1.886835	0.000069	-5.27	1.20
	10	0.282502	0.000032	0.000616	0.000025	0.0202	0.001	1.467185	0.000035	1.886939	0.000089	-11.5	1.13
Johnstons Camp Rhyolite	1	0.282172	0.000045	0.000766	0.000068	0.0266	0.0026	1.467156	0.00004	1.886966	0.000094	-23.2	1.60
	2	0.282208	0.000026	0.000702	0.000047	0.0234	0.0017	1.467156	0.000036	1.886795	0.000084	-21.9	0.921
	3	0.282032	0.000025	0.0006	0.000016	0.01975	0.00049	1.467138	0.000039	1.88694	0.00012	-28.1	0.887
	4	0.282283	0.00012	0.001454	0.000086	0.0399	0.0024	1.467036	0.000094	1.8877	0.00044	-19.3	4.25
	5	0.282016	0.000039	0.000738	0.000044	0.0248	0.0015	1.467139	0.000031	1.886923	0.000092	-28.7	1.38
	6	0.282034	0.000056	0.000954	0.000011	0.03307	0.00041	1.467118	0.000037	1.88675	0.00018	-28.1	1.99
	7	0.281994	0.00003	0.000768	9.2×10^{-6}	0.02634	0.00039	1.467166	0.00003	1.88693	0.0001	-29.5	1.06
	8	0.282748	0.000031	0.000692	0.000012	0.0229	0.0005	1.467181	0.000033	1.88696	0.00012	-2.83	1.10
	9	0.282061	0.000018	0.00141	0.0001	0.0491	0.0035	1.467119	0.000034	1.886824	0.000079	-27.1	0.638
	10 (core)	0.28265	0.000024	0.00229	0.00023	0.0834	0.0092	1.467165	0.000031	1.886953	0.000083	-6.15	0.849
	10 (rim)	0.282688	0.000028	0.002427	0.000062	0.0876	0.0019	1.467159	0.000029	1.88684	0.000085	-4.95	0.991
	11	0.282717	0.000015	0.00051	8.4×10^{-6}	0.01688	0.00038	1.467143	0.000031	1.886851	0.000072	-3.93	0.531
	12	0.282529	0.000036	0.000496	6.5×10^{-6}	0.01532	0.00017	1.467141	0.00004	1.88679	0.00011	-10.6	1.27
	13	0.28238	0.000047	0.000762	0.000066	0.0254	0.0024	1.46718	0.000037	1.886875	0.000086	-15.8	1.66
	14	0.282027	0.000032	0.000905	0.000082	0.0304	0.0029	1.467157	0.000047	1.887	0.00012	-28.3	1.13
	15	0.28201	0.000023	0.000748	0.000015	0.0252	0.00062	1.467179	0.000037	1.886914	0.000088	-28.9	0.816

Table A.5 (continued).

	Grain #	$^{176}Hf/^{177}Hf$	2 s.e.	$^{176}Lu/^{177}Hf$	2 s.e.	$^{176}Yb/^{177}Hf$	2 s.e.	$^{178}Hf/^{177}Hf$	2 s.e.	$^{180}Hf/^{177}Hf$	2 s.e.	ε_{Hf}	2 s.e.
Rough Mountain Rhyolite	1	0.28273	0.000032	0.000634	0.000022	0.01877	0.00069	1.467133	0.000037	1.886822	0.000082	-3.47	1.13
	2	0.282702	0.000035	0.000786	0.000053	0.0243	0.0021	1.467202	0.000036	1.8869	0.00011	-4.46	1.24
	3	0.282761	0.000034	0.00136	0.00016	0.0417	0.0049	1.467157	0.00004	1.88685	0.00011	-2.37	1.20
	4	0.282752	0.000026	0.002302	0.000082	0.0858	0.004	1.467179	0.000034	1.886894	0.000073	-2.69	0.920
	5	0.282552	0.000026	0.000709	0.000015	0.0225	0.0006	1.467155	0.000031	1.886897	0.000084	-9.76	0.920
	6	0.28254	0.000025	0.00294	0.000093	0.0977	0.0034	1.467161	0.000036	1.886972	0.00008	-10.2	0.885
	7	0.282623	0.000022	0.000582	6.7×10^{-6}	0.01782	0.00026	1.467166	0.000035	1.886962	0.00009	-7.25	0.779
	8	0.282806	0.000052	0.000709	0.000027	0.02138	0.00085	1.46719	0.000045	1.88665	0.00019	-0.778	1.84
	9	0.282645	0.000028	0.000701	0.000012	0.02236	0.00052	1.467149	0.000031	1.88699	0.0001	-6.47	0.991
	10	0.282544	0.000026	0.000648	0.000011	0.01984	0.00024	1.46714	0.000032	1.886883	0.000095	-10.0	0.920
Jarbidge Rhyolite	1	0.281827	0.000074	0.00091	0.00015	0.032	0.0069	1.467117	0.000052	1.88663	0.0002	-35.4	2.63
	1	0.281771	0.000038	0.00177	0.00013	0.0668	0.0075	1.467163	0.000044	1.88706	0.00014	-37.4	1.35
	2	0.281758	0.00009	0.000686	0.000017	0.01971	0.00051	1.467154	0.000068	1.88703	0.00033	-37.8	3.19
	3	0.28181	0.000032	0.00159	0.000049	0.0594	0.0037	1.467178	0.000042	1.886875	0.000091	-36.0	1.14
	4	0.281778	0.000027	0.00118	0.00022	0.0411	0.0097	1.46716	0.00003	1.886932	0.000079	-37.1	0.958
	5	0.281821	0.000048	0.001602	0.000088	0.0546	0.0034	1.467169	0.000045	1.88672	0.00014	-35.6	1.70
	6	0.281792	0.000026	0.000815	0.000073	0.0243	0.0023	1.467179	0.000029	1.886793	0.000098	-36.6	0.923
	7	0.281726	0.000022	0.001573	0.000053	0.0486	0.0016	1.467139	0.000027	1.886933	0.000065	-39.0	0.781
	8	0.281834	0.00002	0.000952	0.000072	0.0337	0.0026	1.467167	0.000029	1.886888	0.000076	-35.2	0.710
	9	0.281797	0.000027	0.000692	7.6×10^{-6}	0.02342	0.00042	1.467175	0.00004	1.886885	0.000076	-36.5	0.958
	10	0.28176	0.000027	0.000692	0.000051	0.021	0.0012	1.467148	0.000034	1.886904	0.000092	-37.8	0.958
	11	0.281744	0.000067	0.00062	0.00011	0.0198	0.0041	1.467156	0.000067	1.88701	0.0002	-38.3	2.38

APPENDIX B

MATERIAL FOR CHAPTER III

Contents:

B.1. Detailed methods
B.2. Sources of data for Fig. 3.1
B.3. Sources of data for Figs. 3.2 and 3.3 and Table B.2
B.4. Sample descriptions
B.5. Supplementary figures and tables

B.1. Detailed methods

B.1.1. Phenocryst extraction methods:

Phenocrysts of quartz, plagioclase, and pyroxene to be analyzed for $\delta^{18}O$ by laser fluorination are hand-picked from crushed samples and washed for ~90 minutes in concentrated hydrofluoric acid to remove any attached groundmass or glass. Zircons for SIMS and LA-ICP-MS analyses were obtained by bulk dissolution of crushed 50-100 g samples in concentrated HF at room temperature for 2-3 days. This dissolves most non-zircon material in the rock, allowing zircons to be easily extracted from the resulting residue. Care was taken during the rinsing process and cleaning of equipment to prevent cross-contamination of zircons between samples.

B.1.2. Laser fluorination methods:

When possible, single phenocrysts are used for analyses, otherwise multiple smaller phenocrysts are used in a single analysis (Table B.2). While we preferred single phenocrysts, multiple small phenocryst analyses do have the advantage of possibly being less sensitive to alteration in individual phenocrysts, especially when repeat analyses are performed. Samples are pre-treated with BrF_5 reagent for intervals of 30 seconds, five minutes, and 15 minutes in a vacuum chamber then left in a vacuum overnight. For the analysis, samples are fused with a CO_2 infrared laser at up to 9 W power in the presence of BrF_5 fluorinating reagent to liberate O_2 gas from the sample. Remaining reagent and other gasses are cleaned from the resulting gas via a serious of liquid N_2 traps and a mercury diffusion pump. O_2 is then converted into CO_2 in the presence of a heated carbon filament. The yields are measured by a manometer and were 90-100% of the expected range for most samples. The CO_2 is then passed to a MAT-253 gas-source mass spectrometer. Samples were controlled for reproducibility via intercalibration with a UOG (6.52‰) garnet standard measured relative to a Gore Mountain Garnet standard of 5.8‰ (Valley et al., 1995). Errors on repeat measurements of standards are typically better than 0.2‰ (2 s.d.).

B.1.3. Ion- microprobe methods:

Sample preparation and secondary ion mass spectrometry (SIMS) were conducted at the Canadian Centre for Isotopic Microanalysis, University of Alberta, Canada. Zircons were cast in epoxy and their mid-sections exposed with diamond grinding and polishing. Scanning electron microscopy (SEM) was conducted utilizing a Zeiss EVO MA15 operating at 15 kV and ~3 nA, and equipped with a broadband, high-sensitivity

cathodoluminescence (CL) detector to reveal internal grain structures. The zircon array, cut out to form a ~4 x 6 mm epoxy block, was pressed into the center of custom indium receptacle along with two similar blocks comprising zircon reference materials (RMs). A total of 30 nm Au was sputtered onto the mount (M1248) surface prior to SIMS.

SIMS analyses utilized a Cameca IMS1280 multicollector instrument with 20 keV Cs^+ primary ions (2.5 – 3.0 nA, ⌀12 μm) and extraction of O^- secondary ions through 10 kV. Charge compensation utilized normal incidence low energy electrons. The primary beam was rastered around the spot for 60 s prior to acquisition and rastered 5 x 5 μm during acquisition. Entrance slight and field aperture were 122 μm and 5 x 5 mm, respectively, with 100x image magnification of the transfer optics. Energy filtering was not employed. Secondary ion collection utilized dual Faraday cups at L'2 ($^{16}O^-$, ~3E9 ions/s) and FC2 ($^{18}O^-$, ~6.5E6 ion/s), with mass resolutions of 2000 and 2275, respectively, sufficient to resolve spectral interferences. Each analysis took 4.5 min, including pre-analysis sputtering, automated secondary ion tuning, and a total of 90 s peak counting. The analysis sequence was 4 unknowns followed by one analysis of CCIM reference zircon S0081 ($\delta^{18}O_{VSMOW}$ = +4.87‰), and analysis of TEM2 (S0022) zircon ($\delta^{18}O_{VSMOW}$ = +8.20‰; Black et al., 2004) after every 8 unknowns. Data for 46 analyses of S0081 were processed collectively for session IP13082, for which there was a tiny drift in instrumental mass fractionation (+0.1‰), yielding a linear time-corrected session standard deviation of ±0.07‰. The uncertainties propagated to unknowns include within-spot, between-spot, and between-session components, together giving a median value of ±0.16‰ (2σ) per analysis. The weighted mean $\delta^{18}O$ value of TEM2 (S0022) zircon for this session is +8.26 ±0.03 (N= 27; MSWD = 1.02).

B.1.4. Laser ablation ICP-MS methods

Following analyses for oxygen isotopic composition the mounts were lightly repolished before laser ablation-multicollector-inductively coupled plasma-mass spectrometry (LA-MC-ICPMS). Analysis of the Lu-Hf isotopic composition were conducted at the Radiogenic Isotope and Geochronology (RIGL) lab at Washington State University using a New Wave 213 nm UP Nd:YAG laser coupled with the Thermo-Finnigan Neptune MC-ICPMS. The methods followed are described by Fisher et al. (2014) with the exception that U-Pb ages were not concurrently determined. The measured $^{176}Hf/^{177}Hf$ of unknowns was normalized to the measured 176Hf/177Hf of the Mud Tank zircon standard (Woodhead & Hergt, 2005). Typical correction factors were 1.00016. In order to monitor the accuracy of the ^{176}Yb and ^{176}Lu interference correction, analyses of a Yb-rich synthetic zircon (MUNZirc-4) were interspersed with unknowns and yielded a mean $^{176}Hf/^{177}Hf$ of 0.282123 ± 10 (2SD), within error of the value given by Fisher et al. (2011). Epsilon Hf values were calculated using the CHUR values of Bouvier et al. (2007) and the ^{176}Lu decay constant of Söderlund et al. (2004) (1.867*10−11 year−1). Depleted mantle values used are those of Nowell et al. (1998).

B.2. Sources of data for Fig. 3.1

Outline of areas covered by Columbia River Basalts is modified from Camp and Ross (2004) and Coble and Mahood (2012). CRB dike swarm locations are taken from Wolff et al. (2008). $^{87}Sr/^{86}Sr$ = 0.706 and 0.704 isopleths are taken from Pierce and Morgan (2009). Archean crustal blocks locations are taken from Foster et al. (2006). The

outline of the Oregon-Idaho graben and other grabens to the north are taken from Cummings et al. (2000) and Ferns and McClaughry (2013). Eruptive volumes for syn-CRB rhyolite centers are modified from Coble and Mahood (2012), when available. Syn-CRB rhyolite center locations correspond to collected samples (see Section S4, and references therein). Additional areas not sampled by this study but still mapped here include the High Rock complex (Coble & Mahood, 2012), the Hawks Valley-Lone Mountain rhyolites (Wypych et al., 2011), the Strawberry Mountains rhyolites (Steiner and Streck, 2013), the Santa Rosa-Calico volcanic complex (Amrhein et al., 2013), the J-P Desert and Jarbidge Rhyolites (Colón et al., 2015a), and the Swamp Creek Rhyolite (Camp et al., 2003). The Dinner Creek Tuff and associated Mascall Ignimbrites are assumed to be sourced from the Castle Rock region (Shervais & Hanan, 2008; Streck et al., 2015), and an analysis of "Swisher Mountain Rhyolite" from east of Jordan Valley, Oregon, was grouped with Juniper Mountain (Manley & McIntosh, 2004). $\delta^{18}O$ values for rhyolites at the Santa-Rosa Calico, High Rock, and J-P Desert/Jarbidge complexes are taken from Amrhein et al. (2013), Mallis et al. (2014), and Colón et al. (2015a), respectively. Outlines of post-CRB volcanic complexes of the Snake River Plain hotspot track, including Owyhee-Humboldt, Bruneau-Jarbidge, and Twin Falls are taken from Bonnichsen (2008). Map background is from GeoMapApp (2014; Ryan et al., 2009).

B.3. Sources of data for Figs. 3.2 and 3.3 and Table B.2

For Fig. 3.2, Part (a), when unknown for a given sample, Imnaha basalt was assumed to be 52% SiO_2, Steens Basalt, 50% SiO_2, and Picture Gorge Basalt 48% SiO_2, based on common values for those groups (Carlson et al. 1981; Carlson, 1984; Camp et

al., 2013). For Fig. 3.2, Parts (b) and (c), the CRB field is taken from major phenocryst $\delta^{18}O$ data from this study and Nd isotope compositions from Wolff et al. (2008), converted to ε_{Hf} using the Hf-Nd mantle array of Chauvel et al. (2007).

To get $\delta^{18}O_{melt}$ values for Fig. 3.2a and Fig. 3.3d, we either used the whole rock measurements of Carlson (1984) or estimated from major phenocryst measurements. We used the oxygen isotope fractionation factors of Chiba et al. (1989) and CPIW norms for typical basalt, basaltic andesite, and rhyolite samples to roughly estimate the corrections from phenocryst $\delta^{18}O$ values to melt $\delta^{18}O$ values. The values to add to the phenocryst values were +0.23‰ for plagioclase feldspar, -0.53‰ for quartz, and +1.47‰ for pyroxene (modeled as diopside). For the case of basaltic andesite (~56% silica), we instead added -0.37‰ to a plagioclase value, and for the more mafic basalts (down to 48% silica), we added -0.46‰ to plagioclase $\delta^{18}O$ values and +0.84‰ to olivine values. We prefer to base our estimated $\delta^{18}O_{melt}$ values on more refractory minerals which are more resistant to secondary alteration of their oxygen isotope compositions. As such, we based the $\delta^{18}O_{melt}$ estimates on the average $\delta^{18}O$ values of either quartz, pyroxene, olivine, or plagioclase phenocrysts from the rock in that order. So a sample with quartz and plagioclase will have its $\delta^{18}O_{melt}$ estimated on the measured quartz $\delta^{18}O$ values, not those of plagioclase. For a single sample, the aphyric obsidian EO-08 from Dooley Mountain (see below) we used a whole-rock value to estimate the melt $\delta^{18}O$ value. Multiple minerals are measured as a check on each other, and to check $\Delta^{18}O$ equilibrium between minerals, a sign of freshness of the measured values.

For a handful of samples, only one type of major phenocryst was analyzed, preventing measurements of $\Delta^{18}O$ to check freshness of the grains for implied magmatic

values. When this happened, care was taken to ensure that only fresh samples, typically glass-bearing vitrophyres, were used, and multiple analyses were made to check for consistency. An example is EO-28, the Tuff of Spring Creek from the Lake Owyhee volcanic field, which only yielded plagioclase among major phenocrysts but showed strong consistency between multiple measurements of $\delta^{18}O_{plag}$. The resulting estimated melt $\delta^{18}O$ value was confirmed by SIMS measurements of zircon.

B.4. Sample descriptions

Note: while a small minority samples are not well-constrained and may have been collected out of place, we take pains to note that the samples which are discussed and used in plots in the main text are all well-constrained in their source location. We include all analyzed samples here for completeness only.

Western Small Volume Units:

EO-01: 2m thick ash layer, sampled between successive layers of Picture Gorge Basalt in John Day Fossil Beds National Monument. Shows evidence of water-reworking, including bedding planes. Contains plagioclase and pyroxene. Not mapped in Figs. 3.1 or 3.3 due to uncertain source.

EO-41: Sample of the newly described welded Tuff of Hawk Rim, which has been dated as having a syn-CRB age of ~16.3 Ma by McLaughlin et al. (in prep.). Source unknown but assumed to be relatively proximal due to lack of laterally extensive correlative outcrops (personal communication, Win McLaughlin). It does, however correlate well

geochemically with the Dinner Creek Tuffs (Fig. B.5). This potential new eruptive center not mapped in Figs. 3.1 or 3.3 due to this ambiguity, however.

EO-42: Nearly aphyric basaltic andesite taken from near the summit of the Little Juniper Mountain lava dome complex. This dome is generally composed of dacite and has been dated by Jordan et al. (2004) at 15.65 ± 0.04 Ma.

EO-44: Dacite from north of the summit of Little Juniper Mountain. <5% small plagioclase crystals.

EO-46: Dacite poryphyry with abundant plagioclase from the southern end of the Horsehead Mountain rhyolite dome complex (MacLean, 1994). A date of 15.63 ± 0.03 Ma was obtained from a nearby outcrop by Jordan et al. (2004).

EO-47: Plagioclase-phyric dacite from the summit of Jackass Mountain. This dome dated at 15.34 ± 0.19 Ma by Jordan et al. (2004).

Dooley Mountain Sequence:

EO-08: Obsidian outcrop, partly perlitized, exposed in a roadcut. Mapped by Evans (1992) as Td-2. A late stage rhyolite from this complex was reported as having an age of 14.7 ± 0.4 Ma by Evans (1992).

EO-09: Highly altered rhyolite lava, with obvious secondary quartz. Not used for $\delta^{18}O$ analyses because of the lack of obviously primary phenocrysts. Mapped by Evans (1992) as Td-3.

EO-10: Quartz porphyry rhyolite lava. Mapped by Evans (1992) as Td-9.

EO-11: Pieces of rhyolite lava or rheomorphic tuff being mined at a gravel pit near the top of Dooley Mountain. Not from an in-place outcrop, but almost certainly sourced from within the pit, which all seems to be one unit.

EO-13: Crystal-poor tuff, no useable phenocrysts for $\delta^{18}O$. Likely to be unit Td-4 of Evans (1992).

EO-14: Plagioclase-phyric black vitrophyre dike forming large, competent outcrops up to 20m in height. The freshest rock we observed in the Dooley Mountain area, with nice glass.

Dinner Creek Tuffs:

EO-05: Welded Mascall Ignimbrite, from near the top of the above section. Contains abundant obsidian clasts and other lithics. This is the outcrop described in Streck and Ferns (2004). Dated at 16.2 ± 1.4 Ma (Fiebelkorn et al., 2015).

EO-5B: 1.5" diameter obsidian clast found within EO-5.

EO-17: Partially welded, pumice and crystal rich material from the bottom 2 m of the Dinner Creek Tuff along Highway 20 east of Juntura, OR. Age is approximately 15.5 Ma (Streck et al., 2015).

Malheur Gorge Region:

EO-15: Vitrophyre of plagioclase-phyric dark-colored rhyolite, taken from the entrance to a small slot canyon. Based on XRF analysis and comparison to other samples, this is likely the Cottonwood Mountain Rhyolite. The Cottonwood Mountain Rhyolite has been dated at 15.24 ± 0.31 Ma (Ferns and McClaughry, 2013).

EO-19: Upper part of Littlefield Rhyolite. Sample is black, plagioclase-phyric vitrophyre. Entire outcrop has a height of approximately 30m. Stratigraphically above EO-15, EO-17, and **EO-23.** Contains very minor pyroxene and magnetite.

EO-20: Taken from a dike in the outcrop of EO-19 that shows many mafic inclusions, showing clear evidence of magma mixing. The sampled material is the dark mafic material. Contains large plagioclase phenocrysts up to 1 cm.

EO-21: Cottonwood Mountain Rhyolite, type area (personal communication from Mark Ferns). Sample is mostly black vitric material with many large plagioclase phenocrysts and minor pyroxene and magnetite.

EO-23: Hunter Creek Basalt (actually silica-rich basaltic andesite). Mostly aphyric, contains <1% plagioclase crystals. Taken about 5m stratigraphically above EO-22. The Hunter Creek Basalt has been dated at 15.78 Ma by Lees (1994), even though it lies above the Dinner Creek Tuff and Cottonwood Mountain Rhyolite (see above).

EO-70: Lower Littlefield Rhyolite

EO-71: Lower Littlefield Rhyolite (personal communication from Mark Ferns) taken from a roadside outcrop stratigraphically below EO-19.

Lake Owyhee Region:

EO-26: Basal vitrophyre of the Rhyolite of McIntyre Ridge, which is ~60 m thick where sampled. Contains many large quartz and plagioclase phenocrysts. Directly below is the Tuff of Spring Creek.

EO-72: Rhyolite of McIntyre Ridge, from wall next to road. Less crystal-rich than EO-26.

EO-28: Spring Creek Tuff collected from within the associated Three Fingers Caldera, below **EO-26:** It contains small plagioclase phenocrysts and is altered to a green color in the sample area. The entire exposed outcrop is at least 250m thick. Tuff of Spring Creek is dated at 15.95 ± 0.06 Ma (Benson et al., 2013).

EO-29: Crystal rich rhyolite porphyry, with quartz and plagioclase. Appears to have erupted through the Tuff of Leslie Gulch as a post-caldera dome complex.

EO-30: Pumice-rich Tuff of Leslie Gulch. Part of a large block slumped from higher up the hillside. Almost completely aphyric. Tuff of Leslie Gulch is dated by Benson et al. (2013) at 15.91 ± 0.05 Ma, and assumed to correlate with the Tuff of Spring Creek.

EO-31: Sample taken from very edge of Mahogany Mountain Rhyolite flows. Contains plagioclase up to 1mm. Shows some cm-scale banding and flow structures

EO-73: Rhyolitic dike in Tuff of Leslie Gulch.

EO-74: Tuff of Leslie Gulch. Extremely crystal poor, but contains zircon and minor pyroxene.

McDermitt Sequence:

EO-32: Intracaldera Tuff of McDermitt. Collected intensely banded and rheomorphic porphyry material with ~10% quartz crystals. Nearby other parts of the outcrop are nearly aphyric. Secondary quartz veins are present but was avoided during the collection process. Intermediate in age between the Tuff of Trout Creek Mountains (EO-33) and the Tuff of Whitehorse Creek (EO-65).

EO-33: Tuff of Trout Creek Mountains. Welded pumice and lithic rich tuff. Taken from a 2m thick exposure in the McDermitt Caldera. Dated at 15.9 ± 0.3 by Rytuba and McKee (1984).

EO-34: Pumice from a minimally welded pumice and ash-rich layer. Interpreted as a pyroclastic flow deposit of the Tuff of Trout Creek Mountains (personal communication from Chris Henry). Collected near the rim of the McDermitt Caldera.

EO-35: Welded tuff collected from above EO-34 (with intervening welded Tuff of Trout Creek Mountains), breaks in tabulature, as does EO-32, and contains 5% small crystals. Interpreted as outflow Tuff of McDermitt (Chris Henry personal communication).

EO-36: Densely welded Tuff of Long Ridge (as mapped by Rytuba et al., 1983). Contains fiamme and ~10% crystals. Dated at 15.8 ± 0.6 (Rytuba et al., 1981).

Whitehorse Caldera:

EO-65: Tuff of Whitehorse Creek (Rytuba et al., 1983), collected from an outcrop exposed in a roadbed. Minimally welded and contains sparse plagioclase. Dated at 15.0 ± 0.3 Ma (Henry et al., 2012).

DeLamar-Silver City:

EO-50: Highly altered rhyolite from near DeLamar, Idaho. Rhyolites here erupted quickly around ~16.0 Ma, but precise ages of individual flows, like at Dooley Mountain, remains uncertain. (Halsor et al., 1988).

EO-51: Relatively fresh quartz-bearing rhyolite from near the contact with the Cretaceous granites of Silver City.

EO-53: Rhyolite poryphry from the road turn off to the DeLamar mine. Sampled from a boulder that was not in place.

EO-66: Cretaceous granite from just outside of Silver City.

Juniper Mountain:

EO-54: "Swisher Mountain Rhyolite" collected between DeLamar, Idaho and Jordan Valley, Oregon. Considered to be a lava flow and grouped with the broader Juniper Mountain complex,

and dated at 14.21 ± 0.13 by Manley and McIntosh (2004).

Northern Nevada Rift:

EO-55: Quartz and plagioclase-bearing rhyolite poryphyry from near Izzenhood Ranch, Sheep Creek Mountains, Nevada. Rhyolite from this dome field dated at 14.84 ± 0.04 Ma by John et al. (2000).

EO-56: Similar to EO-55, collected 3 km southeast.

EO-60: Part of the June Bell Rhyolite (Wallace, 1993). Contains sparse quartz.

EO-61: Older rhyolite poryphyry dike, dated at 14.3 ± 0.8 Ma (Wallace, 1993). Contains abundant plagioclase and quartz. Eastern of two separate outcrops interpreted by Wallace (1993) as offset by a fault.

EO-62: Older rhyolite porphyry of Wallace (1993). Collected from the bottom of an at least 150m thick flow sequence.

EO-63: Sample of older rhyolite poryphyry dike collected from the western of two outcrops. Similar to EO-61, but more altered in the glassy matrix. Phenocryst quality remains good.

Picture Gorge Basalts:

CRB-1: Basalt of Donnely Basin, contains sparse (~5%) phenocrysts of olivine, clinopyroxene, and plagioclase, taken from ~1m above the base of the flow. Sample is relatively fresh in appearance.

CRB-3: Taken from 2-3 flows above CRB-1, entablature is present, along with pahoehoe textures.

CRB-5: Columnar-jointed, olivine-bearing basalt.

CRB-7: Taken from under a columnar basalt outcrop.

CRB-9: A vertical dike-like outcrop (matches a dike location from Fig. 3.1) with vertical bedding. Olivines slightly weathered.

Imnaha Basalts:

CRB-IM-2: see GPS coordinates

CRB-IM-3: see GPS coordinates

Steens Basalts:

CRB-ST-1: see GPS coordinates

CRB-ST-2: see GPS coordinates

CRB-ST-3: see GPS coordinates

B.5. Supplementary figures and tables

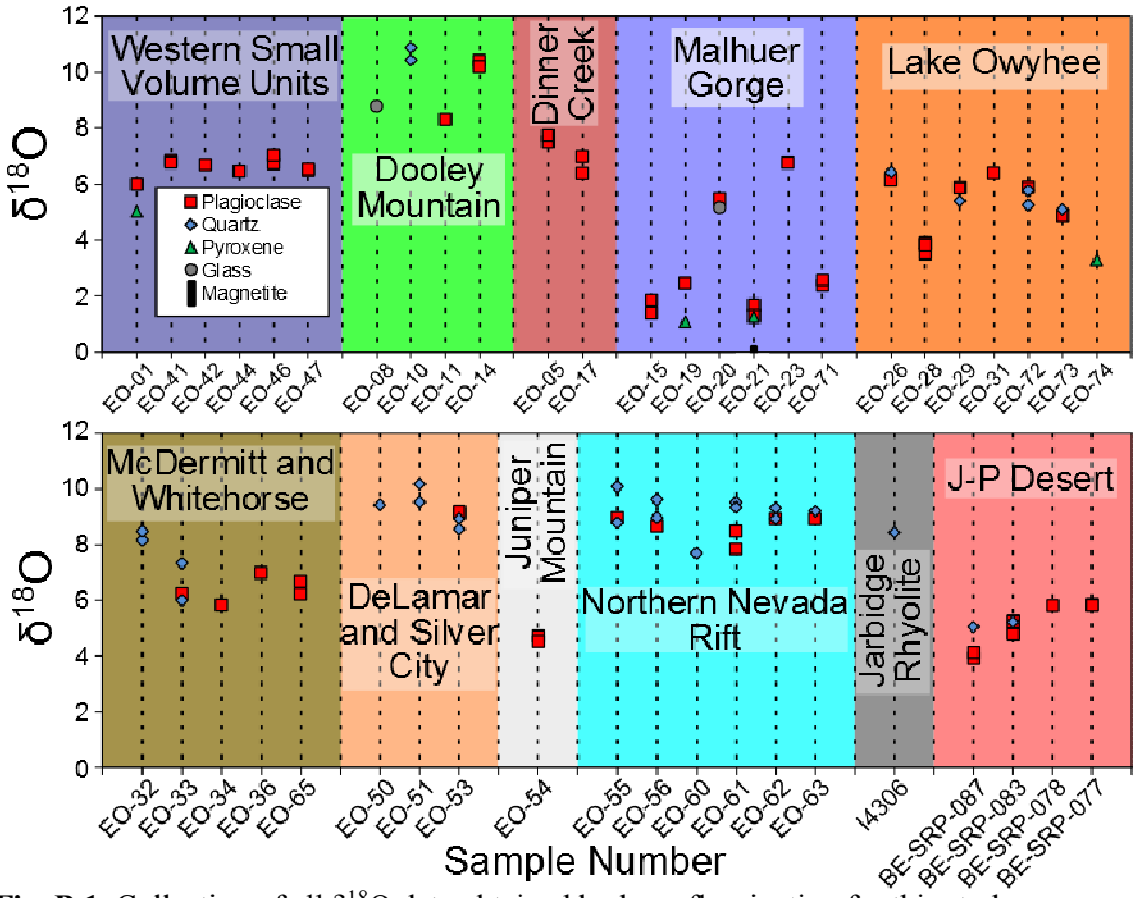

Fig. B.1. Collection of all $\delta^{18}O$ data obtained by laser fluorination for this study. Groupings of samples and sample numbers are as in the sample descriptions. Data for the J-P Desert and the Jarbidge Rhyolite is from Colón et al. (2015a).

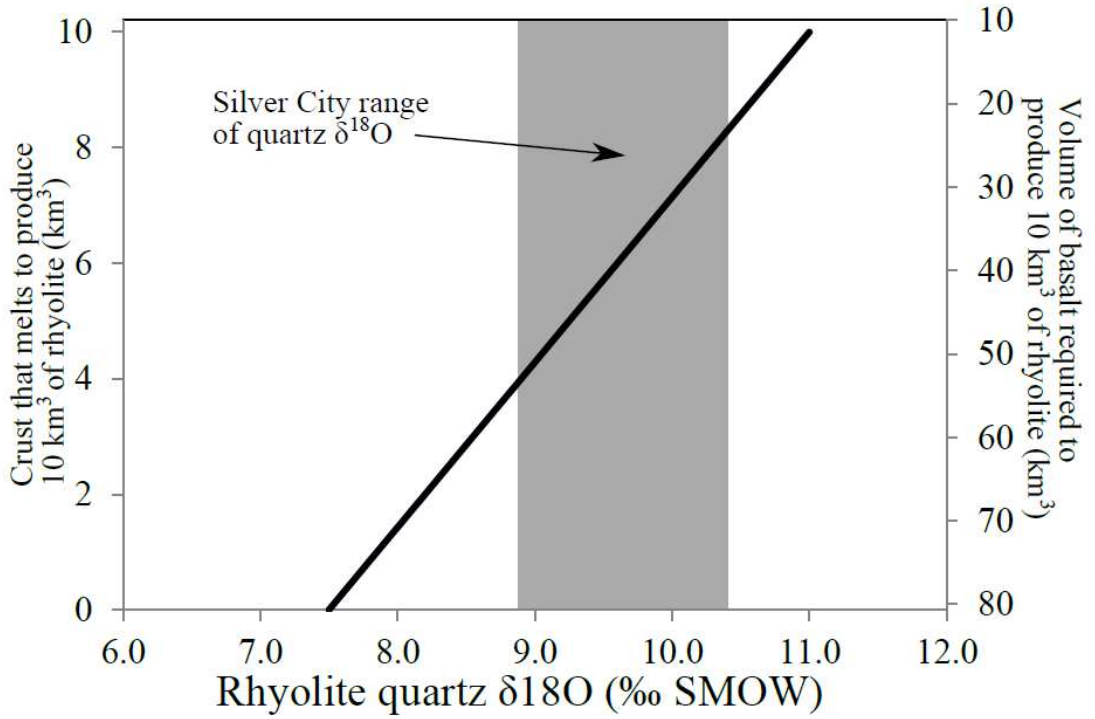

Fig. B.2. Plot calculating the crustal contribution for Silver City rhyolites. Crustal fractions are calculated by simple mass balance between normal quartz $\delta^{18}O = 7.5‰$ magma and melt of pure quartz $\delta^{18}O = 11.0‰$ granitic crust. The amount of required basalt is calculated using the specific and latent heat values for Columbia River Basalt and crustal assimilant from Bohrson and Sepra (2001), assuming that 1300°C basalt melts initially 200°C crust until both are at 950°C, the basalt is frozen, and the crust is completely melted. Remaining rhyolite is assumed to be derived from the fractionation of 10 times the rhyolite mass in basalt. While clearly a simplification, this diagram shows that it is far more energetically efficient to create rhyolite from melting crust than it is to create rhyolite from fractional crystallization of basalt. For these calculations we assumed a basalt specific gravity of 3.1 and a rhyolite specific gravity of 2.5

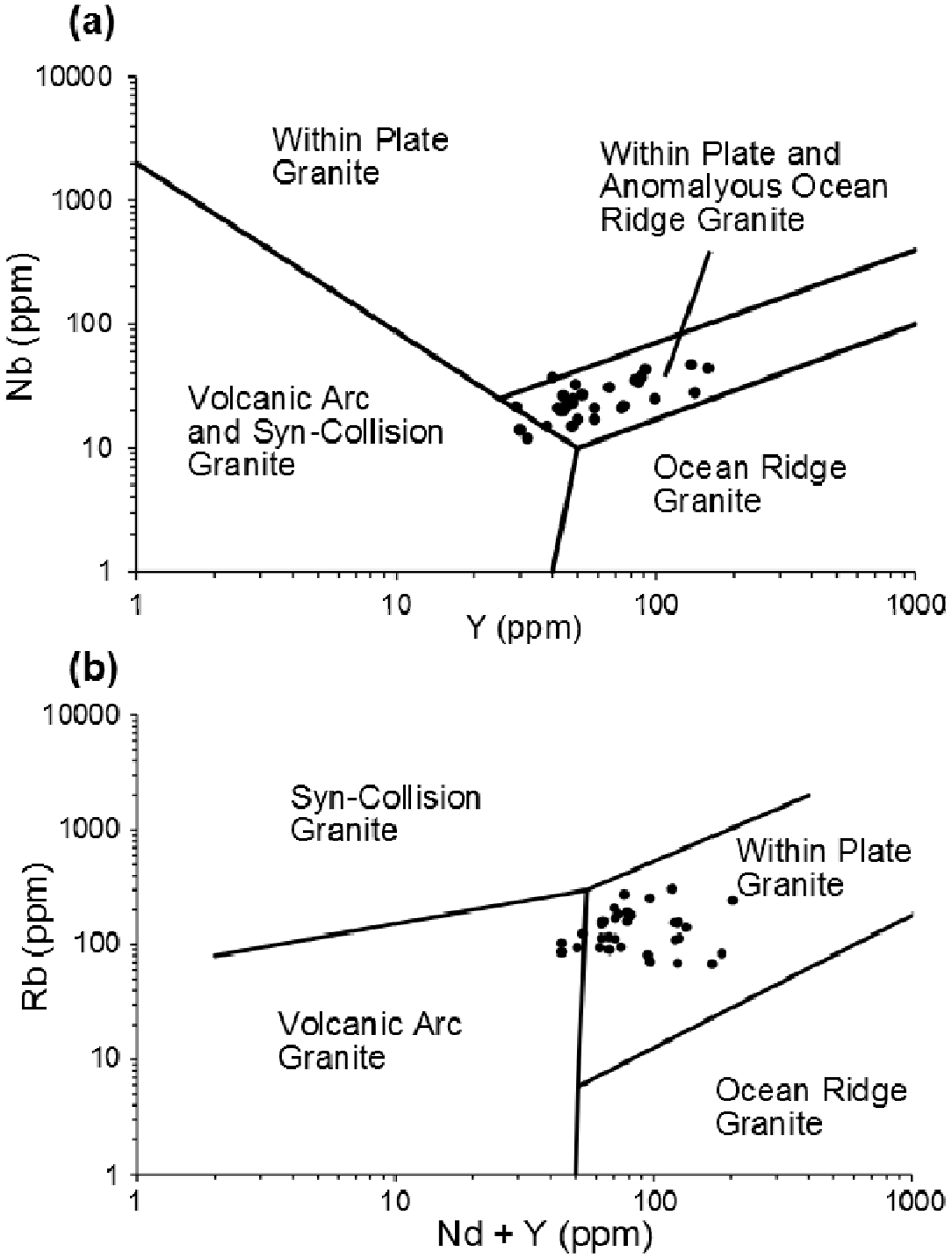

Fig. B.3. (a) Syn-CRB rhyolites from this study plotted on the discrimination diagrams of Pearce (1984) for Nb vs. Y (a) and Rb vs. Nd + Y (b). The syn-CRB rhyolites fall within the within-plate granite fields, providing further evidence that the syn-CRB rhyolites are derived from melting of the continental crust caused by heating from intruding CRB magmas.

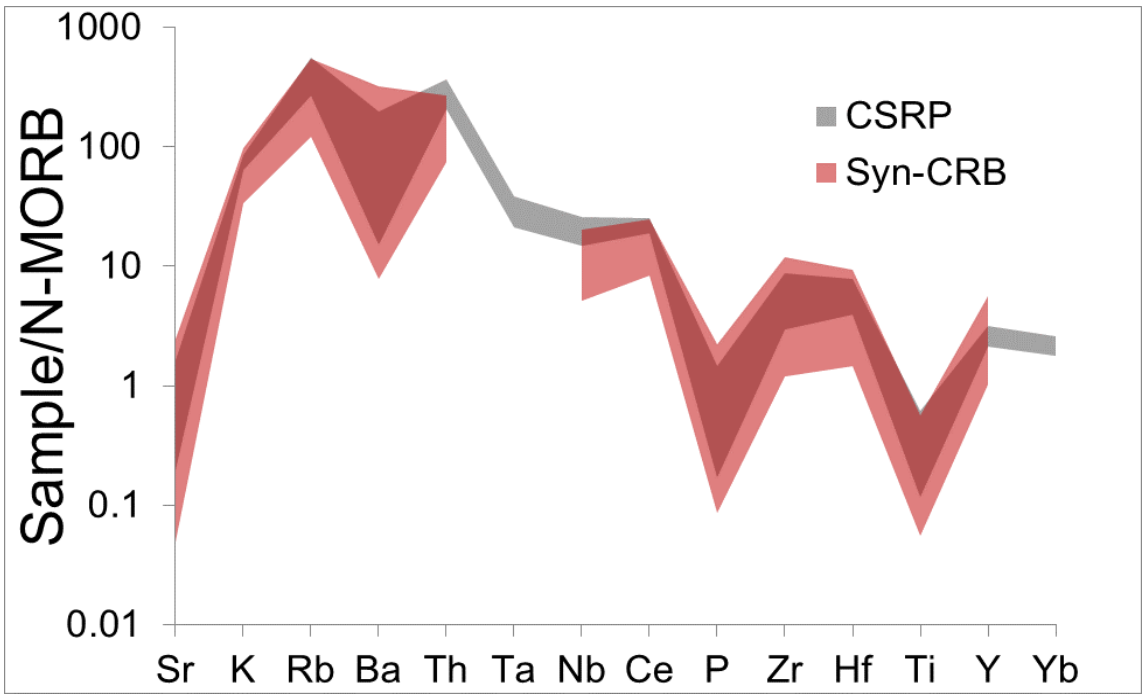

Fig. B.4. Comparison of the trace-element composition of the syn-CRB rhyolites with the range of compositions observed in the Central Snake River Plain (CSRP) by Bonnichsen et al. (2008), using the method of Pearce (1983). All values are normalized to the N-MORB values of Sun and McDonough (1989). The CSRP rhyolites represent the first organized volcanic centers on the Snake River Plain, which forms the classical hotspot track of the Yellowstone plume, and encompasses the Bruneau-Jarbidge and Twin Falls centers (**Fig**. 3.1). All units show relatively high concentrations of high field strength trace elements, in keeping with their intraplate origin.

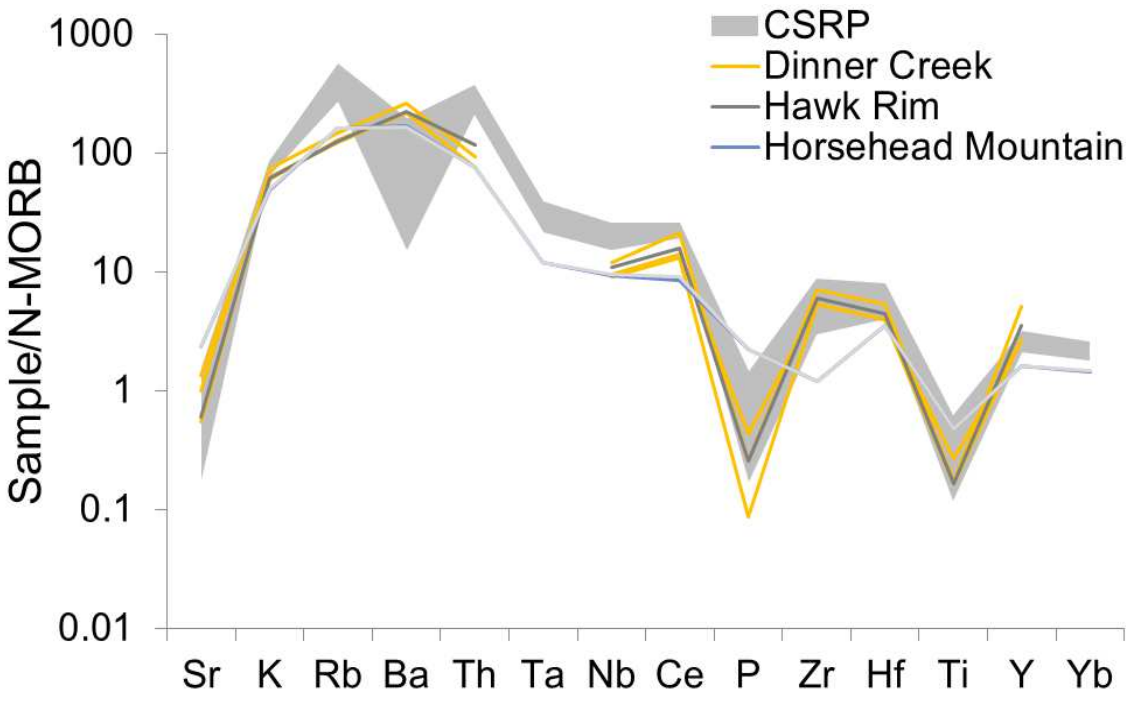

Fig. B.5. Dinner Creek eruptive center trace element compositions (and nearby units).

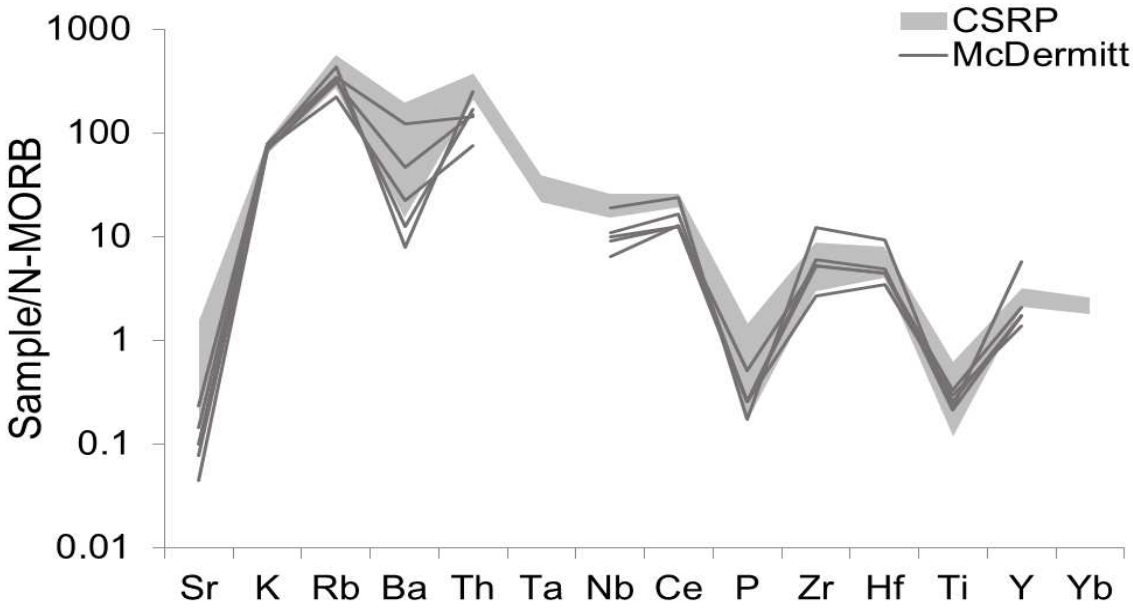

Fig. B.6. McDermitt eruptive center trace element compositions.

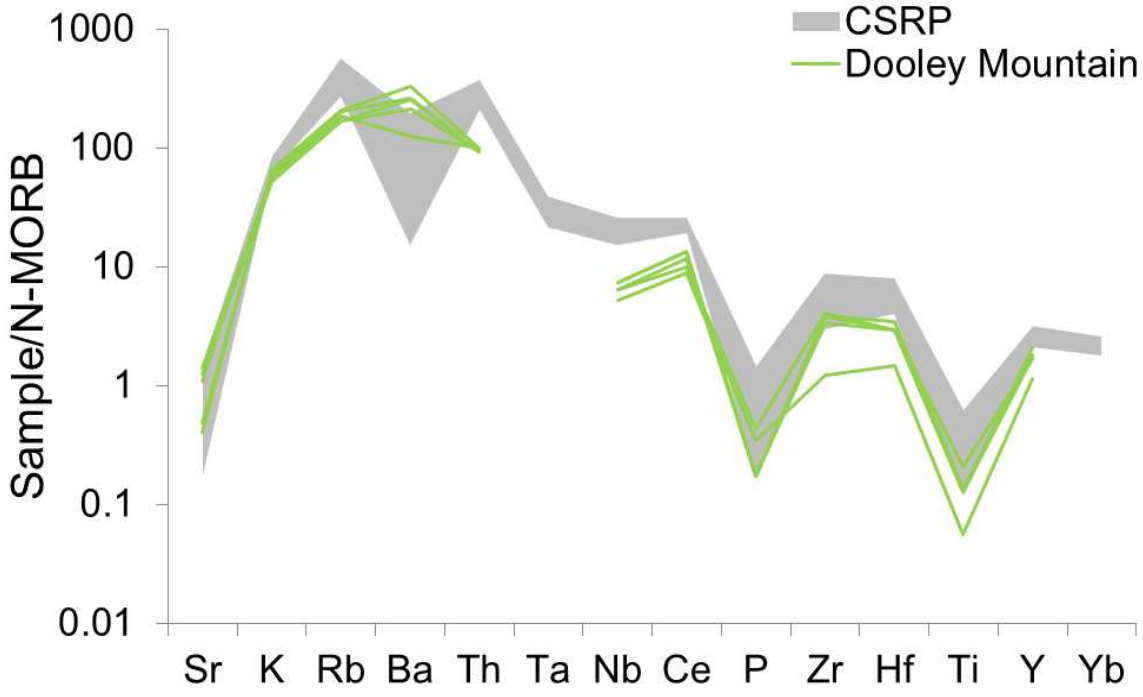

Fig. B.7. Dooley Mountain eruptive center trace element compositions.

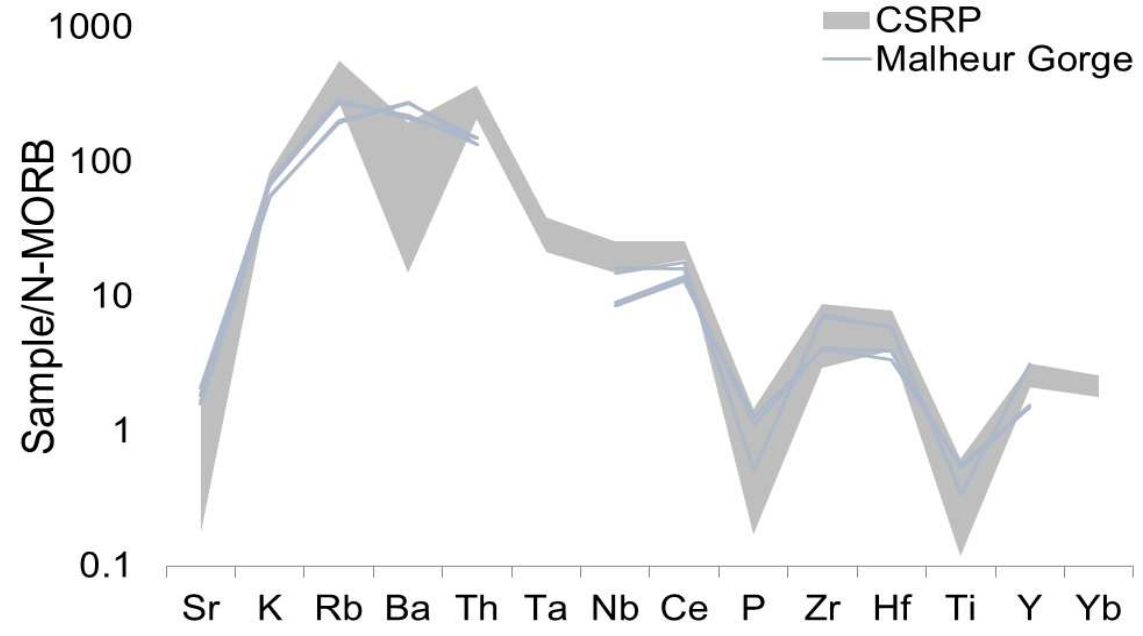

.

Fig. B.8. Malheur Gorge eruptive center trace element compositions.

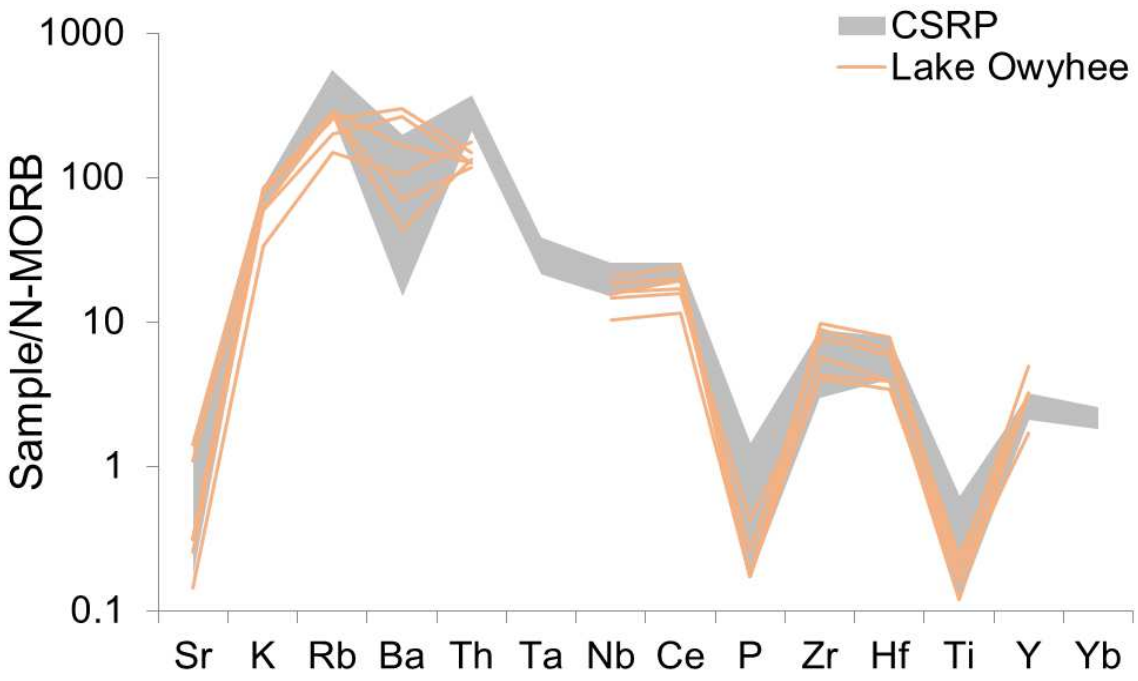

Fig. B.9. Lake Owyhee eruptive center trace element compositions.

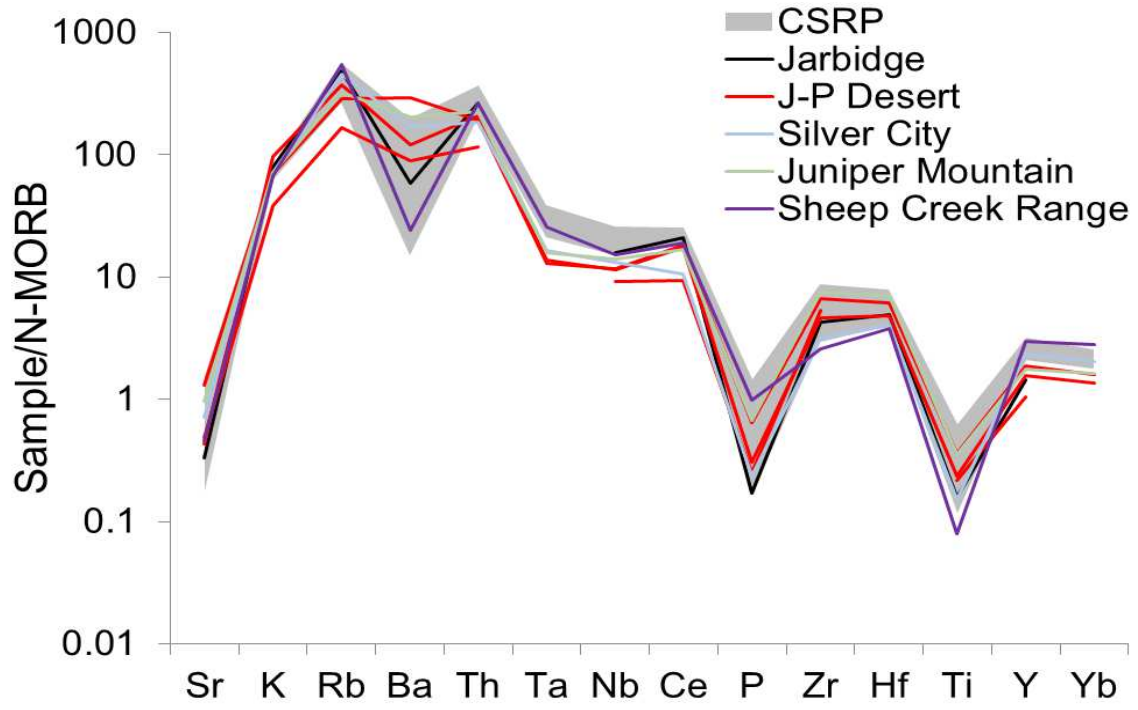

Fig. B.10. Eastern centers and the Northern Nevada Rift trace element compositions.

Figs. B.5-B.10. Comparison of individual syn-CRB eruptive centers to the CSRP data field of Bonnichsen et al. (2008). The McDermitt sequence is notable for its large negative Ba anomaly, which is reflected by CPT III in the Bonnichsen et al. (2008) data, but is not similar to most other syn-CRB or CSRP rhyolites. The Dinner Creek Tuff of the Malheur Gorge and the Mascall Tuff sequence are grouped together as the Dinner Creek Tuff sequence, as they have been correlated as having a source in that area by Streck et al. (2015). The Hawk Rim Tuff is also included here due to its geochemical similarity to the measured sample of Dinner Creek Tuff. EO-1 is not included in this plot because it shows evidence of post-depositional reworking. The here-named Malheur Gorge sequence includes the lower and upper Littlefield Rhyolite and the Rhyolite of Cottonwood Mountain, all of which are low-$\delta^{18}O$. The Lake Owyhee group includes the samples grouped in that category above. Dooley Mountain rhyolites, despite being universally high-$\delta^{18}O$, do not show dramatic trace element compositional differences from other syn-CRB rhyolites, and are broadly similar to the Dinner Creek sequence tuffs. The J-P Desert, Jarbidge, and Northern Nevada Rift (Sheep Creek Range) rhyolites erupted through the craton, and the former two contain zircons with extremely unradiogenic ε_{Hf} values as a result (Colón et al., 2015a). Despite this, they also show no significant differences in the plotted trace elements with other rhyolites erupted to the east through thinner crust, suggesting that the most important differences are indeed isotopic in nature. We also include rhyolites from Juniper Mountain and Silver city in this plot, as they erupted very near the edge of the craton.

Table B.1. Sample Locations

	Sample #	Latitude	Longitude		Sample #	Latitude	Longitude
Western Small Volume Units	EO-1	44.52958	-119.63462	**McDermitt and Whitehorse**	EO-32	42.01561	-117.94966
	EO-41	44.01583	-120.12569		EO-33	42.03786	-118.11494
	EO-42	43.15357	-119.84587		EO-34	42.06853	-118.15830
	EO-44	43.15774	-119.84806		EO-35	42.06870	-118.15869
	EO-46	43.15439	-119.76757		EO-36	42.12797	-118.15958
	EO-47	43.03500	-118.94263		EO-65	42.23831	-118.23201
Dooley Mountain	EO-8	44.52842	-117.84056	**DeLamar and Silver City**	EO-48	43.02249	-116.86279
	EO-9	44.54794	-117.84556		EO-50	43.02383	-116.86013
	EO-10	44.55413	-117.85099		EO-51	43.03112	-116.74268
	EO-11	44.57583	-117.82200		EO-53	43.02533	-116.85237
	EO-13	44.58833	-117.76081		EO-66	43.02578	-116.73234
	EO-14	44.58042	-117.81167	**Juniper Mountain**	EO-54	42.95926	-116.94326
Dinner Creek Tuffs	EO-5	44.47391	-118.77844	**Northern Nevada Rift**	EO-55	40.88692	-116.86920
	EO-5A	44.47419	-118.77944		EO-56	40.86248	-116.85822
	EO-17	43.76583	-118.02997		EO-57	41.25081	-116.80137
Malheur Gorge	EO-15	43.77633	-117.73059		EO-59	41.25756	-116.80120
	EO-19	43.78142	-117.69092		EO-60	41.25452	-116.80228
	EO-20	43.78142	-117.69092		EO-61	41.19101	-116.92813
	EO-21	44.07850	-117.54244		EO-62	41.19690	-116.93327
	EO-23	44.09750	-117.56150		EO-63	41.19396	-116.93439
	EO-71	43.79047	-117.70125	**Picture Gorge Basalt**	CRB-1	44.80628	-119.97703
Lake Owyhee	EO-26	43.48542	-117.13558		CRB-3	44.80731	-119.98111
	EO-28	43.48733	-117.13378		CRB-5	44.78253	-119.67969
	EO-29	43.37517	-117.11915		CRB-7	44.79092	-119.67919
	EO-30	43.31808	-117.21320		CRB-9	44.81328	-119.54261
	EO-31	43.23942	-117.11964	**Imnaha Basalt**	CRB-IM-2		
	EO-72	43.45378	-117.12042		CRB-IM-3		
	EO-73	43.29317	-117.25297	**Steens Basalt**	CRB-ST-1		
	EO-74	43.30469	-117.29067		CRB-ST-2		
					CRB-ST-3		

Table B.1. Locations for all samples taken for this study. These were measured using GPS and checked in Google Earth for accuracy.

Table B.2. Summary of all major phenocryst $\delta^{18}O$ measurements made for this study, along with ranges of zircon $\delta^{18}O$ measurements (see Table B.6), and subjective rankings of the freshness of the samples. These are as follows: (1) a very fresh sample, with preserved glass and minimal signs of chemical weathering, (2) a somewhat altered sample, but with generally good preservation of primary textures, (3) a badly altered sample, with complete loss of glass and the presence of many secondary phenocrysts. For samples in the third category, great care was taken to select the freshest magmatic phenocrysts possible. Secondary phenocrysts were typically easy to identify based on their unique morphology (such as singly-truncated quartz) and typically extremely anomalous $\delta^{18}O$ values (such as +15‰ in a rock with normal-$\delta^{18}O$ other major phenocrysts and zircons). This allows us to have confidence in our estimates of melt $\delta^{18}O$ values. Errors are considered to be 0.20‰ s.d. or better.

Table B.2. Collected major phenocryst oxygen isotopes (laser fluorination)

	Sample Number	Plagioclase $\delta^{18}O$ (‰ SMOW)				Quartz			Pyroxene	Glass	Zircon Range	Alteration Assessment	Melt
Western Small Volume Units	EO-01	5.98^{m}							5.02^{m}			2	6.5
	EO-41	6.83^{s}	6.77^{s}									2	7
	EO-42	6.69^{m}										1	6.9
	EO-44	6.45^{m}										1	6.7
	EO-46	7.01^{s}	6.73^{s}	7.03^{s}								1	7.2
	EO-47	6.48^{m}	6.54^{s}									1	6.7
Dooley Mountain	EO-08									8.78		3	8.8
	EO-10					10.87^{m}	10.42^{s}	10.35^{s}			8.70-9.89	2	10.0
	EO-11	8.30^{m}										3	8.5
	EO-14	10.40^{m}	10.20^{s}								9.51-10.76	1	10.5
Dinner Creek Tuffs	EO-05	7.51^{m}	7.73^{m}									2	7.9
	EO-17	6.98^{m}	6.37^{s}								5.40-6.80	2	6.9
Malheur Gorge	EO-15	1.84^{m}	1.41									1	1.9
	EO-19	2.47^{m}							1.16^{m}			1	2.6
	EO-20	5.46^{s}								5.16		1	5.7
	EO-21	1.68^{m}	1.27^{s}						1.30^{m}	-0.23*		1	2.8
	EO-23	6.76^{s}										1	6.4
	EO-71	2.39^{m}	2.57^{m}									1	2.7
Lake Owyhee	EO-26	6.15^{s}				6.42^{m}						1	5.9
	EO-28	3.52^{s}	3.92^{s}	3.88^{s}	3.82^{m}						1.65-2.78	3	4.0
	EO-29	5.85^{s}				5.40^{m}						2	4.9
	EO-31	6.38^{m}									5.07-6.29	2	6.6
	EO-72	5.87^{s}				5.77^{s}	5.25^{s}					2	5.0
	EO-73	4.86^{m}				5.09^{m}						2	4.6
	EO-74								3.29^{m}		1.95-3.28	3	4.8

*magnetite

Table B.2 (continued).

	Sample Number	Plagioclase $\delta^{18}O$ (‰ SMOW)		Quartz		Olivine				Alteration Assessment	Melt
McDermitt and Whitehorse	EO-32			8.16[m]	8.48[m]					1	7.8
	EO-33	6.24[s]		7.34[s]	6.00[m]					1	6.1
	EO-34	5.83[m]								1	6.1
	EO-36	6.99[s]								1	7.2
	EO-65	6.67[s]	6.22[s]							2	6.7
DeLamar and Silver City	EO-50			9.43[m]						3	8.9
	EO-51			10.18[s]	9.60[m]					2	9.4
	EO-53	9.1[s]	9.2[s]	8.93[s]	8.56[s]					2	8.2
	EO-66	9.7[s]		10.96[s]						1	10.4
Juniper Mountain	EO-54	4.71[s]	4.53[s]							1	4.9
Northern Nevada Rift	EO-55	8.96[s]		8.79[s]	10.09[s]					1	8.9
	EO-56	8.67[s]		8.97[s]	9.62[s]					1	8.8
	EO-60			7.70[s]						2	7.2
	EO-61	7.85[s]	8.48[s]	9.52[s]	9.34[m]					1	8.9
	EO-62	8.92[s]		8.93[s]	9.32[m]					1	8.6
	EO-63	8.92[m]		9.21[s]						2	8.7
Steens Basalt	CRB-ST-1	6.54	6.69			5.72				1	6.6
	CRB-ST-2	6.40	6.47							1	6.0
	CRB-ST-3	6.50	6.48							1	6.1
Picture Gorge Basalt	CRB-1	5.58[m]				5.30	5.08	5.11[m]	5.11[s]	1	6.0
	CRB-3					4.96[s]	5.06[s]	5.14[s]		1	5.9
	CRB-5	5.53[m]				5.00	4.52	4.96[s]	5.12[s]	1	5.9
	CRB-7	6.03[s]				5.33[m]	4.53[m]			1	6.0
	CRB-9	5.64[s]				5.00	5.56	5.07[m]	4.79[s]	1	5.8
Imnaha Basalt	CRB-IM-2	6.04	5.29							1	5.6
	CRB-IM-3	6.45								1	6.1

Table B.3. XRF data for a subset of samples. We also include calculated zircon saturation temperatures of units based on Watson and Harrison (WH, 1983) and Boehnke et al. (B, 2013), and whether zircon was found to be present. Strongly ruling out the presence of zircon is difficult and generally requires long-term dissolution of the rock in HF, so it has not been performed for most samples.

Table B.3. XRF Analyses of selected units

		Western Small Volume Units					Dooley Mountain (DM)
	Sample #	EO-01	EO-41	EO-42	EO-46	EO-46	EO-09
wt. %	SiO_2	68.40	74.38	53.81	67.61	67.65	79.86
	TiO_2	0.70	0.21	1.28	0.60	0.61	0.17
	Al_2O_3	16.62	13.60	17.85	15.01	15.05	13.85
	Fe_2O_3	5.23	2.58	9.98*	5.32*	5.22*	0.64
	MgO	2.82	0.88	4.09	0.77	0.78	0.09
	MnO	0.05	0.24	0.14	0.12	0.12	0.00
	CaO	2.27	0.95	7.71	2.70	2.71	0.14
	K_2O	2.51	4.38	1.33	3.59	3.59	4.80
	Na_2O	1.28	2.75	3.81	4.27	4.28	0.43
	P_2O_5	0.12	0.03	0.37	0.26	0.26	0.02
Ppm	Zr	282	446	128	267	268	285
	Zn	84	180	94	88	89	27
	Y	30	99	23	45	45	50
	V	66	118	213	27	28	8
	U	1	7	1	4	4	4
	Th	7	14	3	9	9	12
	Sr	153	54	557	209	210	36
	Sc	13	6	22	10	9	3
	Rb	86	69	19	90	90	116
	Pr	8	11				10
	Pb	14	20	6	14	14	14
	Ni	3	6	55	3	3	bdl
	Nd	24	46	22	33	30	32
	Nb	14	25	9.1	21.7	22.2	17
	La	28	54	19	35	34	50
	Hf	7	9				7
	Ga	21	25	20	20	20	23
	Cu	24	3	109	13	12	bdl
	Cr	17	4	18	3	2	9
	Ce	53	118	38	63	57	99
	Ba	402	1393	567	1052	1044	2044
Alteration assessment		2	2	1	1	1	3
Contains Zircon?							
Zircon Saturation Temperature (WH)		886	905	698	811	811	909
Zircon Saturation Temperature (B)		881	892	613	759	760	921

Table B.3 (continued).

		DM continued				Dinner Creek Tuffs (DC)	
	Sample #	EO-10	EO-11	EO-13	EO-14	EO-05	EO-05B
wt. %	SiO_2	78.05	76.85	74.96	74.36	72.60	74.54
	TiO_2	0.16	0.16	0.07	0.26	0.34	0.21
	Al_2O_3	13.42	12.81	15.32	13.26	14.36	13.03
	Fe_2O_3	0.53	1.33	1.02	2.64	3.74	2.51
	MgO	0.03	0.07	0.05	0.17	0.43	0.07
	MnO	0.00	0.01	0.03	0.04	0.05	0.06
	CaO	0.21	0.95	0.79	1.45	1.23	0.92
	K_2O	4.40	3.79	4.20	4.14	4.28	5.36
	Na_2O	3.18	4.00	3.51	3.63	2.92	3.30
	P_2O_5	0.02	0.02	0.04	0.05	0.05	0.01
ppm	Zr	251	285	91	299	390	390
	Zn	79	83	49	91	179	123
	Y	48	58	32	47	75	74
	V	14	14	4	12	18	2
	U	4	4	4	3	3	3
	Th	11	11	12	11	9	11
	Sr	97	112	44	125	121	89
	Sc	5	5	7	7	9	2
	Rb	114	95	103	94	71	81
	Pr	11	11	4	7	13	12
	Pb	10	16	18	13	14	6
	Ni	5	4	3	3	11	7
	Nd	51	51	11	34	54	46
	Nb	15	17	12	15	22	21
	La	54	54	34	37	57	51
	Hf	6	6	3	6	8	8
	Ga	20	22	20	20	25	22
	Cu	bdl	3	bdl	3	6	bdl
	Cr	16	16	8	9	7	bdl
	Ce	88	101	66	74	104	98
	Ba	1646	1594	777	1338	1367	1636
Alteration assessment		2	3	2	1	2	2
Contains Zircon?		yes			yes		
Zircon Saturation Temperature (WH)		854	842	760	842	888	868
Zircon Saturation Temperature (B)		833	808	718	804	869	836

Table B.3 (continued).

		DC continued	Malheur Gorge (MG)				
	Sample #	EO-17	EO-15	EO-15	EO-19	EO-20	EO-21
wt. %	SiO_2	73.41	71.89	72.11	70.88	48.74	71.94
	TiO_2	0.22	0.68	0.68	0.43	1.55	0.71
	Al_2O_3	14.38	12.71	12.61	12.41	19.12	13.04
	Fe_2O_3	2.93	4.33	4.28	6.47	10.85	4.05
	MgO	0.66	0.47	0.48	0.25	3.40	0.41
	MnO	0.10	0.09	0.09	0.11	0.22	0.08
	CaO	0.91	1.71	1.72	1.23	13.02	1.68
	K_2O	4.50	5.29	5.28	4.04	0.16	5.00
	Na_2O	2.86	2.69	2.62	4.10	2.58	2.93
	P_2O_5	0.03	0.13	0.13	0.06	0.36	0.15
ppm	Zr	522	303	305	546	63	300
	Zn	219	100	101	183	106	167
	Y	141	44	42	88	42	43
	V	16	13	13	10	300	14
	U	5	6	5	3	bdl	6
	Th	14	18	18	16	bdl	16
	Sr	49	166	165	149	386	190
	Sc	6	13	9	9	35	12
	Rb	68	161	160	114	bdl	151
	Pr	16	13	9	10	bdl	8
	Pb	19	23	22	18	bdl	26
	Ni	7	6	7	3	193	4
	Nd	74	41	34	62	23	37
	Nb	28	20	21	38	5	20
	La	81	55	54	63	8	51
	Hf	11	8	8	12	2	7
	Ga	25	19	19	25	19	19
	Cu	3	3	4	5	114	4
	Cr	7	6	6	10	188	8
	Ce	157	100	105	121	21	98
	Ba	1366	1342	1324	1730	165	1398
Alteration assessment		2	1	1	1	1	1
Contains Zircon?					no		no
Zircon Saturation Temperature (WH)		924	833	835	885	609	835
Zircon Saturation Temperature (B)		917	791	792	850	506	794

Table B.3 (continued).

		MG continued		Lake Owyhee (LO)			
	Sample #	EO-23	EO-71	EO-26	EO-28	EO-29	EO-30
wt. %	SiO_2	71.73	71.73	77.27	74.46	75.75	76.52
	TiO_2	0.43	0.43	0.15	0.30	0.20	0.21
	Al_2O_3	12.58	12.58	12.18	12.39	12.77	11.87
	Fe_2O_3	5.59	5.59	1.49	3.38	1.92	2.61
	MgO	0.20	0.20	0.14	0.43	0.12	0.06
	MnO	0.09	0.09	0.03	0.05	0.01	0.05
	CaO	1.17	1.17	0.45	1.27	0.28	0.20
	K_2O	4.06	4.06	4.44	5.61	6.09	6.10
	Na_2O	4.08	4.08	3.82	2.09	2.80	2.35
	P_2O_5	0.06	0.06	0.02	0.02	0.05	0.03
ppm	Zr	513	513	316	653	298	575
	Zn	179	179	118	187	119	142
	Y	86	86	87	91	86	88
	V	4	4	5	9	15	5
	U	4	4	4	4	2	4
	Th	18	18	16	18	14	15
	Sr	143	143	23	126	28	28
	Sc	12	12	bdl	2	bdl	bdl
	Rb	110	110	154	141	156	159
	Pr	11	11	14	16	12	13
	Pb	18	18	19	14	14	18
	Ni	8	8	4	9	6	7
	Nd	60	60	62	61	49	62
	Nb	35	35	37	43	34	37
	La	73	73	71	80	60	66
	Hf	12	12	8	13	7	12
	Ga	25	25	24	25	24	22
	Cu	2	2	2	3	8	2
	Cr	2	2	4	4	10	7
	Ce	134	134	144	151	118	128
	Ba	1716	1716	273	1900	443	1047
Alteration assessment		1	1	1	3	1	3
Contains Zircon?			no		yes		
Zircon Saturation Temperature (WH)		733	883	852	928	852	923
Zircon Saturation Temperature (B)		646	849	819	913	821	910

Table B.3 (continued).

		LO Continued		McDermitt (MD)			
	Sample #	EO-31	EO-74	EO-32	EO-33	EO-34	EO-35
wt. %	SiO_2	77.09	76.49	71.79	75.68	76.03	75.75
	TiO_2	0.21	0.25	0.42	0.36	0.28	0.27
	Al_2O_3	12.27	14.23	13.02	12.21	10.98	11.43
	Fe_2O_3	1.61	2.87	4.29	1.97	4.97	3.22
	MgO	0.01	0.16	0.13	0.13	0.14	0.03
	MnO	0.02	0.05	0.05	0.00	0.10	0.06
	CaO	0.66	0.35	0.34	0.12	0.28	0.14
	K_2O	4.25	2.44	5.67	5.16	5.47	4.97
	Na_2O	3.85	3.14	4.23	4.35	1.72	4.10
	P_2O_5	0.02	0.02	0.06	0.03	0.02	0.03
ppm	Zr	420	725	386	197	892	438
	Zn	73	222	141	80	296	149
	Y	47	137	58	38	159	48
	V	15	3	10	19	10	10
	U	5	4	4	4	8	6
	Th	15	21	17	9	30	20
	Sr	98	13	21	7	13	4
	Sc	7	3	bdl	17	4	bdl
	Rb	112	84	191	125	244	185
	Pr	11	19	10	14	18	13
	Pb	13	30	8	22	37	26
	Ni	15	3	3	bdl	8	4
	Nd	31	94	36	5	101	66
	Nb	24	47	21	15	44	25
	La	43	99	50	39	90	69
	Hf	8	16	9	7	19	10
	Ga	18	27	23	33	30	26
	Cu	bdl	4	5	bdl	5	2
	Cr	9	5	8	21	6	5
	Ce	86	185	93	95	179	124
	Ba	1644	660	771	141	49	79
Alteration assessment		2	1	1	1	1	1
Contains Zircon?		yes	yes	yes			
Zircon Saturation Temperature (WH)		879	994	854	796	984	870
Zircon Saturation Temperature (B)		851	1022	813	748	993	835

Table B.3 (continued).

		MD continued	Silver City	Juniper Mountain	Northern Nevada Rift
wt. %	Sample #	EO-36	EO-51	EO-54	EO-55
	SiO_2	73.77	76.41	73.24	78.00
	TiO_2	0.32	0.19	0.45	0.10
	Al_2O_3	12.29	12.96	12.99	11.17
	Fe_2O_3	3.86	1.69*	3.35*	1.44*
	MgO	0.08	0.13	0.20	0.16
	MnO	0.09	0.02	0.03	0.02
	CaO	0.35	0.82	1.07	1.09
	K_2O	5.11	5.23	5.28	4.98
	Na_2O	4.09	2.55	3.38	3.03
	P_2O_5	0.03	0.03	0.08	0.12
ppm	Zr	384	232	555	193
	Zn	137	100	62	54
	Y	48	66	49	83
	V	6	9	18	7
	U	5	6	5	7
	Th	18	22	27	32
	Sr	9	64	87	41
	Sc	5	3	5	2
	Rb	170	255	181	307
	Pr	9			
	Pb	22	34	26	33
	Ni	bdl	2	3	1
	Nd	48	47	54	55
	Nb	23	30.8	32.6	35.3
	La	49	46	78	73
	Hf	9			
	Ga	26	25	20	23
	Cu	4	5	6	3
	Cr	3	4	4	3
	Ce	93	79	127	143
	Ba	290	1062	1281	152
Alteration assessment		1	2	1	1
Contains Zircon?					
Zircon Saturation Temperature (WH)		858	834	899	794
Zircon Saturation Temperature (B)		820	802	871	745

*Fe_2O_3 calculated from FeO^T

Table B.4. ICP-MS trace element analyses of selected units

	Western Small Volume			Silver City	Juniper Mountain	Northern Nevada Rift
Sample #	EO-42	EO-46	EO-46*	EO-51	EO-54	EO-55
La ppm	19.35	31.77	32.14	46.17	76.16	74.16
Ce ppm	37.73	62.49	62.64	84.41	134.04	151.40
Pr ppm	5.09	7.94	7.98	12.11	15.88	17.55
Nd ppm	21.12	32.25	32.46	48.13	55.58	59.27
Sm ppm	4.91	7.70	7.69	12.29	10.69	12.07
Eu ppm	1.63	1.88	1.91	0.67	1.42	0.35
Gd ppm	4.73	7.74	7.75	12.41	9.43	10.44
Tb ppm	0.75	1.32	1.28	2.12	1.57	1.96
Dy ppm	4.45	8.12	8.26	12.76	9.65	12.87
Ho ppm	0.87	1.70	1.70	2.56	1.92	2.75
Er ppm	2.34	4.71	4.73	6.86	5.30	8.23
Tm ppm	0.34	0.70	0.71	1.01	0.79	1.32
Yb ppm	2.02	4.41	4.48	6.25	4.96	8.56
Lu ppm	0.30	0.71	0.71	0.91	0.75	1.26
Ba ppm	559	1064	1074	1098	1313	158
Th ppm	1.73	8.86	8.82	22.93	27.96	32.12
Nb ppm	8.41	20.75	21.02	28.85	30.95	34.30
Y ppm	22.72	44.55	44.92	64.75	48.40	80.66
Hf ppm	3.24	7.15	7.14	8.32	14.45	7.71
Ta ppm	0.56	1.57	1.56	2.19	2.09	3.37
U ppm	0.65	3.51	3.55	5.19	5.26	8.79
Pb ppm	5.51	13.67	13.73	32.86	26.30	31.81
Rb ppm	18.1	87.6	87.7	245.5	174.5	294.9
Cs ppm	0.78	3.36	3.44	5.74	2.42	7.63
Sr ppm	554	209	211	65	87	41
Sc ppm	21.3	9.0	9.6	2.4	5.1	1.5
Zr ppm	128	266	269	233	564	192

Table B.5. Zircon Lu-Hf isotope analyses (LA-ICP-MS)

	Grain # (spot #)	$^{176}Hf/^{177}Hf$	2 s.e.	$^{176}Lu/^{177}Hf$	2 s.e.	$^{176}Yb/^{177}Hf$	2 s.e.	$^{178}Hf/^{177}Hf$	2 s.e.	$^{180}Hf/^{177}Hf$	2 s.e.	ε_{Hf}	2 s.e.
EO-14 (Dooley)	1 (1)	0.282879	0.000037	0.002482	0.000032	0.07039	0.00073	1.467203	0.000056	1.88701	0.00014	3.3	1.3
	11 (1)	0.282913	0.000039	0.003591	0.000055	0.1048	0.0022	1.467213	0.000068	1.88711	0.00015	4.5	1.4
	13 (1)	0.282931	0.000036	0.0010430	6.6E-06	0.03020	0.00029	1.467185	0.000059	1.88690	0.00015	5.2	1.3
	22 (1)	0.282900	0.000055	0.003251	0.000070	0.0984	0.0031	1.467141	0.000069	1.88704	0.00015	4.1	1.9
	34 (1)	0.282835	0.000037	0.00626	0.00016	0.2124	0.0044	1.467213	0.000044	1.887006	0.000098	1.8	1.3
EO-17 (Dinner C.)	6 (1)	0.283032	0.000075	0.00254	0.00022	0.0692	0.0061	1.467162	0.000099	1.88705	0.00019	8.7	2.6
	25 (1)	0.282997	0.000038	0.00295	0.00015	0.0841	0.0048	1.467144	0.000053	1.88701	0.00017	7.5	1.3
	29 (1)	0.283012	0.000051	0.00343	0.00016	0.0988	0.0049	1.467112	0.000066	1.88705	0.00012	8.0	1.8
	48 (1)	0.283001	0.000042	0.001413	0.000014	0.03928	0.00062	1.467140	0.000048	1.88693	0.00010	7.6	1.5
	48 (4)	0.283017	0.000042	0.001298	0.000068	0.0360	0.0022	1.467118	0.000050	1.88697	0.00013	8.2	1.5
EO-28 (L. Owyhee)	11 (1)	0.282868	0.000039	0.006214	0.000085	0.2189	0.0053	1.467201	0.000056	1.88690	0.00011	2.9	1.4
	14 (1)	0.282769	0.000064	0.00164	0.00013	0.0477	0.0031	1.467170	0.000046	1.88713	0.00022	-0.6	2.3
	16 (2)	0.282887	0.000035	0.00341	0.00018	0.1153	0.0072	1.467196	0.000044	1.88699	0.00010	3.6	1.2
	19 (1)	0.282848	0.000033	0.001526	0.000041	0.04803	0.00094	1.467197	0.000047	1.88687	0.00010	2.2	1.2
	30 (1)	0.282832	0.000031	0.001668	0.000046	0.05228	0.00092	1.467198	0.000048	1.88702	0.00011	1.7	1.1
EO-31 (L. Ow.)	16 (1)	0.282877	0.000030	0.001442	0.000039	0.0442	0.0013	1.467183	0.000044	1.886873	0.000090	3.3	1.1
	22 (1)	0.282938	0.000034	0.001757	0.000079	0.0506	0.0030	1.467157	0.000043	1.88699	0.00012	5.4	1.2
	36 (3)	0.283008	0.000032	0.00296	0.00032	0.093	0.011	1.467174	0.000059	1.886756	0.000096	7.9	1.1
EO-74 (Lake Owyhee)	11 (1)	0.282906	0.000033	0.0010720	3.6E-06	0.03263	0.00043	1.467190	0.000055	1.88673	0.00024	4.3	1.2
	19 (1)	0.282840	0.000051	0.002409	0.000086	0.0731	0.0035	1.467121	0.000066	1.88713	0.00015	1.9	1.8
	25 (1)	0.282785	0.000040	0.001738	0.000038	0.0500	0.0011	1.467153	0.00006	1.88712	0.00014	0.0	1.4
	41 (1)	0.282831	0.000031	0.002189	0.000031	0.06788	0.00098	1.467180	0.000050	1.887013	0.000097	1.6	1.1
	46 (1)	0.282821	0.000045	0.001670	0.000083	0.0497	0.0019	1.467159	0.000037	1.88711	0.00018	1.3	1.6
	46 (2)	0.282822	0.000055	0.001211	0.000033	0.03283	0.00092	1.467152	0.000052	1.88698	0.00014	1.3	1.9
	49 (1)	0.282970	0.000042	0.00627	0.00066	0.226	0.026	1.467218	0.000037	1.88690	0.00012	6.5	1.5
	49 (3)	0.282837	0.000027	0.000778	0.0000060	0.02425	0.00016	1.467171	0.000042	1.886893	0.000091	1.8	1.0

Table B.6. Zircon oxygen isotope analyses (SIMS)

	Grain # (Spot #)	$\delta^{18}O$ (‰ SMOW)	2 s.e.
EO-10 (Dooley Mountain)	3 (1)	8.85	0.17
	5 (1)	9.49	0.19
	7 (1)	9.53	0.19
	8 (1)	9.89	0.19
	8 (2)	9.67	0.16
	10 (1)	9.72	0.16
	10 (2)	9.49	0.18
	11 (1)	8.94	0.17
	12 (1)	9.56	0.20
	13 (1)	9.12	0.17
	14 (1)	9.53	0.16
	16 (1)	8.70	0.18
EO-14 (Dooley Mountain)	1 (1)	10.40	0.17
	2 (1)	10.33	0.17
	5 (1)	9.88	0.15
	7 (1)	10.29	0.19
	9 (1)	10.03	0.18
	11 (1)	10.76	0.17
	11 (2)	9.92	0.18
	13 (1)	10.61	0.19
	18 (1)	10.27	0.18
	20 (1)	10.00	0.16
	22 (1)	9.88	0.19
	24 (1)	10.33	0.16
	24 (2)	10.16	0.19
	25 (1)	10.22	0.17
	28 (1)	9.62	0.17
	28 (2)	9.51	0.15
	30 (1)	9.73	0.15
	30 (2)	9.68	0.16
	34 (1)	10.32	0.16
	34 (2)	10.32	0.16

	Grain # (Spot #)	$\delta^{18}O$ (‰ SMOW)	2 s.e.
EO-17 (Dinner Creek)	6 (1)	5.61	0.15
	9 (1)	5.60	0.17
	9 (2)	5.43	0.18
	11 (1)	5.58	0.18
	15 (1)	5.57	0.17
	20 (1)	5.52	0.16
	25 (1)	5.56	0.16
	25 (2)	5.40	0.18
	26 (1)	5.58	0.15
	26 (2)	5.46	0.18
	29 (1)	5.62	0.16
	29 (2)	5.51	0.16
	32 (1)	5.43	0.15
	32 (2)	5.64	0.16
	33 (1)	5.54	0.17
	36 (1)	5.71	0.17
	36 (2)	5.73	0.16
	43 (1)	5.63	0.17
	43 (2)	5.72	0.17
	44 (2)	6.65	0.18
	45 (1)	5.60	0.15
	45 (2)	5.64	0.16
	46 (1)	5.61	0.15
	46 (2)	5.69	0.17
	48 (1)	6.42	0.16
	48 (3)	6.64	0.19
	48 (4)	6.80	0.18
	49 (1)	6.00	0.15
	49 (2)	6.17	0.18

Table B.6 (continued).

	Grain # (Spot #)	$\delta^{18}O$ (‰ SMOW)	2 s.e.
EO-28 (Lake Owyhee)	11 (1)	2.77	0.18
	14 (1)	2.31	0.17
	14 (2)	2.78	0.15
	16 (1)	2.45	0.17
	16 (2)	2.78	0.15
	17 (1)	2.48	0.17
	19 (1)	1.65	0.16
	19 (2)	1.65	0.14
	21 (1)	2.29	0.16
	22 (2)	2.49	0.15
	27 (1)	2.66	0.19
	28 (1)	2.31	0.16
	30 (1)	2.35	0.18
	32 (1)	2.28	0.16
	34 (1)	2.41	0.18
	36 (1)	1.97	0.16
EO-31 (Lake Owyhee)	4 (1)	5.07	0.17
	4 (2)	5.22	0.17
	5 (1)	5.38	0.16
	12 (1)	5.58	0.15
	12 (2)	5.31	0.16
	16 (1)	5.67	0.18
	16 (2)	5.29	0.16
	17 (1)	5.36	0.17
	17 (2)	5.44	0.15
	19 (1)	5.46	0.20
	22 (1)	5.30	0.17
	22 (2)	5.15	0.18
	23 (1)	5.44	0.17
	27 (1)	5.40	0.19
	27 (2)	5.56	0.19
	30 (1)	5.54	0.18
	30 (2)	5.47	0.15
	34 (1)	5.28	0.16
	34 (2)	5.71	0.19
	36 (1)	6.29	0.17
	36 (2)	5.31	0.19
	36 (3)	5.83	0.16

	Grain # (Spot #)	$\delta^{18}O$ (‰ SMOW)	2 s.e.
EO-74 (Lake Owyhee)	9 (1)	3.20	0.16
	10 (1)	2.86	0.17
	11 (1)	2.60	0.16
	12 (1)	2.91	0.15
	14 (1)	2.90	0.17
	14 (2)	3.09	0.18
	19 (1)	3.28	0.21
	25 (1)	2.75	0.16
	30 (1)	2.90	0.17
	30 (2)	3.12	0.18
	32 (1)	3.06	0.19
	35 (1)	3.04	0.19
	35 (2)	3.21	0.18
	41 (1)	3.32	0.16
	44 (1)	3.15	0.23
	44 (2)	2.91	0.17
	46 (1)	2.03	0.16
	46 (2)	2.58	0.17
	46 (3)	1.95	0.24
	49 (1)	2.29	0.16
	49 (2)	2.68	0.15
	49 (3)	2.75	0.18

APPENDIX C

MATERIAL FOR CHAPTER IV

Contents:

C.1. Supplementary figures and tables

C.1. Supplementary figures and tables

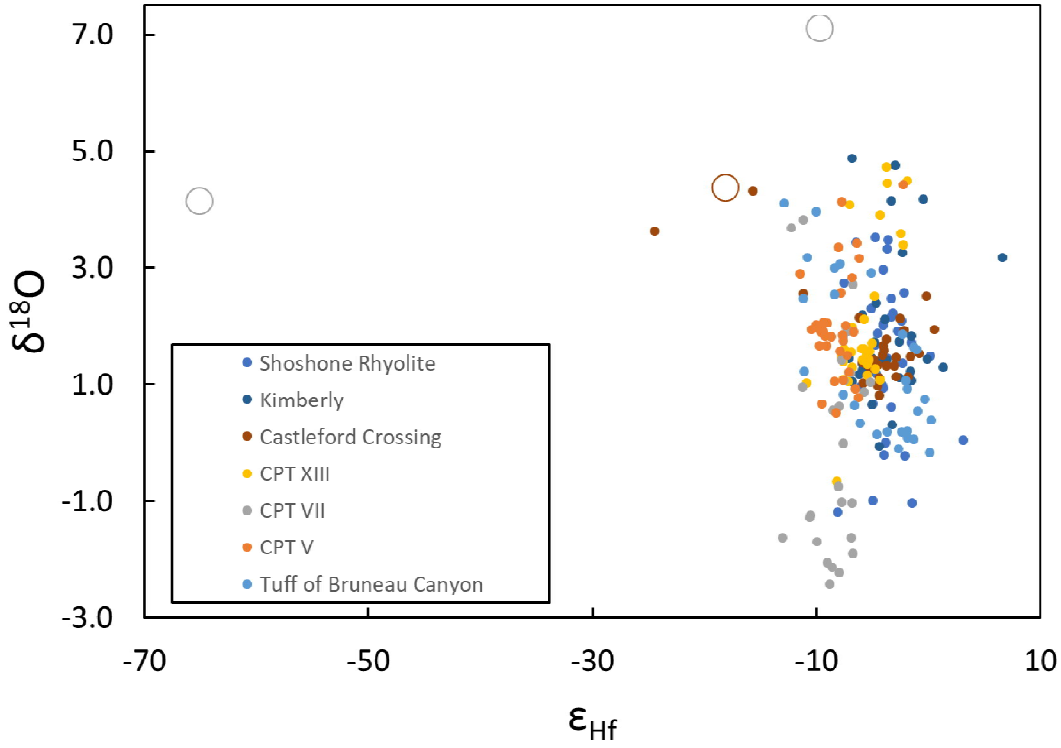

Fig. C.1. Oxygen and hafnium isotopes for zircons from this study. This is a more limited version of Fig. 4.9 from the main text, with only data new to this study. Open circles are xenocrysts.

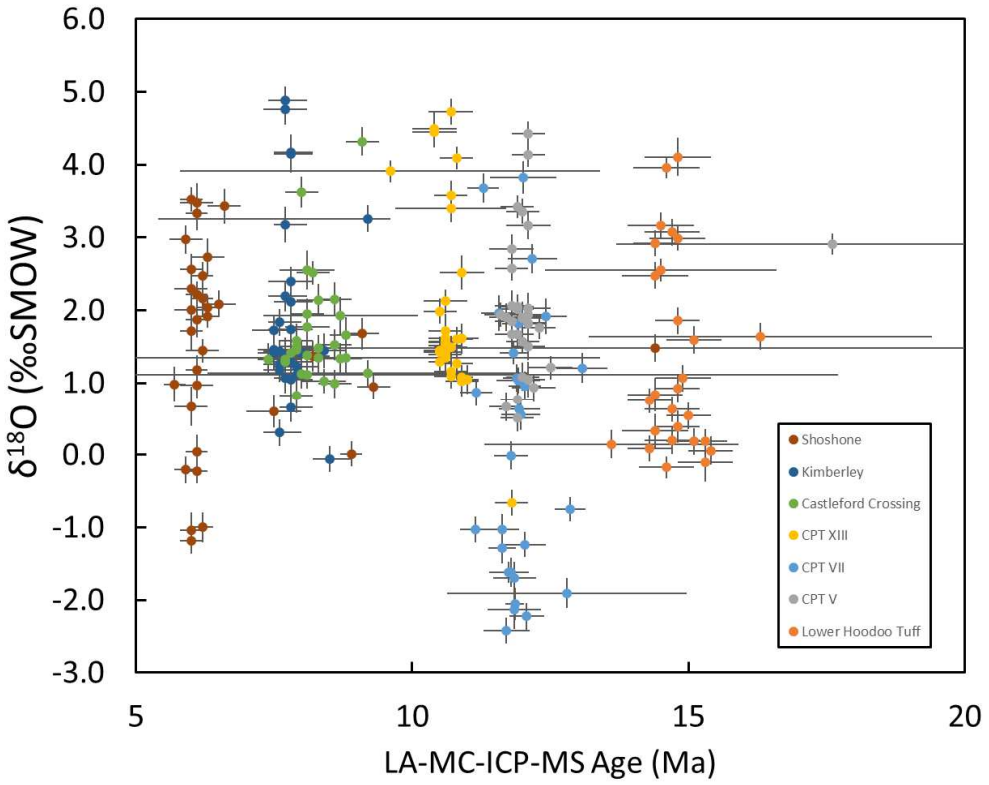

Fig. C.2. Laser ablation MC-ICP-MS ages vs SIMS spot analyses for $\delta^{18}O$ from this study. This data is reproduced along with other data from other centers in Fig. 4.10 in the main text. Errors are 2σ.

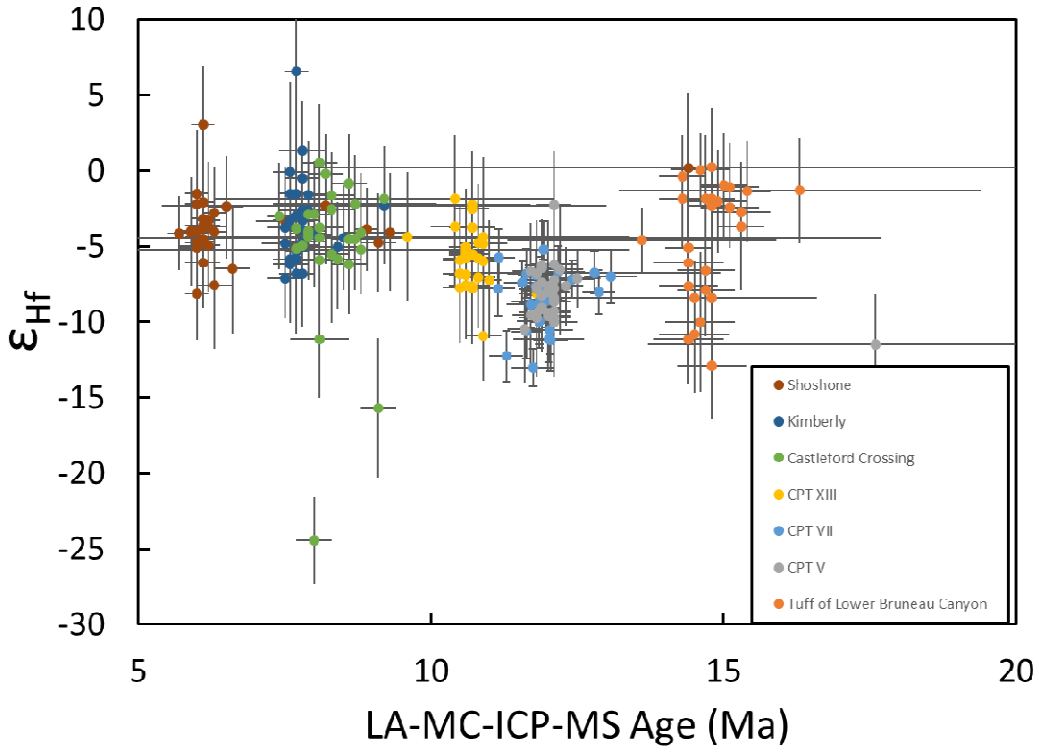

Fig. C.3. Laser ablation MC-ICP-MS ages vs LA-MC-ICP-MS spot analyses for ε_{Hf} from this study. This data is reproduced along with other data from other centers in Fig. 4.10 in the main text. Errors are 2σ.

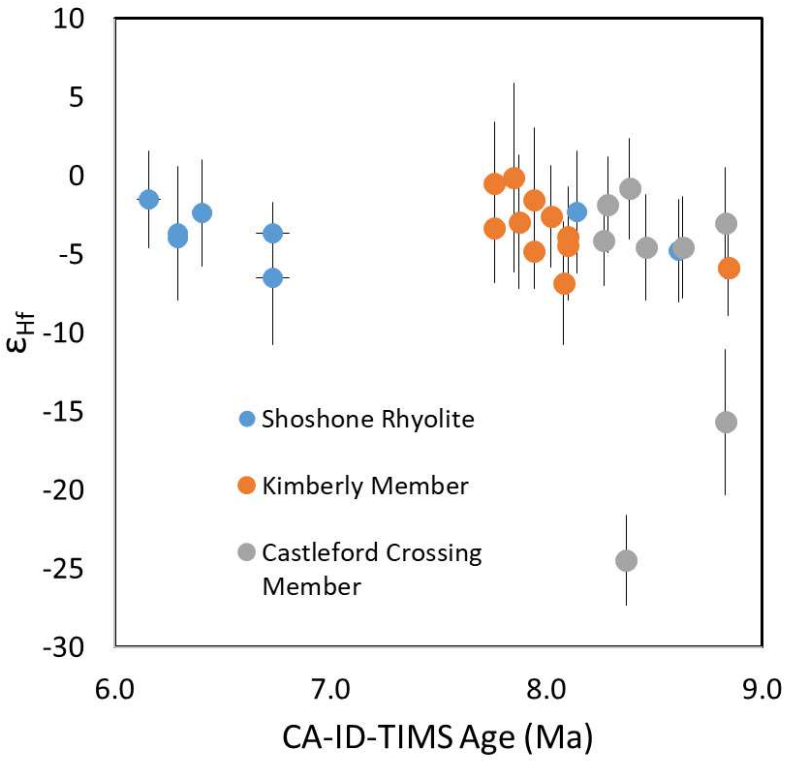

Fig. C.4. CA-ID-TIMS ages vs LA-MC-ICP-MS spot analyses for ε_{Hf} from this study. This figure is complementary to Fig. 4.8 in the main text, but has fewer data points because there are several grains for which we have TIMS ages and SIMS $\delta^{18}O$ analyses but not measurements of ε_{Hf}. Errors are 2σ.

Table C.1. Sample locations for Bruneau-Jarbidge Units

Unit	***Sample Number***	***Latitude***	***Longitude***
Tuff of Bruneau Canyon	ID-14	41°57.602’	-115°39.810’
CPT V	ID-13	41°57.602’	-115°39.810’
CPT VII	ID-3	41°55.995’	-115°25.402’
CPT XIII	ID-9	41°56.576’	-115°25.336’

Table C.2. Zircon laser ablation and ion microprobe data

Unit	*Spot Name*	*Core /Rim**	*Age (Ma)*	*2σ (Ma)*	ε_{Hf}	*2 s.e.*	$\delta^{18}O$ *(SMOW)*	*2σ (‰)*
CPT VII	ID3_2@1	c					-1.27	0.18
	ID3_2@2	r					-1.31	0.22
	ID3_3@1	c					1.62	0.18
	ID3_5@1	c	86.35	1.43	-9.7	1.4	7.10	0.18
	ID3_5@2	r	11.62	0.31	-6.8	1.6	-1.03	0.21
	ID3_4@1	c					-1.19	0.26
	ID3_6@1	c	11.85	0.39	-10.0	1.5	-1.70	0.23
	ID3_7@1	c	1672.26	24.08	-65.0	1.7	4.14	0.19
	ID3_7@2	r	11.75	0.36	-13.0	1.2	-1.62	0.15
	ID3_8@1	c	11.63	0.25	-10.6	1.8	-1.28	0.21
	ID3_9@1	c					-1.68	0.22
	ID3_9@2	r					-1.34	0.16
	ID3_10@1	c	12.18	0.45	-6.7	1.8	2.71	0.20
	ID3_10@2	r	11.15	0.29	-7.8	1.8	-1.03	0.18
	ID3_11@1	c	12.03	0.39	-10.5	1.6	-1.24	0.17
	ID3_12@1	c	12.79	2.17	-6.8	1.4	-1.90	0.21
	ID3_13@1	c	11.86	0.17	-9.0	2.7	-2.06	0.22
	ID3_13@2	r	11.15	0.29	-5.7	1.9	0.87	0.19
	ID3_14@1	c					0.16	0.19
	ID3_15@1	c	11.92	0.39	-5.2	1.9	1.03	0.18
	ID3_15@2	r	11.92	0.30	-7.6	1.8	1.81	0.21
	ID3_16@1	c					-0.33	0.21
	ID3_17@1	c	11.83	0.25	-7.7	1.4	1.42	0.16
	ID3_17@2	r	11.79	0.31	-6.9	1.6	-1.62	0.20
	ID3_18@1	c	11.97	0.36	-8.6	1.8	0.55	0.21
	ID3_18@2	r	11.56	0.31	-7.4	1.4	1.96	0.25
	ID3_19@1	c	11.89	0.25	-7.6	1.9	1.07	0.19
	ID3_19@2	r	11.79	0.31	-7.6	1.2	-0.01	0.20
	ID3_20@1	c					-1.81	0.20
	ID3_20@2	r					-1.32	0.19
	ID3_21@1	c					0.37	0.21
	ID3_21@2	r					0.30	0.19
	ID3_19@3	r2					0.59	0.19
	ID3_22@1	c					-0.55	0.18
	ID3_22@2	r					-1.38	0.20
	ID3_23@1	c	12.01	0.60	-11.1	1.5	3.83	0.22
	ID3_23@2	r	11.28	0.29	-12.2	1.7	3.68	0.20
	ID3_24@1	c	13.07	0.46	-7.0	1.8	1.21	0.21
	ID3_24@2	r	11.84	0.49	-8.6	1.6	-2.13	0.27
	ID3_25@1	c	12.41	0.38	-7.2	1.2	1.92	0.25
	ID3_25@2	r	12.04	0.30	-11.2	2.0	0.95	0.20

Table C.2 (continued).

Unit	*Spot Name*	*Core /Rim**	*Age (Ma)*	*2σ (Ma)*	*ε_{Hf}*	*2 s.e.*	*$\delta^{18}O$ (SMOW)*	*2σ (‰)*
	ID3_26@1	c	12.86	0.28	-8.0	1.4	-0.75	0.17
	ID3_26@2	r	12.07	0.32	-8.0	1.3	-2.22	0.18
	ID3_27@1	r					1.37	0.18
	ID3_28@1	c					-0.18	0.15
	ID3_29@1	c	11.94	0.38	-8.0	2.1	0.63	0.17
	ID3_29@2	r	11.70	0.42	-8.8	1.6	-2.42	0.17
	ID3_30@1	c					-0.10	0.15
	ID3_30@2	r					0.24	0.25
CPT XIII	ID9_3@1	r	10.80	0.30	-4.8	3.9	1.27	0.22
	ID9_4@1	c	10.50	0.20	-6.8	4.6	1.29	0.15
	ID9_4@2	r	10.90	0.20	-4.4	5.3	1.08	0.17
	ID9_5@1	c	10.60	0.30	-5.2	2.6	1.57	0.26
	ID9_5@2	r	10.60	0.30	-6.9	2.7	1.56	0.17
	ID9_6@1	c					1.41	0.18
	ID9_6@2	r					1.52	0.19
	ID9_7@1	r	9.60	3.80	-4.4	4.2	3.91	0.15
	ID9_7@2	c	10.80	0.30	-7.0	3.4	4.09	0.16
	ID9_8@1	c	10.60	0.30	-5.6	3.0	1.52	0.18
	ID9_9@1	c					1.82	0.15
	ID9_10@1	c	10.90	0.30	-10.9	3.0	1.03	0.21
	ID9_10@2	r	10.60	0.30	-5.4	1.7	1.35	0.17
	ID9_11@1	c	10.80	0.30	-5.8	2.5	1.61	0.16
	ID9_11@2	r					1.53	0.18
	ID9_12@1	c					1.50	0.21
	ID9_13@1	c	10.70	0.40	-3.7	3.5	4.73	0.18
	ID9_13@2	c	10.70	1.00	-2.2	3.5	3.40	0.19
	ID9_14@1	c	10.60	0.40	-5.8	3.9	2.12	0.16
	ID9_14@2	r	10.70	0.30	-5.5	3.9	1.16	0.16
	ID9_15@1	c					1.39	0.16
	ID9_16@1	c	10.70	0.30	-2.5	2.8	3.58	0.19
	ID9_16@2	r	10.60	0.30	-5.1	3.9	1.71	0.24
	ID9_17@1	c					1.14	0.23
	ID9_17@2	r					1.37	0.22
	ID9_18@1	c	10.40	0.40	-3.7	3.9	4.45	0.22
	ID9_18@2	r	10.40	0.40	-1.9	4.2	4.49	0.24
	ID9_19@1	c					1.45	0.25
	ID9_20@1	c					1.41	0.23
	ID9_21@1	c	10.70	0.30	-7.6	3.9	1.09	0.17
	ID9_21@2	r	10.70	0.30	-7.8	2.9	1.49	0.17
	ID9_22@1	c	10.90	0.40	-4.8	2.8	2.52	0.23
	ID9_22@2	r	10.90	0.30	-6.0	2.6	1.61	0.20

Table C.2 (continued).

Unit	*Spot Name*	*Core /Rim**	*Age (Ma)*	*2σ (Ma)*	*ε_{Hf}*	*2 s.e.*	*$\delta^{18}O$ (SMOW)*	*2σ (‰)*
	ID9_23@1	c					1.13	0.16
	ID9_23@2	r					1.31	0.16
	ID9_24@1	c	11.80	0.30	-8.1	3.4	-0.66	0.18
	ID9_24@2	r	10.50	0.30	-7.7	2.9	1.45	0.17
	ID9_25@1	c	10.50	0.30	-6.8	3.3	1.99	0.18
	ID9_25@2	r	10.60	0.30	-7.6	3.5	1.40	0.15
	ID9_26@1	c					1.33	0.19
	ID9_27@1	c	10.60	0.30	-5.3	2.9	1.42	0.28
	ID9_27@2	r	10.60	0.30	-7.6	3.2	1.61	0.20
	ID9_28@1	c					1.64	0.21
	ID9_29@1	c					1.08	0.17
	ID9_30@1	c	11.00	0.20	-7.2	3.9	1.05	0.20
	ID9_30@2	r	10.50	0.30	-5.9	2.7	1.42	0.21
CPT V	ID13_4@1	c	12.10	0.30	-2.2	3.5	4.43	0.17
	ID13_4@2	r	11.80	0.30	-9.4	2.8	2.06	0.21
	ID13_5@1	c					0.92	0.22
	ID13_5@2	r					1.75	0.18
	ID13_6@1	c	12.10	0.40	-6.2	3.5	3.16	0.18
	ID13_7@1	c	11.70	0.30	-9.5	3.3	0.67	0.20
	ID13_7@2	r	11.90	0.30	-9.1	2.9	1.67	0.17
	ID13_8@1	c					0.81	0.22
	ID13_8@2	r					1.34	0.16
	ID13_9@1	c					4.68	0.18
	ID13_10@1	c					1.00	0.19
	ID13_10@2	r					1.17	0.21
	ID13_11@1	c	11.90	0.30	-6.3	3.0	0.77	0.20
	ID13_11@2	r	12.00	0.40	-9.4	3.9	1.90	0.21
	ID13_12@1	c	17.60	3.90	-11.5	3.3	2.91	0.14
	ID13_12@2	r	12.10	0.40	-10.0	3.4	2.03	0.20
	ID13_13@1	c	12.00	0.30	-7.9	4.6	1.57	0.17
	ID13_13@2	r	12.10	0.30	-8.7	5.0	1.82	0.19
	ID13_14@1	c	11.90	0.30	-6.4	2.5	3.42	0.16
	ID13_14@2	r					1.87	0.14
	ID13_15@1	c					1.15	0.22
	ID13_15@2	r	12.10	0.30	-9.7	3.9	1.94	0.18
	ID13_16@1	c	11.80	0.30	-7.6	3.4	1.85	0.16
	ID13_17@1	c	12.00	0.30	-8.0	2.2	3.36	0.17
	ID13_17@2	r	12.30	0.30	-7.6	2.6	1.76	0.15
	ID13_18@1	c	12.10	0.30	-8.4	2.7	1.05	0.24
	ID13_18@2	r	11.80	0.30	-9.7	3.9	1.67	0.18
	ID13_19@1	c	12.20	0.40	-6.5	4.2	0.93	0.20

Table C.2 (continued).

Unit	*Spot Name*	*Core /Rim**	*Age (Ma)*	*2σ (Ma)*	*ε_{Hf}*	*2 s.e.*	*$\delta^{18}O$ (SMOW)*	*2σ (‰)*
	ID13_19@2	r	12.10	0.30	-9.3	2.8	1.83	0.19
	ID13_20@1	c					1.22	0.17
	ID13_20@2	r					1.90	0.17
	ID13_21@1	c					1.59	0.18
	ID13_21@2	r					1.89	0.17
	ID13_22@1	c					1.77	0.17
	ID13_23@1	c	11.80	0.30	-7.9	2.3	2.58	0.17
	ID13_23@2	r	11.90	0.30	-9.0	2.2	2.05	0.18
	ID13_24@1	c					1.16	0.20
	ID13_24@2	r					1.81	0.19
	ID13_25@1	c	11.90	0.30	-8.2	2.5	0.51	0.18
	ID13_26@1	c	12.00	0.30	-7.6	3.5	1.08	0.19
	ID13_26@2	r	11.60	0.30	-10.4	3.5	1.94	0.16
	ID13_27@1	c	11.80	0.40	-6.8	3.5	2.84	0.20
	ID13_28@1	c	12.10	0.30	-7.8	2.5	4.14	0.17
	ID13_28@2	r	11.70	0.30	-6.6	3.2	1.90	0.19
	ID13_29@1	c	12.50	0.40	-7.1	1.9	1.21	0.16
	ID13_29@2	r	12.10	0.30	-7.2	3.0	1.51	0.19
	ID13_30@1	c	11.90	0.30	-7.4	2.3	2.02	0.16
	ID13_30@2	r	12.00	0.40	-9.6	2.2	1.90	0.22
Tuff of Bruneau Canyon	ID14_3@1	c	16.30	3.10	-1.3	3.5	1.64	0.19
	ID14_4@1	c	14.70	0.50	-7.9	3.1	3.07	0.19
	ID14_4@2	r	14.80	0.50	-8.4	3.1	2.99	0.18
	ID14_5@1	c	14.80	0.40	0.2	3.9	0.39	0.22
	ID14_5@2	r	14.40	0.60	-6.1	2.5	0.33	0.24
	ID14_6@1	c	14.80	0.40	-2.3	2.4	1.86	0.18
	ID14_6@2	r	14.30	0.40	-1.9	3.2	0.09	0.18
	ID14_7@1	c	15.00	0.40	-1.0	3.4	0.54	0.18
	ID14_7@2	r	13.60	2.30	-4.6	2.2	0.15	0.19
	ID14_8@1	c	15.10	0.50	-2.4	2.7	0.18	0.19
	ID14_9@1	r	15.10	0.50	-1.1	2.8	1.59	0.19
	ID14_10@1	c					1.58	0.22
	ID14_10@2	r					2.37	0.18
	ID14_11@1	c	14.70	0.50	-1.9	4.2	0.20	0.19
	ID14_11@2	r	14.90	0.50	-2.1	3.4	1.06	0.18
	ID14_12@1	c	15.30	0.40	-3.7	4.2	0.18	0.18
	ID14_12@2	r	14.80	0.40	-1.9	4.6	0.92	0.20
	ID14_13@1	c	15.40	0.40	-1.4	3.4	0.06	0.20
	ID14_13@2	r	14.30	0.40	-0.4	2.7	0.76	0.17
	ID14_14@1	c	14.60	0.60	-10.0	4.6	3.96	0.15
	ID14_14@2	r	14.50	0.60	-10.8	3.9	3.17	0.18

Table C.2 (continued).

Unit	*Spot Name*	*Core /Rim**	*Age (Ma)*	*2σ (Ma)*	*ε_{Hf}*	*2 s.e.*	*$\delta^{18}O$ (SMOW)*	*2σ (‰)*
	ID14_15@1	c	14.80	0.60	-12.9	3.5	4.11	0.26
	ID14_15@2	r	14.50	2.10	-8.4	2.5	2.55	0.16
	ID14_16@1	c	14.40	0.40	-5.1	4.2	2.92	0.18
	ID14_16@2	r	14.40	0.60	-11.1	3.0	2.48	0.18
	ID14_17@1	c	14.40	0.50	-7.6	3.9	0.83	0.24
	ID14_17@2	r	14.70	0.50	-6.6	3.2	0.64	0.18
	ID14_18@1	c	14.60	0.50	0.1	2.4	-0.17	0.15
	ID14_19@1	c	15.30	0.50	-2.7	2.8	-0.11	0.27
	ID14_20@1	c			-11.1	6.7	1.23	0.24
Kimberly Member	A21796_15@1	c					0.92	0.21
	A21796_15@2	r					1.39	0.19
	A21796_17@1	c					1.18	0.22
	A21796_21@1	c					0.96	0.18
	A21796_26@1	c					1.50	0.25
	A21796_30@1	c					1.15	0.17
	A21796_31@1	c					1.00	0.17
	A21796_31@2	r					1.16	0.21
	A21796_32@1	c	7.80	0.40	-2.6	3.3	1.74	0.21
	A21796_32@2	r					1.43	0.20
	A21796_33@1	c	9.20	3.80	-2.3	3.9	3.26	0.19
	A21796_34@1	c					1.21	0.18
	A21796_35@1	c	7.80	0.20	-6.8	3.5	1.05	0.24
	A21796_35@2	r	7.70	0.30	-5.9	2.8	1.36	0.20
	A21796_36@1	c	8.50	0.30	-4.4	3.5	-0.06	0.18
	A21796_36@2	r	7.80	0.30	-3.9	3.2	2.12	0.23
	A21796_37@1	c	7.60	0.20	-1.5	4.6	1.84	0.18
	A21796_37@2	r	7.50	0.40	-4.8	2.4	1.73	0.20
	A21796_40@1	c	7.90	0.30	-2.6	4.6	1.11	0.26
	A21796_40@2	r					0.50	0.24
	A21796_40@3	r2	7.60	0.30	-3.3	2.9	0.31	0.19
	A21796_41@1	c	7.70	0.20	-5.3	3.1	1.38	0.25
	A21796_41@2	r					1.21	0.26
	A21796_43@1	c					1.42	0.24
	A21796_43@2	r					1.15	0.24
	A21796_44@1	c					2.18	0.26
	A21796_44@2	r					1.19	0.25
	A21796_45@1	c	7.80	0.20	-5.1	3.5	0.66	0.20
	A21796_45@2	r	7.60	0.30	-6.2	3.9	1.18	0.17
	A21796_46@1	c					1.71	0.25
	A21796_46@2	r					1.54	0.30
	A21796_47@1	c					1.26	0.24

Table C.2 (continued).

Unit	*Spot Name*	*Core /Rim**	*Age (Ma)*	*2σ (Ma)*	*ε_{Hf}*	*2 s.e.*	*$\delta^{18}O$ (SMOW)*	*2σ (‰)*
	A21796_47@2	r					1.37	0.25
	A21796_48@1	c	8.40	0.40	-5.0	2.9	1.44	0.24
	A21796_52@1	c					1.40	0.18
	A21796_53@1	c					1.33	0.17
	A21796_54@1	c					1.10	0.26
	A21796_54@2	r					1.28	0.27
	A21796_55@1	c					1.53	0.25
	A21796_57@1	r	7.80	0.30	-3.3	3.5	4.15	0.26
	A21796_57@2	r	7.80	0.30	-0.5	3.9	4.17	0.19
	A21796_58@1	c	7.70	0.20	6.6	4.2	3.18	0.24
	A21796_63@1	c					1.29	0.19
	A21796_63@2	r					1.36	0.19
	A21796_64@1	c					1.26	0.17
	A21796_66@1	c					1.57	0.27
	A21796_67@1	c					2.18	0.23
	A21796_67@2	r					1.20	0.23
	A21796_68@1	c	7.70	0.30	-6.8	3.9	4.88	0.19
	A21796_69@1	c	7.70	0.20	-1.5	5.0	1.07	0.21
	A21796_70@1	c					2.06	0.21
	A21796_71@1	c					2.45	0.18
	A21796_73@1	c					1.29	0.19
	A21796_74@1	c					2.10	0.21
	A21796_77@1	c					1.27	0.17
	A21796_77@2	r					1.48	0.18
	A21796_78@1	c					1.47	0.21
	A21796_79@1	c					1.32	0.20
	A21796_80@1	c					2.25	0.19
	A21796_80@2	r					1.16	0.20
	A21796_82@1	c	7.80	0.40	-4.7	4.6	2.40	0.19
	A21796_84@1	c					1.15	0.19
	A21796_84@2	r					1.30	0.20
	A21796_86@1	c	7.60	0.30	-0.1	6.0	1.44	0.16
	A21796_87@1	c					1.36	0.22
	A21796_88@1	c	7.70	0.30	-5.9	3.0	2.19	0.21
	A21796_88@2	r	7.60	0.30	-5.9	2.7	1.25	0.22
	A21796_89@1	c					0.93	0.20
	A21796_91@1	c					1.32	0.18
	A21796_92@1	c	7.90	0.40	-1.6	3.5	1.23	0.21
	A21796_93@1	c					1.21	0.16
	A21796_93@2	r					1.29	0.18
	A21796_94@1	c	7.80	0.40	1.3	3.2	1.29	0.19

Table C.2 (continued).

Unit	*Spot Name*	*Core /Rim**	*Age (Ma)*	*2σ (Ma)*	*ε_{Hf}*	*2 s.e.*	*$\delta^{18}O$ (SMOW)*	*2σ (‰)*
	A21796_94@2	r	7.50	0.30	-3.7	2.7	1.42	0.24
	A21796_96@1	c	7.50	0.30	-7.1	2.6	1.46	0.23
	A21796_96@2	r	8.00	0.30	-4.2	3.4	1.41	0.18
	A21796_97@1	c	7.70	0.40	-2.9	4.2	4.76	0.21
Castleford Crossing Member	A26197_1@1	c	8.10	0.40	-3.7	3.3	1.77	0.18
	A26197_1@2	r					1.62	0.21
	A26197_2@1	c	9.10	0.30	-15.7	4.6	4.32	0.20
	A26197_2@2	r	7.40	0.20	-3.0	3.5	1.33	0.22
	A26197_3@1	r					1.35	0.18
	A26197_4@1	c					1.38	0.19
	A26197_4@2	r					1.07	0.20
	A26197_5@1	c	8.60	0.30	-0.8	3.2	1.53	0.21
	A26197_5@2	r					1.33	0.16
	A26197_9@1	c					1.40	0.19
	A26197_10@1	c	8.60	0.30	-6.2	3.3	2.15	0.23
	A26197_10@2	r	7.80	0.30	-4.9	3.3	1.42	0.28
	A26197_11@1	c					1.44	0.24
	A26197_11@2	r					1.28	0.24
	A26197_13@1	c					1.42	0.23
	A26197_14@1	c					1.30	0.23
	A26197_15@1	c					1.14	0.25
	A26197_15@2	r					1.42	0.29
	A26197_17@1	c	631.30	20.80	-18.0	2.3	4.37	0.26
	A26197_17@2	r	7.70	0.30	-3.8	3.4	1.32	0.23
	A26197_18@1	c	8.80	0.30	-4.1	3.9	1.66	0.24
	A26197_18@2	r	7.90	0.30	-4.0	3.0	1.58	0.23
	A26197_19@1	c					1.26	0.19
	A26197_20@1	c	8.10	0.50	-11.1	3.9	2.56	0.27
	A26197_20@2	r	7.90	0.30	-4.4	2.7	0.82	0.24
	A26197_21@1	c					1.52	0.25
	A26197_21@2	r					1.31	0.24
	A26197_22@1	c	8.70	0.40	-4.6	3.4	1.34	0.21
	A26197_22@2	r					1.29	0.19
	A26197_23@1	c	8.10	0.30	0.5	3.9	1.95	0.21
	A26197_23@2	r	8.30	0.40	-2.5	3.4	2.14	0.22
	A26197_24@1	c	7.90	0.30	-2.9	2.1	1.46	0.17
	A26197_32@1	c					1.07	0.19
	A26197_32@2	r					1.42	0.20
	A26197_33@1	c					1.31	0.21
	A26197_34@1	c					1.33	0.20
	A26197_34@2	r					1.27	0.18

Table C.2 (continued).

Unit	*Spot Name*	*Core /Rim**	*Age (Ma)*	*2σ (Ma)*	*ε_{Hf}*	*2 s.e.*	*$\delta^{18}O$ (SMOW)*	*2σ (‰)*
	A26197_36@1	c					1.65	0.21
	A26197_40@1	c					1.29	0.20
	A26197_40@2	r					1.40	0.21
	A26197_41@1	r					1.08	0.17
	A26197_42@1	c					1.92	0.19
	A26197_43@1	c					1.47	0.22
	A26197_43@2	r					1.34	0.18
	A26197_44@1	r					1.34	0.21
	A26197_46@1	c	7.70	0.30	-5.2	2.6	1.29	0.24
	A26197_48@1	c	8.60	0.30	-4.6	3.3	0.99	0.19
	A26197_49@1	c	8.00	0.30	-2.9	3.5	1.13	0.20
	A26197_49@2	r	8.40	0.40	-5.8	3.3	1.03	0.17
	A26197_51@1	c					1.37	0.21
	A26197_51@2	r					1.43	0.19
	A26197_55@1	c					2.00	0.20
	A26197_64@1	c	8.00	0.30	-24.4	2.9	3.62	0.21
	A26197_66@1	c	7.90	0.30	-4.1	2.8	1.50	0.23
	A26197_68@1	c	9.20	2.90	-1.8	3.0	1.13	0.18
	A26197_68@2	r					1.37	0.17
	A26197_70@1	c	8.10	9.60	-4.4	3.9	1.11	0.19
	A26197_70@2	r	8.80	4.60	-5.2	3.0	1.35	0.21
	A26197_72@1	c	8.20	0.30	-0.2	2.6	2.51	0.17
	A26197_72@2	r	8.30	0.40	-1.6	2.9	1.48	0.19
	A26197_73@1	c	8.70	1.40	-2.2	3.3	1.93	0.26
	A26197_76@1	c					1.43	0.18
	A26197_77@1	r	8.30	0.30	-5.5	4.6	1.34	0.24
	A26197_82@1	r	8.10	0.30	-5.9	2.5	1.38	0.20
	A26197_85@1	c					1.35	0.19
Shoshone Rhyolite	A2716_25@1	c					2.51	0.19
	A2716_25@2	r					0.77	0.16
	A2716_30@1	c	6.00	0.20	-1.5	3.1	-1.04	0.25
	A2716_31@1	c					2.95	0.20
	A2716_33@1	c	6.10	0.20	-2.1	3.4	-0.22	0.17
	A2716_36@1	c					2.64	0.21
	A2716_36@2	r					-1.32	0.19
	A2716_38@1	c	5.90	0.30	-4.1	3.5	2.97	0.20
	A2716_38@2	r					2.55	0.19
	A2716_44@1	c	9.30	0.30	-4.1	3.9	0.94	0.18
	A2716_44@2	r					2.36	0.22
	A2716_44@3	r2	8.90	0.20	-3.9	2.8	0.01	0.17
	A2716_45@1	c	6.00	0.30	-4.0	4.2	2.01	0.19

Table C.2 (continued).

Unit	*Spot Name*	*Core /Rim**	*Age (Ma)*	*2σ (Ma)*	*ε_{Hf}*	*2 s.e.*	*$\delta^{18}O$ (SMOW)*	*2σ (‰)*
	A2716_47@1	c	6.20	0.30	-3.7	4.2	1.45	0.16
	A2716_47@2	r	5.90	0.20	-4.0	3.5	-0.21	0.18
	A2716_48@1	c	9.10	0.30	-4.8	3.3	1.68	0.22
	A2716_48@2	r					2.01	0.16
	A2716_48@3	r					0.15	0.24
	A2716_49@1	c					2.76	0.27
	A2716_49@2	r					2.21	0.29
	A2716_49@3	r2					1.11	0.27
	A2716_49@4	r3					1.12	0.20
	A2716_54@1	c	14.40	6.40	0.2	5.0	1.48	0.19
	A2716_56@1	c					2.01	0.21
	A2716_57@1	c					3.46	0.24
	A2716_57@2	r					-1.15	0.23
	A2716_58@1	c	7.50	0.50	-3.4	3.5	0.61	0.23
	A2716_58@2	r	5.70	0.20	-4.1	2.4	0.98	0.25
	A2716_58@3	r2					-1.21	0.25
	A2716_59@1	c	6.60	0.30	-6.5	4.2	3.43	0.24
	A2716_59@2	r	6.10	0.30	-3.6	1.9	3.48	0.26
	A2716_60@1	c	6.10	0.20	-4.5	3.5	1.87	0.24
	A2716_60@2	r					1.86	0.19
	A2716_61@1	c	6.20	0.20	-3.3	3.5	2.16	0.23
	A2716_62@1	c	6.00	0.20	-1.5	4.2	1.72	0.26
	A2716_63@1	c	6.30	0.30	-7.5	4.2	2.74	0.26
	A2716_63@2	r	6.10	0.20	-3.7	3.9	3.33	0.24
	A2716_63@3	c					2.54	0.17
	A2716_64@1	c					1.70	0.28
	A2716_65@1	c	6.10	0.20	3.1	3.9	0.05	0.23
	A2716_66@1	c	6.00	0.30	-5.0	3.3	0.67	0.28
	A2716_66@2	r	6.00	0.30	-5.1	2.3	2.30	0.25
	A2716_67@1	c					2.24	0.26
	A2716_67@2	r					2.54	0.17
	A2716_68@1	c	6.10	0.20	-3.1	3.0	2.22	0.18
	A2716_68@2	r					0.77	0.17
	A2716_68@3	r	6.10	0.30	-6.0	3.0	0.97	0.18
	A2716_68@4	r2	6.00	0.20	-8.1	3.1	-1.18	0.18
	A2716_69@1	c	6.50	0.30	-2.4	3.4	2.09	0.19
	A2716_70@1	c					2.31	0.22
	A2716_70@2	r					-1.22	0.20
	A2716_71@1	c	6.30	0.20	-2.8	3.0	1.92	0.16
	A2716_71@2	r					1.65	0.21
	A2716_72@1	c					1.79	0.20

Table C.2 (continued).

Unit	*Spot Name*	*Core /Rim**	*Age (Ma)*	*2σ (Ma)*	*ε_{Hf}*	*2 s.e.*	*$\delta^{18}O$ (SMOW)*	*2σ (‰)*
	A2716_72@2	r					1.04	0.24
	A2716_74@1	c	6.20	0.20	-3.3	3.5	2.48	0.18
	A2716_74@2	r	6.10	0.20	-4.7	3.1	1.19	0.20
	A2716_75@1	c					1.43	0.20
	A2716_75@2	r					1.15	0.18
	A2716_76@1	c	6.30	0.20	-4.0	2.9	2.04	0.16
	A2716_76@2	r					0.96	0.24
	A2716_77@1	c	6.00	0.20	-2.2	2.5	2.57	0.20
	A2716_78@1	c	8.20	0.30	-2.3	3.9	1.37	0.21
	A2716_79@1	c	6.00	0.20	-4.7	2.6	3.52	0.16
	A2716_79@2	r	6.20	0.20	-5.0	3.1	-1.00	0.20
	A2716_80@1	c					1.57	0.22
	A2716_80@2	r					2.30	0.21
	A2716_81@1	c					3.16	0.19
	A2716_81@2	r					2.99	0.20
	A2716_82@1	c					2.55	0.22
	A2716_83@1	c					2.38	0.22
	A2716_83@2	r					0.72	0.19
	A2716_84@1	c					1.22	0.17
	A2716_84@2	r					1.41	0.16
	A2716_85@1	r					1.44	0.20
	A2716_86@1	c					1.41	0.23
	A2716_86@2	r					-1.42	0.21
	A2716_87@1	c					1.06	0.20
	A2716_88@1	c					1.79	0.22
	A2716_89@1	c					1.99	0.16

*c=core analysis, r=rim analysis, r2=outer rim analysis, r3=extreme outer rim analysis.

Table C.3. CA-ID-TIMS data part 1

	Dates (Ma)						*Composition*			
Member	**^{206}Pb/ ^{238}U Age**	**±2σ abs**	**^{206}Pb/ ^{238}U Age <Th> [b]**	**±2σ abs**	**^{207}Pb/ ^{235}U [a]**	**±2σ abs**	**Th/ U [c]**	**Pb* (pg) [d]**	**Pbc (pg) [e]**	**Pb*/ Pbc [f]**
Castleford										
6197_z66	8.179	0.016	**8.267**	**0.016**	8.28	0.29	0.64	0.58	0.11	5.2
6197_z68	8.196	0.023	**8.284**	**0.022**	8.57	0.46	0.74	0.85	0.29	2.9
6197_z34	8.208	0.031	**8.295**	**0.031**	8.98	0.66	0.66	0.69	0.36	1.9
6197_z64	8.282	0.024	**8.369**	**0.023**	8.41	0.44	0.56	0.46	0.14	3.4
6197_z5	8.298	0.017	**8.386**	**0.017**	8.32	0.29	0.73	0.64	0.12	5.5
6197_z22	8.378	0.029	**8.461**	**0.029**	8.92	0.59	0.64	1.19	0.54	2.2
6197_z48	8.545	0.013	**8.632**	**0.013**	8.59	0.24	0.59	0.58	0.08	7.4
6197_z2	8.742	0.007	**8.829**	**0.007**	8.92	0.11	0.42	3.43	0.29	12.0
Kimberly										
1796_z57	7.672	0.008	**7.760**	**0.008**	7.75	0.12	0.71	1.22	0.10	12.7
1796_z86	7.763	0.012	**7.849**	**0.012**	7.67	0.21	0.71	0.81	0.08	10.2
1796_z52	7.781	0.004	**7.869**	**0.004**	7.98	0.07	0.63	8.45	0.49	17.2
1796_z97	7.786	0.020	**7.873**	**0.020**	7.65	0.34	0.69	0.44	0.08	5.3
1796_z73	7.825	0.003	**7.912**	**0.003**	7.97	0.02	0.69	9.59	0.06	162.2
1796_z30	7.838	0.023	**7.930**	**0.023**	7.76	0.41	0.55	0.45	0.12	3.7
1796_z32b	7.842	0.059	**7.929**	**0.057**	8.44	1.14	0.60	0.20	0.17	1.2
1796_z37	7.855	0.023	**7.942**	**0.022**	8.04	0.41	0.64	0.53	0.12	4.3
1796_z32a	7.930	0.042	**8.021**	**0.041**	7.77	0.69	0.62	0.22	0.09	2.3
1796_z68	7.992	0.011	**8.080**	**0.011**	8.15	0.16	0.65	1.21	0.11	10.7
1796_z36	8.014	0.019	**8.100**	**0.019**	8.20	0.35	0.66	0.91	0.22	4.2
1796_z88	8.756	0.041	**8.843**	**0.040**	9.66	0.84	0.68	0.65	0.41	1.6
Shoshone										
716_z30	6.069	0.054	**6.156**	**0.054**	6.73	1.14	1.02	0.49	0.56	0.9
716_z47	6.206	0.018	**6.294**	**0.018**	6.60	0.33	0.59	0.62	0.19	3.2
716_z69	6.318	0.039	**6.406**	**0.038**	6.94	0.81	0.69	0.55	0.46	1.2
716_z88	6.342	0.019	**6.429**	**0.018**	6.34	0.30	0.59	0.44	0.09	4.7
716_z59	6.645	0.078	**6.732**	**0.077**	7.85	1.66	0.72	1.80	2.96	0.6
716_z78	8.053	0.026	**8.141**	**0.026**	8.60	0.55	0.93	1.14	0.48	2.4
716_z48	8.524	0.028	**8.611**	**0.027**	9.21	0.57	0.56	2.14	0.97	2.2

Table C.4. CA-ID-TIMS data part 2

	Isotopic Ratios							
Member	**$^{206}Pb/^{204}Pb$ [g]**	**$^{206}Pb/^{238}U$ [h]**	**±2σ %**	**$^{207}Pb/^{235}U$ [h]**	**±2σ %**	**$^{207}Pb/^{206}Pb$ [h]**	**±2σ %**	**Corr. coef.**
Castleford								
6197_z66	316	0.00126964	0.20156479	0.00819089	3.51325676	0.04681064	3.38066091	0.673
6197_z68	181	0.00127225	0.27731770	0.00847530	5.39367890	0.04833653	5.22400873	0.628
6197_z34	129	0.00127407	0.38369611	0.00887941	7.35275113	0.05056889	7.12572485	0.608
6197_z64	216	0.00128553	0.28474054	0.00831783	5.19496827	0.04694839	5.00167688	0.693
6197_z5	329	0.00128813	0.20661446	0.00823101	3.46173759	0.04636471	3.31701985	0.715
6197_z22	143	0.00130041	0.35163678	0.00882134	6.59744484	0.04922059	6.39096081	0.604
6197_z48	446	0.00132635	0.15792787	0.00850010	2.74737116	0.04650077	2.63602145	0.718
6197_z2	744	0.00135708	0.07889540	0.00882184	1.23872958	0.04716807	1.19544166	0.565
Kimberly								
1796_z57	735	0.00119088	0.10203635	0.00765994	1.55805360	0.04667132	1.49676642	0.618
1796_z86	593	0.00120498	0.15860589	0.00758077	2.71167364	0.04564844	2.59399924	0.754
1796_z52	1005	0.00120783	0.05667445	0.00788814	0.86097933	0.04738725	0.83407051	0.489
1796_z97	316	0.00120856	0.25870419	0.00756691	4.43448461	0.04543034	4.23518001	0.782
1796_z73	9194	0.00121453	0.04107373	0.00788165	0.20768660	0.04708736	0.18289332	0.604
1796_z30	237	0.00121654	0.29452296	0.00767028	5.34552532	0.04574859	5.12543169	0.759
1796_z32b	86	0.00121729	0.74954105	0.00835009	13.61506521	0.04977276	13.10844874	0.691
1796_z37	265	0.00121927	0.28910518	0.00794964	5.09394750	0.04730883	4.88300312	0.743
1796_z32a	154	0.00123084	0.52989221	0.00768118	8.92164240	0.04528161	8.51184169	0.785
1796_z68	628	0.00124057	0.13477261	0.00805753	1.92386749	0.04712761	1.82751109	0.730
1796_z36	257	0.00124390	0.24219611	0.00810724	4.33383056	0.04729130	4.16345076	0.717
1796_z88	108	0.00135920	0.46817567	0.00955543	8.77146785	0.05101060	8.50203962	0.593
Shoshone								
716_z30	64	0.00094184	0.89760975	0.00665376	17.04940522	0.05126056	16.53528100	0.590
716_z47	207	0.00096319	0.28999719	0.00652321	4.99909851	0.04914090	4.81024367	0.668
716_z69	85	0.00098062	0.61135056	0.00685814	11.68462295	0.05074585	11.33383616	0.591
716_z88	292	0.00098436	0.29184433	0.00626500	4.67806017	0.04618071	4.45834238	0.766
716_z59	52	0.00103126	1.18036322	0.00775761	21.19575682	0.05458235	20.52937620	0.584
716_z78	145	0.00125007	0.32869015	0.00850371	6.37500612	0.04935908	6.18614257	0.592
716_z48	146	0.00132310	0.32586397	0.00910795	6.24281924	0.04994863	6.05608715	0.590

Notes on Tables C.3 and C.4.

[a] Isotopic dates calculated using the decay constants λ238 = 1.55125E-10 and λ235 9.8485E-10 (Jaffey et al. 1971).

[b] Corrected for initial Th/U disequilibrium using radiogenic ^{208}Pb and DTh/U=0.2.

[c] Th contents calculated from radiogenic ^{208}Pb and the $^{206}Pb/^{238}U$ date of the sample, assuming concordance between U-Th and Pb systems.

[d] Total mass of radiogenic Pb.

[e] Total mass of common Pb.

[f] Ratio of radiogenic Pb (including ^{208}Pb) to common Pb.

[g] Measured ratio corrected for fractionation and spike contribution only.

[h] Measured ratios corrected for fractionation, tracer and blank

APPENDIX D

MATERIAL FOR CHAPTER V

Contents:

D.1. Introduction
D.2. Detailed methods
D.3. Supplementary models
D.4. Supplementary figures and tables

D.1. Introduction

This supporting information consists of two main sections. The first, which comprises section D.2, Figs. D.1- D.3, and Table D.1, provides detailed methods and information about the algorithms used to perform our computer models, in enough detail to allow their reproduction. The second part, which comprises section D.2, Figs. D.4- D.11, and Table D.2, detail additional model results beyond those discussed in the main text, which allow for many of the free parameters in our models to be constrained. Importantly, while there are many results here with implications for our model methodology, we do not present any major new scientific findings not discussed in the main text. Finally, we present several additional models of slightly different mantle plume conditions and crustal compositions, in addition to those presented in Fig. 5.4 of the main text, to further demonstrate the robustness of our overall conclusions.

D.2. Detailed methods

D.2.1. Model setup

We employ a high-resolution finite difference Lagrangian marker-in-cell thermomechanical model incorporating viscoplastic rheology of the crust and mantle based on the I2VIS code developed by Gerya and Yuen (2003). 16 Lagrangian markers are randomly distributed in each 2×2 km cell at the start of the model. Individual time steps are 5000 years, to balance computational efficiency and a small enough time step that large bodies of melt can persist without solidifying between time steps. To avoid boundary effects, we use a relatively large 1000 km×300 km model space with a fully staggered 2 km×2 km finite difference grid. The top 20 km of the model is occupied by a "sticky air" low viscosity layer to simulate a free surface condition on the top of the crust (Crameri et al., 2012). The crust is initially set to be 35 km thick, and consists in our base model of a 15 km-thick upper crust layer with a density of 2700 kg/m^3 and a 20 km-thick lower crust layer with a density of 2900 kg/m^3. The upper crust uses the wet quartzite rheology of Ranalli (1995), while the lower crust layer uses the stronger An75 rheology. The rest of the model area is occupied by mantle, using the dry olivine rheology of Ranalli (1995). Lithospheric and asthenospheric mantle are assumed to have identical compositions, and are only distinguished in different colors in the figures for clarity, though they do of course have different temperatures. Material properties for all rock and melt types in the model are summarized in Table D.1.

We assume an initial linear (for simplicity) crustal geothermal gradient of 20 K/km, resulting in a Moho temperature of 700 °C. In the asthenospheric mantle, we assume an initial adiabatic temperature gradient of 0.5 K/km that corresponds to a

potential mantle temperature of ~1350°C, typical of the region surrounding the Yellowstone hotspot track (Lee et al., 2009). The mantle lithosphere then has a linear initial temperature gradient which connects the temperatures at the Moho and LAB determined by the previous constraints, resulting in a LAB temperature of 1390°C in the case of an 80 km-thick lithosphere, which we use in our standard model. Left and right temperature boundary conditions are a symmetry condition, and the lower boundary has a fixed temperature of 1490°C (at a depth of 280 km), while the top is fixed at 0°C. The exception to this is the center 80 km on the bottom of the model, which has a fixed higher temperature of 1665°C in the standard model (175 K hotter than the surrounding mantle) that generates a purely thermal mantle plume. Above this boundary, the initial plume head is simply modeled as a hemisphere at the bottom of the model with a diameter of 160 km and a uniform temperature of 1665°C.

Tectonic motion of the lithosphere over the mantle plume at a velocity of 2.5 cm/yr is achieved by specifying fixed velocity boundary conditions for where the lithosphere and the top 10 km of the asthenosphere meet the edge of the model. Below this zone, left and right edge velocity boundary conditions are an infinity-like external free-slip boundary condition for (Gerya, 2010) for the vertical component of velocity and fixed at 0 for the x-direction. For the lower velocity boundary condition, we use a fixed velocity plume input of ~4.5 cm/yr for the central 80 km, corresponding with the temperature anomaly, and a corresponding fixed downward velocity outside the plume to ensure mass conservation in the model space. The upper velocity boundary condition is external free-slip.

D.2.2. Governing equations

The model solves a slow-flow Stokes equation and the continuity equation, where we use the summation convention of Einstein (1916):

$$\frac{\partial \sigma'_{ij}}{\partial x_j} - \frac{\partial P_i}{\partial x_i} = -\rho g_i \qquad D.1$$

$$\frac{\partial v_i}{\partial x_i} = \Gamma \qquad D.2$$

In these equations v is velocity, P pressure, σ' is the deviatoric stress tensor, ρ is density, g is (purely vertical) gravitational acceleration, x_i are the spatial coordinates, and Γ is a source term that accounts for local melt extraction and emplacement. We couple these fluid-flow equations with a Lagrangian heat equation that includes shear heating and radiogenic heating:

$$\rho C_p \left(\frac{DT}{Dt}\right) = \frac{\partial}{\partial x_i}\left(k \frac{\partial T}{\partial x_i}\right) + H_r + H_s + H_a \qquad D.3$$

$$k = \left(k_0 + \frac{k_f}{T + 77}\right) e^{k_p \cdot P} \qquad D.4$$

Here T is temperature in kelvin, C_p is the heat capacity, k is thermal conductivity, k_0 k_f, and k_p are experimentally defined parameters (Table D.1), H_r is radiogenic heating, which is a predefined constant, H_s is shear heating, and H_a is adiabatic heating. The latter two are defined by:

$$H_s = \sigma_{ij} \dot{\varepsilon}_{ij} \quad H_a = \alpha T \frac{dP}{dt} \qquad D.5, D.6$$

where α is the coefficient of thermal expansion and $\dot{\varepsilon}$ is the strain rate tensor. These equations are solved on a two-dimensional fully staggered finite difference grid and temperature advection is performed with markers. For full discussion of the methods via which these equations are solved see Gerya and Yuen (2003) and Gerya (2010).

D.2.3. Rheology of rocks and melts

Rocks undergo simultaneous viscous and brittle/plastic deformation, which is implemented in the model by using an effective viscosity η_{eff}, calculated by considering a combination of Newtonian, power law, and Pierls ductile creep mechanisms, and Drucker-Prager brittle/plastic failure. Effective ductile viscosity is calculated via summation of inverse viscosities:

$$\frac{1}{\eta_{ductile}} = \frac{1}{\eta_{newt}} + \frac{1}{\eta_{powl}} \qquad D.7$$

where η_{newt} and η_{powl} represent the contributing viscosities from Newtonian diffusion creep and plastic power law dislocation creep, respectively. These are calculated as follows:

$$\eta_{newt} = \frac{1}{2}\frac{A_D}{\sigma_{Cr}^{n-1}} e^{\frac{E+PV}{RT}} \qquad D.8$$

$$\eta_{powl} = \frac{1}{2}\left(A_D e^{\frac{E+PV}{RT}}\right)^{\frac{1}{n}} \dot{\varepsilon}_{II}^{\frac{1-n}{n}} \qquad D.9$$

where A_D, E, n, and V are experimentally defined parameters (Table D.1), σ_{cr} is the critical stress for dislocation to diffusion stress transition, P is dynamic pressure, T is temperature, R is the gas constant, and $\dot{\varepsilon}_{II}$ is the square root of the second invariant of the stain rate tensor. Under high strain rates and low temperatures, ductile behavior gives way to Peierls strain creep:

$$\dot{\varepsilon}_{II} = A_{pei}\sigma_{II}^2 e^{\left\{\frac{E+PV}{RT}\left[1-\left(\frac{\sigma_{II}}{\sigma_{pei}}\right)^m\right]^n\right\}} \qquad D.10$$

$$\eta_{pei} = \frac{\sigma_{II}}{2\dot{\varepsilon}_{II}} \qquad D.11$$

$$\sigma_{II} = \left(\frac{1}{2}\sigma_{ij}\sigma_{ij}\right)^{\frac{1}{2}} \qquad D.12$$

where σ_{II} is the square root of the second invariant of deviatoric stress, and $\sigma_{pei} = 9.1\times10^{9}$ Pa, $A_{pei} = 6.3\times10^{-5}$ $Pa^{-2}s^{-1}$, m = 1, and n = 1 are experimentally determined parameters (Katayama & Karato, 2008). Brittle failure is modeled by using the brittle/plastic viscosity derived from the Drucker-Prager failure criteria:

$$\eta_{brit} = \frac{\sigma_{brit}}{2\dot{\varepsilon}_{II}} \qquad D.13$$

$$\sigma_{brit} = a + bP\lambda \qquad D.14$$

Strain weakening occurs when the brittle/plastic strain tensor reaches a critical value, and affects brittle/plastic failure (equation D.14) as follows:

$$\begin{gathered} a = a_0 + (a_1 - a_0)\epsilon_{II} \;\;,\;\; b = b_0 + (b_1 - b_0)\epsilon_{II} \;\; if\; \epsilon_{II} < 1 \\ a = a_0 \;\;,\;\; b = 0 \;\; if\; \epsilon_{II} < 1 \\ a = a_1 \;\;,\;\; b = b_1 \;\; if\; \epsilon_{II} \geq 1 \end{gathered} \qquad D.15$$

where a_0, a_1, b_0 and b_1 are chosen strain weakening parameters (Table D.1). λ is melt-induced weakening factor (e.g., Gerya et al., 2015), which is set to 10^{-3} in the presence of melt and is 1.0 otherwise. The final effective viscosity used in the model is calculated using the criteria:

$$\eta_{eff} = min\left(\eta_{ductile}, \eta_{pei}, \eta_{brit}\right) \qquad D.16$$

Finally, lower (10^{18} Pa·s) and upper (10^{24} Pa·s) effective viscosity cutoff values are used for numerical stability, and any viscosities which are calculated to fall out of this range are reset to the appropriate extreme value.

D.2.4. Melting of mantle and crust

For mantle melting, we use the parameterization of Katz et al., (2003) for dry mantle melting (Fig. D.1). For all crustal rock types, volumetric melt fractions of partially molten rocks are determined though simple linear interpolation between solidus and liquidus temperature as follows:

$$X_{melt} = 0 \; at \; T \leq T_{solidus}$$
$$X_{melt} = \frac{T - T_{solidus}}{T_{liquidus} - T_{solidus}} \; at \; T_{solidus} < T < T_{liquidus} \qquad D.17$$
$$X_{melt} = 1 \; at \; T \geq T_{liquidus}$$

A more complex model is used for crystallization of basalts extracted from the mantle to more accurately reflect the hydrous enrichment of basalts as they crystallize, which creates a long "tail" on the low-temperature end of the X_{melt} vs. temperature curve, with strong melting only occurring near liquidus temperatures (e.g., Ghiorso & Gualda, 2015). We take the melt fractions computed above and readjust them as follows:

$$X_{melt\,new} = \frac{0.2}{0.75} \cdot X_{melt} \; if X_{melt} < 0.75$$
$$X_{melt\,new} = \frac{T - T_{Xmelt=0.75}}{T_{liquidus} - T_{Xmelt=0.75}} \; if X_{melt} > 0.75 \qquad D.18$$

Liquidus and solidus temperature curves used for crustal rocks and intruding basalts in this model can be seen in Fig. D.1. We use two liquidus temperature curves, one for wet fertile upper crust, and one for basalts and the lower crust. Three separate basalt liquidus temperatures are used for hydrous (normal) basalts and lower crust, moderately dry/refactory crust (Fig. D.1), and completely dry mafic cumulates (green in figures) (e.g. Schmidt & Poli, 1998). Finally, our lowest temperature liquidus parametrizes the melting of wet granites or minimally metamorphosed sediments in the upper crust.

Latent heat of fusion, Q_L, is accounted for implicitly by using an increased effective heat capacity and thermal expansion coefficient in D.6:

$$C_{p_{eff}} = C_p + Q_L \left(\frac{\partial X_{melt}}{\partial T}\right)_P \quad D.19$$

$$\alpha_{eff} = \alpha + \rho_{eff} \frac{Q_L}{T} \left(\frac{\partial X_{melt}}{\partial P}\right)_T \quad D.20$$

We also account for the density effects of melting by using an effective density ρ_{eff} which considers contributions from the solid and molten parts of the bulk, as well as the compressibility of both components:

$$\rho_{eff} = \rho_{solid}\left(1 - X_{melt} + X_{melt}\frac{\rho_{molten}}{\rho_{solid}}\right) \quad D.21$$

$$\rho_{(solid\ or\ molten)} = \rho_{r\ (solid\ or\ molten)}[1 + \beta(P - P_r)][1 - \alpha(T - T_r)] \quad D.22$$

where ρ_r is the reference density of each solid or liquid at temperature and pressure T_r and P_r which are 298.15 K and 10^5 Pa·s, respectively.

D.2.5. Melting Equations

The Katz et al. (2003) mantle melting parameterization gives a volumetric melt fraction X_{melt} of:

$$X_{melt} = X_{cpx-out} + \left(1 - X_{cpx-out}\right)\left[\frac{T - T_{cpx-out}}{T_{liquidus} - T_{cpx-out}}\right]^{1.5} \quad if\ T > T_{cpx-out} \quad D.23$$

$$X_{melt} = \left[\frac{T - T_{solidus}}{T_{liquidus}^{lherz} - T_{solidus}}\right]^{1.5} \quad if\ T \leq T_{cpx-out} \quad D.24$$

using the experimentally defined parameters:

$$T_{cpx-out} = X_{cpx-out}^{\frac{1}{1.5}} \cdot \left(T_{liquidus}^{lherz} - T_{solidus}\right) + T_{solidus} \quad D.25$$

$$X_{cpx-out} = \frac{0.15}{0.5 + 0.08P} \quad D.26$$

$$T_{liquidus}^{lherz} = 273.15 + 1475.0 + 80.0P - 3.2P^2 \quad D.27$$

$$T_{liquidus} = 273.15 + 1780 + 45.0P - 2.0P^2 \quad D.28$$

$$T_{soldus} = 273.15 + 1085.7 + 132.9P - 5.1P^2 \qquad D.29$$

In these equations, P is expressed in GPa and T in kelvin. For mafic melts we use three different solidus curves (Fig. D.1; Hess, 1989; Schmidt & Poli,1998):

$$T_{basalt\,wet\ solidus} = 972.6 - \frac{2111}{\frac{P}{3000} + 10.63} + \frac{70033}{\left(\frac{P}{3000} + 10.63\right)^2} \qquad D.30$$

$$T_{basalt\,dry\ solidus} = 935.4 + 0.1162 \cdot \frac{P}{3000} + 0.006937 \cdot \left(\frac{P}{3000}\right)^2 \qquad D.31$$

$$T_{basalt\,intermed.\ solidus} = \frac{1}{2}\left(\begin{array}{c} 972.6 - \frac{2111}{\frac{P}{3000} + 10.63} + \frac{70033}{\left(\frac{P}{3000} + 10.63\right)^2} \\ +935.4 + 0.1162 \cdot \frac{P}{3000} + 0.006937 \cdot \left(\frac{P}{3000}\right)^2 \end{array}\right) \qquad D.32$$

All of these solidus curves are paired with a single liquidus temperature:

$$T_{basalt\,liquidus} = 1423.15 + \frac{3.5P}{3000} \qquad D.33$$

For upper crustal rocks we use the most fertile curve (Johannes, 1985; Poli & Schmidt, 2002):

$$T_{sediment\,solidus} = 889 + \frac{536}{\frac{P}{3000} + 1.609} + \frac{18.21}{\left(\frac{P}{3000} + 1.609\right)^2} \quad if\ \frac{P}{3000} < 36$$

$$T_{sediment\,solidus} = 831.3 + \frac{2P}{3000} \quad if\ \frac{P}{3000} \geq 36 \qquad D.34$$

$$T_{sediment\,liquidus} = 1262 + \frac{3P}{3000} \qquad D.35$$

D.2.6. Melt extraction, transport and emplacement

The critical difficulty in modeling magmatic processes is accurately modeling magma transport and emplacement in the crust (e.g., Keller et al., 2013). We cannot directly use the governing equations (D.1-D.3) discussed above, because (1) magmatic

viscosities are many orders of magnitude smaller than the minimum cutoff viscosity of 10^{18} Pa·s (e.g., Shaw, 1972) chosen to ensure the numerical stability of our long-term experiments, (2) we do not explicitly consider elastic deformation (e.g., Gerya & Burg, 2007; Keller et al., 2013; Schubert et al., 2013) because the timescales of the elastic processes which govern dike propagation are much smaller than the time steps in this model (e.g. Jellinek & DePaolo, 2003, Karlstrom et al., 2009), and (3) the width of realistic dikes is several orders of magnitude smaller than the resolution of our regional-scale model. As such, we model melt extraction from a source magma chamber to shallower depths and/or the surface as an instantaneous purely vertical "teleportation" of melt in lieu of attempting to directly model dike propagation, as is done in the smaller-scale models (e.g., Gerya & Burg, 2007; Keller et al., 2013; Schubert et al., 2013).

Melt extraction from a partially molten rock is performed when a Lagrangian marker in the model satisfies two criteria:

$$M_1 < X_{melt} - M_{ex} < E_{max} \qquad D.36$$

$$M_{ex} < E_{max} \qquad D.37$$

where M_{ex} is the volume fraction of melt previously extracted in earlier time steps, M_1 is the minimum melt fraction to begin extraction, and E_{max} is the maximum cumulative melt fraction that can be extracted from a given rock type before a refactory cumulate is produced. Melt will be extracted from the marker in a volume of

$$V_{melt} = (X_{melt} - M_{ex} - M_0) \cdot V_{source} \qquad D.38$$

where M_0 is the melt fraction remaining after extraction, decreasing the volume V_{source} of the melting marker by the amount V_{melt} in the process. Constants governing melting are summarized in D.1.

We assume that all melt extraction is purely vertical and instantaneous. The main task is then to determine the height to which a rising dike will propagate before stopping. We refer to three main mechanisms via which a rising dike may arrest to form a sill (Annen et al., 2015): (1) a rising dike encounters a rheologically strong layer of rock and spreads beneath it, as demonstrated in the gelatin experiments of Kavanagh et al. (2006), (2) a rheologically weak contact between two distinct rock layers becomes a conduit for horizontal melt transport (e.g. Gudmundsson, 2011, Miller et al., 2011), and (3) contrasting rheology and/or density between two layers of rock distort the local stress field and redirect a dike along the boundary between them. Finally, the buoyancy of the melt in the dike relative to the surrounding rock is important, but overpressure in a dike can allow it to propagate through rocks less dense than the melt. These scenarios are obviously not mutually exclusive, and the first and third scenarios tend to also eventually include the second, as two rock types that strain differently to the stress field around a propagating dike tip create shear which weakens the boundary between them (Gudmundsson et al., 2011). Particularly strong rheological discontinuities are produced by regions of partial melt, promoting the growth of existing intrusions. Frequently the above processes lead to the creation of a sill fed by a rising dike but do not stop the dike's ascent above that sill, or lead to the immediate creation of a new dike from that sill fed by the suddenly increased pressure. This was elegantly demonstrated by one of the gelatin experiments of Kavanagh et al. (2006) which produced a diminished but still rising dike moving up from a growing sill being fed by a lower dike. Therefore, we must not only determine the maximum height to which a dike will rise as dictated by buoyancy and

crustal rheology, but also the locations where a rising dike will feed intermediate intrusions.

In our model, we only consider intrusions in the crust (melt crosses the mantle with 100% efficiency, leaving none behind along the way), and leave intrusions in the subcontinental lithospheric mantle to future research as higher temperatures and very different rheologies in the mantle likely produce very different melt propagation physics than in most of the crust. To capture the processes discussed above in a numerically efficient manner, we first calculate melt overpressure within a propagating dike connecting all points above the source of melt (Vogt et al., 2013):

$$P_{overpressure} = P_{source} - P_{dike\,tip} - \rho_{melt} g\left(depth_{source} - depth_{dike\,tip}\right) \qquad D.39$$

where P values are pressures, ρ is density, and g is the acceleration of gravity. While subordinate to rheological contrasts, major changes in melt overpressure will likely also drive the arresting of dikes to produce or feed sills, so we consider melt overpressure and viscosity together in the local volumetric intrusion rate (Vogt et al., 2013):

$$D = \frac{P_{overpressure}}{\eta_{eff}} \qquad D.40$$

here D is locally maximized in the crustal column above a rising dike, we assume melt will be trapped and accumulate (Fig. D.2). This value may also be nondimensionalized by multiplying by the timestep Δt (5 kyr in our models), as we do in the main text discussion. Local maxima are defined as any point along a melt column where D is more than 10% larger than both neighboring minima, and we assume that this is a "sweet spot" where magma will accumulate in a sill. The factor of 10% appears to be sufficiently small to capture nearly all weak zones within the resolution of the model, though the smaller ones (in terms of contrast with surroundings) typically will trap much less melt. Sites of

existing sills will nearly always constitute such "sweet spots" because they are weakened by their greater temperature, the possible presence of melt, and strain weakening of the surrounding rocks, ensuring that any dike that crosses a partially molten sill likely contribute to that sill's growth unless it is very old and cold.

The key problem is then to determine the relative amounts of magma that accumulate along the various sweet spots crossed by a rising dike. We assume that sweet spots with large contrasts between their respective high in D and the next highest local minimum in D (regions of strong rheological contrast) in the crust will trap more melt along a rising melt column (Fig. D.2). More simply, more dramatic viscosity increases in the crust above a sill will make the sill more effective at trapping a rising dike. We calculate the volume fraction of all melt in a rising dike that is trapped by an individual "sweet spot" as follows:

$$locally\ intruding\ melt\ fraction \propto \left(\frac{D_{max}}{D_{min}}\right)^n - 1 \qquad D.41$$

$$W = \sum_{all\ intrusions} \left(\frac{D_{max}}{D_{min}}\right)^n - 1 \qquad D.42$$

D_{max} is the sill D value and D_{min} is the D value of the next relative minimum in D (as in Fig. D.2), and n is an empirically determined model constant (Table D.1). We further introduce another empirical model constant L (Table D.1) that governs the local volcanic/plutonic ratio. If W<L, the fraction that erupts is (L-W)/L, and the fraction of the remaining melt that accumulates at each intrusive depth is calculated in accordance with equation D.41. If W≥L, no volcanism occurs and all melt is distributed between different intrusions. This essentially means that it is easier to erupt melts that do not have many large rheological barriers between them and the surface (or one very large one).

We use n=0.5 to preserve numerical stability, as since viscosity varies by many orders of magnitude, the melt fraction captured by one sweet spot in a melt column will approach 100%, especially for larger rates of intrusion. On the other hand, if n is too small, melt is distributed so evenly throughout all parts of the crust that the formation of large, coherent magma chambers is suppressed to an unrealistic degree. We also point out here that we intentionally limit the model resolution to 2 km when using this regional melt extraction scheme, because our empirical n and L constants are resolution-dependent, but more importantly because considering the effective viscosity over too small and area (cell size) when computing D as per equation D.40 leads to unrealistic behavior. Our test calculations show that higher spatial resolutions produce more rheological barriers that are tiny in spatial extent but which have very significant D_{max}/D_{min} values, creating a diffuse pattern of intrusions which eventually eliminates crustal melting (see below). Extending our large-scale methodology in a stable manner to higher resolutions and calibrating and testing it against fully coupled emplacement models accounting for melt percolation (e.g., Keller et al., 2013) is a topic of future research.

Next, we consider the effect of the dikes connecting the zones of intrusion seen in situations like Fig. D.2. Over time, dikes are also a volumetrically significant component of any intrusive system (consider a 10×10 km sheet-like dike with a diameter of 10 m, this will have a volume of 1 km^3). We therefore assume that a fixed portion (f in main text equation 5.2) of every melt extraction event is evenly distributed along the dike path taken by the rising melt, in addition to the zones of accumulation found using equations D.41-D.42 with identical single tiny new Lagrangian markers providing this melt in each 2×2 cell crossed by the dike. The extremely large amount of new Lagrangian markers

produced this way is mitigated by a scheme to recombine small adjacent Lagrangian markers of the same material type into a smaller number that can be dealt with more numerically efficiently (see below). We also set λ from equation D.14 to 10^{-3} for all markers adjacent to the dike, to account for the loss of brittle/plastic strength in melt-bearing rocks (Gerya et al., 2015). The exception to this is that λ is not changed for the crust between the shallowest intrusion and the surface, because eruption repose times in Yellowstone-like volcanoes (Christiansen, 2001) are much longer than the time step (5000 years) used in our model; the model otherwise produces unrealistic weakening of the uppermost crust by assuming a state of constant volcanism at every time step. Even if volcanic repose time is small, we expect dikes in the very shallow and cold crust (<5 km depth) to solidify nearly instantly after forming, negating this weakening effect. Schemes that allow λ weakening all of the way to the surface, as long as the ambient crust is above a certain minimum temperature produce similar results, but with a less natural constraint on the depth of the uppermost magma bodies.

Finally, to prevent intrusion of more magma than an existing weak zone can accommodate (the room problem, e.g. Jellinek & DePaolo, 2003), we check that the value of the local volumetric intrusion rate D at a given sill is not exceeded by the actual volume of melt being intruded there divided by the time step. If this is the case, the volume of the melt marker intruding into the sill is decreased until this condition is no longer violated, and the new excess melt is distributed proportionally to equation D.41 among the shallower sills and the surface. If no shallower sills exist, and the melt is not buoyant enough to reach the surface and erupt, the excess melt remains at depth to be extracted again in the next time step. This prevents the volcanic-plutonic ratio from ever

reaching zero (instead finding minimum values under 1%), even for very small values of L.

D.2.7. Recombination of Lagrangian markers

The melt extraction process produces many thousands of new markers at each time step, as new melt markers appear along the entire dike path above each source of melt. If these melt markers are allowed to in turn be the source of additional melt markers in future time steps, the number of Lagrangian markers in the entire model grows at an exponential rate, quickly destroying the ability of even low-resolution models with large allocated memory to run. The solution is to allow closely adjacent markers to recombine into new markers with weights that reflect the combined weights of the original markers. All combined marker characteristics, including position, are interpolated linearly, with the exception of marker viscosity and strain, in which the lowest and highest values of the contributing markers are used, respectively. This produces better matches with runs that do not use marker recombination, and is justifiable in that a rock/fluid will only be as strong as its weakest component. Melt content, which is a simple on/off property, is on if any of the contributing markers contain melt. We of course only combine markers of the same material type.

This approach does cause numerical diffusion, which is exacerbated when material velocities are high. To limit it, we limit marker recombination only to juvenile intruded markers, and only combine markers with a physical separation that is less than 0.5 times the grid size, and do not attempt to combine markers with weights of more than 0.25 times the original weight of all markers. This seems to preserve the overall structure

of the model, unlike interpolation on the entire grid, which causes much more rapid divergence from models without recombination. In Fig. D.3, we show a comparison of the effects of using vs not using such a marker interpolation scheme for a case with a simplified melt extraction protocol (the full protocol described in the main text cannot function without recombination), demonstrating that model outputs are not strongly changed by the application of recombination as described above.

D.2.8. Topography and Erosion

We compute topography by using a low-viscosity (10^{18} Pa·s) "sticky air" (Crameri et al., 2012) layer at the top of the model with a density of 1 kg/m^3 (air) or 1000 kg/m^3 (water) which allows the top of the underlying rock to behave as a free surface. Erosion of topography is considered at the end of each time step using the equations

$$\frac{\partial z_s}{\partial t} = v_z - v_x \frac{\partial z_s}{\partial x} - v_s + v_e \qquad D.43$$

$$v_s, v_e = 0, \quad 0.3 \times \frac{10^{-11} m}{s} \qquad if\ z_s > 0\ (sea\ level) \qquad D.44$$

$$v_s, v_e = 0.3 \times \frac{10^{-11} m}{s}, \quad 0 \qquad if\ z_s < 0 \qquad D.45$$

$$v_s = v_e = 0 \qquad if\ z_s = 0 \qquad D.46$$

where z_s is the surface elevation, v_x and v_z are the horizontal and vertical material velocities, respectively, and v_s and v_e are the sedimentation and erosion rates. If the topographic surface has a steepness of more than a 10% grade between any two adjacent surface cells, the level of the surface in these two adjoining cells is raised and lowered by an equal amount necessary to lower the steepness to a 10% grade. This mass-conserving slope instability-like process is repeated iteratively until that critical steepness is not

exceeded at any part of the model. The sticky air layer is modeled as air (low density) if its elevation is above sea level and as water (higher density) otherwise.

D.3. Supplementary models

The following figures and table show a representative set of models with different initial conditions and melting parameters, showing further tests of our melt extraction model in a wide variety of mantle and crust conditions. Here we explore the effects of several model parameters not discussed in the main text. We emphasize, however, that none of these parameters appear to be able to change our primary observation that intrusions are concentrated into two separate regions in the upper-mid and lower crust without also altering eruption rates or the structure of intrusions in the crust in unrealistic ways. As such, our investigation here is mainly for purposes of demonstrating model stability with respect to these parameters.

D.3.1. Fraction of melt that cools in dikes

The relative volume of intruded melts that resides in dikes and sills depends on the thickness and spacing of the dikes connecting the sources of melt with shallower intrusions and the surface. We combine these parameters into a simple percentage of the volume of every melt extraction event which ends up in dikes (f in equation 5.2, main text), as opposed to accumulating in "sweet spots" defined by local maxima in D or erupting at the surface; the effects of varying this parameter are documented in Fig. D.4. 0% essentially means true teleportation of melt between different zones of intrusion, and the intervening crust is relatively cool and rigid. This produces overly simple melt

geometries, and favors all melt intruding at a single depth at a time, as seen in Fig. D.4. Very high percentages tend to suppress the formation of large magma bodies by spreading melt very evenly throughout the crust, in addition to being geometrically unrealistic. Moderately low percentages of 10-33% produce the complex multi-tiered structure of melt bodies observed in Yellowstone today (Fig. 5.2), without spreading melt so thin that crustal melting is suppressed. Hence, we prefer a value of 20% of all melt associated with a given eruption event to be distributed evenly between crustal intrusions along dikes.

D.3.2. Parameters governing melt distribution between sills

Equations 40-42 govern how melt rising through a column of "sweet spots" defined by local maxima in D are reproduced here:

$$D = \frac{P_{overpressure}}{\eta_{eff}} \qquad D.40$$

$$locally\ intruding\ melt\ fraction \propto \left(\frac{D_{max}}{D_{min}}\right)^{n} - 1 \qquad D.41$$

$$W = \sum_{all\ intrusions} \left(\frac{D_{max}}{D_{min}}\right)^{n} - 1 \qquad D.42$$

If we use the simplest n=1 value, the large variability in the weights of the different peaks means that one peak will always strongly dominate all others, producing an overly simple intrusion geometry (Fig. D.5), similar to making the fraction intruded into dikes 0 (Fig. D.4). Models with n=1 are also more prone to numerical instabilities caused by the ability of the ratio in equation D.41 to grow to extreme values. Very small values of n, however, spread melt too evenly between the major melt bodies and other more minor rheological discontinuities, suppressing the ability of melt to accumulate in to large magma chambers

(Fig. D.5), similar to making the dike fraction too high. An n value of 0.5 produces the best fit with observation, but we again emphasize that basalts rising from the mantle still either accumulate in either the mid-crustal sill or at the Moho, and that no major changes to this fundamental geometry are produced by changing the value of n.

Large values of the parameter L produce larger volcanic/plutonic ratios, as is clearly demonstrated in Figs. D.6 and D.7. As described above, when the W is smaller than L, the fraction W/L of the melt available in the given intrusive event is erupted at the surface, after accounting for the fraction input into dikes (which remains fixed). We find that L=15 gives eruption rates of basalt and rhyolite that are broadly realistic with respect to observations of volcanic activity in the field (Christiansen, 2001; Knott et al., 2016). At this point we have performed experiments in varying the value of L for different types of melt, but choose not to reproduce them here.

D.4. Supplementary figures and tables

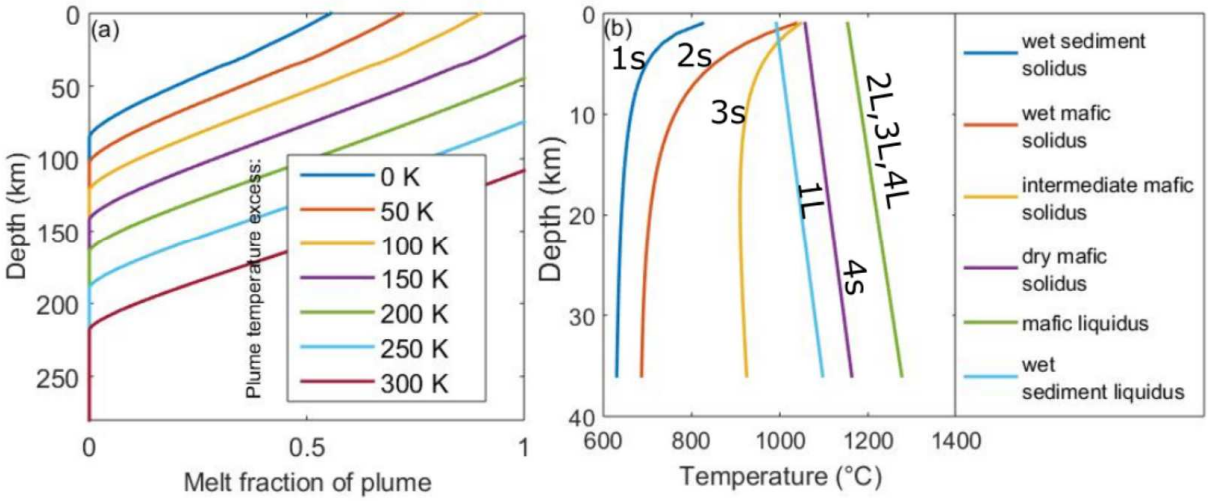

Fig. D.1. (a) Depth vs. melt fraction curves for mantle plumes of different temperatures above ambient mantle with a potential temperature of 1350 °C from the dry mantle melting model of Katz et al. (2003). Our preferred model takes the +175 °C plume to a minimum depth of 80 km under the mantle lithosphere, but melt fractions in the mantle never 3-4% because excess melt is continuously extracted into the crust. Note very strong dependence of mantle melting on pressure and temperature, leading to the strong dependence of model behavior on those parameters seen in Figs. D.6-D.9. **(b)** Melting curves for materials in the crust. Melting curves are numbered for easy referencing in Fig. D.11 and the tables (s=solidus, L=liquidus).

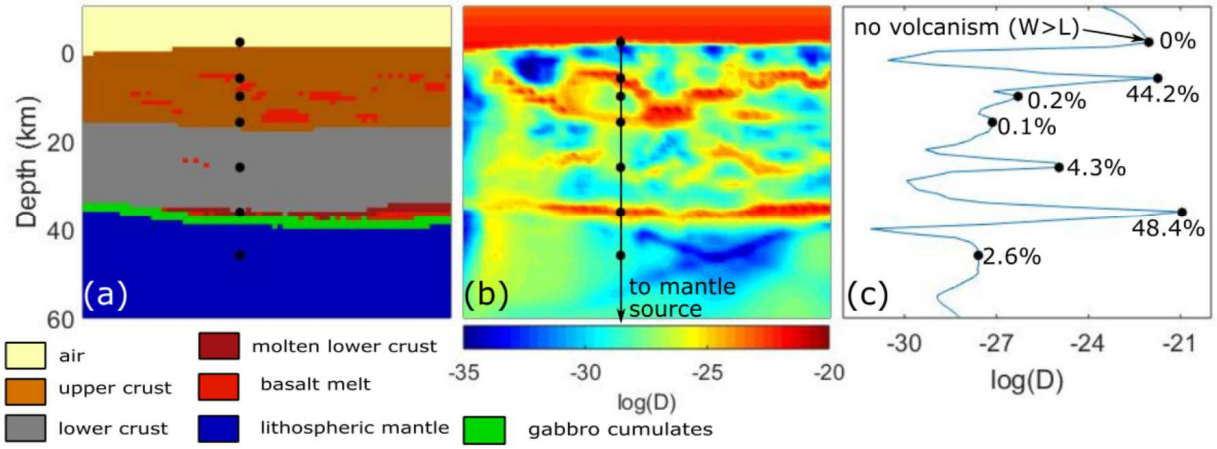

Fig. D.2. Melt transport and accumulation protocol. **(a)** and **(b)** material and D = overpressure/viscosity (equation D.40), respectively, black dots denote areas where basalts rising vertically from the mantle stall and feed into a sill due to the presence of a local maximum in the value of D (equation D.41). **(c)** log(D) along the line seen in **(b)** shows local maxima where melt accumulates. Large drops in D from one local maximum to another cause these areas to accumulate rising melt. Percentages show the fraction of a given dike's magma which will accumulate at each maximum as determined by equation D.42.

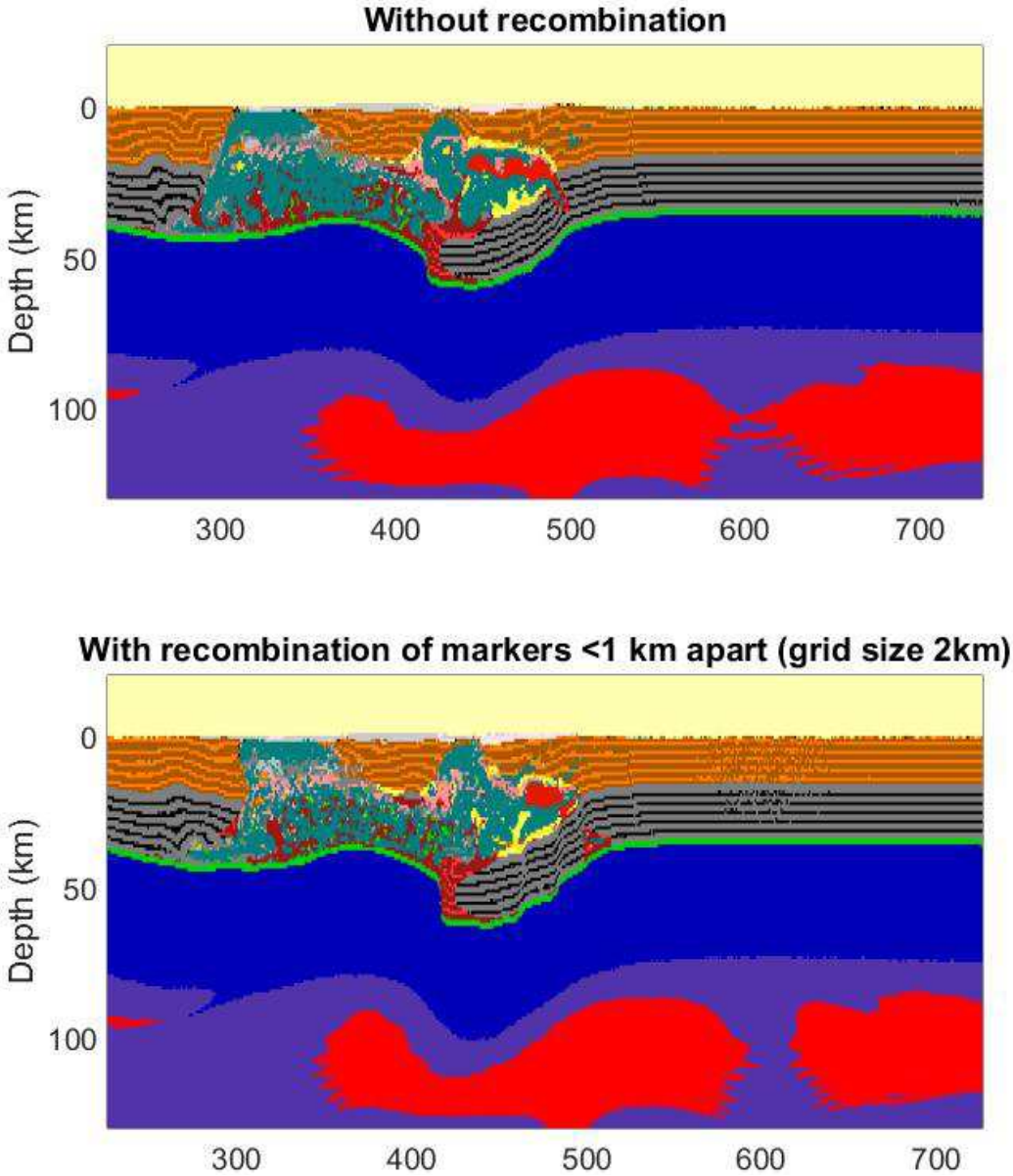

Fig. D.3. We see two models that have been allowed to run for 7.0 Myr using a simplified melt extraction protocol, where all melt is extracted to the point of highest D. While there is loss of information in the model with marker interpolation and recombination, we see that the overall structure is preserved, and the model in the lower panel has approximately one third as many markers to comprise the same image as the original one (this difference can be far larger in more complex models that permit the use of small makers to trace dikes, etc.). We also avoid large numerical diffusion issues because marker recombination is only active in areas of melt accumulation, and no part of the crust experiences significant melt accumulation for more than a few Myr in the model, before significant problems arise. These models are of no further scientific value as they depict unrealistic physics. Models with the physics described in the main paper cannot run without marker recombination.

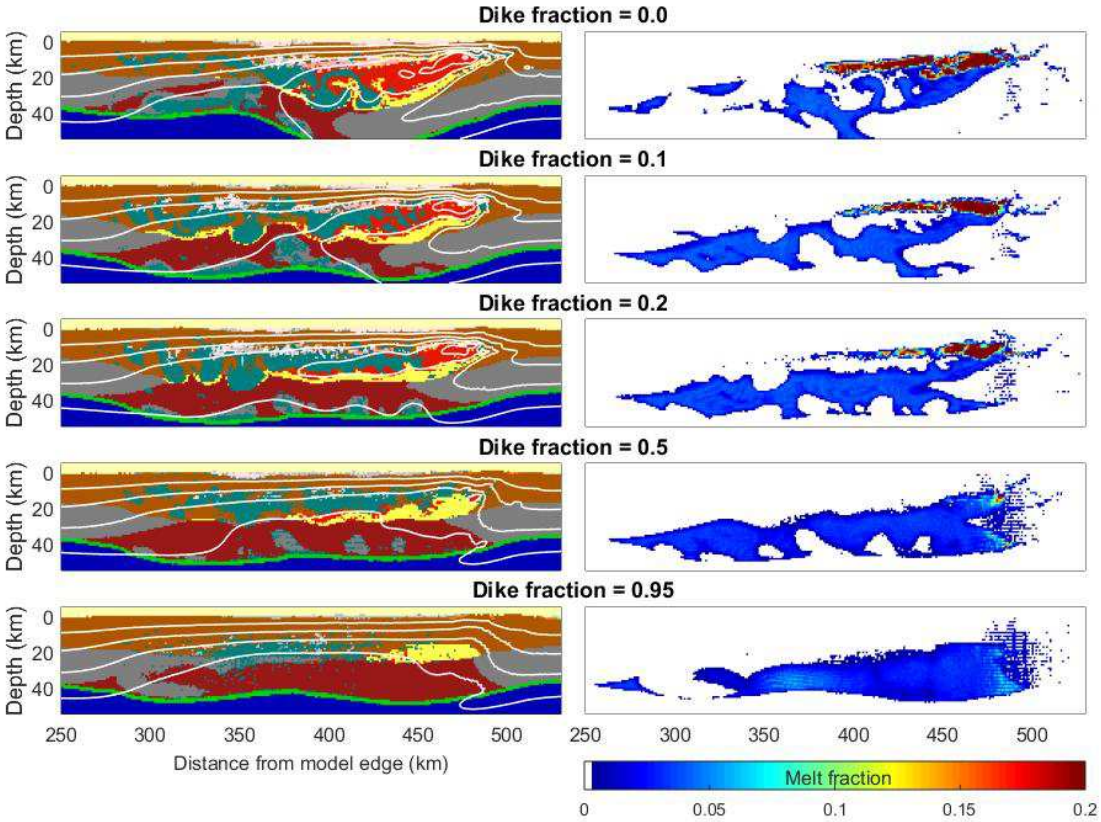

Fig. D.4. Demonstration of the effect of changing the fraction of intruding melt distributed along dike paths vs. in the "sweet spots" defined by local maxima in D (f in equation 5.2, main text; Fig. D.2). Having no magma in dikes tends to concentrate melt all at one depth while the rest of the crust becomes more cool and rigid. On the contrary, having very large fractions of intruding melts reside in cooled dikes (fatter dikes) produces an unrealistically smooth distribution of melting in the crust, similar to the effect of low n values (Fig. D.5). A dike fraction of 0.2 is our base model, as it produces a broad distribution of melt in the crust without losing the large shallow magma body necessary to fuel eruptions.

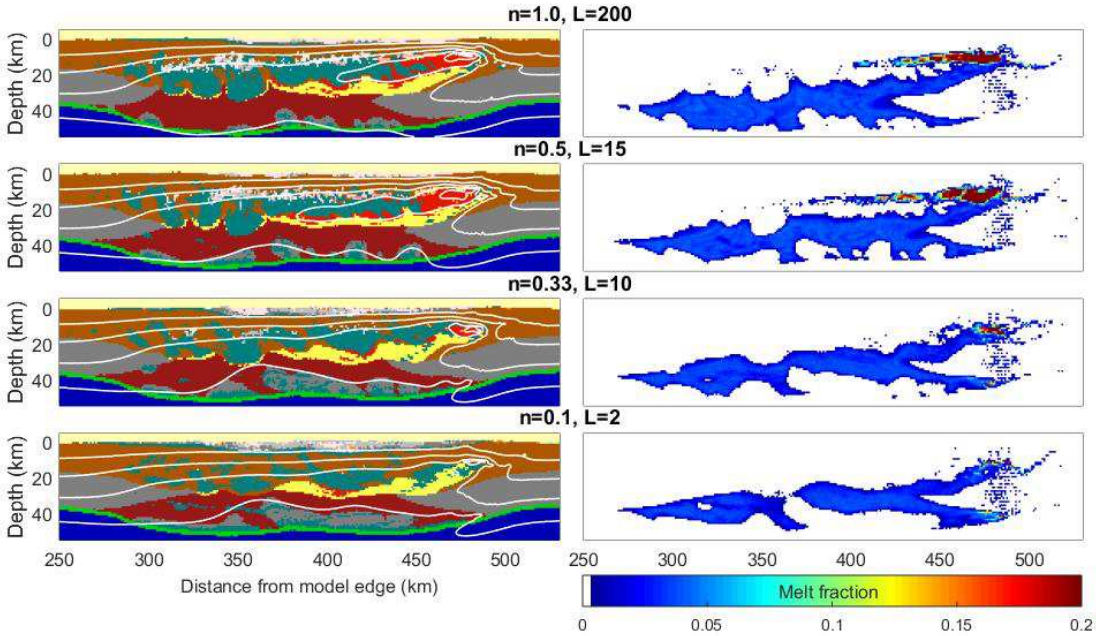

Fig. D.5. Effect of varying n in equation 5.2 (equation D.41 here) in the main text. n=1.0 models are prone to numerical instability, and concentrate melt overwhelmingly at one depth of intrusion, similar to making the dike fraction (Fig. D.4) too small. In contrast, too low n values (bottom panels), spread melt too evenly between different "sweet spots," making heat too distributed in the crust to produce significant magma bodies. We prefer an n value of 0.5 for all models used in the main text.

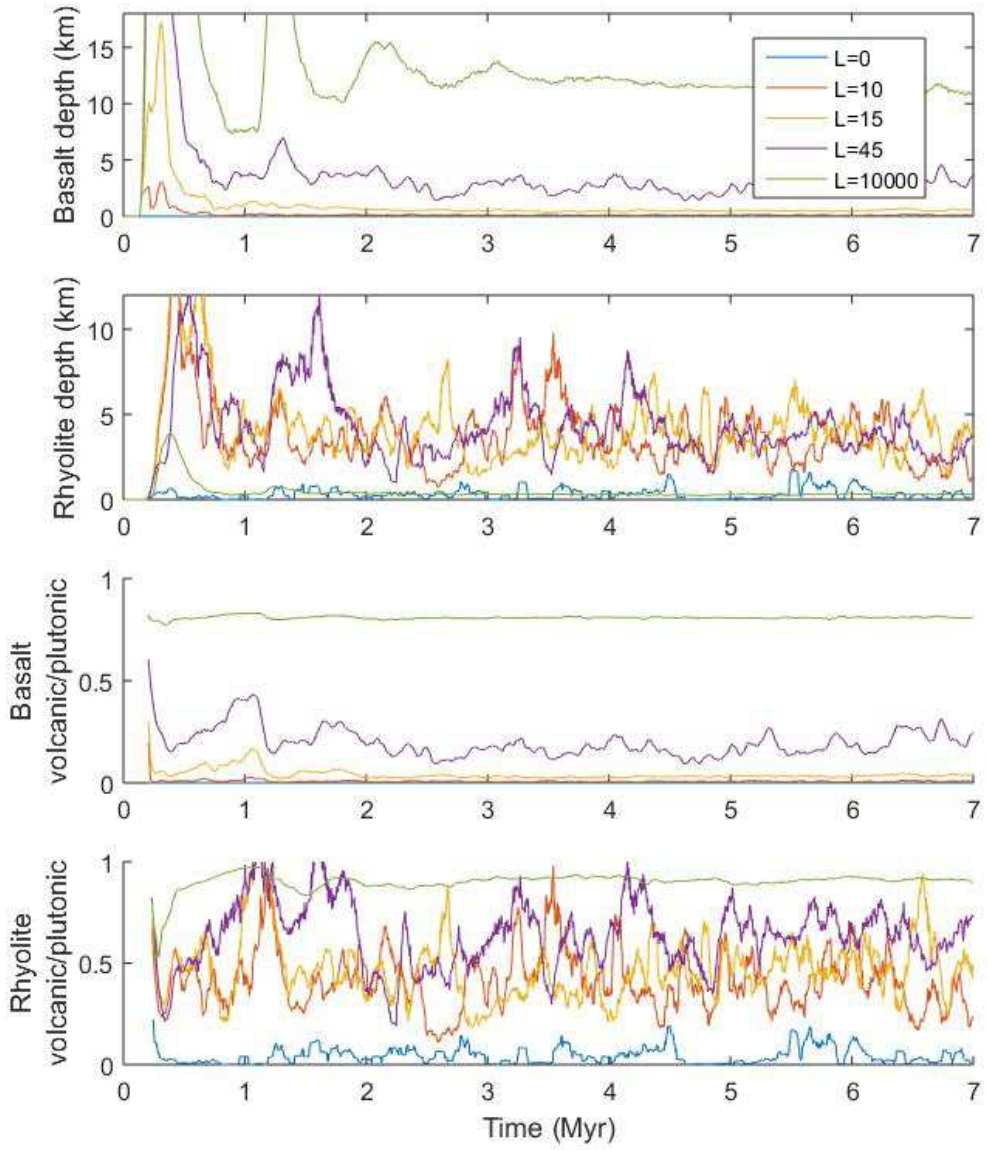

Fig. D.6. Effect of varying L on rates of volcanic eruption. Erupted material thicknesses are computed in the same way as sill thicknesses in Fig. D.6 in the main text, dividing 2D intrusion rates in area/time by the velocity of the lithosphere over the mantle plume. We see that too large L values produce unrealistically large volcanic eruption rates, particularly for basalts. Rhyolite eruption rates do not increase without bound in the same way as removing rhyolite from the crust removes the heat needed to melt crust to produce more rhyolite, whereas the supply of eruptible basalt has no such limitation.

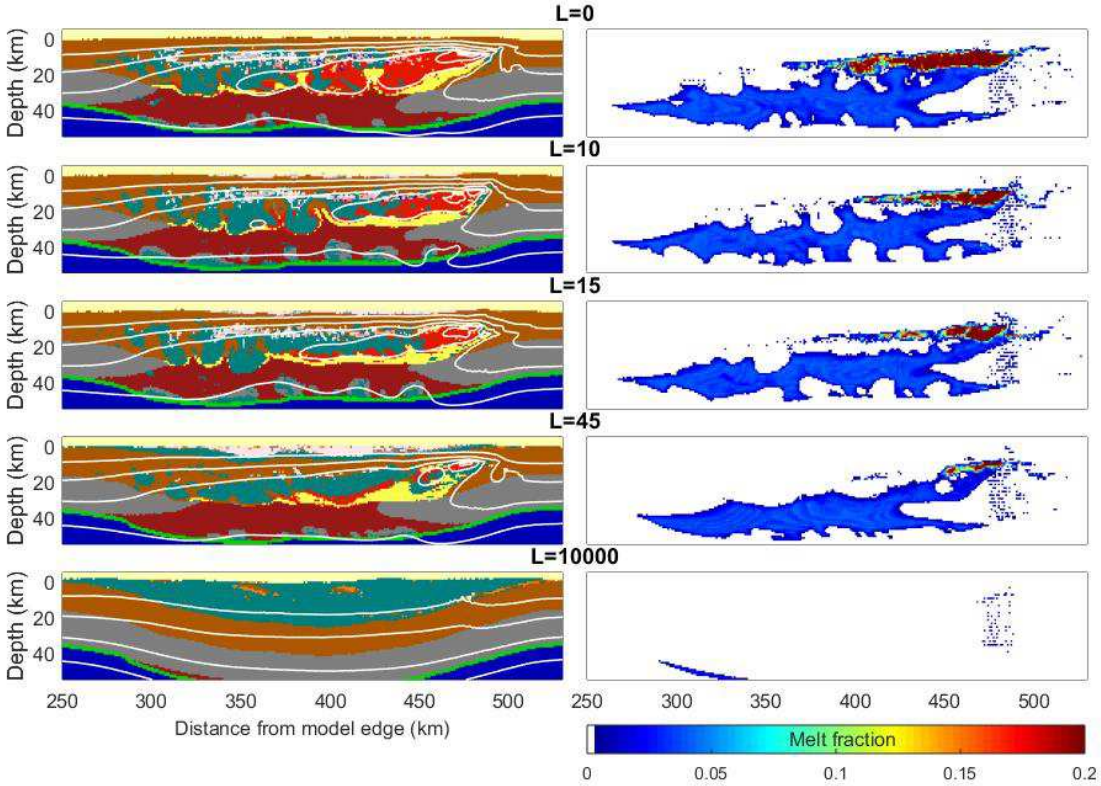

Fig. D.7. Further illustration of the effect of varying the value of L. At L=0, there are no volcanic eruptions (except for when the viscosity of the crust is so low as to prevent intrusions, see main text). Larger values of L decrease the amount of intrusion of basalt into the crust and resultant melting of the both the upper and lower crust (right panels), eventually leading to a system where all basalt erupts at the surface. L=15, our preferred value, produces a robust mid-crustal sill that can be cooled through eruptions enough that it does not develop the large Rayleigh-Taylor instabilities seen in lower L-value models. Our primary constraint, however, in determining L is the eruption rates documented in Fig. D.4.

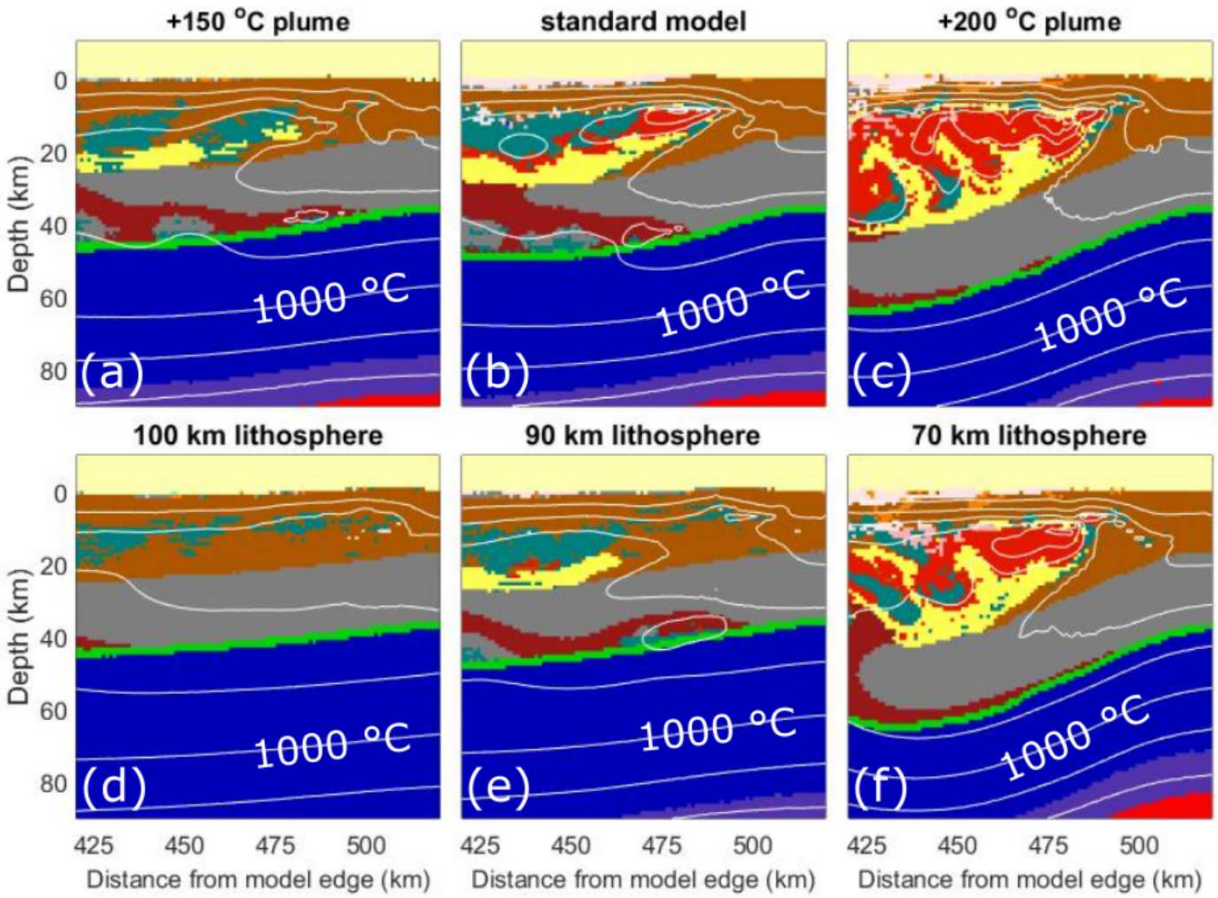

Fig. D.8. Plume temperature **(a-c)** and lithospheric thickness **(d-f)** effects on the tectonomagmatic evolution of Yellowstone system. White contour lines denote temperature and are in intervals of 200 °C. All models are identical to the reference model (top center) except for differences in the title of each panel. Note the fact that while the size and degree of melt contained within the mid-crustal sill varies strongly, the depth to its top is very consistently approximately 10 km. Also note that increasing the plume temperature by 25 °C or decreasing the lithospheric thickness by 10 km (or vice versa) have nearly identical effects on the behavior of the intrusions in the crust. Note the similarity between parts **(a)** and **(c)** here and Fig. 5.4c and Fig. 5.4d in the main text.

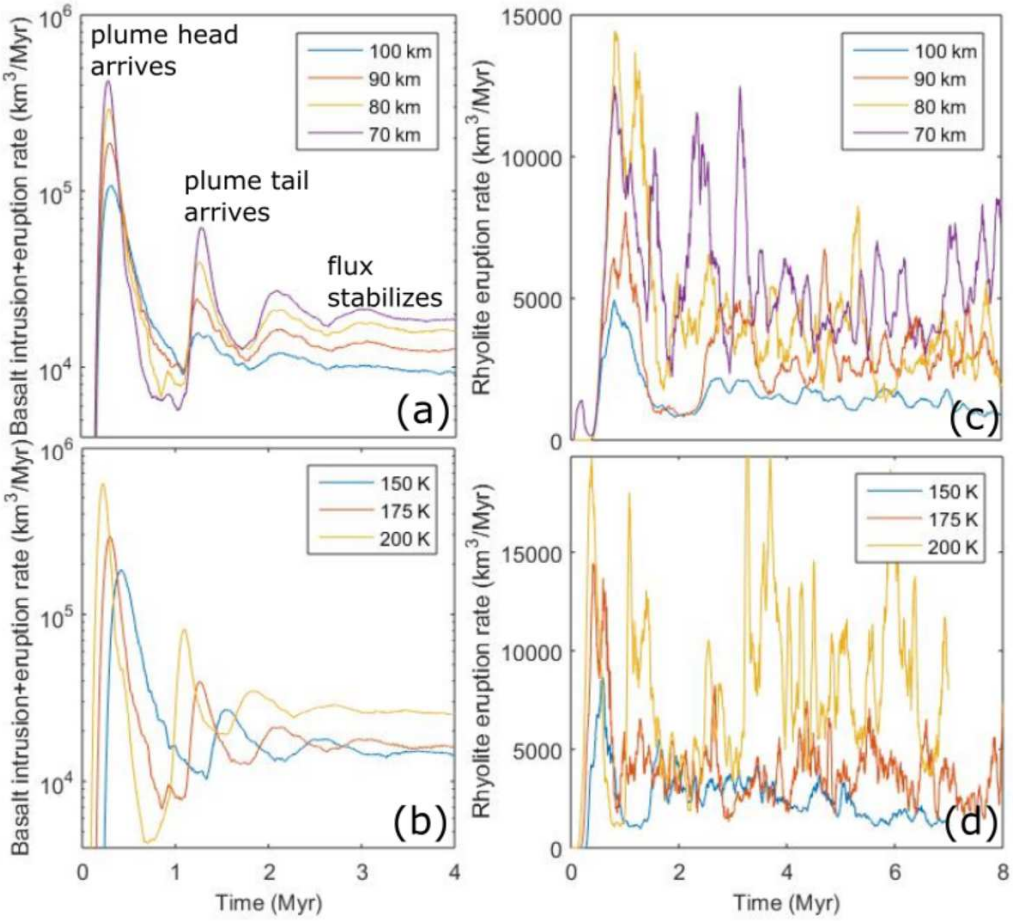

Fig. D.9. Illustration of the effect of changing the lithospheric thickness and the temperature of the mantle plume as in Fig. D.8 and Fig. 5.5 in the main text. **(a)** Basalt intrusion rates as a function of time for varying thickness of the lithosphere (as in Figs. D.8, 5.5 in main text). We also note the three main phases of the melting behavior in and above the plume head discussed in the main text. Note a large initial peak at 0.25 Myr caused by the melting of the plume head, followed by a much smaller secondary peak (note the logarithmic axis) when the plume tail arrives at 1.25 Myr. After this, the basalt production rate in the plume tail becomes remarkably stable. **(b)** Basalt intrusion rates as a function of differences in plume temperature. The pattern is very similar to that of part **(a)**, except that hotter plumes are less viscous and rise more quickly, meaning that the plume head and tail both arrive more quickly for hotter plumes. Finally, we plot rhyolite eruption rates for **(c)** varying lithospheric thicknesses and **(d)** varying plume temperatures, showing a similarly strong dependence on both. These rates are much less stable, showing rapid oscillations, as rhyolite eruption rates are controlled by paths to the surface provided by faults connecting the upper crustal melt zone to the surface (see Fig. 5.2). All plots are 75,000 year moving averages, and calculate volumes by multiplying areas in the model by an assumed thickness in the third dimension of 40 km.

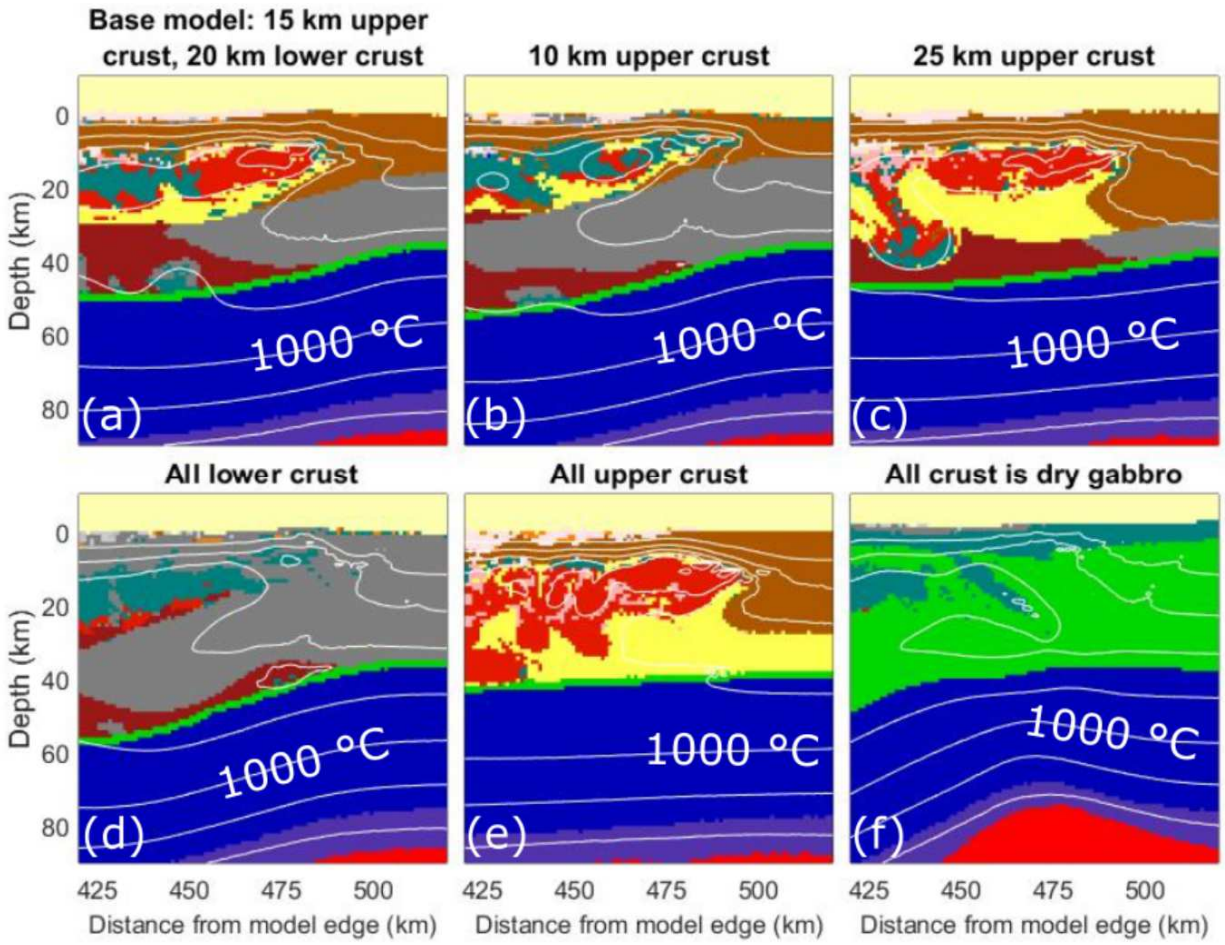

Fig. D.10. Comparison of different crustal compositions on the intrusion geometry produced. All models are identical to the base model and are seen at 7 Myr after the start of the run, with the exception of **(f)** (all dry gabbro crust) which is shown at 6 Myr due to numerical issues that arose later in the run. White lines are 200 °C temperature contours. Note that with the exception of the very dry mafic crust (melting curve 4 in Fig. D.1b), the mid-crustal sill forms consistently at depths of ~10-20 km. The degree of crustal melting varies strongly, however, and the extraction of large volumes of crustal melt into the mid-crustal sill from below keeps it molten for longer in the cases where there is more fertile upper crust. The models seen in parts **(b)** and **(d)** appear in Figs. 5.4a and 5.4b in the main text.

Fig. D.11. Additional experiments testing the robustness of our model against variations in crustal composition, showing effects of varying crustal rheological and melting properties. Many of these models, such as weak lower crust, are likely geologically very unrealistic. These experiments only vary the rheology or, separately, the melting properties of the upper or lower crust to discern the main causes of the dramatic differences observed in Fig. D.10. In models **(a)** and **(b)**, we vary the strength but not the melting properties of the crust, making the lower crust identical in rheology to the upper crust and vice versa. We see no dramatic change when we strengthen the upper crust to be like the lower crust **(b)**, but dramatically increased melting of the lower crust when is weakened like the upper crust, as in part **(a)**. This is because of the increase in the rheological contrast in the Moho, and the lower crust's lack of ability to support the dense mid-crustal sill from flowing down into it. When melting curves are changed, as in **(c)** and **(d)**, all accompanying melting constants in Table D.1 (E_{max}, Q_L) are changed accordingly. We see that we can effectively shut off crustal melting in the lower crust with a relatively minor increase in solidus temperature **(c)**, while other changes in melting properties **(d, e)** make less dramatic changes. Very fertile lower crust **(d)** produces increased melting, but to a much lesser degree than weakening it. Finally, in part **(f)** we show heterogeneous lower crust, which alternates between curve 2 and 3 and weak and strong rheologies (black is weak and fertile). Melting curve numbers are a reference to Fig. D.1. These models allow us to rule out very refractory lower crust for the Yellowstone system.

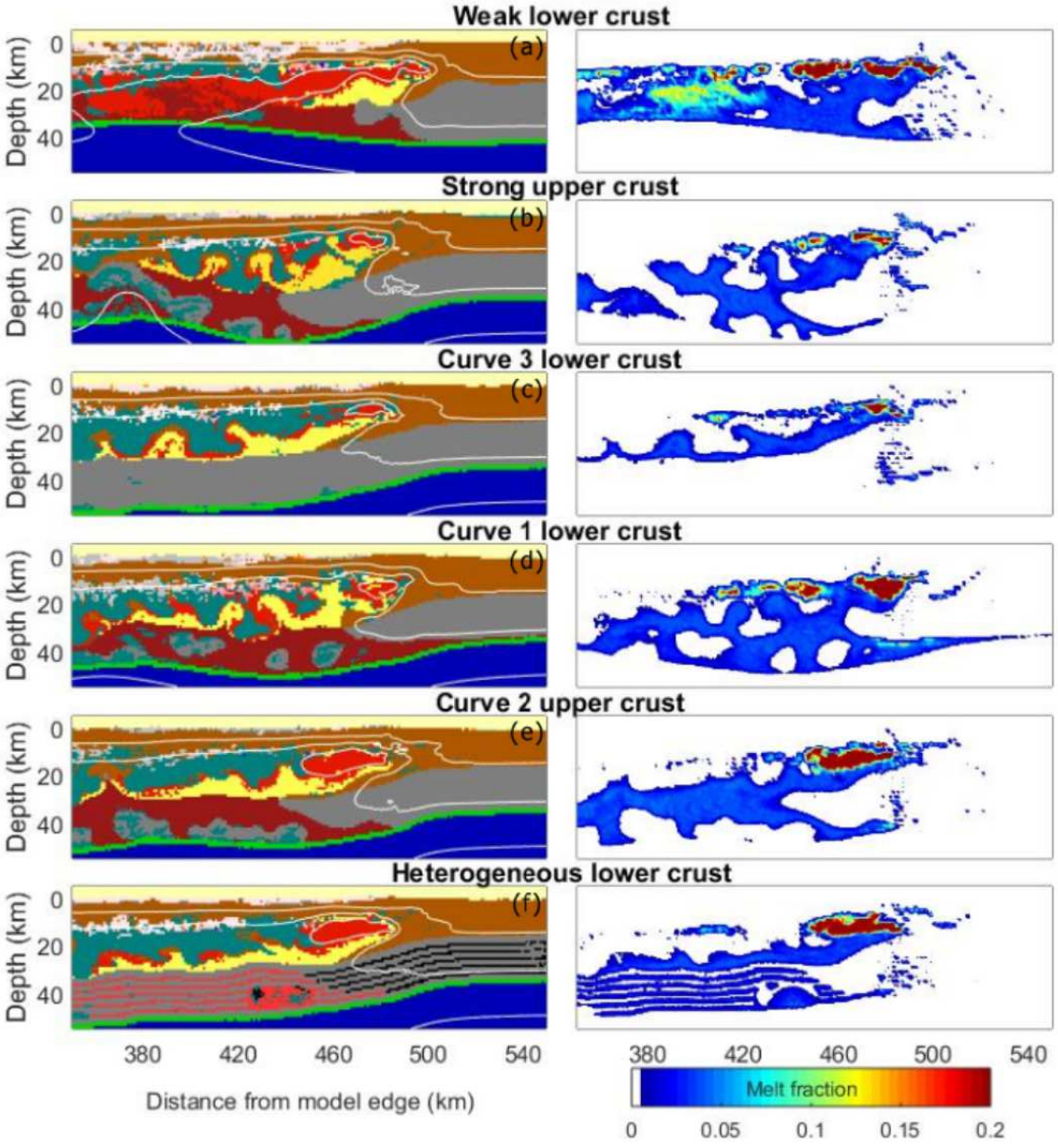
Weak lower crust
(a)
Strong upper crust
(b)
Curve 3 lower crust
(c)
Curve 1 lower crust
(d)
Curve 2 upper crust
(e)
Heterogeneous lower crust
(f)
Depth (km)
0
20
40
380
420
460
500
540
Distance from model edge (km)
Melt fraction
0
0.05
0.1
0.15
0.2

Table D.1. Rheological parameters of rock types

	A_D ($Pa^n \cdot s$)	E (J)	V (J/bar)	n	ρ_r solid ($kg \cdot m^{-3}$)	ρ_r melt ($kg \cdot m^{-3}$)	H_r (W/kg)	K_0 (W/(m·K))	K_f (W/m)	Melting Curve	Q_L ($kJ \cdot K^{-1} \cdot kg^{-1}$)	M_0	M_1	E_{max}
See equation	5.9	5.9	5.9	5.9	5.22	5.22	5.3	5.4	5.4		5.19	5.38	5.36	5.36
Upper crust	$1.97 \cdot 10^{17}$	$1.54 \cdot 10^5$	0.0	2.3	2700	2400	$2.00 \cdot 10^{-6}$	0.64	$8.07 \cdot 10^2$	[6,7]1	[4]300	0.03	0.05	0.9
Lower crust	$4.80 \cdot 10^{22}$	$2.38 \cdot 10^5$	0.0	3.2	2900	2600	$0.25 \cdot 10^{-6}$	1.18	$4.74 \cdot 10^2$	[8,9]2	[4]380	0.03	0.05	0.33
Mafic cumulate	$4.80 \cdot 10^{22}$	$2.38 \cdot 10^5$	0.0	3.2	3000	2800	$0.10 \cdot 10^{-6}$	1.18	$4.74 \cdot 10^2$	[9]4	[4]380	0.03	0.05	0.2
Mantle	$3.98 \cdot 10^{16}$	$5.32 \cdot 10^5$	0.8	4.0	3300	2900	$2.20 \cdot 10^{-8}$	0.73	$12.93 \cdot 10^2$	See Katz et al. (2003)	[5]400	0.01	0.03	0.4
Basalt from mantle	$4.80 \cdot 10^{22}$	$2.38 \cdot 10^5$	0.0	3.2	3000	2600	$0.25 \cdot 10^{-6}$	1.18	$4.74 \cdot 10^2$	[8,9]2	[4]380		0.0.0305	0.15
Dacite from basalt	$1.97 \cdot 10^{17}$	$1.54 \cdot 10^5$	0.0	2.3	2700	2500	$1.00 \cdot 10^{-6}$	1.18	$4.74 \cdot 10^2$	[6,7]1	[4]300	0.03	0.05	0.9
Rhyolites	$1.97 \cdot 10^{17}$	$1.54 \cdot 10^5$	0.0	2.3	2700	2300	$2.00 \cdot 10^{-6}$	0.64	$8.07 \cdot 10^2$	[6,7]1	[4]300	0.03	0.05	0.9
Source	1	1	1	1	n/a	n/a	2	3	3	see above	see above	n/a	n/a	n/a

Other parameters: Eq. D.3: $C_p = 1000$ J/kg; Eq. D.4: $K_p = 0$; Eq. D.8: $\sigma_{cr} = 3.0 \cdot 10^4$ Pa; Eq. D.14-D.15: $\lambda=1$, $a_{0\ subsolidus} = 10^7$ $a_{0\ molten} = 10^6$, $a_1 = 10^6$, $b_{0(subsolidus)} = 0.15$, $b_{1(subsolidus)} = 0.075$, $b_{0(molten)} = 0$, $b_{1(molten)} = 0$; Eq. D.22: $\alpha = 10^{-3}$ $kbar^{-1}$, $\beta = 3 \cdot 10^{-5}$ K^{-1}

Sources: [1]Ranalli (1995); [2]Clauser and Huenges (1995), [3]Clauser and Huenges (1995), Hofmeister (1999), [4]Bittner and Schmeling (1995), [5]Turcotte and Schubert (1982), [6]Johannes (1985), Poli and Schmidt (2002), [7]Johannes (1985), [8]Schmidt and Poli (1998), [9]Hess (1989)

Table D.2. Summary of selected representative models

Model number	Differences from standard model	Notes
Base Model		
***p1n95**	base model, no differences	Figs. 5.3, 5.4, 5.5
Varying lithosphere thickness:		
***p1n96**	70 km lithosphere	Fig. 5.5
***p1n97**	90 km lithosphere	Fig. 5.5
***p1n140**	60 km lithosphere	Delaminates rapidly
***p1n141**	100 km lithosphere	Fig. 5.5
Plume temperature:		
p1n138	+150K	Fig. 5.5
p1n139	+200K	Fig. 5.5
p1n142	+125K	Almost no melting
p1n143	+225K	Rapid delamination and melting of entire lower crust
Crustal composition (basic):		
p1n136	all dry mafic crust	Fig. D.10
p1n144	all felsic crust	Fig. D.10
p1n137	all wet mafic crust	Fig. D.10
p1n156	Same as p1n137 but upper crust retains normal heat properties	No major changes
p1n149	Same as p1n156 but densities of upper and lower crust are different	No major changes, density does NOT drive intrusion geometry
p1n154	Upper crust 10 km thick	Fig. D.10
p1n155	Upper crust 25 km thick	Fig. D.10
p1n157	Upper crust same density as lower crust ($2.9 g/cm^3$)	No major changes from base model
Crustal Rheology		
p1n145	Lower crust has wet quartzite rheology, cannot form cumulates	Fig. D.11
p1n146	Upper crust has An75 rheology	Fig. D.11
p1n147	Striped rheology, 1 km stripes	No major changes, see p1n158
p1n148	Striped rheology, 5 km stripes	No major changes, see p1n158
Crustal fertility:		
p1n150	Upper crust melts like lower crust but is still wet quartzite rheology	Fig. D.11

Table D.2 (continued).

Model number	Differences from standard model	Notes
p1n151	Lower crust has dry mafic fertility (curve 4), upper crust intermediate (curve 3)	Mid-crustal sill forms, but almost no crustal melting, no intrusions in lower crust
p1n94	Lower crust has intermediate mafic fertility	Fig. D.11
p1n98	Lower crust has wet sediment fertility	Fig. D.11
p1n152	Lower crust has striped intermediate/wet mafic fertility, all An75 rheology	Crustal melting only occurs in areas of greater fertility in lower crust.
p1n158	Striped+one large fertile anomaly in lower crust	Fig. D.11
p1n159	Above but with no stripes	No increase in lower crustal melting at large anomaly relative to p1n158, no lower crustal melting otherwise, as per p1n94
Other parameters		
p1n153	Melts from mantle are dry (Curve 4)	Mid-crustal sill entirely solid, overall geometry preserved
p1n162	25 C/km geotherm	Delaminates rapidly, lower crust starts out well above solidus temperature
p1n163	Melts from mantle are saturated (wet melting curve 2)	Entire mid-crustal sill stays partially molten for a long time, overall geometry preserved
p1n164	Melts from mantle have intermediate melting	Melt in mid-crustal sill suppressed relative to base model, but not as much as p1n153
p1n166	Entire mantle advects parallel to the lithosphere	Plume carried away by mantle flow to edge of model, suggest further 3D modeling to test non-parallel flows.
p1n167	Dikes cross mantle, but no peaks in mantle	
p1n168	Plume advection speed 33% higher	Similar result to p1n96
p1n169	Plume advection speed 33% lower	Similar result to p1n97

Table D.2 (continued).

Model number	Differences from standard model	Notes
Tests of varying n values:		
p1n106	n=1.0 (0.5 normal) L=200 (15 normal)	Fig. D.5
p1n107	n=0.33 L=10	Fig. D.5
p1n108	n=0.1 L=2	Fig. D.5
Tests of dike width/spacing:		
p1n109	dike fraction = 0% (20% normal)	Fig. D.4
p1n110	dike fraction = 10%	Fig. D.4
p1n111	dike fraction = 50%	Fig. D.4
p1n133	dike fraction = 95%	Fig. D.4
Tests of varying resolution (base=2 km):		
p1n112	striped crust like p1n158, 1 km resolution	Intermediate between base and p1n116
p1n114	striped crust like p1n158, 1.33 km resolution	Similar to base model
p1n115	striped crust like p1n158, 1.66 km resolution	Similar to base model
p1n116	striped crust like p1n158, .5 km resolution	Melt distributed into too many small melt lenses, inappropriately small area in each cell to calculate D (equation D.40)
Comparison of basic models with/without recombination of markers:		
p1n119	no recombination	Fig. D.3
p1n120	with recombination	Fig. D.3
Tests of varying L values:		
p1n124	L=0 (15 normal)	Figs. D.6, D.7
p1n125	L=10	Figs. D.6, D.7
p1n126	L=45	Figs. D.6, D.7
p1n127	L=10000	Figs. D.6, D.7
These models with only mantle melting, to build Fig. 5.5 (main text):		
p1n48	+200K plume, 60 km lithosphere	These models only measured for basalt melting in the mantle, crustal processes ignored
p1n49	+200K plume, 100 km lithosphere	
p1n50	+150K plume, 60 km lithosphere	
p1n51	+150K plume, 100 km lithosphere	

Table D.2 (continued).

Model number	Differences from standard model	Notes
p1n52	+175K plume, 100 km lithosphere	
p1n53	+175K plume, 60 km lithosphere	
p1n59	+150K plume, 80 km lithosphere	
p1n60	+175K plume, 80 km lithosphere	
p1n61	+200K plume, 80 km lithosphere	

APPENDIX E

MATERIAL FOR CHAPTER VI

Contents:

E.1. Melt transport detailed methods
E.2. Modeling melt propagation through melt bodies
E.3. Compositional changes in markers during melt extraction
E.4. Marker recombination
E.5. Detailed Heat2D methods

E.1. Melt transport detailed methods

Every marker is checked during every time step to see whether there is melt available for extraction. The type of melt transport which occurs depends on the melt fraction of the source Lagrangian marker, and the melt content of the surrounding material. To model dikes, we assume, as per Solano et al. (2012), that a minimum melt fraction of 50% must exist in the source Lagrangian marker in order to initiate a dike. Individual markers in this model can be quite large, with an area of 0.25 km^2, corresponding to a volume of as much as 12.5 km^3 if we multiply by a presumed model thickness of 50 km. A single marker that is more than 50% molten should therefore easily be able to generate a dike. We further assume that the bulk melt-crystal mixture can travel as a unit in this system, and both the solid and liquid parts of the marker are extracted in the dike. If the melt is buoyant enough, we further assume that all melt is extracted from the melt body into the dike. For now, we assume this is done with near perfect efficiency, and that a given diking event extracts 99% of the material from a given marker; improving estimates of this value based things like melt viscosity and crystallinity is a topic of future research.

Once a dike has been initiated, we must then determine how melt is distributed along the dike. If the given time step does not include an eruption, we define the non-dimensional melt intrusion efficiency parameter, D (see also Colón et al., 2018a):

$$D = \frac{(P_0 - P_x) - \rho g (y_x - y_0)}{\eta} \Delta t \qquad E.1$$

where Δt is the 5 kyr timestep, η is the viscosity of the crust next to a given part of the dike, P_0 is the ambient pressure at the source of the melt, P_x is the ambient pressure at the given point along the dike, ρ is the melt density, g is the acceleration of gravity (9.8 m/s^2), and h is the vertical distance between the point along the dike and the source melt. Places where the value of D is large, with- high melt overpressure (ΔP) and low ambient rock strength, should be more amenable to accumulating melt. Field work and modeling of dikes (e.g. Annen et al., 2015; Kavanagh et al., 2006; Menand, 2011) have demonstrated that the primary phenomenon that arrests rising dikes is rheological contrast in the source rocks, so we combine these two ideas to assume that melt accumulates at local maxima in D, and that melt preferentially accumulates at those local maxima where the contrast with the overlying local minimum in D is greatest (we assume D must be 10% greater than the value at adjacent minima). These local maxima can be thought of as sills fed by the rising dike, which may be new intrusions, or preexisting melt bodies grown by a new dike, and they frequently serve as traps for later rising melts due to their low viscosity (equation 4). Finally, we consider that some material must accumulate between these local maxima along the dike. This is assumed to be some fixed fraction of all dikes (20% in most models, see Colón et al., 2018a). When there are not eruptions, the fraction of the total melt in a dike which intrudes along any portion of it is thus:

$$intrusion\ fraction = s + d \qquad E.2$$

$$s = \left(\frac{D_{max}}{D_{min}}\right)^{0.5} * \frac{1}{L} * (1 - f) \quad if \ \ at\ a\ sill\ location\ (D\ local\ maximum) \qquad E.3$$

$$s = 0 \qquad if\ not\ at\ a\ sill \qquad E.4$$

$$d = f * \frac{dy}{y_b - y_t} \qquad E.5$$

$$L = \sum \left(\frac{D_{max}}{D_{min}}\right)^{0.5} \qquad E.6$$

For a description of variables see Table E.1. In the uncommon case where y_t is defined by buoyancy and is also a local maximum in D, the value of D_{max}/D_{min} is assumed to be 0.1 by default.

Variable	Explanation	Variable	Explanation
D	Melt extraction efficiency parameter	dy	Model resolution
D_{max}	Value of D at local maximum, always compared to the overlying local maximum	y_b	Depth of bottom of intrusion column, equal to y_0 or the depth to the Moho, whichever is shallower
D_{min}	Value of D at a local minimum, always compared to the underlying local maximum	y_0	Depth of source melt
P_0	Pressure at site of source melt	y_t	Depth of shallowest intrusion (0 if erupting)
P_x	Pressure at new intrusion	y_x	Depth of a new intrusion
ρ	Density of melt	d	Intrusion fraction at a certain depth due to dike
g	Gravitational acceleration (9.8 m/s^2)	s	Intrusion fraction at a certain depth due to sill (at local maximum of D along dike)
η	Average effective viscosity of material in cell containing new intrusion	f	Fraction of all intrusion devoted to dikes (0.2, empirically determined, see Colón et al., 2018a)
Δt	Timestep of model (5 kyr)		

Table E.1. Summary of melting-related variables used to determine the distribution of extracted melts from a zone of initial partial melt (Equations 4-9).

Of the four melt transport mechanisms, only dikes can produce volcanic eruptions, because the uppermost crust will always be brittle and solid, and therefore

inaccessible to porous flow or convective transport of melt. Eruption triggering mechanisms in large caldera-forming systems are poorly understood and very complex (e.g. Allen et al., 2012; Gregg et al., 2015; Karlstrom et al., 2012), requiring an understanding of the elastic and brittle failure properties of the uppermost crust on timescales smaller than our computational timestep (typically 5 kyr), and therefore are beyond the scope of this study. Instead, we assume that eruptions occur at roughly random intervals, and give each time step in the model an equal chance of having an eruption. When an eruption is decided to occur at a given timestep, all melt rising through dikes that is buoyant enough to reach the surface does so, with the exception of material left behind in the dikes (equation 8) and the 1% that remains in the source material. We temporarily set melt densities to 1000 kg/m^3 during eruptions in order to ensure that all available melt erupts, otherwise only the least buoyant and evolved melt at the top of a magma body will be considered buoyant relative to its surroundings during an eruption, as sudden changes in melt buoyancy due to the removal of overlying melt cannot be considered within a single time step. Finally, we disallow basalt eruptions, and only erupt silicic melts, to force a match with the observation that there are no basaltic eruptions within the caldera system at Yellowstone during the caldera cycle (Christiansen, 2001).

E.2. Modeling melt propagation through melt bodies

With the exception of basalts coming from the mantle, most melt transport within the crust in our models is not in the form of dikes but rather consists of porous flow within mostly solid rock or naturally (computationally) arises as material redistribution via buoyancy-driven convection/advection of melt within a large liquid melt body. If a

small pocket of melt within the crust (a single Lagrangian marker) has less than 50% liquid by volume, and thus cannot flow as a dike, and is surrounded by solid rock, there is no melt extraction. However, if a partially molten marker exists in an environment (the local cell of the finite difference grid) that is at least 2% molten, we say that melt is able to be extracted and flow via porous flow (Rosenberg & Handy, 2005; Solano et al., 2012). Unlike in dikes, the extracted material is strictly molten, and all solid material is left behind in the original source marker along with 1% of the total melt volume in the source marker (1% of the melt fraction, which itself may be as low as 2%; melt extraction is assumed to be 99% efficient from one cell to the next). Melt moves either up or down depending on local buoyancy, unlike in dikes where only upward movement is possible, and either finds its point of neutral buoyancy within the local melt zone, or travels all of the way to the top or the bottom of the melt zone, depending on its density. These melts are not assumed to be able to travel through solid rock which is less than 1% liquid, and this means of melt transport can only redistribute melt within a given magma body, not transport it to a separate system or the surface.

In the case where the initial marker melt fraction is greater than 50%, and the surrounding material is also partially molten, the bulk melt and crystal material is extracted, as for a dike traveling through solid rock, and equations 4-9 are used to determine the distribution of material produced by this intrusion. These melts can be transported out of their host melt zone to shallower intrusions or to the surface. Additionally, if a rising dike encounters a melt body (of at least 20% melt), the pressure term P_0 will be reset to the ambient pressure at the base of the melt body, and the value of D in equation 4 will be recalculated to make sure that a dense mafic melt does not ascent

through a body of less dense liquid (though the reverse is permitted). Finally, any melt markers assigned to local maxima of D within melt bodies of at least 50% melt which are partially molten are allowed to move up and down and find their point of neutral buoyancy, as is the case for porous flow. This allows us to produce zoned magmatic systems where the coolest, most evolved, and least dense magmas are on the top of the system, and more mafic magmas are underneath.

These systems for treating magma transport within melt zones are extremely simplified relative to models which solve porous fluid flow equations (e.g. Solano et al., 2012) or fluid flow equations for convecting magma bodies (e.g. Ruprecht & Bergantz, 2008 (check); Simakin & Bindeman, 2012). For porous flow, in particular, we have no limit on the distance that extracted melt can travel during a single 5 kyr timestep, which while appropriate for dikes and convective flow, may overestimate the efficiency with which low-percentage melt zones can release and consolidate their liquid portion, particularly for the high-viscosity fluids which should be most common at low melt fractions. Implementing better two-phase fluid flow schemes and modeling non-purely vertical dike transport are perhaps the two most important fields for future improvement for these models. For the time being, however, we consider based on the discussion below that these methods allow us to derive a good rough approximation of the distribution of melts in a continental hot spot magmatic system.

E.3. Compositional changes in markers during melt extraction

When determining the amount of melt available for extraction from a given Lagrangian marker, we first calculate the value X_{melt}:

$$X_{melt} = 0 \; at \; T \leq T_{solidus}$$
$$X_{melt} = \frac{T - T_{solidus}}{T_{liquidus} - T_{solidus}} \; at \; T_{solidus} < T < T_{liquidus}$$
$$X_{melt} = 1 \; at \; T \geq T_{liquidus} \qquad E.7$$

which we correct for the highly non-linear melting behavior of a fractionating basalt as follows:

$$X_{melt\,new} = \frac{0.2}{0.75} \cdot X_{melt} \; if X_{melt} < 0.75$$
$$X_{melt\,new} = \frac{T - T_{Xmelt=0.75}}{T_{liquidus} - T_{Xmelt=0.75}} \; if X_{melt} > 0.75 \qquad E.8$$

Here $T_{liquidus}$ and $T_{solidus}$ are computed from specific melting curves which we use for different types of materials, such as upper crust, lower crust, and mafic cumulate (described in detail in Colón et al., 2018a, though we use a 120°C cooler solidus temperatures for the most evolved rhyolites, which we will correct in later revisions). However, markers which have already given up melt in previous extraction events will be less fertile for melting at a given temperature. We crudely account for this by keeping track of the volume fraction of a marker's original size which has been lost to melt extraction, which we call M_{ex} (Table E.2). We then calculate the volume fraction of a given marker which is liquid as follows:

$$Melt\ fraction = \frac{X_{melt} - M_{ex}}{1 - M_{ex}} \qquad E.9$$

Here we can see that the melt fraction is greatest when the value of M_{ex} is 0, for a fixed temperature and therefore X_{melt}. If M_{ex} is greater than X_{melt} than there has already been an extraction from that marker at an equal or greater temperature, and the material is solid.

Variable	Explanation
M_{ex}	Fraction extracted
M_{wt}	Marker volume, not including extraction
M_{frac}	Fraction remaining (even after multiple extraction events)
M_{d18o}	Marker oxygen isotope composition
M_{ehf}	Marker hafnium isotope composition
M_{sio2}	Marker silica content (percent)
M_0	Fraction of material to be left behind after extraction

Table E.2. Summary of melting-related variables attached to individual Lagrangian markers in our I2VIS model. These are saved between time steps, whereas variables like X_{melt} are computed from the above variables independently at each timestep.

To manage changes in melt composition and track melt volume, we keep track of four variables which are associated with each Lagrangian marker, M_{ex}, M_{wt}, $M_{k,}$ M_{frac}, and M_{sio2}. M_k is simply the temperature of a given marker in Kelvin, which is interpolated onto grid nodes in order to solve a heat equation, and then back onto the markers at the end of the time step (Gerya, 2010; Gerya and Yuen, 2003). M_{wt} and M_{ex} together constrain the (two-dimensional) volume of a given marker, M_{vol}, which is given as:

$$M_{vol} = (1 - M_{ex})(1 - M_{wt}) * M_{dx} * M_{dy} \qquad E.10$$

where M_{dx} and M_{dy} are fixed variables that are ¼ of the grid size of the model (so 500 m for a 2 km-square finite difference grid). At the outset of the model, M_{wt} and M_{ex} are both set to 0 for all markers. Melt extraction from a partially (or fully) molten Lagrangian marker is accomplished by shrinking the source marker by changing its M_{ex} value to a new value as follows:

$$M_{ex}(new) = M_{ex} + (X_{melt} - M_{ex} - (1 - M_{ex}) * M_0) * (1 - W) \qquad E.11$$

Here X_{melt} is the fraction of the source marker which is calculated as being molten using equations 11-13 below, M_0 is the minimum volume fraction of melt which is always left behind after extraction, and W is the fraction of melt available for extraction which is not extracted because of lack of buoyancy relative to the source region; this value is nearly always 0. This modifies M_{vol} without changing the value of M_{wt}, which reflects the volume of the marker upon its original creation and is not ever changed afterwards, except during marker recombination (see below). Extracted melt is treated in the model by creating one or more new markers with the composition of the melt material. These are given M_{ex} values of 0, indicating that they themselves have not yet had any melt extracted from them. The new M_{wt} values of the markers sum up to the following, which ensures the conservation of mass:

$$\sum M_{wt} = 1 - (1 - M_{wt}) * (X_{melt} - M_{ex} - (1 - M_{ex}) * M_0) * W \qquad E.12$$

Similarly to the way that the source marker is made more refractory after melt extraction by increasing M_{ex}, the composition of the extracted markers must be more fusible at a given temperature than the source marker, which we track using the marker-associated variable M_{frac}:

$$M_{frac}(extracted\ melt) = M_{frac}(source) * \frac{(X_{melt} - M_{ex} - (1 - M_{ex}) * M_0)}{(1 - M_{ex} - (1 - M_{ex}) * M_0)} \qquad E.13$$

We then compute:

$$M_{sio2}(extracted\ melt) = M_{sio2}(source) + \\ (78 - M_{sio2}(source)) * (1 - M_{frac}(extracted\ melt) \qquad E.14$$

where M_{sio2} is the silica content in percent, assuming a vastly simplified situation where SiO_2 content in a melt varies linearly with the fractionation percentage (a 10% fractional melt will have twice the silica increase above the source as a 20% fractional melt). For

this model, we assume that all basalts have initial SiO_2 values of 48%, upper crust is 70% SiO_2, and lower crust is 50% SiO_2, and let the system evolve from there. As mentioned above, melt density is critical to determining the direction of melt propagation within a melt body, and it is computed as:

$$\rho_{melt} = 2300 + \frac{M_{frac} * (melt\ fraction) - 0.12}{1 - 0.12} * (\rho_{primitive} - 2300) \qquad E.15$$

$$if\ \rho_{melt} < 2300,\ \rho_{melt} = 2300 \qquad E.16$$

where densities are expressed in kg/m^3, ρ_{melt} is the density of the extracted melt, and $\rho_{primitive}$ is the density of a pure melt of the source rock type (basalt, lower crust, upper crust, etc., detailed properties in Colón et al., 2018a). The above equation treats the density of an extracted melt as a linear function of the melt fraction, except for the final 12% of fractionation, when the melt density reaches a minimum of 2300 kg/m^3, in line with calculations of basalt equilibrium crystallization performed by us in rhyoliteMELTS (Ghiorso & Gualda, 2015).

Finally, markers that have experienced significant extraction of melt can have their composition changed to be mafic cumulates. If fertile upper crust has more than 50% melt extracted from it, 20% melt is extracted from the lower crust, or more than 15% melt is extracted from a basalt, the marker is converted to a cumulate with melting properties equivalent to an anhydrous basalt (Hess et al., 1989), and chemical and rheological properties identical to the lowermost crust (green in Fig. 6.2). M_{ex} is reset to 0, M_{frac} to 1, and M_{wt} is adjusted correspondingly to ensure conservation of mass when this happens.

E.4. Marker recombination

The melt extraction process produces many thousands of new markers at each time step. To prevent the obvious resulting numerical issues, we allow closely adjacent markers of the same material type to recombine into new markers with weights that reflect the combined weights of the original markers at the end of each time step. All combined marker characteristics, including position, composition, and temperature, are interpolated linearly, with the exception of marker viscosity and strain, in which the lowest and highest values of the contributing markers are used, respectively. This is because a rock/fluid will only be as strong as its weakest component. Melt content, which is a simple on/off property, is on if any of the contributing markers contain melt. Markers must be within 1 km of each other in the 2×2 km grid, and must have volumes of no greater than 0.25 the maximum size of any marker. These limits on which markers will be combined serve to minimize the resulting numerical diffusion (Colón et al., 2018a).

The combination of adjacent markers, particularly in melts, is what allows intermediate isotopic values to be formed in melts, between the initial end-member compositions described above, and it serves as a useful analog to the localized mixing of melts in small magma bodies, supported by other observations of zircon isotopic heterogeneity (see above).

E.5. Detailed Heat2D methods

To test certain results from the complex I2VIS thermomechanical code, we use the Heat2D code of Annen and Sparks (2002) and Annen et al. (2006, 2009, 2015). We modified this code to include the effects of volcanic eruptions, and to track the sources of

the crustal melts, which contribute to eruptions (melts of upper vs. lower crust). The Heat2D code solves the heat diffusion equation for a cylindrically symmetric space that experiences repeated discrete intrusions of mafic magma. A crucial advantage of Heat2D compared to the much more complex I2VIS code described below is that its simplicity allows us to test the effect of varying a single parameter, such as intrusion depth or eruption repose time, which is more difficult in the less constrained I2VIS models, which always produce complicating structural features in both intrusions and the surrounding crust, and have varying and uncontrolled intrusion depths and geometries. We assume that basaltic intrusions accumulate to a cumulative thickness of 15 km over 2 Myr with a constant rate of intrusion, mimicking the situation in the I2VIS models. Basalts intrude at a fixed depth in axisymmetric disks which are 50 km in diameter (roughly equivalent to major calderas on the Yellowstone hot spot track; Christiansen, 2001; Morgan and McIntosh, 2005), a thickness of 500 m, and which overplate earlier intrusions, pushing them down to greater depth in the crust. Individual intrusions match a 500m finite-difference cell resolution, and while the individual 500m-thick intrusions are obviously unrealistically voluminous (up to 4000 km^3), testing at higher resolutions and smaller intrusion volumes and repose times show that the total volume of crustal melting and eruptions is not strongly affected by having fewer larger intrusions (supporting information). Furthermore, the simplicity of the Heat2D code allows us to not have to consider the mechanical implications, and consider the purely thermal effect of strongly discontinuous rates of intrusion. For the majority of models which we run and compare in Heat2D, we avoid higher spatial resolutions because the implicit nature of the heat equation solver code means that the timestep needed to ensure stability is inversely

proportional to the square of the thickness of the intruding basalt sills (see Gerya, 2010), meaning that doubling of model resolution produces a nearly 20-fold increase in model run time. We assume that all intrusions are basaltic and that they are intruded into a fairly fertile granitic (rhyolitic) upper crust (for temperature-melt fraction curves see Colón et al., 2018a). We also assume an initial geothermal gradient of 20°C/km at all depths.

To investigate the possible role of caldera collapse in producing the isotopic and geochemical trends discussed above, we modified the original Heat2D code to include volcanic eruptions which occur at preset even intervals. For an eruption to occur, we find all areas of country rock heating to above an assumed unlocking composition of 50% melt (Rosenberg & Handy, 2005; Solano et al., 2012), and instantaneously remove them from the model to the top as intracaldera tuff or lava. All remaining material is simultaneously advected downwards to fill the resulting void, creating a "caldera" which can then be perfectly filled with the original removed material, which can now be considered an intracaldera tuff or lave, and which then quickly cools at the surface. We only consider eruptions of crustal melts and do not allow the eruption of basaltic liquids or their fractionates, for two reasons. First, basaltic eruptions are absent within the Yellowstone caldera today (Christiansen, 2001), presumably because of the presence of less dense rhyolitic melts which inhibit their buoyant rise, so neglecting them is not likely to strongly affect the usefulness of our model. Second, while extreme fractionates of intruding basalts are certainly able to rise buoyantly to the surface and erupt, there is no simple way to extract a rhyolite from a mostly-solidified basalt (considering the need for >90% solidification of basalt to reach high-silica rhyolite; e.g. McCurry et al., 2009) in

Heat2D without some sort of melt extraction and concentration scheme, which are much better suited for implementation in the marker-in-cell I2VIS models.

REFERENCES CITED

Allan, A. S. R., Wilson, C. J. N., Millet, M. A., & Wysoczanski, R. J. (2012). The invisible hand: Tectonic triggering and modulation of a rhyolitic supereruption. *Geology*, *40*(6), 563–566. https://doi.org/10.1130/G32969.1

Almeev, R. R., Bolte, T., Nash, B. P., Holtz, F., Erdmann, M., & Cathey, H. E. (2012). High-temperature, low-H 2O silicic magmas of the yellowstone hotspot: An experimental study of rhyolite from the Bruneau-Jarbidge eruptive center, Central Snake River Plain, USA. *Journal of Petrology*, *53*(9), 1837–1866. https://doi.org/10.1093/petrology/egs035

Amrhein, K.E., Brueseke, M.E., Larson, P. B. (2013). Oxygen isotope constraints on mid-Miocene rhyolite production in the Santa Rosa-Calico volcanic field, NV. In *Geological Society of America Annual Meeting*.

Anders, M. H., Rodgers, D. W., Hemming, S. R., Saltzman, J., Divenere, V. J., Hagstrum, J. T., … Walter, R. C. (2014). A fixed sublithospheric source for the late Neogene track of the Yellowstone hotspot: Implications of the Heise and Picabo volcanic fields. *Journal of Geophysical Research: Solid Earth*, *119*(4), 2871–2906. https://doi.org/10.1002/2013JB010483

Annen, C. (2009). From plutons to magma chambers: Thermal constraints on the accumulation of eruptible silicic magma in the upper crust. *Earth and Planetary Science Letters*, *284*(3–4), 409–416. https://doi.org/10.1016/j.epsl.2009.05.006

Annen, C., & Sparks, R. S. J. (2002). Effects of repetitive emplacement of basaltic intrusions on thermal evolution and melt generation in the crust. *Earth and Planetary Science Letters*, *203*(3–4), 937–955. https://doi.org/10.1016/S0012-821X(02)00929-9

Annen, C., Blundy, J. D., & Sparks, R. S. J. (2006). The genesis of intermediate and silicic magmas in deep crustal hot zones. *Journal of Petrology*, *47*(3), 505–539. https://doi.org/10.1093/petrology/egi084

Annen, C., Blundy, J. D., Leuthold, J., & Sparks, R. S. J. (2015, August). Construction and evolution of igneous bodies: Towards an integrated perspective of crustal magmatism. *Lithos*. https://doi.org/10.1016/j.lithos.2015.05.008

Archibald, D. B., Collins, A. S., Foden, J. D., Payne, J. L., Holden, P., Razakamanana, T., … Pitfield, P. E. J. (2016). Genesis of the Tonian Imorona-Itsindro magmatic Suite in central Madagascar: Insights from U-Pb, oxygen and hafnium isotopes in zircon. *Precambrian Research*, *281*, 312–337. https://doi.org/10.1016/j.precamres.2016.05.014

Arndt, N. T., & Goldstein, S. L. (1987). Use and abuse of crust-formation ages. *Geology*, *15*(10), 893–895. https://doi.org/10.1130/0091-7613(1987)15<893:UAAOCA>2.0.CO;2

Belousova, E. A., Griffin, W. L., O'Reilly, S. Y., & Fisher, N. I. (2002). Igneous zircon: Trace element composition as an indicator of source rock type. *Contributions to Mineralogy and Petrology*, *143*(5), 602–622. https://doi.org/10.1007/s00410-002-0364-7

Benson, Thomas R., Mahood, G., & A., Grove, M. (2013). New geologic and geochronologic data on the Lake Owyhee Volcanic Field, Oregon: A silicic center contemporaneous with flood basalt volcanism. In *Geological Society of America Annual Meeting2*.

Berglund, M., & Wieser, M. E. (2011). Isotopic compositions of the elements 2009 (IUPAC Technical Report). *Pure and Applied Chemistry*, *83*(2), 397–410. https://doi.org/10.1351/PAC-REP-10-06-02

Bernt, J., Bonnichsen, B. (1982). Pre-Cougar Point Tuff volcanic rocks near the Idaho-Nevada border, Owyhee County, Idaho. *Idaho Bureau of Mines and Geology Bulletin*, *26*, 321–330.

Bindeman, I. N., & Simakin, A. G. (2014). Rhyolites-Hard to produce, but easy to recycle and sequester: Integrating microgeochemical observations and numerical models. *Geosphere*, *10*(5), 930–957. https://doi.org/10.1130/GES00969.1

Bindeman, I. (2008). Oxygen Isotopes in Mantle and Crustal Magmas as Revealed by Single Crystal Analysis. *Reviews in Mineralogy and Geochemistry*, *69*(1), 445–478. https://doi.org/10.2138/rmg.2008.69.12

Bindeman, I. N. (2003). Crystal sizes in evolving silicic magma chambers. *Geology*, *31*(4), 367–370. https://doi.org/10.1130/0091-7613(2003)031<0367:CSIESM>2.0.CO;2

Bindeman, I. N., & Melnik, O. E. (2016). Zircon survival, rebirth and recycling during crustal melting, magma crystallization, and mixing based on numerical modelling. *Journal of Petrology*, *57*(3), 437–460. https://doi.org/10.1093/petrology/egw013

Bindeman, I. N., & Valley, J. W. (2001). Low-delta O-18 rhyolites from Yellowstone: Magmatic evolution based on analyses of zircons and individual phenocrysts. *Journal of Petrology*, *42*(8), 1491–1517. https://doi.org/10.1093/petrology/42.8.1491

Bindeman, I., Gurenko, A., Carley, T., Miller, C., Martin, E., & Sigmarsson, O. (2012). Silicic magma petrogenesis in Iceland by remelting of hydrothermally altered crust based on oxygen isotope diversity and disequilibria between zircon and magma with

implications for MORB. *Terra Nova*, *24*(3), 227–232. https://doi.org/10.1111/j.1365-3121.2012.01058.x

Black, L. P., Kamo, S. L., Allen, C. M., Davis, D. W., Aleinikoff, J. N., Valley, J. W., … Foudoulis, C. (2004). Improved 206Pb/238U microprobe geochronology by the monitoring of a trace-element-related matrix effect; SHRIMP, ID-TIMS, ELA-ICP-MS and oxygen isotope documentation for a series of zircon standards. *Chemical Geology*, *205*(1–2), 115–140. https://doi.org/10.1016/j.chemgeo.2004.01.003

Blum, T. B., Kitajima, K., Nakashima, D., Strickland, A., Spicuzza, M. J., & Valley, J. W. (2016). Oxygen isotope evolution of the Lake Owyhee volcanic field, Oregon, and implications for the low-$\delta^{18}O$ magmatism of the Snake River Plain?Yellowstone hotspot and other low-$\delta^{18}O$ large igneous provinces. *Contributions to Mineralogy and Petrology*, *171*(11), 92. https://doi.org/10.1007/s00410-016-1297-x

Blum, Tyler, KitaJima, K., Nakashima, D., Valley, J. W. (2013). Oxygen isotope evolution of the Lake Owyhee volcanic field, Oregon, and implications for low-$\delta^{18}O$ magmas of the Snake River Plain-Yellowstone hotspot. In *American Geophysical Union Fall Meeting2*.

Boehnke, P., Watson, E. B., Trail, D., Harrison, T. M., & Schmitt, A. K. (2013). Zircon saturation re-revisited. *Chemical Geology*, *351*, 324–334. https://doi.org/10.1016/j.chemgeo.2013.05.028

Bohrson, W. A. (2001). Energy-Constrained Open-System Magmatic Processes II: Application of Energy-Constrained Assimilation-Fractional Crystallization (EC-AFC) Model to Magmatic Systems. *Journal of Petrology*, *42*(5), 1019–1041. https://doi.org/10.1093/petrology/42.5.1019

Bolte, T., Holtz, F., Almeev, R., & Nash, B. (2015). The Blacktail Creek Tuff: an analytical and experimental study of rhyolites from the Heise volcanic field, Yellowstone hotspot system. *Contributions to Mineralogy and Petrology*, *169*(2), 15. https://doi.org/10.1007/s00410-015-1112-0

Bonnichsen, B., Leeman, W. P., Honjo, N., McIntosh, W. C., & Godchaux, M. M. (2008). Miocene silicic volcanism in southwestern Idaho: Geochronology, geochemistry, and evolution of the central Snake River Plain. *Bulletin of Volcanology*, *70*(3), 315–342. https://doi.org/10.1007/s00445-007-0141-6

Bonnichsen, Citron, B. (1982). The Cougar Point Tuff, Southwestern Idaho and Vicinity. *Idaho Bureau of Mines and Geology*. Retrieved from http://geology.isu.edu/Digital_Geology_Idaho/papers/B-26Ch5-3.pdf

Boroughs, S., Wolff, J. A., Ellis, B. S., Bonnichsen, B., & Larson, P. B. (2012). Evaluation of models for the origin of Miocene low-$\delta^{18}O$ rhyolites of the

Yellowstone/Columbia River Large Igneous Province. *Earth and Planetary Science Letters*, *313–314*(1), 45–55. https://doi.org/10.1016/j.epsl.2011.10.039

Boroughs, S., Wolff, J., Bonnichsen, B., Godchaux, M., & Larson, P. (2005). Large-volume, low-$\delta^{18}O$ rhyolites of the central Snake River Plain, Idaho, USA. *Geology*, *33*(10), 821–824. https://doi.org/10.1130/G21723.1

Bouvier, A., Vervoort, J. D., & Patchett, P. J. (2008). The Lu-Hf and Sm-Nd isotopic composition of CHUR: Constraints from unequilibrated chondrites and implications for the bulk composition of terrestrial planets. *Earth and Planetary Science Letters*, *273*(1–2), 48–57. https://doi.org/10.1016/j.epsl.2008.06.010

Branney, M. J., Bonnichsen, B., Andrews, G. D. M., Ellis, B., Barry, T. L., & McCurry, M. (2008). "Snake River (SR)-type" volcanism at the Yellowstone hotspot track: Distinctive products from unusual, high-temperature silicic super-eruptions. *Bulletin of Volcanology*, *70*(3), 293–314. https://doi.org/10.1007/s00445-007-0140-7

Brueseke, M. E., Callicoat, J. S., Hames, W., & Larson, P. B. (2014). Mid-Miocene rhyolite volcanism in northeastern Nevada: The Jarbidge rhyolite and its relationship to the Cenozoic evolution of the northern Great Basin (USA). *Bulletin of the Geological Society of America*, *126*(7–8), 1047–1067. https://doi.org/10.1130/B30736.1

Bryan, S. E., & Ferrari, L. (2013, July 1). Large igneous provinces and silicic large igneous provinces: Progress in our understanding over the last 25 years. *Bulletin of the Geological Society of America*. GeoScienceWorld. https://doi.org/10.1130/B30820.1

Buiter, S. J. H., Babeyko, A. Y., Ellis, S., Gerya, T. V., Kaus, B. J. P., Kellner, A., … Yamada, Y. (2006). The numerical sandbox: comparison of model results for a shortening and an extension experiment. *Geological Society, London, Special Publications*, *253*(1), 29–64. https://doi.org/10.1144/GSL.SP.2006.253.01.02

Burov, E., Guillou-Frottier, L., D'Acremont, E., Le Pourhiet, L., & Cloetingh, S. (2007). Plume head-lithosphere interactions near intra-continental plate boundaries. *Tectonophysics*, *434*(1–4), 15–38. https://doi.org/10.1016/j.tecto.2007.01.002

Burov, E., & Guillou-Frottier, L. (2005). The plume head-continental lithosphere interaction using a tectonically realistic formulation for the lithosphere. *Geophysical Journal International*, *161*(2), 469–490. https://doi.org/10.1111/j.1365-246X.2005.02588.x

Burov, E., & Gerya, T. V. (2014). Asymmetric three-dimensional topography over mantle plumes. *Nature*, *513*(7516), 85–9. https://doi.org/10.1038/nature13703

Callicoat, J. S. (2010). *Significance of mid-Miocene volcanism in northeast Nevada: Petrographic, Chemical, Isotopic, and Temporal Importance of the Jarbidge Rhyolite*. Kansas State University.

Camp, V., Ross, M., Duncan, R. a., Jarboe, N. a., Coe, R. ., Hanan, B. B., & Johnson, J. a. (2013). The Steens basalt: Earliest lavas of the Columbia River basalt group. *The Columbia River Flood Basalt Province: Geological Society of America Special Paper 497*, *2497*(4), 87–116. https://doi.org/10.1130/2013.2497(04).

Camp, V. E., & Hanan, B. B. (2008). A plume-triggered delamination origin for the Columbia River Basalt Group. *Geosphere*, *4*(3), 480. https://doi.org/10.1130/GES00175.1

Camp, V. E., Pierce, K. L., & Morgan, L. A. (2015). Yellowstone plume trigger for Basin and Range extension, and coeval emplacement of the Nevada-Columbia Basin magmatic belt. *Geosphere*, *11*(2), 203–225. https://doi.org/10.1130/GES01051.1

Camp, V. E., & Ross, M. E. (2004). Mantle dynamics and genesis of mafic magmatism in the intermontane Pacific Northwest. *Journal of Geophysical Research B: Solid Earth*, *109*(8). https://doi.org/10.1029/2003JB002838

Camp, V. E., Ross, M. E., & Hanson, W. E. (2003). Genesis of flood basalts and Basin and Range volcanic rocks from Steens Mountain to the Malheur River Gorge, Oregon. *Bulletin of the Geological Society of America*, *115*(1), 105–128. https://doi.org/10.1130/0016-7606(2003)115<0105:GOFBAB>2.0.CO;2

Cao, W., Kaus, B. J. P., & Paterson, S. (2016). Intrusion of granitic magma into the continental crust facilitated by magma pulsing and dike-diapir interactions: Numerical simulations. *Tectonics*, *35*(6), 1575–1594. https://doi.org/10.1002/2015TC004076

Carlson, R. W., Lugmair, G. W., & Macdougall, J. D. (1981). Columbia River volcanism: the question of mantle heterogeneity or crustal contamination. *Geochimica et Cosmochimica Acta*, *45*(12), 2483–2499. https://doi.org/10.1016/0016-7037(81)90100-9

Carlson, R. W. (1984). Isotopic constraints on Columbia River flood basalt genesis and the nature of the subcontinental mantle. *Geochimica et Cosmochimica Acta*, *48*(11), 2357–2372. https://doi.org/10.1016/0016-7037(84)90231-X

Cathey, H. E., & Nash, B. P. (2004). The Cougar Point Tuff: Implications for Thermochemical Zonation and Longevity of High-Temperature, Large-Volume Silicic Magmas of the Miocene Yellowstone Hotspot. *Journal of Petrology*, *45*(1), 27–58. https://doi.org/10.1093/petrology/egg081

Cathey, H., Nash, B., Seligman, A., Valley, J. W., Kita, N., Allen, C., … Wooden, J. (2011). Low $\delta^{18}O$ zircons from the Bruneau-Jarbidge eruptive center: a key to crustal anatexis along the track of the Yellowstone hotspot. *American Geophysical Union Fall Meeting Abstracts*. Retrieved from http://adsabs.harvard.edu/abs/2011AGUFM.V11A2510C

Cathey, H. E., & Nash, B. P. (2009). Pyroxene thermometry of rhyolite lavas of the Bruneau-Jarbidge eruptive center, Central Snake River Plain. *Journal of Volcanology and Geothermal Research*, *188*(1–3), 173–185. https://doi.org/10.1016/j.jvolgeores.2009.05.024

Chadwick, R. A. (1985). Overview of Cenozoic Volcanism in the West-Central United States, 359–381. Retrieved from http://archives.datapages.com/data/rocky_sepm/data/023/023001/359_rocky_mount230359.htm

Chauvel, C., Lewin, E., Carpentier, M., Arndt, N. T., & Marini, J. C. (2008). Role of recycled oceanic basalt and sediment in generating the Hf-Nd mantle array. *Nature Geoscience*, *1*(1), 64–67. https://doi.org/10.1038/ngeo.2007.51

Chen, C. W., James, D. E., Fouch, M. J., & Wagner, L. S. (2013). Lithospheric structure beneath the High Lava Plains, Oregon, imaged by scattered teleseismic waves. *Geochemistry, Geophysics, Geosystems*, *14*(11), 4835–4848. https://doi.org/10.1002/ggge.20284

Chiang, C. S., & Braile, L. W. (1984). An example of two-dimensional synthetic seismogram modeling. *Bulletin of the Seismological Society of America*, *74*(2), 509–519. Retrieved from http://www.bssaonline.org/content/74/2/509.short

Chiba, H., Chacko, T., Clayton, R. N., & Goldsmith, J. R. (1989). Oxygen isotope fractionations involving diopside, forsterite, magnetite, and calcite: Application to geothermometry. *Geochimica et Cosmochimica Acta*, *53*(11), 2985–2995. https://doi.org/10.1016/0016-7037(89)90174-9

Christiansen, E. H., Haapala, I., & Hart, G. L. (2007). Are Cenozoic topaz rhyolites the erupted equivalents of Proterozoic rapakivi granites? Examples from the western United States and Finland. *Lithos*, *97*(1–2), 219–246. https://doi.org/10.1016/j.lithos.2007.01.010

Christiansen, E. H., & McCurry, M. (2008). Contrasting origins of Cenozoic silicic volcanic rocks from the western Cordillera of the United States. *Bulletin of Volcanology*, *70*(3), 251–267. https://doi.org/10.1007/s00445-007-0138-1

Christiansen, R. L. (2001). The Quaternary and Pliocene Yellowstone Plateau volcanic field of Wyoming, Idaho, and Montana. *U. S. Geological Survey Professional Paper*, *729–G*, 145. Retrieved from https://pubs.er.usgs.gov/publication/pp729G

Christiansen, R. L., Foulger, G. R., & Evans, J. R. (2002). Upper-mantle origin of the Yellowstone hotspot. *Bulletin of the Geological Society of America*, *114*(10), 1245–1256. https://doi.org/10.1130/0016-7606(2002)114<1245:UMOOTY>2.0.CO;2

Christopher, J. (2010). Volatiles , major oxide , trace element and isotope geochemistry in the Snake River Plain and Colum ... Retrieved from https://deepblue.lib.umich.edu/handle/2027.42/77741

Clauser, C., & Huenges, E. (1992). Thermal Conductivity of Rocks and Minerals. *Rock Physics and Phase Relatioins: A Handbook of Physical Constants*, (1), 105–126. Retrieved from http://gfzpublic.gfz-potsdam.de/pubman/faces/viewItemOverviewPage.jsp?itemId=escidoc:228983

Coats, R. R. (1987). Geology of Elko County. *Nevada Bureau of Mines and Geology Bulletin*, 101.

Coble, M. A., & Mahood, G. A. (2012). Initial impingement of the Yellowstone plume located by widespread silicic volcanism contemporaneous with Columbia River flood basalts. *Geology*, *40*(7), 655–658. https://doi.org/10.1130/G32692.1

Coleman, D. S., Mills, R. D., & Zimmerer, M. J. (2016). The pace of plutonism. *Elements*, *12*(2), 97–102. https://doi.org/10.2113/gselements.12.2.97

Colgan, J. P. (2013). Reappraisal of the relationship between the northern Nevada rift and Miocene extension in the northern Basin and Range Province. *Geology*, *41*(2), 211–214. https://doi.org/10.1130/G33512.1

Colgan, J. P., & Henry, C. D. (2009). Rapid middle Miocene collapse of the Mesozoic orogenic plateau in north-central Nevada. *International Geology Review*, *51*(9–11), 920–961. https://doi.org/10.1080/00206810903056731

Collerson, K. D., & Kamber, B. S. (1999). Evolution of the continents and the atmosphere inferred from Th-U-Nb systematics of the depleted mantle. *Science*, *283*(5407), 1519–1522. https://doi.org/10.1126/science.283.5407.1519

Collins, W. J., Beams, S. D., White, A. J. R., & Chappell, B. W. (1982). Nature and origin of A-type granites with particular reference to southeastern Australia. *Contributions to Mineralogy and Petrology*, *80*(2), 189–200. https://doi.org/10.1007/BF00374895

Colón, D. P., Bindeman, I. N., Ellis, B. S., Schmitt, A. K., & Fisher, C. M. (2015). Hydrothermal alteration and melting of the crust during the Columbia River Basalt-Snake River Plain transition and the origin of low-$\delta^{18}O$ rhyolites of the central Snake River Plain. *Lithos*, *224–225*, 310–323. https://doi.org/10.1016/j.lithos.2015.02.022

Colón, D. P., Bindeman, I. N., & Gerya, T. V. (2018). Thermomechanical modeling of the formation of a multilevel, crustal-scale magmatic system by the Yellowstone plume. *Geophysical Research Letters*, *45*(9), 3873–3879. https://doi.org/10.1029/2018GL077090

Colón, D. P., Bindeman, I. N., Stern, R. A., & Fisher, C. M. (2015). Isotopically diverse rhyolites coeval with the Columbia River Flood Basalts: Evidence for mantle plume interaction with the continental crust. *Terra Nova*, *27*(4), 270–276. https://doi.org/10.1111/ter.12156

Colón, D. P., Bindeman, I. N., Wotzlaw, J.-F., Christiansen, E. H., & Stern, R. A. (2018). Origins and evolution of rhyolitic magmas in the central Snake River Plain: insights from coupled high-precision geochronology, oxygen isotope, and hafnium isotope analyses of zircon. *Contributions to Mineralogy and Petrology*, *173*(2), 11. https://doi.org/10.1007/s00410-017-1437-y

Condon, D. J., Schoene, B., McLean, N. M., Bowring, S. A., & Parrish, R. R. (2015). Metrology and traceability of U-Pb isotope dilution geochronology (EARTHTIME Tracer Calibration Part I). *Geochimica et Cosmochimica Acta*, *164*, 464–480. https://doi.org/10.1016/j.gca.2015.05.026

Corfu, F., Hanchar, J. M., Hoskin, P. W. O., & Kinny, P. (2003). Atlas of Zircon Textures. *Reviews in Mineralogy and Geochemistry*, *53*(1), 469–500. https://doi.org/10.2113/0530469

Couper, S. (n.d.). *Dual multicollector laser ablation split stream mass spectrometry: Application to the Bruneau-Jarbidge volcanic center, central Snake River Plain, Idaho*. University of Utah.

Crameri, F., Schmeling, H., Golabek, G. J., Duretz, T., Orendt, R., Buiter, S. J. H., … Tackley, P. J. (2012). A comparison of numerical surface topography calculations in geodynamic modelling: An evaluation of the “sticky air” method. *Geophysical Journal International*, *189*(1), 38–54. https://doi.org/10.1111/j.1365-246X.2012.05388.x

Cummings, M. L., Evans, J. G., Ferms, M. L., & Lees, K. R. (2000). Stratigraphic and structural evolution of the middle miocene synvolcanic Oregon-Idaho graben. *Bulletin of the Geological Society of America*, *112*(5), 668–682. https://doi.org/10.1130/0016-7606(2000)112<668:SASEOT>2.0.CO;2

Curtis, C. G., Harris, C., Trumbull, R. B., De Beer, C., & Mudzanani, L. (2013). Oxygen isotope diversity in the anorogenic Koegel Fontein complex of South Africa: A case for basement control and selective melting for the production of low-$\delta^{18}O$ magmas. *Journal of Petrology*, *54*(7), 1259–1283. https://doi.org/10.1093/petrology/egt011

Dannberg, J., & Sobolev, S. V. (2015). Low-buoyancy thermochemical plumes resolve controversy of classical mantle plume concept. *Nature Communications*, *6*, 6960. https://doi.org/10.1038/ncomms7960

Darold, A., & Humphreys, E. (2013). Upper mantle seismic structure beneath the Pacific Northwest: A plume-triggered delamination origin for the Columbia River flood basalt eruptions. *Earth and Planetary Science Letters*, *365*, 232–242. https://doi.org/10.1016/j.epsl.2013.01.024

Depaolo, D. J. (1981). Neodymium isotopes in the Colorado Front Range and crust-mantle evolution in the Proterozoic. *Nature*, *291*(5812), 193–196. https://doi.org/10.1038/291193a0

Doe, B. R., Leeman, W. P., Christiansen, R. L., & Hedge, C. E. (1982). Lead and strontium isotopes and related trace elements as genetic tracers in the Upper Cenozoic rhyolite-basalt association of the Yellowstone Plateau Volcanic Field. *Journal of Geophysical Research*, *87*(B6), 4785–4806. https://doi.org/10.1029/JB087iB06p04785

Dorsey, R. J., & LaMaskin, T. A. (2008). Mesozoic collision and accretion of oceanic terranesin the Blue Mountains province of northeastern Oregon: New insights from the stratigraphic record. *Arizona Geological Society Digest*, *22*, 325–332.

Drew, D. L., Bindeman, I. N., Loewen, M. W., & Wallace, P. J. (2016). Initiation of large-volume silicic centers in the Yellowstone hotspot track: insights from H2O- and F-rich quartz-hosted rhyolitic melt inclusions in the Arbon Valley Tuff of the Snake River Plain. *Contributions to Mineralogy and Petrology*, *171*(1), 1–20. https://doi.org/10.1007/s00410-015-1210-z

Drew, D. L., Bindeman, I. N., Watts, K. E., Schmitt, A. K., Fu, B., & McCurry, M. (2013). Crustal-scale recycling in caldera complexes and rift zones along the Yellowstone hotspot track: O and Hf isotopic evidence in diverse zircons from voluminous rhyolites of the Picabo volcanic field, Idaho. *Earth and Planetary Science Letters*, *381*, 63–77. https://doi.org/10.1016/j.epsl.2013.08.007

Dufek, J., & Bergantz, G. W. (2005). Lower crustal magma genesis and preservation: A stochastic framework for the evaluation of basalt-crust interaction. *Journal of Petrology*, *46*(11), 2167–2195. https://doi.org/10.1093/petrology/egi049

Duncan, R. A. (1982). A captured island chain in the Coast Range of Oregon and Washington. *Journal of Geophysical Research*, *87*(B13), 10827–10837. https://doi.org/10.1029/JB087iB13p10827

Einstein, A. (1916). The foundation of the general theory of relativity. *Annalen Phys*, *49*, 769–822. https://doi.org/10.1097/ACM.0b013e31816bf1fd

Ellis, B. S., Wolff, J. A., Boroughs, S., Mark, D. F., Starkel, W. A., & Bonnichsen, B. (2013). Rhyolitic volcanism of the central Snake River Plain: A review. *Bulletin of Volcanology*, *75*(8), 1–19. https://doi.org/10.1007/s00445-013-0745-y

Ellis, B. S., Branney, M. J., Barry, T. L., Barfod, D., Bindeman, I., Wolff, J. A., & Bonnichsen, B. (2012). Geochemical correlation of three large-volume ignimbrites from the Yellowstone hotspot track, Idaho, USA. *Bulletin of Volcanology*, *74*(1), 261–277. https://doi.org/10.1007/s00445-011-0510-z

Ellis, B. S., & Wolff, J. A. (2012). Complex storage of rhyolite in the central Snake River Plain. *Journal of Volcanology and Geothermal Research*, *211–212*, 1–11. https://doi.org/10.1016/j.jvolgeores.2011.10.002

Elsworth, D., Mattioli, G. S., Taron, J., Voight, B., & Herd, R. A. (2008). Implications of magma transfer between multiple reservoirs on eruption cycling. *Science*, *322*(5899), 246–248. https://doi.org/10.1126/science.1161297

Evans, J. G. (1992). Geologic Map of the Dooley 7 1./2' Quadrangle, Baker County, Oregon. U.S. Geological Survey.

Farrell, J., Smith, R. B., Husen, S., & Diehl, T. (2014). Tomography from 26years of seismicity revealing that the spatial extent of the Yellowstone crustal magma reservoir extends well beyond the Yellowstone caldera. *Geophysical Research Letters*, *41*(9), 3068–3073. https://doi.org/10.1002/2014GL059588

Ferns, M. L., & McClaughry, J. D. (2013). Stratigraphy and volcanic evolution of the middle Miocene to Pliocene La Grande-Owyhee eruptive axis in eastern Oregon. *Geological Society of America Special Paper*, *497*(16), 401–427. https://doi.org/10.1130/2013.2497(16).

Ferry, J. M., & Watson, E. B. (2007). New thermodynamic models and revised calibrations for the Ti-in-zircon and Zr-in-rutile thermometers. *Contributions to Mineralogy and Petrology*, *154*(4), 429–437. https://doi.org/10.1007/s00410-007-0201-0

Fiebelkorn, R.B., Walker, G.W., MacLeod, N.S., McKee, E.H., Smith, J. G. (1982). Index to K-Ar age determinations for the State of Oregon. U.S. Geological Survey Open-File Report.

Fisher, C. M., Hanchar, J. M., Samson, S. D., Dhuime, B., Blichert-Toft, J., Vervoort, J. D., & Lam, R. (2011). Synthetic zircon doped with hafnium and rare earth elements: A reference material for in situ hafnium isotope analysis. *Chemical Geology*, *286*(1–2), 32–47. https://doi.org/10.1016/j.chemgeo.2011.04.013

Fisher, C. M., Vervoort, J. D., & Dufrane, S. A. (2014). Accurate Hf isotope determinations of complex zircons using the "laser ablation split stream" method.

Geochemistry, Geophysics, Geosystems, *15*(1), 121–139. https://doi.org/10.1002/2013GC004962

Fisher, C. M., Vervoort, J. D., & Hanchar, J. M. (2014). Guidelines for reporting zircon Hf isotopic data by LA-MC-ICPMS and potential pitfalls in the interpretation of these data. *Chemical Geology*, *363*, 125–133. https://doi.org/10.1016/j.chemgeo.2013.10.019

Foster, D. A., Mueller, P. A., Mogk, D. W., Wooden, J. L., & Vogl, J. J. (2006). Proterozoic evolution of the western margin of the Wyoming craton: implications for the tectonic and magmatic evolution of the northern Rocky Mountains. *Canadian Journal of Earth Sciences*, *43*(10), 1601–1619. https://doi.org/10.1139/e06-052

Fournier, R. O. (1989). Geochemistry and Dynamics of the Yellowstone National Park Hydrotherm System. *Annual Review of Earth Planetary Sciences*, *17*(1), 13–53. https://doi.org/10.1146/annurev.ea.17.050189.000305

Fu, B., Kita, N. T., Wilde, S. A., Liu, X., Cliff, J., & Greig, A. (2013). Origin of the Tongbai-Dabie-Sulu Neoproterozoic low-$\delta^{18}O$ igneous province, east-central China. *Contributions to Mineralogy and Petrology*, *165*(4), 641–662. https://doi.org/10.1007/s00410-012-0828-3

Gans, P. B. (1987). An open□system, two□layer crustal stretching model for the Eastern Great Basin. *Tectonics*, *6*(1), 1–12. https://doi.org/10.1029/TC006i001p00001

Gaschnig, R. M., Vervoort, J. D., Lewis, R. S., & McClelland, W. C. (2010). Migrating magmatism in the northern US Cordillera: In situ U-Pb geochronology of the Idaho batholith. *Contributions to Mineralogy and Petrology*, *159*(6), 863–883. https://doi.org/10.1007/s00410-009-0459-5

Gautason, B., & Muehlenbachs, K. (1998). Oxygen isotopic fluxes associated with high-temperature processes in the rift zones of Iceland. *Chemical Geology*, *145*(3–4), 275–286. https://doi.org/10.1016/S0009-2541(97)00148-4

Gerstenberger, H., & Haase, G. (1997). A highly effective emitter substance for mass spectrometric Pb isotope ratio determinations. *Chemical Geology*, *136*(3–4), 309–312. https://doi.org/http://dx.doi.org/10.1016/S0009-2541(96)00033-2

Gerya, T. V, Stern, R. J., Baes, M., Sobolev, S. V, & Whattam, S. A. (2015). Plate tectonics on the Earth triggered by plume-induced subduction initiation. *Nature*, *527*(7577), 221–225. https://doi.org/10.1038/nature15752

Gerya, T. V., & Burg, J. P. (2007). Intrusion of ultramafic magmatic bodies into the continental crust: Numerical simulation. *Physics of the Earth and Planetary Interiors*, *160*(2), 124–142. https://doi.org/10.1016/j.pepi.2006.10.004

Gerya, T. V., & Yuen, D. A. (2003). Characteristics-based marker-in-cell method with conservative finite-differences schemes for modeling geological flows with strongly variable transport properties. *Physics of the Earth and Planetary Interiors*, *140*(4), 293–318. https://doi.org/10.1016/j.pepi.2003.09.006

Gerya, T. (2010). *Introduction to Numerical Geodynamic Modelling*. Cambridge University Press. https://doi.org/10.1017/CBO9780511809101

Ghiorso, M. S., & Gualda, G. A. R. (2015). An H<inf>2</inf>O–CO<inf>2</inf> mixed fluid saturation model compatible with rhyolite-MELTS. *Contributions to Mineralogy and Petrology*, *169*(6), 53. https://doi.org/10.1007/s00410-015-1141-8

Glazner, A. F., & Ussler, W. (1988). Trapping of magma at midcrustal density discontinuities. *Geophysical Research Letters*, *15*(7), 673–675. https://doi.org/10.1029/GL015i007p00673

Glen, J. M. G., & Ponce, D. A. (2002). Large-scale fractures related to inception of the Yellowstone hotspot. *Geology*, *30*(7), 647–650. https://doi.org/10.1130/0091-7613(2002)030<0647:LSFRTI>2.0.CO;2

Graham, D. W., Reid, M. R., Jordan, B. T., Grunder, A. L., Leeman, W. P., & Lupton, J. E. (2009). Mantle source provinces beneath the Northwestern USA delimited by helium isotopes in young basalts. *Journal of Volcanology and Geothermal Research*, *188*(1–3), 128–140. https://doi.org/10.1016/j.jvolgeores.2008.12.004

Gregg, P. M., Grosfils, E. B., & de Silva, S. L. (2015). Catastrophic caldera-forming eruptions II: The subordinate role of magma buoyancy as an eruption trigger. *Journal of Volcanology and Geothermal Research*, *305*, 100–113. https://doi.org/10.1016/j.jvolgeores.2015.09.022

Gudmundsson, A. (2011). Deflection of dykes into sills at discontinuities and magma-chamber formation. *Tectonophysics*, *500*(1–4), 50–64. https://doi.org/10.1016/j.tecto.2009.10.015

Guillong, M., Meier, D. L., Allan, M. M., Heinrich, C. A., & Yardley, B. W. D. (2008). SILLS: A Matlab-Based Program for the Reduction of Laser Ablation ICP–MS Data of Homogeneous Materials and Inclusions. *Mineralogical Association of Canada Short Course*, *40*, 328–333. Retrieved from https://s3.amazonaws.com/academia.edu.documents/41210236/SILLS_A_MATLAB-based_program_for_the_red20160114-7295-wmu6z.pdf20160115-19908-9gehr5.pdf?AWSAccessKeyId=AKIAIWOWYYGZ2Y53UL3A&Expires=1528611859&Signature=gKOHynYlZaUzBlCWE3Ka%2Bre6e7A%3D&response-co

Halsor, S. P., Bornhorst, T. J., Beebe, M., Richardson, K., & Strowd, W. (1988). Geology of the DeLamar silver mine, Idaho - a volcanic dome complex and genetically

associated hydrothermal system. *Economic Geology*, *83*(6), 1159–1169. https://doi.org/10.2113/gsecongeo.83.6.1159

Harris, C., & Ashwal, L. D. (2002). The origin of low $\delta^{18}O$ granites and related rocks from the Seychelles. *Contributions to Mineralogy and Petrology*, *143*(3), 366–376. https://doi.org/10.1007/s00410-002-0349-6

Harris, C., & Erlank, A. J. (1992). The production of large-volume, low-$\delta^{18}O$ rhyolites during the rifting of Africa and Antarctica: The Lebombo Monocline, southern Africa. *Geochimica et Cosmochimica Acta*, *56*(9), 3561–3570. https://doi.org/10.1016/0016-7037(92)90399-4

Hart, William K., Carlson, R. W. (1985). Distribution and geochronology of Steens Mountain-type basalts from the northwestern Great Basin. *Isochron/West*, *43*, 5–10.

Hess, P. C. (1995). *Origins of Igneous Rocks*. Harvard University Press.

Hiess, J., Bennett, V. C., Nutman, A. P., & Williams, I. S. (2011). Archaean fluid-assisted crustal cannibalism recorded by low $\delta^{18}O$ and negative εHf(T)isotopic signatures of West Greenland granite zircon. *Contributions to Mineralogy and Petrology*, *161*(6), 1027–1050. https://doi.org/10.1007/s00410-010-0578-z

Hildreth, W., Christiansen, R. L., & O'Neil, J. R. (1984). Catastrophic isotopic modification of rhyolitic magma at times of caldera subsidence, Yellowstone Plateau Volcanic Field. *Journal of Geophysical Research*, *89*(B10), 8339–8369. https://doi.org/10.1029/JB089iB10p08339

Hildreth, W., Halliday, A. N., & Christiansen, R. L. (1991). Isotopic and chemical evidence concerning the genesis and contamination of basaltic and rhyolitic magma beneath the yellowstone plateau volcanic field. *Journal of Petrology*, *32*(1), 63–138. https://doi.org/10.1093/petrology/32.1.63

Hirt, W. H. (2004). Transition from ash-flow to voluminous lava-flow activity, Bruneau-Jarbidge eruptive center, southwestern Idaho. *Bulletin - Idaho Geological Survey*, 195. Retrieved from http://www.idahogeology.org/Products/bulletin30_TOC.htm

Hofmeister, A. M. (1999). Mantle Values of Thermal Conductivity and the Geotherm from Phonon Lifetimes. *Science*, *283*(5408), 1699–1706. https://doi.org/10.1126/science.283.5408.1699

Honjo, N., Bonnichsen, B., Leeman, W. P., & Stormer, J. C. (1992). Mineralogy and geothermometry of high-temperature rhyolites from the central and western Snake River Plain. *Bulletin of Volcanology*, *54*(3), 220–237. https://doi.org/10.1007/BF00278390

Hooper, P. R., & Hawkesworth, C. J. (1993). Isotopic and geochemical constraints on the origin and evolution of the Columbia river basalt. *Journal of Petrology*, *34*(6), 1203–1246. https://doi.org/10.1093/petrology/34.6.1203

Hopper, E., Ford, H. A., Fischer, K. M., Lekic, V., & Fouch, M. J. (2014). The lithosphere-asthenosphere boundary and the tectonic and magmatic history of the northwestern United States. *Earth and Planetary Science Letters*, *402*(C), 69–81. https://doi.org/10.1016/j.epsl.2013.12.016

Huang, H.-H., Lin, F.-C., Schmandt, B., Farrell, J., Smith, R. B., & Tsai, V. C. (2015). The Yellowstone magmatic system from the mantle plume to the upper crust. *Science*, *348*(6236), 773–776. https://doi.org/10.1126/science.aaa5648

Huppert, H. E., & Sparks, R. S. J. (1988). The generation of granitic magmas by intrusion of basalt into continental crust. *Journal of Petrology*, *29*(3), 599–624. https://doi.org/10.1093/petrology/29.3.599

Hurwitz, S., Hunt, A. G., & Evans, W. C. (2012). Temporal variations of geyser water chemistry in the Upper Geyser Basin, Yellowstone National Park, USA. *Geochemistry, Geophysics, Geosystems*, *13*(12). https://doi.org/10.1029/2012GC004388

Jaffey, A. H., Flynn, K. F., Glendenin, L. E., Bentley, W. C., & Essling, A. M. (1971). Precision measurement of half-lives and specific activities of U235 and U238. *Physical Review C*, *4*(5), 1889–1906. https://doi.org/10.1103/PhysRevC.4.1889

Jellinek, A. M., & DePaolo, D. J. (2003). A model for the origin of large silicic magma chambers: Precursors of caldera-forming eruptions. *Bulletin of Volcanology*, *65*(5), 363–381. https://doi.org/10.1007/s00445-003-0277-y

Jenkins, Emily N., Streck, M. J., & Ramos, R.C., Bindeman, I. N. (2013). Radiogenic and stable isotope of mid-Miocene silicic volcanism in eastern Oregon: Evidence for variable and high Sr/low-$\delta^{18}O$ domains west of the terrane-cratonic lithosphere transition. In *Geological Society of America Fall Meeting*.

Johannes, W. (1985). The significance of experimental studies for the formation of migmatites. In *Migmatites* (pp. 36–85). Boston, MA: Springer US. https://doi.org/10.1007/978-1-4613-2347-1_2

John, D.A., Ponce, A.R., Fleck, R.B., C. J. E. (2000). New Perspectives on the geology and origin of the northern Nevada Rift. In *Geology and Ore Deposits 2000: Geological Society of Nevada Symposium Proceedings* (pp. 127–154).

John, D. A., Henry, C. D., & Colgan, J. P. (2008). Magmatic and tectonic evolution of the Caetano caldera, north-central Nevada: A tilted, mid-Tertiary eruptive center and

source of the Caetano Tuff. *Geosphere*, *4*(1), 75–106. https://doi.org/10.1130/GES00116.1

Jordan, B. T., Grunder, A. L., Duncan, R. A., & Deino, A. L. (2004). Geochronology of age-progressive volcanism of the Oregon High Lava Plains: Implications for the plume interpretation of Yellowstone. *Journal of Geophysical Research: Solid Earth*, *109*(10). https://doi.org/10.1029/2003JB002776

Karakas, O., Degruyter, W., Bachmann, O., & Dufek, J. (2017). Lifetime and size of shallow magma bodies controlled by crustal-scale magmatism. *Nature Geoscience*, *10*, 446–450. https://doi.org/10.1038/NGEO2959

Karlstrom, L., Dufek, J., & Manga, M. (2009). Organization of volcanic plumbing through magmatic lensing by magma chambers and volcanic loads. *Journal of Geophysical Research: Solid Earth*, *114*(10), B10204. https://doi.org/10.1029/2009JB006339

Katayama, I., & Karato, S. ichiro. (2008). Low-temperature, high-stress deformation of olivine under water-saturated conditions. *Physics of the Earth and Planetary Interiors*, *168*(3–4), 125–133. https://doi.org/10.1016/j.pepi.2008.05.019

Katz, R. F., Spiegelman, M., & Langmuir, C. H. (2003). A new parameterization of hydrous mantle melting. *Geochemistry, Geophysics, Geosystems*, *4*(9), n/a-n/a. https://doi.org/10.1029/2002GC000433

Kavanagh, J. L., Menand, T., & Sparks, R. S. J. (2006). An experimental investigation of sill formation and propagation in layered elastic media. *Earth and Planetary Science Letters*, *245*(3–4), 799–813. https://doi.org/10.1016/j.epsl.2006.03.025

Keller, T., May, D. A., & Kaus, B. J. P. (2013). Numerical modelling of magma dynamics coupled to tectonic deformation of lithosphere and crust. *Geophysical Journal International*, *195*(3), 1406–1442. https://doi.org/10.1093/gji/ggt306

Knott, T. R., Branney, M. J., Reichow, M. K., Finn, D. R., Coe, R. S., Storey, M., … McCurry, M. (2016). Mid-Miocene record of large-scale Snake River-type explosive volcanism and associated subsidence on the Yellowstone hotspot track: The Cassia Formation of Idaho, USA. *Bulletin of the Geological Society of America*, *128*(7), 1121–1146. https://doi.org/10.1130/B31324.1

Konstantinou, A., Valley, J., Strickland, A., Miller, E. L., Fisher, C., Vervoort, J., & Wooden, J. (2013). Geochemistry and geochronology of the Jim Sage volcanic suite, southern Idaho: Implications for Snake River Plain magmatism and its role in the history of Basin and Range extension. *Geosphere*, *9*(6), 1681–1703. https://doi.org/10.1130/GES00948.1

Krogh, T. E. (1973). A low-contamination method for hydrothermal decomposition of zircon and extraction of U and Pb for isotopic age determinations. *Geochimica et Cosmochimica Acta*, *37*(3), 485–494. https://doi.org/10.1016/0016-7037(73)90213-5

Kylander-Clark, A. R. C., Hacker, B. R., & Cottle, J. M. (2013). Laser-ablation split-stream ICP petrochronology. *Chemical Geology*, *345*, 99–112. https://doi.org/10.1016/j.chemgeo.2013.02.019

Lee, C. T. A., Luffi, P., Plank, T., Dalton, H., & Leeman, W. P. (2009). Constraints on the depths and temperatures of basaltic magma generation on Earth and other terrestrial planets using new thermobarometers for mafic magmas. *Earth and Planetary Science Letters*, *279*(1–2), 20–33. https://doi.org/10.1016/j.epsl.2008.12.020

Leeman, W. P. (1982). Evolved and Hybrid Lavas from the Snake River Plain, Idaho. *Idaho Bureau of Mines and Geology Bulletin*, *26*, 193–202.

Leeman, W. P., Annen, C., & Dufek, J. (2008). Snake River Plain - Yellowstone silicic volcanism: implications for magma genesis and magma fluxes. *Geological Society, London, Special Publications*, *304*(1), 235–259. https://doi.org/10.1144/SP304.12

Leeman, W. P., Menzies, M. A., Matty, D. J., & Embree, G. F. (1985). Strontium, neodymium and lead isotopic compositions of deep crustal xenoliths from the Snake River Plain: evidence for Archean basement. *Earth and Planetary Science Letters*, *75*(4), 354–368. https://doi.org/10.1016/0012-821X(85)90179-7

Leeman, W. P., Oldow, J. S., & Hart, W. K. (1992, January 1). Lithosphere-scale thrusting in the western US Cordillera as constrained by Sr and Nd isotopic transitions in Neogene volcanic rocks. *Geology*. GeoScienceWorld. https://doi.org/10.1130/0091-7613(1992)020<0063:LSTITW>2.3.CO;2

Lees, K. R. (1994). *Magmatic and Tectonic Changes Through Time in the Neogene Volcanic Rocks of the Vale Area, Oregon, Northwestern USA*. Open University, Ph.D. Thesis.

Leng, W., & Zhong, S. (2010). Surface subsidence caused by mantle plumes and volcanic loading in large igneous provinces. *Earth and Planetary Science Letters*, *291*(1–4), 207–214. https://doi.org/10.1016/j.epsl.2010.01.015

Liberty, L. M., Schmitt, D. R., & Shervais, J. W. (2015). Seismic imaging through the volcanic rocks of the Snake River Plain: Insights from Project Hotspot. *Geophysical Prospecting*, *63*(4), 919–936. https://doi.org/10.1111/1365-2478.12277

Link, P. K. (2002). Owyhee County. Retrieved from https://imnh.iri.isu.edu/digitalatlas/counties/geomaps/geomap.htm

Lipman, P. (2007). Incremental assembly and prolonged consolida- tion of Cordilleran magma chambers: Evidence from the Southern Rocky Mountain volcanic field. *Geosphere*, *3*(1), 42. Retrieved from http://geosphere.gsapubs.org/content/3/1/42.short

Liu, L., & Stegman, D. R. (2012). Origin of Columbia River flood basalt controlled by propagating rupture of the Farallon slab. *Nature*, *482*(7385), 386–389. https://doi.org/10.1038/nature10749

Loewen, M. W., & Bindeman, I. N. (2016). Oxygen isotope thermometry reveals high magmatic temperatures and short residence times in Yellowstone and other hot-dry rhyolites compared to cold-wet systems. *American Mineralogist*, *101*(5), 1222–1227. https://doi.org/10.2138/am-2016-5591

Lowenstern, J. B., & Hurwitz, S. (2008). Monitoring a supervolcano in repose: Heat and volatile flux at the yellostone caldera. *Elements*, *4*(1), 35–40. https://doi.org/10.2113/GSELEMENTS.4.1.35

Ludwig, K. R. (2003). Isoplot 3.00: a geochronological toolkit for microsoft excel. *Berkeley Geochonology Center Special Publication*.

Maccaferri, F., Bonafede, M., & Rivalta, E. (2011). A quantitative study of the mechanisms governing dike propagation, dike arrest and sill formation. *Journal of Volcanology and Geothermal Research*, *208*(1–2), 39–50. https://doi.org/10.1016/j.jvolgeores.2011.09.001

MacLean, J. W. (1994). *Geology and Geochemistry of Juniper Ridge, Horsehead Mountain, and Burns Butte: Implications for the Petrogenesis of Silicic Magma on the High Lava Plains, Southeastern Oregon*. Oregon State University, M.S. Thesis.

Mahon, K. I. (1996). The new "york" regression: Application of an improved statistical method to geochemistry. *International Geology Review*, *38*(4), 293–303. https://doi.org/10.1080/00206819709465336

Mallis, J.D., Mahood Gail A., V. J. W. . (2014). $\delta^{18}O$ of rhyolite of at High Rock caldera complex, NW Nevada: Implications for silicic magma genesis associated with mid-Miocene flood basalts. In *Geological Society of America Rocky Mountain and Cordilleran Joint Meeting*.

Manley, C.R., McIntosh, W. C. (2004). The Juniper Mountain Volcanic Center, Owyhee County, Southwestern Idaho: Age Relations and Physical Volcanology. *Idaho Geological Survey Bulletin*, *30*, 205–277.

Mattinson, J. M. (2005). Zircon U-Pb chemical abrasion ("CA-TIMS") method: Combined annealing and multi-step partial dissolution analysis for improved

precision and accuracy of zircon ages. *Chemical Geology*, *220*(1–2), 47–66. https://doi.org/10.1016/j.chemgeo.2005.03.011

McCurry, M., Hayden, K. P., Morse, L. H., & Mertzman, S. (2008). Genesis of post-hotspot, A-type rhyolite of the Eastern Snake River Plain volcanic field by extreme fractional crystallization of olivine tholeiite. *Bulletin of Volcanology*, *70*(3), 361–383. https://doi.org/10.1007/s00445-007-0143-4

Mccurry, M., & Rodgers, D. W. (2009). Mass Transfer along the Yellowstone hotspot track I: petrologic constraints on the volume of mantle-derived magma. *Journal of Volcanology and Geothermal Research*, *188*, 86–98. https://doi.org/10.1016/j.jvolgeores.2009.04.001

McDonough, W. F., & Sun, S. s. (1995). The composition of the Earth. *Chemical Geology*, *120*(3–4), 223–253. https://doi.org/10.1016/0009-2541(94)00140-4

Menand, T. (2011, March 8). Physical controls and depth of emplacement of igneous bodies: A review. *Tectonophysics*. Elsevier. https://doi.org/10.1016/j.tecto.2009.10.016

Menzies, C. D., Teagle, D. A. H., Craw, D., Cox, S. C., Boyce, A. J., Barrie, C. D., & Roberts, S. (2014). Incursion of meteoric waters into the ductile regime in an active orogen. *Earth and Planetary Science Letters*, *399*, 1–13. https://doi.org/10.1016/j.epsl.2014.04.046

Milisenda, C. C., Liew, T. C., Hofman, A. W., & Kroner, A. (1988). Isotopic Mapping of Age Provinces in Precambrian High-Grade Terrains : Sri Lanka. *The Journal of Geology*, *96*(5), 608–615. https://doi.org/10.1086/629256

Miller, C. F., Furbish, D. J., Walker, B. A., Claiborne, L. L., Koteas, G. C., Bleick, H. A., & Miller, J. S. (2011). Growth of plutons by incremental emplacement of sheets in crystal-rich host: Evidence from Miocene intrusions of the Colorado River region, Nevada, USA. *Tectonophysics*, *500*(1–4), 65–77. https://doi.org/10.1016/j.tecto.2009.07.011

Morgan, L. A., & McIntosh, W. C. (2005). Timing and development of the Heise volcanic field, Snake River Plain, Idaho, western USA. *Bulletin of the Geological Society of America*, *117*(3–4), 288–306. https://doi.org/10.1130/B25519.1

Muir-Wood, R., & King, G. C. P. (1993). Hydrological signatures of earthquake strain. *Journal of Geophysical Research: Solid Earth*, *98*(B12), 22035–22068. https://doi.org/10.1029/93JB02219

Myers, M. L., Wallace, P. J., Wilson, C. J. N., Morter, B. K., & Swallow, E. J. (2016). Prolonged ascent and episodic venting of discrete magma batches at the onset of the

Huckleberry Ridge supereruption, Yellowstone. *Earth and Planetary Science Letters*, *451*, 285–297. https://doi.org/10.1016/j.epsl.2016.07.023

Nash, B. P., Perkins, M. E., Christensen, J. N., Lee, D. C., & Halliday, A. N. (2006). The Yellowstone hotspot in space and time: Nd and Hf isotopes in silicic magmas. *Earth and Planetary Science Letters*, *247*(1–2), 143–156. https://doi.org/10.1016/j.epsl.2006.04.030

Norman, M. D., & Mertzman, S. A. (1991). Petrogenesis of Challis Volcanics From Central and Southwestern Idaho - Trace-Element and Pb Isotopic Evidence. *Journal of Geophysical Research-Solid Earth and Planets*, *96*(B8), 13279–13293. https://doi.org/10.1029/91jb00285

Norton, D., & Taylor, H. P. (1979). Quantitative simulation of the hydrothermal systems of crystallizing magmas on the basis of transport theory and oxygen isotope data: An analysis of the skaergaard intrusion. *Journal of Petrology*, *20*(3), 421–486. https://doi.org/10.1093/petrology/20.3.421

Nowell, G. M., Kempton, P. D., Noble, S. R., Fitton, J. G., Saunders, A. D., Mahoney, J. J., & Taylor, R. N. (1998). High precision Hf isotope measurements of MORB and OIB by thermal ionisation mass spectrometry: insights into the depleted mantle. *Chemical Geology*, *149*(3–4), 211–233. https://doi.org/10.1016/S0009-2541(98)00036-9

Paces, J. B., & Miller, J. D. (1993). Precise U-Pb ages of Duluth Complex and related mafic intrusions, northeastern Minnesota: Geochronological insights to physical, petrogenetic, paleomagnetic, and tectonomagmatic processes associated with the 1.1 Ga Midcontinent Rift System. *Journal of Geophysical Research*, *98*(B8), 13997. https://doi.org/10.1029/93JB01159

Pearce, J. A. (1983). Role of the Sub-continental Lithosphere in Magma Genseis at Active Continental Margins. In M. J. Hawkesworth, C.J., Norry (Ed.), *Continental Basalts and Mantle Xenoliths* (pp. 230–249). Nantwich, Cheshire, England: Shiva Publications.

Pearce, J. A., Harris, N. B. W., & Tindle, A. G. (1984). Trace element discrimination diagrams for the tectonic interpretation of granitic rocks. *Journal of Petrology*, *25*(4), 956–983. https://doi.org/10.1093/petrology/25.4.956

Peng, X., & Humphreys, E. D. (1998). Crustal velocity structure across the eastern Snake River Plain and the Yellowstone swell. *Journal of Geophysical Research*, *103*(B4), 7171–7186. https://doi.org/10.1029/97JB03615

Perkins, M. E., Brown, F. H., Nash, W. P., McIntosh, W., & Williams, S. K. (1998). Sequence, age, and source of silicic fallout tuffs in middle to late Miocene basins of the northern Basin and Range province. *Bulletin of the Geological Society of*

America, *110*(3), 344–360. https://doi.org/10.1130/0016-7606(1998)110<0344:SAASOS>2.3.CO;2

Pierce, Kenneth L.; Morgan, L. A. (1992). The track of the Yellowstone hotspot: volcanism, faulting, and uplift. *Geological Society of America Memoirs*, *179*, 1–54.

Pierce, K. L., & Morgan, L. A. (2009). Is the track of the Yellowstone hotspot driven by a deep mantle plume? - Review of volcanism, faulting, and uplift in light of new data. *Journal of Volcanology and Geothermal Research*, *188*(1–3), 1–25. https://doi.org/10.1016/j.jvolgeores.2009.07.009

Poli, S., & Schmidt, M. W. (2002). Petrology of Subducted Slabs. *Annual Review of Earth and Planetary Sciences*, *30*(1), 207–235. https://doi.org/10.1146/annurev.earth.30.091201.140550

Rahl, J. M., McGrew, A. J., & Foland, K. A. (2002). Transition from Contraction to Extension in the Northeastern Basin and Range: New Evidence from the Copper Mountains, Nevada. *The Journal of Geology*, *110*(2), 179–194. https://doi.org/10.1086/338413

Ramberg, H. (1971). Dynamic models simulating rift valleys and continental drift. *LITHOS*, *4*(3), 259–276. https://doi.org/10.1016/0024-4937(71)90006-5

Ranalli, G. (1995). *Rheology of the Earth* (2nd ed.). Springer Netherlands. Retrieved from https://books.google.com/books?hl=en&lr=&id=cBezMivXS2YC&oi=fnd&pg=PP13&dq=ranalli+rheology&ots=_JFHA-AJ4N&sig=_4zB7ABuL1_kDiho2Rurdea5pQw#v=onepage&q=ranalli rheology&f=false

Reidel, S. P., Camp, V. E., Tolan, T. L., & Martin, B. S. (2013). The Columbia River flood basalt province: Stratigraphy, areal extent, volume, and physical volcanology. *Geological Society of America Special Papers*, *497*(1), 1–43. https://doi.org/10.1130/2013.2497(01).

Rivera, T. A., Darata, R., Lippert, P. C., Jicha, B. R., & Schmitz, M. D. (2017). The duration of a Yellowstone super-eruption cycle and implications for the age of the Olduvai subchron. *Earth and Planetary Science Letters*, *479*, 377–386. https://doi.org/10.1016/j.epsl.2017.08.027

Rivera, T. A., Schmitz, M. D., Crowley, J. L., & Storey, M. (2014). Rapid magma evolution constrained by zircon petrochronology and 40Ar/39Ar sanidine ages for the Huckleberry Ridge Tuff, Yellowstone, USA. *Geology*, *42*(8), 643–646. https://doi.org/10.1130/G35808.1

Rivera, T. A., Schmitz, M. D., Jicha, B. R., & Crowley, J. L. (2016). Zircon petrochronology and 40Ar/39Ar sanidine dates for the mesa falls tuff: Crystal-scale records of magmatic evolution and the short lifespan of a large yellowstone magma chamber. *Journal of Petrology*, *57*(9), 1677–1704. https://doi.org/10.1093/petrology/egw053

Rodgers, D. W., & McCurry, M. (2009). Mass transfer along the Yellowstone hotspot track II: Kinematic constraints on the volume of mantle-derived magma. *Journal of Volcanology and Geothermal Research*, *188*(1–3), 99–107. https://doi.org/10.1016/j.jvolgeores.2009.05.014

Rosenberg, C. L., & Handy, M. R. (2005, January 1). Experimental deformation of partially melted granite revisited: Implications for the continental crust. *Journal of Metamorphic Geology*. Wiley/Blackwell (10.1111). https://doi.org/10.1111/j.1525-1314.2005.00555.x

Ruprecht, P., Bergantz, G. W., & Dufek, J. (2008). Modeling of gas-driven magmatic overturn: Tracking of phenocryst dispersal and gathering during magma mixing. *Geochemistry, Geophysics, Geosystems*, *9*(7), n/a-n/a. https://doi.org/10.1029/2008GC002022

Ryan, W. B. F., Carbotte, S. M., Coplan, J. O., O'Hara, S., Melkonian, A., Arko, R., … Zemsky, R. (2009). Global multi-resolution topography synthesis. *Geochemistry, Geophysics, Geosystems*, *10*(3), n/a-n/a. https://doi.org/10.1029/2008GC002332

Rytuba, J.J., Bateson, J.T., Curtis, D.L. Jr., Cox, G. A. (1983). Geologic map of the Little Whitehorse Creek Quadrangle, Harney and Malheur Counties, Oregon. United States Geological Survey Miscellaneous Field Studies Map MF-1472.

Rytuba, J.J., Minor, S.A., McKee, E. H. (1981). Geology of the Whitehorse caldera and caldera-fill deposits, Malheur County, Oregon. United States Geological Survey Open-File Report 81-1092.

Rytuba, J. J., & McKee, E. H. (1984). Peralkaline ash flow tuffs and calderas of the McDermitt Volcanic Field, southeast Oregon and north central Nevada. *Journal of Geophysical Research: Solid Earth*, *89*(B10), 8616–8628. https://doi.org/10.1029/JB089iB10p08616

Rytuba, J. J., & McKee, E. H. (1984). Peralkaline ash flow tuffs and calderas of the McDermitt Volcanic Field, southeast Oregon and north central Nevada. *Journal of Geophysical Research: Solid Earth*, *89*(B10), 8616–8628. https://doi.org/10.1029/JB089iB10p08616

Schmandt, B., Dueker, K., Humphreys, E., & Hansen, S. (2012). Hot mantle upwelling across the 660 beneath Yellowstone. *Earth and Planetary Science Letters*, *331–332*, 224–236. https://doi.org/10.1016/j.epsl.2012.03.025

Schmidt, M. W., & Poli, S. (1998). Experimentally based water budgets for dehydrating slabs and consequences for arc magma generation. *Earth and Planetary Science Letters*, *163*(1–4), 361–379. https://doi.org/10.1016/S0012-821X(98)00142-3

Schubert, M., Driesner, T., Gerya, T. V., & Ulmer, P. (2013). Mafic injection as a trigger for felsic magmatism: A numerical study. *Geochemistry, Geophysics, Geosystems*, *14*(6), 1910–1928. https://doi.org/10.1002/ggge.20124

Seligman, A. N., Bindeman, I. N., McClaughry, J., Stern, R. A., & Fisher, C. (2014). The earliest low and high-$\delta^{18}O$ caldera-forming eruptions of the Yellowstone plume: implications for the 30â€“40 Ma Oregon calderas and speculations on plume-triggered delaminations. *Frontiers in Earth Science*, *2*, 34. https://doi.org/10.3389/feart.2014.00034

Shaw, H. R. (1972, November 1). Viscosities of magmatic silicate liquids: an empirical method of prediction. *American Journal of Science*. American Journal of Science. https://doi.org/10.2475/ajs.272.9.870

Shervais, J. W., Evans, J. P., Schmitt, D. R., Christiansen, E. H., & Prokopenko, A. (2014). Drilling into the track of the yellowstone hot spot. *Eos*, *95*(10), 85–86. https://doi.org/10.1002/2014EO100001

Shervais, J. W., & Hanan, B. B. (2008). Lithospheric topography, tilted plumes, and the track of the Snake River-Yellowstone hot spot. *Tectonics*, *27*(5), n/a-n/a. https://doi.org/10.1029/2007TC002181

Shervais, J. W., Vetter, S. K., & Hanan, B. B. (2006). Layered mafic sill complex beneath the eastern Snake River Plain: Evidence from cyclic geochemical variations in basalt. *Geology*, *34*(5), 365–368. https://doi.org/10.1130/G22226.1

Shirley, E. K. (2013). *Precambrian history of cratonic North American crust beneat the Snake River Plain, Idaho*. Boise State University, M.S. Thesis.

Simakin, A. G., & Bindeman, I. N. (2012). Remelting in caldera and rift environments and the genesis of hot, "recycled" rhyolites. *Earth and Planetary Science Letters*, *337–338*, 224–235. https://doi.org/10.1016/j.epsl.2012.04.011

Sláma, J., Košler, J., Condon, D. J., Crowley, J. L., Gerdes, A., Hanchar, J. M., … Whitehouse, M. J. (2008). Plešovice zircon - A new natural reference material for U-Pb and Hf isotopic microanalysis. *Chemical Geology*, *249*(1–2), 1–35. https://doi.org/10.1016/j.chemgeo.2007.11.005

Sobolev, S. V, Sobolev, A. V, Kuzmin, D. V, Krivolutskaya, N. A., Petrunin, A. G., Arndt, N. T., … Vasiliev, Y. R. (2011). Linking mantle plumes, large igneous provinces and environmental catastrophes. *Nature*, *477*(7364), 312–316. https://doi.org/10.1038/nature10385

Söderlund, U., Patchett, P. J., Vervoort, J. D., & Isachsen, C. E. (2004). The176Lu decay constant determined by Lu-Hf and U-Pb isotope systematics of Precambrian mafic intrusions. *Earth and Planetary Science Letters*, *219*(3–4), 311–324. https://doi.org/10.1016/S0012-821X(04)00012-3

Solano, J. M. S., Jackson, M. D., Sparks, R. S. J., Blundy, J. D., & Annen, C. (2012). Melt segregation in deep crustal hot zones: A mechanism for chemical differentiation, crustal assimilation and the formation of evolved magmas. *Journal of Petrology*, *53*(10), 1999–2026. https://doi.org/10.1093/petrology/egs041

Stachnik, J. C., Dueker, K., Schutt, D. L., & Yuan, H. (2008). Imaging Yellowstone plume-lithosphere interactions from inversion of ballistic and diffusive Rayleigh wave dispersion and crustal thickness data. *Geochemistry, Geophysics, Geosystems*, *9*(6), n/a-n/a. https://doi.org/10.1029/2008GC001992

Steiner, A., & Streck, M. J. (2013). The Strawberry Volcanics: generation of "orogenic" andesites from tholeiite withan an intra-continental volcanic suite centered on the Columbia River flood basalt province, USA. *Geological Society, London, Special Publications*, *385*, 281–302.

Stelten, M. E., Cooper, K. M., Vazquez, J. A., Reid, M. R., Barfod, G. H., Wimpenny, J., & Yin, Q. zhu. (2013). Magma mixing and the generation of isotopically juvenile silicic magma at Yellowstone caldera inferred from coupling 238U-230Th ages with trace elements and Hf and O isotopes in zircon and Pb isotopes in sanidine. *Contributions to Mineralogy and Petrology*, *166*(2), 587–613. https://doi.org/10.1007/s00410-013-0893-2

Stelten, M. E., Cooper, K. M., Wimpenny, J. B., Vazquez, J. A., & Yin, Q. Z. (2017). The role of mantle-derived magmas in the isotopic evolution of Yellowstone's magmatic system. *Geochemistry, Geophysics, Geosystems*, *18*(4), 1350–1365. https://doi.org/10.1002/2016GC006664

Streck, M. J. (2014, September 1). Evaluation of crystal mush extraction models to explain crystal-poor rhyolites. *Journal of Volcanology and Geothermal Research*. Elsevier. https://doi.org/10.1016/j.jvolgeores.2014.07.005

Streck, M. J., Ferns, M. L., & McIntosh, W. (2015). Large, persistent rhyolitic magma reservoirs above Columbia River Basalt storage sites: The Dinner Creek Tuff Eruptive Center, eastern Oregon. *Geosphere*, *11*(2), 226–235. https://doi.org/10.1130/GES01086.1

Streck, Martin, Ferns, Mark, Haller, K.M., Wook, S. H. (2004). The Rattlesnake Tuff and other Miocene silicic volcanism in eastern Oregon. In S. H. Haller, K.M., Wood (Ed.), *Geological Field Trips in Southern Idaho, Eastern Oregon, and Northern Nevada* (pp. 5–19). United States Geological Survey Open-File Report 2004-1222.

Streck, M., Ferns, M. L., Ricker, C., & Steiner, A. (2011). The Dinner Creek Tuff and other mid-Miocene Rhyolites at the magmatic focal zone of the Columbia River Basalt Group. *Geological Society of America Abstracts with Programs*, *43*(4), 5. Retrieved from https://gsa.confex.com/gsa/2011RM/finalprogram/abstract_187459.htm

Sun, S. -s., & McDonough, W. F. (1989). Chemical and isotopic systematics of oceanic basalts: implications for mantle composition and processes. *Geological Society, London, Special Publications*, *42*(1), 313–345. https://doi.org/10.1144/GSL.SP.1989.042.01.19

Swallow, E. J., Wilson, C. J. N., Myers, M. L., Wallace, P. J., Collins, K. S., & Smith, E. G. C. (2018). Evacuation of multiple magma bodies and the onset of caldera collapse in a supereruption, captured in glass and mineral compositions. *Contributions to Mineralogy and Petrology*, *173*(4), 33. https://doi.org/10.1007/s00410-018-1459-0

Szymanowski, D., Ellis, B. S., Wotzlaw, J. F., Buret, Y., von Quadt, A., Peytcheva, I., … Bachmann, O. (2016). Geochronological and isotopic records of crustal storage and assimilation in the Wolverine Creek–Conant Creek system, Heise eruptive centre, Snake River Plain. *Contributions to Mineralogy and Petrology*, *171*(12), 106. https://doi.org/10.1007/s00410-016-1314-0

Szymanowski, D., Ellis, B. S., Bachmann, O., Guillong, M., & Phillips, W. M. (2015). Bridging basalts and rhyolites in the Yellowstone-Snake River Plain volcanic province: The elusive intermediate step. *Earth and Planetary Science Letters*, *415*, 80–89. https://doi.org/10.1016/j.epsl.2015.01.041

Taylor, H. P. (1974). The application of oxygen and hydrogen isotope studies to problems of hydrothermal alteration and ore deposition. *Economic Geology*, *69*, 843–883.

Taylor, H. P., & Forester, R. W. (1979). An oxygen and hydrogen isotope study of the skaergaard intrusion and its country rocks: A description of a 55 M.Y. old fossil hydrothermal system. *Journal of Petrology*, *20*(3), 355–419. https://doi.org/10.1093/petrology/20.3.355

Trail, D., Mojzsis, S. J., Harrison, T. M., Schmitt, A. K., Watson, E. B., & Young, E. D. (2007). Constraints on Hadean zircon protoliths from oxygen isotopes, Ti-thermometry, and rare earth elements. *Geochemistry, Geophysics, Geosystems*, *8*(6), n/a-n/a. https://doi.org/10.1029/2006GC001449

Trinquier, A., Hu, Z., Zhang, A., Schwieters, J. B., & von Quadt, A. (2016). High-precision zircon U/Pb geochronology by ID-TIMS using new 10 13 ohm resistors. In *Goldschmidt Conference Abstracts* (Vol. 31, p. 3177). The Royal Society of Chemistry. https://doi.org/10.1039/C5JA00457H

Troch, J., Ellis, B. S., Harris, C., Ulmer, P., & Bachmann, O. (2018). The effect of prior hydrothermal alteration on the melting behaviour during rhyolite formation in Yellowstone, and its importance in the generation of low-$\delta^{18}O$ magmas. *Earth and Planetary Science Letters*, *481*, 338–349. https://doi.org/10.1016/j.epsl.2017.10.039

Troch, J., Ellis, B. S., Mark, D. F., Bindeman, I. N., Kent, A. J. R., Guillong, M., & Bachmann, O. (2017). Rhyolite generation prior to a yellowstone supereruption: Insights from the Island Park-Mount Jackson rhyolite series. *Journal of Petrology*, *58*(1), 29–52. https://doi.org/10.1093/petrology/egw071

Turcotte, D. L., & Schubert, G. S. (1982). *Geodynamics: Applications of continuum mechanics to geological problems* (1st ed.). Cambridge Univ. Press.

Valley, J. W., Kitchen, N., Kohn, M. J., Niendorf, C. R., & Spicuzza, M. J. (1995). UWG-2, a garnet standard for oxygen isotope ratios: Strategies for high precision and accuracy with laser heating. *Geochimica et Cosmochimica Acta*, *59*(24), 5223–5231. https://doi.org/10.1016/0016-7037(95)00386-X

Vogt, K., Gerya, T. V., & Castro, A. (2012). Crustal growth at active continental margins: Numerical modeling. *Physics of the Earth and Planetary Interiors*, *192–193*, 1–20. https://doi.org/10.1016/j.pepi.2011.12.003

von Quadt, A., Wotzlaw, J.-F., Buret, Y., Large, S. J. E., Peytcheva, I., & Trinquier, A. (2016). High-precision zircon U/Pb geochronology by ID-TIMS using new 10 13 ohm resistors. *J. Anal. At. Spectrom.*, *31*(3), 658–665. https://doi.org/10.1039/C5JA00457H

Wagner, L., Forsyth, D. W., Fouch, M. J., & James, D. E. (2010). Detailed three-dimensional shear wave velocity structure of the northwestern United States from Rayleigh wave tomography. *Earth and Planetary Science Letters*, *299*(3–4), 273–284. https://doi.org/10.1016/j.epsl.2010.09.005

Wallace, A. R. (1993). Geologic map of the Snowstorm Mountains and vicinity, Elko and Humboldt counties, Nevada. United States Geological Survey Miscellaneous Investigations Series Map I-2394.

Wang, R., Tafti, R., Hou, Z. qian, Shen, Z. chao, Guo, N., Evans, N. J., … Li, W. kai. (2017). Across-arc geochemical variation in the Jurassic magmatic zone, Southern Tibet: Implication for continental arc-related porphyry Cu[sbnd]Au mineralization. *Chemical Geology*, *451*, 116–134. https://doi.org/10.1016/j.chemgeo.2017.01.010

Wang, W., Cawood, P. A., Zhou, M.-F., Pandit, M. K., Xia, X.-P., & Zhao, J.-H. (2017). Low-δ 18 O Rhyolites From the Malani Igneous Suite: A Positive Test for South China and NW India Linkage in Rodinia. *Geophysical Research Letters*, *44*(20), 10,298-10,305. https://doi.org/10.1002/2017GL074717

Watson, E. B., & Harrison, T. M. (1983). Zircon saturation revisited: temperature and composition effects in a variety of crustal magma types. *Earth and Planetary Science Letters*, *64*(2), 295–304. https://doi.org/10.1016/0012-821X(83)90211-X

Watts, K. E., Bindeman, I. N., & Schmitt, A. K. (2012). Crystal scale anatomy of a dying supervolcano: An isotope and geochronology study of individual phenocrysts from voluminous rhyolites of the Yellowstone caldera. *Contributions to Mineralogy and Petrology*, *164*(1), 45–67. https://doi.org/10.1007/s00410-012-0724-x

Watts, K. E., Bindeman, I. N., & Schmitt, A. K. (2011). Large-volume rhyolite genesis in caldera complexes of the Snake River Plain: Insights from the Kilgore Tuff of the Heise volcanic field, Idaho, with comparison to Yellowstone and Bruneau-Jarbidge rhyolites. *Journal of Petrology*, *52*(5), 857–890. https://doi.org/10.1093/petrology/egr005

Watts, K. E., Leeman, W. P., Bindeman, I. N., & Larson, P. B. (2010). Supereruptions of the Snake River Plain: Two-stage derivation of low-$\delta^{18}O$ rhyolites from normal-$\delta^{18}O$ crust as constrained by Archean xenoliths. *Geology*, *38*(6), 503–506. https://doi.org/10.1130/G30735.1

Werner, C., & Brantley, S. (2003). CO2 emissions from the Yellowstone volcanic system. *Geochemistry, Geophysics, Geosystems*, *4*(7). https://doi.org/10.1029/2002GC000473

Wiedenbeck, M., Hanchar, J. M., Peck, W. H., Sylvester, P., Valley, J., Whitehouse, M., … Zheng, Y.-F. (2004). Further Characterisation of the 91500 Zircon Crystal. *Geostandards and Geoanalytical Research*, *28*(1), 9–39. https://doi.org/10.1111/j.1751-908X.2004.tb01041.x

Wolff, J. A., Ramos, F. C., Hart, G. L., Patterson, J. D., & Brandon, A. D. (2008). Columbia River flood basalts from a centralized crustal magmatic system. *Nature Geoscience*, *1*(3), 177–180. https://doi.org/10.1038/ngeo124

Wolff, J. A., & Ramos, F. C. (2013). Source materials for the main phase of the Columbia River Basalt Group: Geochemical evidence and implications for magma storage and transport. *Geological Society of America Special Papers*, *497*(11), 273–291. https://doi.org/10.1130/2013.2497(11)

Woodhead, J. D., & Hergt, J. M. (2005). A preliminary appraisal of seven natural zircon reference materials for in situ Hf isotope determination. *Geostandards and Geoanalytical Research*, *29*(2), 183–195. https://doi.org/10.1111/j.1751-908X.2005.tb00891.x

Wotzlaw, J. F., Bindeman, I. N., Watts, K. E., Schmitt, A. K., Caricchi, L., & Schaltegger, U. (2014). Linking rapid magma reservoir assembly and eruption

trigger mechanisms at evolved yellowstone-type supervolcanoes. *Geology*, *42*(9), 807–810. https://doi.org/10.1130/G35979.1

Wotzlaw, J. F., Schaltegger, U., Frick, D. A., Dungan, M. A., Gerdes, A. G., & Günther, D. (2013). Tracking the evolution of large-volume silicic magma reservoirs from assembly to supereruption. *Geology*, *41*(8), 867–870. https://doi.org/10.1130/G34366.1

Wotzlaw, J.-F., Bindeman, I. N., Stern, R. A., D'Abzac, F.-X., & Schaltegger, U. (2015). Rapid heterogeneous assembly of multiple magma reservoirs prior to Yellowstone supereruptions. *Scientific Reports*, *5*, 14026. https://doi.org/10.1038/srep14026

Wotzlaw, J.-F., Buret, Y., Large, S. J. E., Szymanowski, D., & von Quadt, A. (2017). ID-TIMS U-Pb geochronology at the 0.1 ‰ level using 1013 Ω resistors and simultaneous U and $^{18}O/^{16}O$ isotope ratio determination for accurate UO2 interference correction. *J. Anal. At. Spectrom.*, *32*(3), 1–8. https://doi.org/10.1039/C6JA00278A

Wypych, A., Hart, W., Scarberry, K., Pasquale, S.A., Legge, P. W. (2010). Geologic map of the Hawks Valley-Lone Mountain region, Harney County, Oregon. Oregon Department of Geology and Mineral Industries Open-file Report 0-11-12.

Yuan, H., Dueker, K., & Stachnik, J. (2010). Crustal structure and thickness along the Yellowstone hot spot track: Evidence for lower crustal outflow from beneath the eastern Snake River Plain. *Geochemistry, Geophysics, Geosystems*, *11*(3), n/a-n/a. https://doi.org/10.1029/2009GC002787

Zheng, Y. F., Zhang, S. B., Zhao, Z. F., Wu, Y. B., Li, X., Li, Z., & Wu, F. Y. (2007). Contrasting zircon Hf and O isotopes in the two episodes of Neoproterozoic granitoids in South China: Implications for growth and reworking of continental crust. *Lithos*, *96*(1–2), 127–150. https://doi.org/10.1016/j.lithos.2006.10.003

Zhou, Q., Liu, L., & Hu, J. (2018). Western US volcanism due to intruding oceanic mantle driven by ancient Farallon slabs. *Nature Geoscience*, *11*(1), 70–76. https://doi.org/10.1038/s41561-017-0035-y

Zierenberg, R. A., Schiffman, P., Barfod, G. H., Lesher, C. E., Marks, N. E., Lowenstern, J. B., … Elders, W. A. (2013). Composition and origin of rhyolite melt intersected by drilling in the Krafla geothermal field, Iceland. *Contributions to Mineralogy and Petrology*, *165*(2), 327–347. https://doi.org/10.1007/s00410-012-0811-z